Search for the associated production of a single top quark and a Z or Higgs boson with the CMS experiment

Nicolas Tonon

Université de Strasbourg

UNIVERSITÉ DE STRASBOURG

ECOLE DOCTORALE pcp

ÉCOLE DOCTORALE DE PHYSIQUE ET CHIMIE PHYSIQUE

Institut Pluridisciplinaire Hubert Curien (IPHC), UMR 7178

THÈSE

présentée par:

Nicolas Tonon

soutenue le : **1er Octobre 2019**

pour obtenir le grade de: **Docteur de l'Université de Strasbourg**
Discipline/Spécialité: Physique des particules

Recherche de la production d'un quark top solitaire associé à un boson Z ou un boson de Higgs avec l'expérience CMS au LHC

THÈSE dirigée par:

M. Jérémy ANDREA	Institut Pluridisciplinaire Hubert Curien

RAPPORTEURS:

M. Wolfgang ADAM	Institut für Hochenergiephysik
M. Dirk ZERWAS	Laboratoire de l'Accélérateur Linéaire

AUTRES MEMBRES DU JURY:

Mme Sandrine COURTIN	Institut Pluridisciplinaire Hubert Curien, Unistra
M. Marco MUSICH	Karlsruhe Institute of Technology
Mme Justine SERRANO	Centre de physique des particules de Marseille
M. Jean-Laurent AGRAM	Institut Pluridisciplinaire Hubert Curien,
(co-encadrant)	Université de Haute Alsace
M. Nicolas CHANON	Institut de Physique Nucléaire de Lyon
(co-encadrant)	

A ma famille.

Acknowledgements

Ce manuscript représente l'aboutissement d'une thèse de 3 ans réalisée à l'IPHC, ainsi que le point culminant de mes 8 années d'études à l'Université de Strasbourg. Rétrospectivement, ce qui me frappe le plus, c'est la combinaison d'évènements fortuits ou provoqués qui m'ont mené jusqu'ici, et qui pourraient donner l'impression d'un parcours linéaire et prémédité vu de l'extérieur.

Au contraire, que ce soit à la fin du lycée (lorsque j'ai, un peu par hasard et en-dehors des cours, commencé à sérieusement m'intéresser à la physique et à considérer de poursuivre dans cette voie), en licence (dont chaque année fut marquée par sot lot d'incertitude quant à la suite), ou durant mon master (que l'on m'a heureusement encouragé à suivre, ne serait-ce que pour la satisfaction d'aller "au bout" de cette passion, même si une thèse me semblait alors inaccessible), je me suis rarement senti en pleine maitrîse de mon propre parcours.

A présent, être arrivé aussi loin me paraît à la fois relever d'un concours de circonstances heureuses, et représenter la conclusion inéluctable de ce parcours entamé il y a plusieurs années. Quoiqu'il en soit, je veux profiter de ces lignes pour remercier tous ceux qui m'ont accompagné durant cette période.

Tout d'abord, j'aimerais remercier tous les membres de mon jury pour avoir accepté d'en faire partie, et pour l'investissement que cela représente. En particulier, je remercie mes rapporteurs Wolfgang Adam et Dirk Zerwas pour avoir lu attentivement mon manuscript et m'avoir fait des retours pertinents.

Ensuite, j'aimerais remercier très chaleureusement mes directeurs de thèse : Jérémy, Nicolas et Jean-Laurent. Je me considère très chanceux d'avoir travaillé et appris auprès de vous durant ces 3 années. La complémentarité de vos domaines d'expertise (et de vos disponibilités !) a été très profitable pour moi et se reflète directement dans mon travail.

Mais ce qui a le plus compté était vos points communs : votre patience et votre disponibilité pour m'aider à comprendre des concepts avancés et développer mon sens critique, votre bonne humeur au travail et en-dehors, et surtout votre enthousiasme et vos encouragements répétés tout au long de cette thèse qui ont été déterminants pour que je trouve du sens et de la sastisfaction à réaliser mes analyses. Ajoutons à cela l'optimisme communicatif (et l'humour parfois douteux) de Jérémy, l'équilibre décontraction-sérieux de Nicolas (dont la participation à l'organisation des JRJC était absolument nécessaire... c'était *cher bien* !), le flegme et la gentillesse de Jean-Laurent (qui heureusement était présent physiquement à l'IPHC, car nos téléphones auraient rendu compliquées des communications via Skype), et l'on obtient les conditions idéales pour être motivé à fournir le meilleur de soi-même.

Au final Jérémy, nous n'avons toujours pas définitivement tranché la question de savoir qui avait eu le plus de "chance" : toi parce que j'ai choisi ton sujet et ai mené à bien le projet, ou bien (plus probablement) moi pour m'être trouvé au bon endroit au bon moment pour obtenir une bourse de thèse sur un sujet qui me convenait parfaitement.

En tout cas, je crois que cette thèse s'est déroulée au mieux pour nous tous. Comme vous l'avez gentiment mentionné à l'issue de ma soutenance, notre relation a très rapidement évolué au-delà d'un simple rapport "directeur-étudiant" ; je vous considère avant tout comme des collègues et amis, et espère que nos chemins seront amenés à se recroiser très souvent dans le futur. Et laissez-moi répéter une dernière fois ici que je vous dois beaucoup.

Au-delà de mes directeurs, c'est l'ensemble du groupe CMS de Strasbourg que je tiens à remercier, et avec lequel je compte bien garder le contact. Un groupe accueillant, bienveillant, disponible. Partager les pause-cafés (et plus) avec vous a parfois constitué une soupape nécessaire pour garder un moral élevé. Merci aussi aux informaticiens et à Nadine pour leur efficacité et leur soutien technique et logistique.

Une mention spéciale pour Eric Chabert, qui m'a accepté en stage en L3 puis à nouveau en M1, à des moments clés pour mon orientation. Tu as ainsi directement influé sur mon parcours en prenant beaucoup de ton temps pour me faire découvrir l'expérience CMS et me transmettre de ta curiosité scientifique. Merci beaucoup pour ta disponibilité au cours de ma thèse, pour nos discussions très enrichissantes (le plus souvent au pas de course, littéralement) qui m'ont aidé à prendre du recul sur mes travaux.

Je salue également tous les doctorants du groupe : Michaël (l'ancien), Xavier (le turbo-capitaliste), Marketa (it was a pleasure to share the office with you during these 2 years !), Guillaume (qui a un immense respect pour le punch), Clément, Robin et Natalia. Je souhaite bonne chance aux petits nouveaux, Douja et Dylan, la relève est assurée !

Plus généralement, je salue tous les étudiants et post-docs que j'ai cotoyé ces dernières années, qu'ils ont largement contribué à rendre agréables, surtout durant les pauses déjeuner suivies de parties de Dourak endiablées, de parties de fléchettes, et parfois même d'exterminations de robots en réalité virtuelle (on n'arrête pas le progrès). Mentionnons en vrac : Salva, Rodrigo, Sviat, Luka, Reem, Feifei, Irene, Guigui, Rémi, ... et les autres.

J'en profite aussi pour mentionner ici tous ceux et celles rencontrés dans le cadre du foot sur le campus, et qui m'ont aidé à garder la forme pendant la thèse !

Une mention très spéciale pour Bart, une belle rencontre (grazie per tutte le cene che hai preparato... spero che ne condivideremo tante altre !), et surtout Daniel, mon alter ego rencontré en M2 (en moins ginseng, moins gendre idéal, et moins stakhanoviste peut-être). L'un des meilleurs souvenirs de cette thèse restera la

semaine de conférence passée à Lake Louise entre hôtel de rêve et ski dans les Rocheuses... vite éclipsée par la semaine passée à New-York. On ne le répètera jamais assez : "on a fait ça très bien" (et big up à Vinnie's).

Un grand merci à mes amis avec qui j'ai évolué pendant toutes ces années (allez, par ordre alphabétique) : les anciens (Lucien, Momo, Nico), tout le groupe "du lycée" toujours fidèle au poste et avec lequel on n'a pas fini de passer des super moments (Adri, Caro, Charly, Emilie, Flo, Hugo, Laura, Léa, Mathilde, Morgane, Myriam, Pauline, Perrine, ...), les collègues de licence qui sont devenus bien plus que ça (JY, Manu, Olivia, Rodrigue, Tim, Thomas, Victor 1 et 2, ...). Big up à "la coloc" chez qui j'ai passé bon nombre de soirées arrosées (Aurélie, Colin, Hector, Jacques, Thibaut) et à la "Churchill connection" (Aurel, Franz, Lucas, Seb).

Désolé à ceux que j'oublie ici, j'essayerai de me faire pardonner quand on se reverra... !

Je veux terminer par remercier toute ma famille, dont l'amour et le soutien sans faille ont rendu possible ma réussite. Je remercie du fond du coeur mes parents de m'avoir toujours encouragé et permis d'étudier dans les meilleures conditions possibles ; chacun à votre manière, vous avez fait de moi qui je suis aujourd'hui. J'embrasse mon grand frère Diego : toi toujours plus au sud, moi toujours plus au nord, mais on finira toujours par se retrouver quand on en prend le temps !

Je remercie de tout mon coeur mon parrain et ma marraine, qui depuis tout petit ont stimulé ma curiosité et contribué à m'ouvrir l'esprit, et avec qui je n'ai pas fini d'avoir des échanges passionants sur tout type de sujet.

Une pensée à tous les autres membres de ma famille proche, dont certains sont partis mais continuent de m'inspirer : mes grand parents, Giordano, mes oncles et tantes et mes chers cousins.

Enfin je veux dire tout mon amour à Eva, qui est à mes côtés depuis le début de mon voyage en physique des particules, et a rendu toutes ces années heureuses.

Contents

Introduction

Developed between the late 1960s and the mid-1970s, the standard model (SM) of particle physics represents our best understanding of physics phenomena at the most fundamental scales. It provides a unified picture for all known elementary particles — the building blocks of matter — and the way they interact via 3 of the 4 fundamental forces. Over the decades, the SM has been tested extensively by a broad variety of experiments. It is able to successfully explain almost all experimental results over a wide energy range, at times with a precision unmatched in any other field of physics. Its great predictive power was again remarkably exemplified by the discovery of the long sought-after Higgs boson in 2012 at CERN's Large Hadron Collider (LHC), the last predicted SM particle which had not yet been observed.

However, the SM is not the ultimate theory of everything, and falls short of explaining several well-established observations: for instance it does not incorporate the gravitational force, nor does it explain what is dark matter, or how neutrinos acquire mass. This suggests that the SM only corresponds to a low-energy approximation to a more fundamental theory beyond the standard model (BSM). Modern high-energy physics experiments seek to probe as precisely as possible the predictions of the SM, and to search for new phenomena predicted by BSM scenarios, in order to gain deeper insight into the laws underlying the physics of the subatomic world.

The LHC is the world's largest and most powerful accelerator, conceived to cover a broad physics programme. It can collide protons and heavy ions, and hosts 4 major experiments: ALICE, LHCb, ATLAS and CMS. The latter two are general-purpose

experiments. They observed jointly the Higgs boson in 2012 at a mass of 125 GeV, less than 3 years after the start of the LHC. This thesis started in October 2016, 1 year after the beginning of the Run 2 data-taking period (2015–2018). During this period, the LHC produced collisions at the unprecedented centre-of-mass energy $\sqrt{s} = 13$ TeV and with increased instantaneous luminosity, allowing the experiments to collect statistics at an ever-faster rate.

The very high energy reached at the LHC makes it the only accelerator in the world currently capable of producing the Higgs boson and the yet heavier top quark. Due to its unique properties, among which its very strong coupling to the Higgs boson, physicists are wondering whether the top quark may play a special role in the theory. Since its discovery in 1995 at the Tevatron, the precise measurement of its properties gave rise to a very interesting and fertile research field.

This thesis focuses on the searches for the associated production of a single top quark and a Z boson (tZq) or a Higgs boson. The latter mechanism is commonly denoted tH, which refers both to the tHq and tHW processes, corresponding to different production modes of the single top quark (t- or tW-channel). Single top quarks are produced alone via the electroweak interaction, by opposition to the predominant pair production mode related to the strong interaction.

These studies are based on the data collected at $\sqrt{s} = 13$ TeV by CMS, and target events wherein the unstable particles (top quark, Z or Higgs boson) decay into leptons. The very rare tZq and tH processes could be studied at the LHC for the first time. Both of these studies are well motivated, as they probe the SM in unique ways while being sensitive to potential new physics effects. These analyses are quite challenging, as they both target a very rare signal in the presence of much larger background processes, which requires the use of advanced signal extraction techniques.

However, the extended experimental reach of the LHC comes at the cost of increased radiation damages for the detectors. In particular, the CMS silicon tracker is the device closest to the interaction point, and is subjected to extreme levels of radiation. This may degrade the properties of the tracker sensors in the long-run, a process called ageing. This detector allows for the precise measurement of the trajectories and momenta of charged particles, hence maintaining its excellent performance is of crucial importance for the CMS experiment. During this thesis, I carried out a study aimed at monitoring the ageing of the silicon strip tracker using dedicated data.

This thesis is organised as follows. The first chapter gives a description of the standard model, its main theoretical ingredients and its shortcomings. All the concepts necessary to understand the physics analyses are introduced. A particular emphasis is put on the description of the properties of the top quark and the Higgs boson, as they are at the core of this thesis work.

The second chapter presents the LHC and the CMS detector. It aims at explaining the way the data are produced, and how they are processed in order to provide an accurate description of the outcome of a collision. The role of each subdetector is described and its performance discussed. The algorithm used to reconstruct particles is presented. Moreover, the typical workflow for the generation of the simulations which are compared to the data is introduced.

Chapter 3 presents a study aimed at monitoring the ageing of the CMS strip tracker. After introducing the main concepts related to silicon sensors and radiation damages, the principle of this analysis and the processing of the dedicated data are explained. Different methods are compared for the extraction of results, with a focus on the method which I improved significantly. This method is the one used to produce the final results, several of which were approved and made public. Finally, the limitations of this analysis are discussed, as well as possible solutions and alternatives.

Chapter 4 describes a search for the associated production of a single top quark and a Z boson (tZq). This rare process is very interesting because it probes directly the coupling of the top quark to the Z boson. It is also sensitive to the possible existence of BSM particles or interactions, such as flavour-changing neutral currents (FCNCs). In addition, it represents a background to other important analyses, such as the one described in Chapter 5, which motivates the precise measurement of the tZq cross section.

After introducing the context and motivations of this analysis in more details, the sources of backgrounds contaminating this search are discussed. The particle reconstruction and the selections used to define different *regions* enriched either in signal or background events are presented, and the estimation of the most challenging background directly from the data is detailed. We motivate the use of advanced techniques based on machine-learning and the matrix element method in order to signicantly improve the separation of the signal from background processes. The sources of systematic uncertainty are listed, and an overall description of the statistical model used to obtain the results is given. Finally, the results are presented and discussed. They represent the first statistical evidence for the existence of the tZq process.

Lastly, Chapter 5 presents a search for the associated production of a single top quark and a Higgs boson (tH). This process is of special interest, as it is the only process which is sensitive at the same time to the magnitude and relative sign of the top-Higgs coupling without requiring any assumption regarding new physics. It is also sensitive to the possible violation of the charge-parity (CP) symmetry in interactions of the top quark with scalar particles like the Higgs boson, and to different

types of FCNC interactions. This makes the tH process a unique probe of a key SM parameter, and a potential gateway to new physics.

After giving a broad overview of the context and motivations to study the tH process, the particle reconstruction and event selection are detailed. The data-driven procedure for the estimation of reducible backgrounds is explained. The treatment of systematic uncertainties and the signal extraction are described. The final results are presented and put into perspective.

Furthermore, this main analysis was re-adapted in order to search for top-Higgs FCNC interactions, denoted tH-FCNC. FCNC interactions are strongly suppressed within the SM and are expected to be undetectable, hence any indication to the contrary would represent an unambiguous sign of new physics. After recalling the context of this study, the differences with the main analysis are highlighted. Finally, the results are discussed. This analysis places the most stringent upper limits to date on the cross sections of the tH-FCNC processes.

Introduction (FR)

Développé entre la fin des années 1960 et le milieu des années 1970s, le modèle standard (*standard model*, SM) de la physique des particules représente l'état actuel de la connaissance des lois physiques aux échelles les plus fondamentales. Il fournit une vision d'ensemble de toutes les particules élémentaires connues – les constituants de base de la matière – et de leurs interactions via 3 des 4 forces fondamentales. Au cours des décennies suivantes, les prédictions du SM ont été vérifiées par un grand nombre d'expériences diverses. Ce modèle est en mesure d'expliquer presque tous les résultats expérimentaux, couvrant une vaste échelle d'énergie, parfois avec un niveau de précision sans équivalent dans d'autres domaines de la physique. Récemment, son pouvoir prédictif a été illustré une nouvelle fois de façon remarquable par la découverte du boson de Higgs en 2012 au Grand Collisionneur de Hadrons (*Large Hadron Collider*, LHC) du CERN, près de 50 ans après que son existence ait été postulée. Il s'agissait de la dernière particule prédite par le SM à n'avoir pas été encore observée.

Cependant, le SM ne constitue pas une ultime théorie du tout, et n'est pas en mesure d'expliquer un certain nombre d'observations solidement établies : par exemple il n'inclut pas la force gravitationnelle, n'explique pas de quoi

est constituée la matière noire, ni comment les neutrinos obtiennent leurs masses. Ceci suggère que le SM ne représente qu'une approximation à basse énergie d'une théorie plus fondamentale "au-delà du modèle standard" (*beyond the standard model*, BSM). De nos jours, les expériences de physique des hautes énergies visent à sonder en profondeur les prédictions du SM, ainsi qu'à rechercher des phénomènes de nouvelle physique postulés par les nombreux modèles BSM, dans le but de raffiner notre compréhension des lois physiques qui régissent le monde subatomique.

Le LHC est l'accélérateur le plus grand et le plus puissant au monde, conçu pour couvrir un vaste programme de physique. Il peut produire des collisions de protons et d'ions lourds, et accueille quatre expériences principales : ALICE, LHCb, ATLAS et CMS. Les deux derniers sont des détecteurs dits généralistes. Ils ont observé conjointement le boson de Higgs pour la première fois en 2012 à une masse de 125 GeV, moins de trois ans après le démarrage du LHC.

Cette thèse a débuté en octobre 2016, un an après le début de la période de prise de données appelée "Run 2" (2015–2018). Durant cette période, le LHC a produit des collisions de protons à une énergie dans le centre de masse inégalée $\sqrt{s} = 13$ TeV, et avec une luminosité instantanée accrue, ce qui a permis aux expériences de collecter des données à un rythme encore plus rapide qu'auparavant.

L'énergie record atteinte par le LHC fait de lui le seul accélérateur au monde actuellement en mesure de produire le boson de Higgs, ainsi que le quark top qui est encore plus massif. Les propriétés uniques du quark top, parmis lesquelles son couplage très intense au boson de Higgs, suggèrent que cette particule pourrait jouer un rôle à part dans le SM. Depuis sa découverte en 1995 au Tevatron, les mesures de précision des propriétés du quark top ont donné lieu à un champ de recherche particulièrement fertile.

L'axe principal de cette thèse est la recherche de la production associée d'un quark top solitaire et d'un boson Z (tZq) ou un boson de Higgs. Ce dernier mécanisme est communément noté tH, ce qui désigne à la fois les processus tHq et tHW, qui correspondent à deux modes de production distincts du quark top solitaire (*canaux t* et *tW* respectivement). Les quarks top solitaires sont

produits seuls via l'interaction électrofaible, par opposition au mode dominant de production par paire via l'interaction forte.

Ces études utilisent des données collectées à $\sqrt{s} = 13$ TeV par CMS, et recherchent des évènements dans lesquels les particules instables (quark top, boson Z, boson de Higgs) se désintègrent en leptons. Les processus rares tZq et tH ont été étudiés pour la première fois au LHC. Ces deux études présentent un grand intérêt, car elles permettent toutes deux de sonder le SM de façons uniques, tout en étant sensible à de potentiels effets de nouvelle physique. Le principal défi posé par ces analyses est le besoin d'isoler un signal très rare en présence de bruits de fond bien plus conséquents, ce qui rend nécessaire l'utilisation de techniques avancées pour l'extraction du signal.

La réussite du vaste programme de physique du LHC dépend en très grande partie de l'excellente performance des détecteurs, qui doivent fonctionner dans des conditions extrêmes. En particulier, le trajectographe à pistes de silicium de CMS est le sous-détecteur le plus proche du point de collision, et est soumis à des niveaux de radiation très élevés. Ceci pourrait engendrer une dégradation progressive des propriétés de ses senseurs, ce que l'on appelle le *vieillissement*. Le trajectographe permet la mesure précise des trajectoires et impulsions des particules chargées ; c'est pourquoi il est primordial pour l'expérience CMS de maintenir les excellentes performances de ce détecteur. Au cours de cette thèse, j'ai réalisé une étude visant à surveiller l'évolution du vieillissement du trajectographe à pistes.

Cette thèse est organisée de la façon suivante. Le premier chapitre décrit le contenu du modèle standard, ses principaux fondements théoriques ainsi que ses limites. Nous introduirons tous les concepts nécessaires à la compréhension des analyses présentées par la suite. Un accent particulier est mis sur la description des propriétés du quark top et du boson de Higgs, qui sont au coeur de ce travail de thèse.

Le deuxième chapitre présente le LHC et l'expérience CMS. Le but de ce chapitre est d'expliquer la façon dont sont produites les données, ainsi que la façon dont elles sont traitées afin d'obtenir une description fiable du résultat

d'une collision. Le rôle de chaque sous-détecteur sera décrit, et ses performances discutées. L'algorithme utilisé pour reconstruire les particules à partir des informations des sous-détecteurs sera présenté. De plus, nous donnerons une vue d'ensemble des principales étapes nécessaires à la génération des simulations Monte-Carlo qui sont comparées aux données.

Le Chapitre 3 présente une étude visant à étudier le vieillissement du trajectographe à pistes de CMS. Après avoir introduit les principaux concepts liés aux détecteurs en silicium et aux dégâts causés par les radiations, le principe de l'analyse et le traitement des données seront décrits. Différentes méthodes seront comparées pour l'obtention des résultats, dont une méthode que j'ai sensiblement améliorée durant ma thèse. Cette méthode est utilisée pour produire les résultats finaux, dont plusieurs ont été approuvés par la collaboration CMS et rendus publics. Enfin seront discutées les limites de cette analyse, ainsi que de possibles solutions et alternatives.

Le Chapitre 4 décrit une recherche de la production associée d'un quark top solitaire et d'un boson Z (tZq). Ce processus rare est très intéressant car il permet de sonder directement le couplage du quark top au boson Z. Il est également sensible à l'existence éventuelle de particules ou interactions de nouvelle physique, tels que les changements de saveur par courant neutre (*flavour-changing neutral current*, FCNC). De plus, ce processus constitue un bruit de fond pour d'autres analyses importantes, telles que celle qui est présentée dans le Chapitre 5, ce qui justifie d'autant plus la mesure précise de la section efficace de tZq.

Après avoir introduit le contexte et les motivations de cette analyse en détails, les sources de bruit de fond qui compliquent cette étude seront discutées. La reconstruction des particules et les sélections utilisées pour définir différentes *régions* enrichies soit en évènements de signal ou de bruit de fonds seront présentées, et l'estimation du bruit de fond principal directement à partir des données sera décrite. Nous justifierons l'usage de techniques avancées basée sur l'apprentissage automatisé (*machine learning*) et la méthode des éléments de matrice (*matrix element method*, MEM), qui permettent d'améliorer significativement la séparation du signal et des processus de bruit de fond.

Nous décrirons les sources d'incertitude systématique qui sont considérées, et donnerons une description du modèle statistique utilisé pour obtenir les résultats. Enfin, les résultats seront discutés. Ils représentent la première "évidence" (au sens statistique du terme) de l'existence du processus tZq.

Le Chapitre 5 présente une recherche de la production associée d'un quark top solitaire et d'un boson de Higgs (tH). Ce processus est particulièrement intéressant car il est le seul à être sensible à la fois à la magnitude et au signe relatif du couplage top-Higgs, sans qu'il soit nécessaire de faire des hypothèses concernant d'éventuels phénomènes de nouvelle physique. Ce processus est également sensible à une possible violation de la symmétrie de charge-parité (CP) dans les interactions du quark top avec des particules scalaires comme le boson de Higgs, et à différents types d'interactions FCNC. Le processus tH permet donc de sonder de façon unique un paramètre clé du SM, et son étude pourrait constituer une piste privilégiée vers la nouvelle physique.

Après avoir donné une vision d'ensemble du contexte et des motivations pour l'étude du processus tH, nous présenterons la reconstruction des particules et la sélection des évènements. Nous détaillerons les procédures d'estimation des bruits de fond réductibles à partir des données. Nous décrirons le traitement des incertitudes systématiques considérées, ainsi que la procédure d'extraction du signal. Puis, les résultats finaux seront présentés et mis en perspective.

D'autre part, cette analyse principale a été ré-adaptée dans le but de rechercher des interactions FCNC mettant en jeu le quark top et le boson de Higgs, notées tH-FCNC. De façon générale, les interactions FCNC sont fortement supprimées dans le cadre du SM et sont a priori largement hors de portée de la précision expérimentale actuelle ; c'est pourquoi la preuve du contraire constituerait un signe clair de nouvelle physique. Après avoir rappelé le contexte de cette étude, les différences avec l'analyse principales seront explicitées. Enfin, les résultats seront présentés et discutés. Cette analyse place les meilleures limites actuelles sur les sections efficaces des processus tH-FCNC.

CHAPTER 1

The standard model of particle physics

1.1 Introduction to the standard model

Developed throughout the second half of the XXth century, the standard model (SM) of particle physics describes the elementary particles and their interactions. Built upon the mathematical foundations of quantum field theory and gauge symmetries, it results from a constant back and forth between theory and experiment. The SM provides a unified picture and a valid description of the physics phenomena observed at the scales probed by ever more powerful particle accelerators. The discovery of the Higgs boson [1, 2] at the LHC [3, 4] in 2012, almost 50 years after its existence was first postulated, demonstrated once more the great predictive power of the SM.

The standard model describes fundamental interactions as the exchange of mediator particles called *gauge bosons*. All gauge bosons included in the SM are vector bosons: they have a spin equal to 1 and obey Bose-Einstein statistics. The best-known among them is the photon, which is the force-carrier associated with the electromagnetic interaction. The $W^{\pm}$ and Z bosons are the mediators of the weak nuclear force, while the strong nuclear force is mediated by gluons. Although the gravitational force is not accounted for in the SM, its intensity is so weak compared to the other interactions (many orders

of magnitude lower) that it can be neglected at the considered energy scales. Finally, the recently discovered Higgs boson plays a unique role. It is a scalar boson of spin 0 associated with the so-called Higgs mechanism, through which the $W^{\pm}$ and Z bosons acquire their masses (as explained in section 1.5).

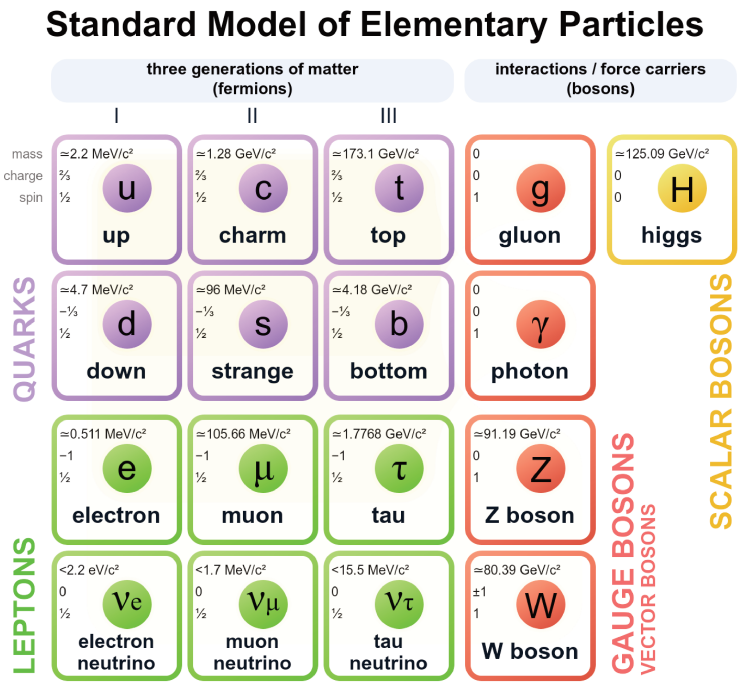

Figure 1.1: Categorisation of the elementary particles of the standard model.

In opposition to bosons, the *fermions*, which are the constituents of matter, are half-spin particles satisfying the Fermi-Dirac statistics and the Pauli exclusion principle. They are further categorised as leptons or quarks.

The six *flavours* of leptons are grouped in 3 separate generations, composed respectively of the electron (e), muon (μ) and tau (τ) leptons, and the corresponding electrically-neutral neutrinos (ν_e, ν_μ, ν_τ). Charged leptons are sensitive to the electromagnetic and weak interactions, and have an integer electric charge of -1. Neutrinos only interact via the weak force and are considered massless in the SM, although it was proven experimentally that their masses must be extremely small but non-zero (see Sec. 1.8.1). Thus they interact very weakly and can only be detected with dedicated experiments.

Quarks also come in 6 different flavours and are organised in 3 generations, comprising respectively the up (u) and down (d) quarks, the charm (c) and strange (s) quarks, and the top (t) and bottom (b) quarks. They are sensitive to the 3 interactions included in the SM, and they have a fractional electric charge of either $+\frac{2}{3}$ or $-\frac{1}{3}$. Due to the particular behaviour of the strong force, quarks can not exist freely but only confined together into composite *hadrons*, such as protons and neutrons.

All fermions also exist as *antiparticles*, which are identical in every aspect except that they have opposite internal quantum numbers (such as the electric charge). For both leptons and quarks, the 3 generations are ordered by increasing mass, and particles of higher generations will decay into lower mass ones. For this reason, 3 first-generation particles only make up all the ordinary matter: up and down quarks bound into protons and neutrons which form the atoms' nuclei, around which electrons orbit (in the semi-classic formalism). The study of higher-generation particles requires high-energy experiments, using either accelerators or cosmic rays. Figure 1.1 summarises all the particles included in the SM and their categorisations.

1.2 Introduction to quantum field theory

Quantum field theory (QFT) is the theoretical framework used to build the physics models describing the subatomic world. Its development started with the advent of special relativity (SR) and quantum mechanics (QM) at the beginning of the XXth century, out of the need for a theory compatible with the new paradigms introduced by these two scientific revolutions. Notably, the discovery of wave-particle duality motivated the introduction of fields as the most fundamental objects describing reality.

1.2.1 Fields and symmetries

Fields and Lagrangian formulation

At the very core of QFT lies the idea that any particle or wave in the universe corresponds to the excitation of a quantum field. A field is a quantity whose values are defined everywhere in spacetime. Similarly to classical field theory from which it inherits, QFT expresses the dynamics and interactions of a system using the Lagrangian mathematical formulation.

To describe the continuous systems considered by QFT, one has to define the *Lagrangian density* $\mathcal{L}(\psi_i, \partial_\mu \psi_i, x^\mu)$, hereinafter simply referred to as Lagrangian, depending on the fields ψ_i and their derivatives $\partial_\mu \psi_i$ with respect to the spacetime coordinates $x^\mu = (t, x, y, z)$.

For example, let us consider the Dirac Lagrangian defined as:

$$\mathcal{L}_\mathcal{D} = i\bar{\psi}\gamma^\mu \partial_\mu \psi - m\bar{\psi}\psi\,, \tag{1.1}$$

where γ^μ are the Dirac matrices and $\bar{\psi} \equiv \psi^\dagger \gamma^0$ is the Dirac adjoint of ψ. The action S is defined as the integral of the Lagrangian density over the spacetime coordinates:

$$S = \int \mathcal{L}\ dt\ dx\ . \tag{1.2}$$

From the principle of least action:

$$\partial S = \frac{\partial \mathcal{L}}{\partial \psi} - \partial_\mu \left(\frac{\partial \mathcal{L}}{\partial(\partial_\mu \psi)}\right) = 0\,, \tag{1.3}$$

one can obtain the equations of motion of the system. For the Dirac Lagrangian, solutions to these equations are 4-components spinor fields. They can be interpreted as free fermions (and antifermions) of mass m, satisfying the dispersion relation $E^2 = (pc)^2 + (mc^2)^2$.

Symmetries

Symmetries play a major role in our understanding of particle physics, and are a central concept to many important theories in general. For instance, special relativity is based upon the Lorentz symmetry, making the speed of light constant in all reference frames. Symmetries can either be *continuous* (e.g. the rotational symmetry of a circle), or *discrete* (e.g. the rotational symmetry of a square, as only rotations by specific amounts will preserve its appearance). Furthermore, it is possible to distinguish between *external* symmetries, which correspond to transformations of the spacetime coordinates, and *internal* symmetries acting specifically on the fields (independently of spacetime).

From the QM standpoint, a system is said to exhibit a symmetry if its physical predictions are *invariant* under a wave function transformation:

$$\psi \to \psi' = \hat{\mathcal{U}}\psi\,, \tag{1.4}$$

where $\hat{\mathcal{U}}$ is a transformation operator. If the operator is constant everywhere in spacetime, the symmetry is said to be *global* (otherwise *local*). Invariant quantities lead to conservation laws: for example the conservation of energy is a consequence of physics being invariant under time translation. A set of symmetry operations which satisfies specific properties (*closure*, *identity*, *inverse* and *associativity*) forms a *group* [5]. If all elements of a group commute[1], it is said to be *Abelian*. Any symmetry group can be represented by a group of matrices.

Noether's theorem [6, 7] states that if the Lagrangian of a system is invariant under a continuous symmetry, it implies that an associated quantity must be conserved. For example it can be trivially seen that applying the global U(1)[2] transformation:

$$\begin{aligned} \psi &\to e^{i\alpha}\psi\,, \\ \bar{\psi} &\to e^{-i\alpha}\bar{\psi}\,, \end{aligned} \tag{1.5}$$

[1] Two elements $\hat{A}$ and $\hat{B}$ of a group commute if they satisfy: $[\hat{A}, \hat{B}] = \hat{A}\hat{B} - \hat{B}\hat{A} = 0$.

[2] U(1) is the one-dimensional unitary group, i.e. any of its elements can be expressed as a 1×1 matrix whose inverse is equal to its transpose conjugate ($U^{-1} = \tilde{U}^*$). Applying a U(1) transformation amounts to a multiplication by a complex phase. It is an Abelian group.

to the Dirac Lagrangian (Eq. 1.1) will leave it invariant. As a consequence of Noether's theorem, this symmetry gives rise to a conserved current $j^\mu(x)$ implying a conserved charge $\mathcal{Q}$:

$$\begin{aligned} \partial_\mu j^\mu(x) &= 0\,, \\ \mathcal{Q} = \int d^3x \frac{\partial j^0}{\partial t} &= 0\,. \end{aligned} \tag{1.6}$$

We say that this Lagrangian possesses a global U(1) symmetry.

1.2.2 Gauge theories

There is a particular kind of invariance which is of crucial importance for QFT, called *gauge invariance*. Gauge invariance does not arise from a physical symmetry, but rather from a redundancy in the mathematical description of a system. A *gauge transformation* can be seen as the arbitrary rotation of the phase ("gauge") associated with this degree of freedom, leaving the predictions unchanged. A possible analogy is the arbitrary definition of the zero ("ground") potential when using a voltmeter, since we are only measuring *differences* of potential.

Applying such a transformation is trivial in the case of global gauge invariance. On the opposite, making the gauge transformation depend on the spacetime location:

$$\begin{aligned} \psi \to \psi' &= \psi e^{iq\alpha(x)}\,, \\ \bar{\psi} \to \bar{\psi}' &= \bar{\psi} e^{-iq\alpha(x)}\,, \end{aligned} \tag{1.7}$$

yields very important results.

For instance, the Dirac Lagrangian of Eq. 1.1 is not invariant under this local gauge transformation, as the derivative will now act upon $\alpha(x)$, and it becomes:

$$\mathcal{L}_\mathcal{D} \to \mathcal{L}'_\mathcal{D} = \mathcal{L}_\mathcal{D} - q\bar{\psi}\gamma^\mu \partial_\mu \alpha(x)\psi\,. \tag{1.8}$$

However, the invariance can be recovered through the procedure of *gauge fixing*, which will cancel the problematic term. This is achieved by replacing ordinary derivatives with *covariant derivatives* defined as:

$$D_\mu = \partial_\mu + iqA_\mu(x)\,, \tag{1.9}$$

and requiring that the new vector field $A_\mu(x)$ transforms according to:

$$\psi \to \psi e^{iq\alpha(x)}\,,\; A_\mu \to A_\mu(x) - \frac{1}{q}\partial_\mu \alpha(x)\,, \tag{1.10}$$

where the constant q is the coupling strength indicating the magnitude of the coupling of $A_\mu(x)$ to other fields. For this field to be physical, a dedicated kinetic term must be added to the Lagrangian. It describes the propagation of the spin-1 quanta associated with A_μ, called gauge bosons.

Therefore, enforcing the local gauge invariance of the Lagrangian induces the existence of a field having its own dynamics and interactions, and which according to Noether's theorem is associated with a conserved charge. The SM describes the 3 fundamental forces with gauge theories obtained with such procedures, as presented in Sec. 1.3 and 1.4.1.

1.2.3 Feynman diagrams

Feynman diagrams are graphical representations of the mathematical description of the interactions between subatomic particles. They were introduced by Richard Feynman [8, 9], both to visualize transitions between states in QFT and as a tool to facilitate the computation of the probability amplitudes of these transitions.

Path integrals

Feynman diagrams rely on the computation of *path integrals* in the paradigm of quantum mechanics. In classical mechanics, the principle of least action (Eq. 1.3) states that the path taken by a particle to go from A to B in spacetime is the one which makes the action stationary ($\partial S = 0$). However, Feynman suggested [10] that in the quantum realm, instead of taking one such definite path, a particle would take *every* possible trajectory at once. Each path is equally probable and contributes with a factor e^{iS}.

The probability amplitude for the particle to go from A to B, specified by a function called *propagator*, is obtained by summing over all the paths. The rationale behind this approach is that the complex phases of random paths interfere with one another, effectively cancelling out these paths from the computation of the amplitude. On the other hand, paths arbitrarily close to the classical trajectory with stationary action all have similar phases. Thus, the net in-phase contribution from paths closest to the classical trajectory contributes the most to the probability amplitude.

Perturbative expansion

Likewise, the probability amplitude for a system of particles to go from an initial state to a final state involves all the possible Feynman diagrams representing this transition. The computation takes the form of a sum of integrals, each of which can be derived from its associated diagram by applying defined rules. The result is approximated using perturbative expansion in power series of the coupling constant α of the considered gauge field, as illustrated in Fig. 1.2. *Leading-order* (LO) or *tree-level* diagrams correspond to the first order of the power series; *Next-to-leading order* (NLO) diagrams correspond to the second order, and so on. Each interaction vertex is associated with a *matrix element* $\mathcal{M}$, which is a Lorentz scalar proportional to the coupling constant. The interaction probability is proportional to $\mathcal{M}^2$.

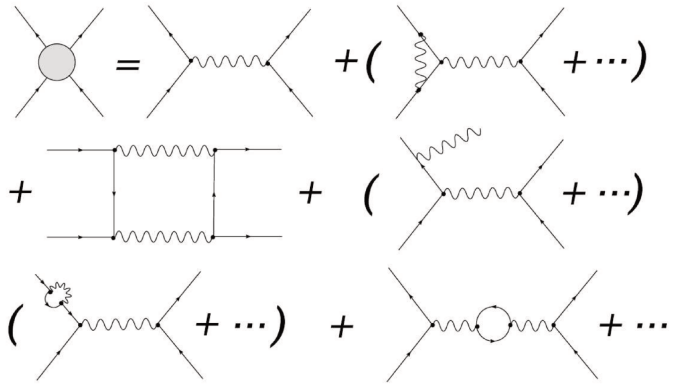

Figure 1.2: Illustration of the perturbative expansion for an interaction involving 2 fermions with Feynman diagrams. The probability amplitude is obtained by summing over all the possible diagrams, i.e. accounting for the higher-order corrections to the tree-level diagram. Taken from Ref. [11].

Renormalization

The strength of an interaction as well as the mass of a massive particle vary with the considered length scale (or likewise, with the exchanged four-momentum Q^2 of the interaction) [12]. This is a consequence of the fact that, in order to describe the physical reality, one needs to take into account the infinite set of higher-order corrections to a particle's propagator. These corrections correspond to the interaction of the particle with the vacuum as it propagates (*vacuum polarization* or *self-energy*), and virtual fluctuations which alter the interactions between particles. While self-energy results in a change of the particle's effective mass or charge, the second phenomenon modifies the effective coupling constant of the interaction [13]. For instance, the strength of the tree-level $e^-\gamma e^-$ interaction vertex shown in Fig. 1.3 (a) is modified by the photon's self-energy terms, one of which is represented in Fig. 1.3 (b).

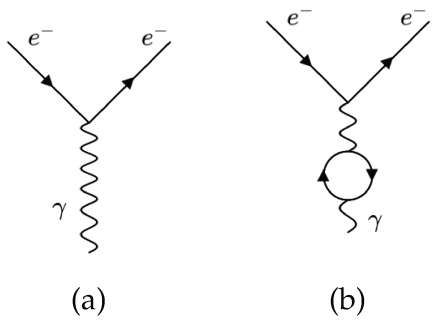

Figure 1.3: (a) Tree-level $e^-\gamma e^-$ interaction vertex. (b) Example of one-loop self-energy diagram of the photon, which modifies the strength of the interaction.

These loop corrections involve integrals over the four-momenta of the particles entering the loops, which can cary arbitrarily large momenta (i.e. short wavelengths). This gives rise to *ultraviolet* (UV) divergences making the result infinite, thus non-physical. To solve this problem, one needs to *regularize* the theory by introducing an arbitrary cut-off

scale Λ. This amounts to ignoring the states with momenta much larger than Λ. To avoid running into divergences in the limit $\Lambda \to \infty$, formulas need to be rewritten in terms of *renormalized* quantities, which are the ones we actually measure experimentally. They correspond to a shift of the tree-level "bare" quantities with counterterms (corresponding to Feynman diagrams) which absorb the UV divergences and yield finite, physical quantities.

As a result of this procedure, renormalized quantities depend on the energy scale of the process. The physical quantities that we measure are expressed at an arbitrary *renormalization scale* μ_R. To simplify the calculations (avoid large higher-order corrections in the perturbative expansion), it is common to choose μ_R to be of the order of the momentum scale of the considered process. In the 1970s, 't Hooft proved that all theories with local gauge invariance can be renormalized in such a way [14–16].

1.3 QED and QCD

1.3.1 Quantum electrodynamics

Quantum electrodynamics (QED) is the gauge theory describing the electromagnetic force. It was the first gauge theory to be developed, and served as a basis for the subsequent ones.

The QED Lagrangian is obtained from the Dirac Lagrangian (Eq. 1.1) by adding a kinetic term for the photon field. This term can be expressed using Maxwell's tensor $F_{\mu\nu} = \partial_\mu A_\nu - \partial^\mu A^\nu$. Hence the Lagrangian describing the interaction of a fermionic field with the electromagnetic field is:

$$\begin{aligned}
\mathcal{L}_{QED} &= \mathcal{L}_{Dirac} - \frac{1}{4} F_{\mu\nu} F^{\mu\nu} \\
&= \underbrace{i\bar{\psi}\gamma^\mu \partial_\mu \bar{\psi}}_{\text{kinetic } \psi} - \underbrace{m\bar{\psi}\psi}_{\text{mass } \psi} - \underbrace{e\bar{\psi}\gamma^\mu \partial_\mu \alpha(x)\psi}_{\text{interaction } \psi/A_\mu} - \underbrace{\frac{1}{4} F_{\mu\nu} F^{\mu\nu}}_{\text{kinetic } A_\mu} \\
&= \bar{\psi}(i\gamma^\mu D_\mu - m)\psi - \frac{1}{4} F_{\mu\nu} F^{\mu\nu} ,
\end{aligned} \tag{1.11}$$

where D_μ is the covariant derivative defined in Eq. 1.9. Since this Lagrangian possesses a U(1) gauge invariance, it ensues from Noether's theorem that an associated charge Q (identified with the electric charge) is a conserved quantity in interactions (see Eq. 1.6). The gauge boson of the electromagnetic field is the photon, and it bears no charge due to U(1) being abelian. Moreover, adding a mass term for the photon field in $\mathcal{L}_{QED}$ would spoil its local gauge invariance. As a result theoreof, the photon is massless and the electric force has an infinite range. The coupling constant α_{QED} of this interaction, also known as the *fine-structure constant*, depends directly on the electric charge e of the electron via $\alpha_{QED} = \frac{e^2}{4\pi}$ (in natural units).

The first formulation of QED as a gauge theory of electromagnetism with symmetry group $U(1)_{EM}$ came independently from Tomonaga [17, 18], Schwinger [19–22] and Feynman [8]. As simple as its construction may appear, it is one of the most stringently validated theories in physics. Its most precise test is the measurement of the *anomalous magnetic dipole moment* of the electron: the prediction for this quantum correction to the electron magnetic moment, which depends on higher-order Feynman diagrams, agrees with the experimental results to approximately one part per trillion [23]. It can be used to determine the dimensionless fine-structure constant, which equates $\alpha_{QED} \sim \frac{1}{137}$ (at an energy scale $Q^2 = 0$) with a relative precision of about one part per billion [24].

1.3.2 Quantum chromodynamics

First experimental milestones

Quantum chromodynamics (QCD) is the gauge theory describing the strong interaction. During the 1950s, alongside the development of bubble and spark chambers, more and more hadrons were discovered experimentally. In 1963, Gell-Mann [25] and Zweig [26] suggested that the pattern of this group of particles could be explained by the existence of quarks as the building blocks of hadrons. These quarks would come in 3 flavours (labelled u, d and s) and hold an electric charge of either $+\frac{2}{3}$ or $-\frac{1}{3}$ that of the electron. They would combine to form *mesons* (1 quark plus 1 antiquark) and *baryons* (3 quarks).

Soon after, the discovery of spin-$\frac{3}{2}$ particles such as the Ω^- (sss), Δ^- (ddd) or Δ^{++} (uuu) baryons underpinned the idea that quarks must carry a new quantum number. Indeed, these baryons are all composed of 3 quarks in the same quantum state, which goes against Pauli's exclusion principle for fermions. Consequently, each quark got assigned a *colour charge* (blue, green or red), and each antiquark a corresponding anticolour. Bound states of quarks can only exist if they are colourless; e.g. if a meson contains a green quark, its antiquark must be antigreen.

From 1967 to 1973, deep inelastic scattering (DIS) experiments [27, 28] were conducted at the Stanford Linear Accelerator Center (SLAC) [29, 30] to probe the internal structure of hadrons. This gave the first direct confirmation of quarks being physical particles [31], and not just a convenient theoretical construct. Furthermore, it was found that a quark which is impacted by a highly energetic particle behaves as if it were free, i.e. its coupling to other quarks is small. This property of the strong interaction is called *asymptotic freedom*. It implies that at short distances (higher energies) the coupling strength of the strong interaction is small, and perturbation theory at low orders provides a good approximation. On the opposite, at larger distances (lower energies), the coupling strength increases and non-perturbative approaches must be used (such as *lattice QCD* [32, 33]).

A related attribute of the strong interaction is *colour confinement*, stating that quarks can not be isolated as free particles, and must bound into colourless hadrons (*colour singlet* states). As a result, quarks produced at colliders *hadronize* well before they reach the

detectors, and are observed as collimated *jets* of hadrons. A notable exception is the top quark which decays before hadronization, as explained in Sec. 1.6.

The gauge theory of strong interaction

All these observations could be understood in the framework of a non-abelian gauge theory. Such theories had been developed by Yang and Mills in 1954, who tried to extend the concept of local gauge invariance to more complicated symmetry groups. This led to the construction of QCD as a gauge theory with symmetry group $SU(3)_C$[3]. There are 8 gluons, related to the $3^2 - 1 = 8$ generators T^a of the group. These generators can be expressed [13] in terms of the 3×3 Gell-Mann matrices as $T^a \equiv \frac{1}{2}\lambda^a$. They obey the commutation relations $[T^a, T^b] = i\sum_{c=1}^{8} f^{abc}T^c$, where the f^{abc} are the structure constants of the $SU(3)_C$ group, which encode its commutation relations.

In analogy with the QED Lagrangian (Eq. 1.11), the QCD Lagrangian can be expressed as:

$$\mathcal{L}_{QCD} = \bar{\psi}(i\gamma^\mu D_\mu - m)\psi - \frac{1}{4}G^a_{\mu\nu}G^{\mu\nu}_a \,, \tag{1.12}$$

where ψ are the quark fields. The covariant derivative D_μ is defined as:

$$D_\mu = \partial_\mu - ig_s T_a G^a_\mu \,, \tag{1.13}$$

where g_s is the coupling constant of the strong interaction. The gluon field strength tensor $G^a_{\mu\nu}$ is given by:

$$G^a_{\mu\nu} = \partial_\mu G^a_\nu - \partial_\nu G^a_\mu - g_s f^{abc} G^b_\mu G^c_\nu \,, \tag{1.14}$$

where G^a_μ is the gluon field. Quarks are the only fermions carrying a colour charge and sensitive to the strong force. The last term of Eq. 1.12 stems from the non-abelian nature of $SU(3)_C$, and reflects the self-interaction of gluons: unlike photons, gluons carry a (colour) charge and couple to one another. In QED, the quantum fluctuations of the photon field tend to produce electron-positron pairs, which have a screening effect and make the electromagnetic interaction weaker at larger distances. This also happens for QCD with quark-antiquark pairs, but this phenomenon is exceeded by the counter-effect of the gluon self-interaction; this is the cause of asymptotic freedom (larger coupling strength at larger distances).

Parton Distribution Functions

The constituents of hadrons are called *partons*. When the internal structure of a hadron is probed with a particle having moderately high momentum, its 2 or 3 *valence quarks* behave as free particles each carrying a fraction x of its momentum (*Bjorken x* [34]). However, as the momentum of the probe increases, it is able to resolve smaller values of x and the picture becomes more elaborate. High-energy DIS measurements revealed

[3] S stands for "special", meaning that the group matrices have determinant 1. C stands for "colour", which is the conserved quantity associated with the symmetry.

the existence of the *sea* of quarks and gluons within hadrons, originating from constant quark-antiquark ($q\bar{q}$) annihilation and gluon splitting. Although the electrically-neutral gluons from the sea can not be directly observed through DIS, their physical existence was validated by the observation that charged partons do not carry the totality of the hadron's momentum [31].

The probability densities for gluons and the different quark flavours are encoded in *Parton Distribution Functions* (PDFs) as a function of x, and for a given resolution scale Q^2. At hadron colliders, it is of utmost importance to have a precise knowledge of the PDFs in order to accurately describe the initial state of the system, and the distribution of momentum among the partons. It also represents an important source of theoretical uncertainty limiting the precision of measurements.

As the PDF dependence on x involves low-scale non-perturbative dynamics, it can not be directly derived from perturbative QCD. Instead, it is estimated with a global fit to data from many different sensitive experiments. There are several sets of PDFs derived using different methodologies and measurements, of which one is represented in Fig. 1.4. It can be observed that the PDFs of the sea partons strongly depend on the exchanged momentum, and that at high energies, a large fraction of the proton's momentum is carried by gluons.

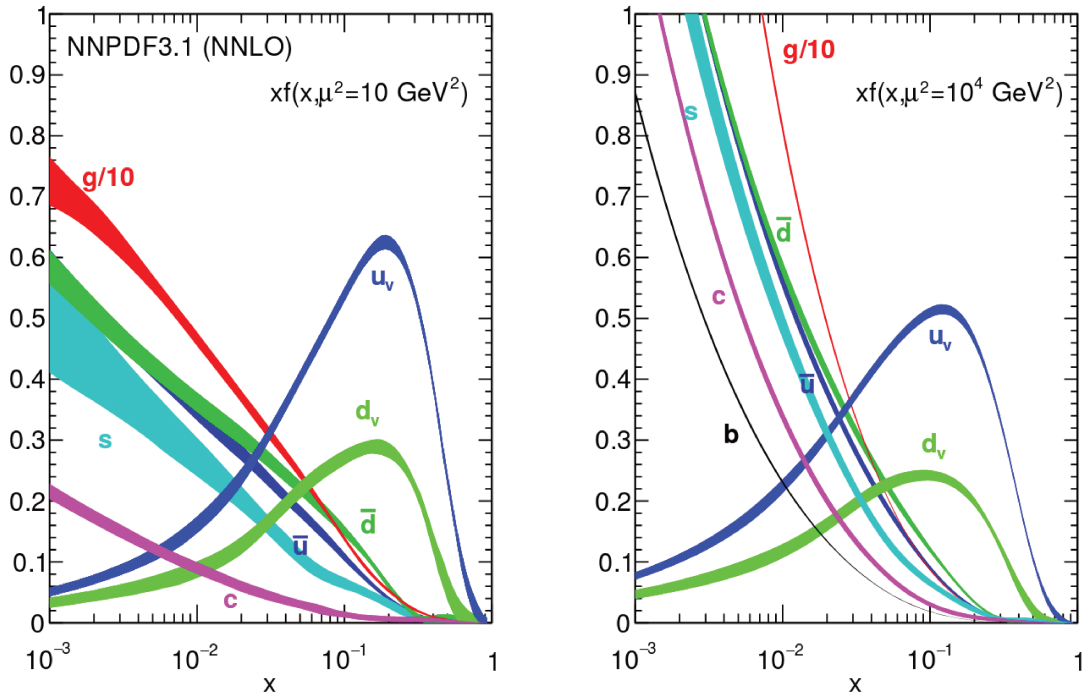

Figure 1.4: Proton PDFs from the NNPDF3.1 set, evaluated at $Q^2 = 10\,\text{GeV}^2$ (left) and $Q^2 = 10^4\,\text{GeV}^2$ (right). Taken from [35].

1.4 The electroweak interaction

1.4.1 Electroweak unification

The weak interaction

The first model of the weak interaction was proposed in 1933 by Fermi, who described the β decay in radioactive nuclei as a four-fermion contact interaction [36, 37]. In 1957, to the astonishment of many in the particle physics community, a famous experiment conducted by Wu et al. [38] proved that parity is maximally violated by the charged weak interaction: it only couples to particles of left-handed[4] chirality (and antiparticles of right-handed chirality). There also exists a neutral weak interaction, which couples both to left-handed and right-handed particles. This discovery motivated the introduction of the vector-axial (V-A) structure of the Lagrangian of the weak force. It relies on the splitting of a fermionic field ψ into its left-handed and right-handed components:

$$\begin{aligned} \psi &= \psi_L + \psi_R \,, \\ \psi_L &= P_L\,\psi = (\frac{1-\gamma^5}{2})\,\psi \,, \\ \psi_R &= P_R\,\psi = (\frac{1+\gamma^5}{2})\,\psi \,, \end{aligned} \tag{1.15}$$

where P_L and P_R are the projection operators of left and right chirality.

The model of the weak interaction was subsequently promoted to a gauge theory by requiring local invariance under symmetries of the SU(2) group, and it was associated with a conserved quantity called the *weak isospin*[5].

Each generation of left-handed fermions forms a doublet satisfying $\mathrm{I}_3 = \pm\frac{1}{2}$, while right-handed fermions correspond to singlets of null isospin.

The electroweak unification

The electromagnetic and weak forces have distinct properties. For instance, all fermions are sensitive to the weak force, but only charged particles are subject to electromagnetism. In addition, the weak interaction violates parity while electromagnetism does not.

Despite these apparent differences, Glashow [39], Salam [40] and Weinberg [41] proposed that these forces can be understood as two aspects of a single *electroweak* interaction. This breakthrough towards the unification of forces was based on the assumption of the invariance under an $\mathrm{SU(2)}_L \otimes \mathrm{U(1)}_Y$ gauge symmetry. The conserved quantity associated with $\mathrm{U(1)}_Y$ is the *hypercharge* Y. It is directly related to the electric charge Q and

[4] A left-handed (right-handed) particle has the projection of its spin in the opposite (same) direction as its momentum.

[5] Weak isospin obeys the same rules as the spin angular momentum. In particular the possible values of its third component are $\mathrm{I}_3 = \{+\frac{1}{2}; -\frac{1}{2}\}$ for a field with I=$\frac{1}{2}$, and $\mathrm{I}_3\{+1; -1; 0\}$ for a field with I=1.

Table 1.1: Values of the electric charge Q, the third component of the weak isospin I_3 and the hypercharge Y for fermions (left-handed and right-handed) and the electroweak gauge bosons.

		Q	I_3	Y
Leptons	$(e, \mu, \tau)_L$	-1	-1/2	-1
	$(\nu_e, \nu_\mu, \nu_\tau)_L$	0	+1/2	
	$(e, \mu, \tau)_R$	-1	0	-2
	$(\nu_e, \nu_\mu, \nu_\tau)_R$	0	0	0
Quarks	$(u, c, t)_L$	+2/3	+1/2	+1/3
	$(d, s, b)_L$	-1/3	-1/2	
	$(u, c, t)_R$	+2/3	0	+4/3
	$(d, s, b)_R$	-1/3	0	-2/3
EWK bosons	W^1	+1	+1	0
	W^2	-1	-1	0
	W^0	0	0	
	B^0	0	0	

the weak isospin via:

$$Y = 2 \times (Q - I_3)\,. \tag{1.16}$$

The $SU(2)_L$ group provides $2^2 - 1 = 3$ generators T^a, which can be written [10] in terms of the 2×2 Pauli matrices as $T^a \equiv \frac{1}{2}\sigma^a$. These operators satisfy the commutation relations $[T^a, T^b] = i\sum_{c=1}^{3} f^{abc}T^c$, where the f^{abc} are the structure constants of the SU(2) group. The corresponding massless gauge bosons are labelled W^1, W^2 (electrically charged) and W^0 (electrically neutral) and have I_3 =+1, -1 and 0 respectively. They couple to the doublets of left-handed fermions with the same coupling strength g. The $U(1)_Y$ group provides 1 massless boson B^0, which is a singlet of null isospin. It couples to all fermions with coupling strength g'. All of these 4 bosons can be assigned a null hypercharge Y=0, which determines their electric charges. Table 1.1 summarises the values of Q, Y and I_3 for all fermions (depending on their chiralities) and electroweak bosons. The hypothetical right-handed neutrinos would have null weak isospin and hypercharge, and hence would not participate to any of the interactions of the SM (*sterile neutrinos* [42, 43]).

By analogy with the Lagrangians of QED (Eq. 1.11) and QCD (Eq. 1.12), the Lagrangian for the electroweak interaction can be expressed as:

$$\mathcal{L}_{EWK} = (i\bar{\psi}_L\gamma_\mu D^L_\mu\psi_L) + (i\bar{\psi}_R\gamma_\mu D^R_\mu\psi_R) - \frac{1}{4}W^a_{\mu\nu}W^{\mu\nu}_a - \frac{1}{4}B^0_{\mu\nu}B^{\mu\nu}_0\,, \tag{1.17}$$

where the index a runs from 0 to 2.

The covariant derivatives (for left-handed and right-handed fermions) and field strength tensor are [10]:

$$\begin{aligned} D_\mu^L &= \partial_\mu - igT^a W_\mu^a + \frac{i}{2} g' B_\mu \,, \\ D_\mu^R &= \partial_\mu + ig' B_\mu \,, \\ W_{\mu\nu}^a &= \partial_\mu W_\nu^a - \partial_\nu W_\mu^a + g f^{abc} W_\mu^b W_\nu^c \,, \\ B_{\mu\nu}^0 &= \partial_\mu B_\nu^0 - \partial_\nu B_\mu^0 \,. \end{aligned} \tag{1.18}$$

As in the case of the gluon field strength tensor $G_{\mu\nu}$ (see Eq. 1.14), the penultimate term of the electroweak Lagrangian leads to the *trilinear coupling* of the W_μ^a fields.

As for QED and QCD, the gauge bosons of the electroweak interaction must be massless to preserve local gauge invariance. However, contrary to the photon and the gluon, the W and Z bosons, discovered at CERN [44–47] in 1983, were found to be massive[6]. Their masses are currently estimated to be [24]:

$$\begin{aligned} m_Z &= 91.1876 \pm 0.0021 GeV/c^2 \,, \\ m_W &= 80.379 \pm 0.012 GeV/c^2 . \end{aligned} \tag{1.19}$$

The fact that the weak interaction is mediated by heavy bosons is the reason why it is both weak and short-ranged. In order to generate these masses in a gauge-invariant way, it is necessary to introduce a mechanism breaking the symmetry of the electroweak interaction (described in Section 1.5). One consequence of this phenomenon is that the W^a and B^0 bosons of the $SU(2)_L$ and $U(1)_Y$ symmetry groups do not correspond to physical particles, but mix to form mass eigenstates. The physical $W^\pm$ bosons can be identified as the linear combinations:

$$W^\pm = \frac{1}{\sqrt{2}} (W^1 \mp iW^2) \,, \tag{1.20}$$

while the Z boson and the photon are admixtures of W^0 and B^0:

$$\begin{pmatrix} Z_0 \\ \gamma \end{pmatrix} = \begin{pmatrix} \cos(\theta_W) & -\sin(\theta_W) \\ \sin(\theta_W) & \cos(\theta_W) \end{pmatrix} \begin{pmatrix} W^0 \\ B^0 \end{pmatrix} \,, \tag{1.21}$$

where θ_W is the *weak mixing angle*. This angle is a free parameter of the SM which can be measured in many different ways (e.g. from ν-e scattering). It is more frequently expressed in the form [24]:

$$sin^2(\theta_W) = 0.23122 \pm 0.00004 \,. \tag{1.22}$$

[6] The masses of the W and Z bosons had been predicted before their observation, as explained in the references

1.4.2 GIM mechanism and FCNC

Until the beginning of the 1970s, the only three light quarks u, d and s known at this time could explain the observed hadron spectrum. The observed weak decays of pions and kaons were mostly in good agreement with the predictions of the *Cabibbo mechanism*. This mechanism was introduced to accomodate the empirical observation that, contrary to leptons, quarks do not couple universally to the weak force. It postulates a mismatch between the weak eigenstates d' and s' (taking part in the weak interaction) and mass eigenstates d ans s (freely propagating), which are related via:

$$\begin{pmatrix} d' \\ s' \end{pmatrix} = \begin{pmatrix} cos(\theta_c) & sin(\theta_c) \\ -sin(\theta_c) & cos(\theta_c) \end{pmatrix} \begin{pmatrix} d \\ s \end{pmatrix}, \tag{1.23}$$

where $\theta_c \sim 13°$ is the Cabibbo angle.

An interaction between a neutral boson and a fermion in which the flavour of the fermion changes, but not its electric charge, is called *flavour-changing neutral current* (FCNC). In the three-quarks picture, and according to the Cabibbo mechanism alone, s $\rightarrow$ d transitions via FCNC processes would be possible at all orders of the perturbation expansion. For example, the $K_L \rightarrow \mu^+\mu^-$ FCNC decay could be mediated by a Z boson at leading order, as illustrated in Fig. 1.5 (a). It could also take place at higher orders, for example via the "box-diagram" of Fig. 1.5 (b), where an up quark is exchanged. However, this was in contradiction with several searches targeting kaon decays, which placed stringent upper limits on such FCNC processes, implying cross sections much smaller than predicted.

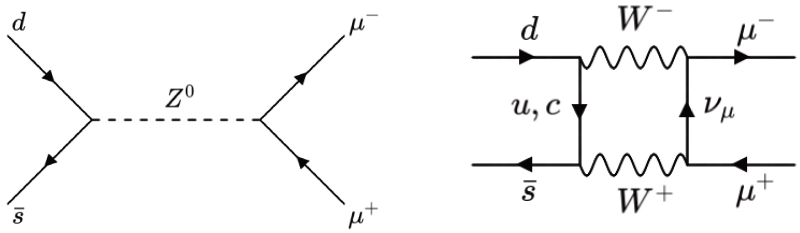

(a) (b)

Figure 1.5: Examples of (a) leading-order and (b) higher-order Feynman diagrams for the $K_L \rightarrow \mu^+\mu^-$ FCNC decay. The GIM mechanism forbids the first process, and strongly suppresses the second.

These experimental results could be explained by the introduction of the GIM[7] mechanism, which postulated the existence of a fourth quark flavour labelled "charm", making it possible to group quarks into the doublets (u, d') and (c, s'). In addition to this major

[7] Named after S. Glashow, J. Iliopoulos and L. Maiani.

prediction, the GIM mechanism led to the prediction that FCNC processes are forbidden at leading order (cancellation of terms in the amplitudes). Another consequence is that higher-order processes such as the one represented in Fig. 1.5 (b), could also proceed via the exchange of a virtual charm quark. The two diagrams involving either an up or charm quark share the same final state, hence their amplitudes interfer and must be summed. Their opposite contributions essentially cancel out, and only a very tiny contribution remains due to the mass difference between the up and charm quarks ($\propto m_c^2 - m_u^2$). The branching ratios of several FCNC decays of the top quark in the SM are given in Table 1.2.

Table 1.2: Branching ratios for top quark FCNC interactions in the SM. Adapted from Ref. [48].

	$\mathbf{t \to uZ}$	$\mathbf{t \to u\gamma}$	$\mathbf{t \to ug}$	$\mathbf{t \to uH}$	$\mathbf{t \to cZ}$	$\mathbf{t \to c\gamma}$	$\mathbf{t \to cg}$	$\mathbf{t \to cH}$
BR	8×10^{-17}	3.7×10^{-16}	3.7×10^{-14}	2×10^{-17}	1×10^{-14}	4.6×10^{-14}	4.6×10^{-12}	3×10^{-15}

Therefore the study of FCNC processes directly contributed to the construction of the SM, and is still motivated nowadays by their many interests [49] (sensitivity to particles in the loop, probing the precise cancellation of diagrams, etc.). Their production is also sensitive to numerous new physics models, as is mentioned in more details in Chapter 5.

1.4.3 CKM matrix

The charged weak interaction, mediated by $W^{\pm}$ bosons, is the only type of interaction which can change the flavour of fermions (let aside the extremely rare FCNC interactions). For example, it is responsible for the reaction of β decay in neutron-rich nuclei, which transforms a neutron into a proton by turning one of its down quark into an up quark. The probabilities of the transitions within and in-between the 3 generations of quarks are encoded in the Cabibbo-Kobayashi-Maskawa (CKM) 3×3 matrix [50, 51]. It is an extension of the Cabibbo mechanism to the 3 generations of quarks, which relates the weak eigenstates of the down-type quarks to their mass eigenstates via:

$$\begin{pmatrix} d' \\ s' \\ b' \end{pmatrix} = V_{CKM} \begin{pmatrix} d \\ s \\ b \end{pmatrix} = \begin{pmatrix} V_{ud} & V_{us} & V_{ub} \\ V_{cd} & V_{cs} & V_{cb} \\ V_{td} & V_{ts} & V_{tb} \end{pmatrix} \begin{pmatrix} d \\ s \\ b \end{pmatrix} . \tag{1.24}$$

It is therefore the weak eigenstates d', s' and b' which are the partners of the up-type quarks within the weak isospin doublets. By convention, the *up-type* quarks are taken to be pure states (no mismatch of their eigenstates).

The CKM matrix is fully defined by 4 independent parameters, which must be determined experimentally. It is often parameterised with 3 mixing angles and 1 CP-mixing phase, which violates the CP[8] symmetry in the SM [52, 53]. Currently the values of the

[8] Charge transformation followed by a parity transformation.

CKM matrix elements are estimated to be [24]:

$$\begin{pmatrix} V_{ud} & V_{us} & V_{ub} \\ V_{cd} & V_{cs} & V_{cb} \\ V_{td} & V_{ts} & V_{tb} \end{pmatrix} = \begin{pmatrix} 0.97446 \pm 0.00010 & 0.22452 \pm 0.00044 & 0.00365 \pm 0.00012 \\ 0.22438 \pm 0.00044 & 0.97359^{+0.00010}_{-0.00011} & 0.04214 \pm 0.00076 \\ 0.00896^{+0.00024}_{-0.00023} & 0.04133 \pm 0.00074 & 0.999105 \pm 0.000032 \end{pmatrix} \tag{1.25}$$

The probability of a transition is proportional to the corresponding matrix element squared. The diagonal elements of the CKM matrix are close to 1, reflecting the fact that transitions are favoured between quarks of the same generation. The CKM matrix is believed to be unitary, i.e. the sum of the transition probabilities for any quark flavour is equal to 1. If this assumption was to be disproved, it could imply the existence of a fourth quark generation.

1.5 Electroweak symmetry breaking

1.5.1 The Higgs mechanism

In Section 1.4.1, we mentioned that the gauge theory of the electroweak interaction requires its bosons to be massless to preserve gauge invariance. A similar problem arises if one tries to add a mass term for a fermion field, which could be written as $-m(\bar{\psi}_R\psi_L + \bar{\psi}_L\psi_R)$. Since fermions of left-handed and right-handed chiralities have different representations under the $SU(2)_L$ symmetry group, such a term would also spoil the local gauge invariance. This contradicts the experimental evidence that fermions and the $W^{\pm}$ and Z bosons are actually massive.

This major issue is solved by the introduction of the Brout-Englert-Higgs mechanism[9] (hereinafter abbreviated as Higgs mechanism), which generates masses for bosons and fermions in a gauge-invariant way [54–56].

The Higgs mechanism introduces two complex scalar fields grouped in a weak isospin doublet:

$$\phi = \begin{pmatrix} \phi^+ \\ \phi^0 \end{pmatrix} = \frac{1}{\sqrt{2}} \begin{pmatrix} \phi^1 + i\phi^2 \\ \phi^3 + i\phi^4 \end{pmatrix} , \tag{1.26}$$

and a potential of the form $V(\phi) = \mu^2\phi^\dagger\phi + \lambda(\phi^\dagger\phi)^2$, where μ and λ are constants. The corresponding contribution to the Lagrangian of the electroweak interaction is:

$$\mathcal{L}_{Higgs} = (D_\mu\phi)^\dagger(D_\mu\phi) - V(\phi) , \tag{1.27}$$

where D_μ is the covariant derivative defined in Eq. 1.18.

The shape of the Higgs potential energy density $V(\phi)$ depends on the sign of μ; λ must be positive for the potential to be bounded from below. The case $\mu^2 > 0$ corresponds to a potential well around a trivial minimum state $\phi_0 = 0$ (ground state or *vacuum*). The Lagrangian of Eq. 1.27 would then represent a scalar particle with mass μ

[9] Articles describing this mechanism were published in 1964 by three independent groups: Peter Higgs; R. Brout and F. Englert; G. Guralnik, C.R. Hagen and T. Kibble [54–56].

and a four-point self-interaction with coupling λ. On the other hand, requiring $\mu^2 < 0$ produces the so-called "Mexican-hat" potential illustrated in Fig. 1.6.

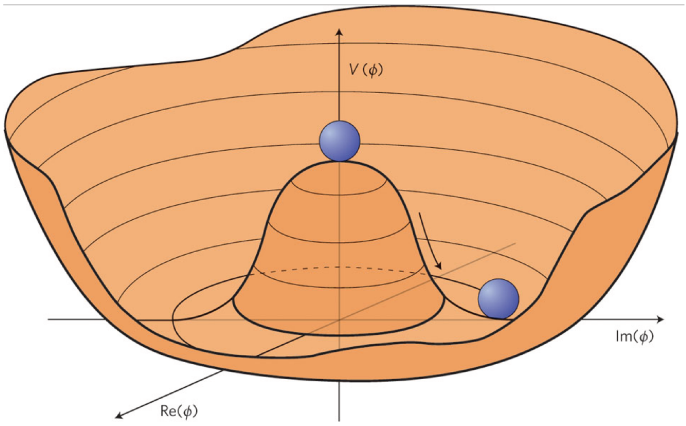

Figure 1.6: Shape of the potential of the Higgs field. Taken from Ref. [57].

In this configuration, there exists an infinity of degenerated minima, and the Higgs field has a non-zero *vacuum expectation value* v:

$$\phi_0^\dagger \phi_0 = \frac{-\mu^2}{2\lambda} \equiv \frac{v}{2}. \tag{1.28}$$

This makes the system unstable and forces it to choose one particular value for its ground state among all possibilities, which is what is called *spontaneous symmetry breaking* (SSB). The ensemble of all the possible solutions shares the symmetry of the Lagrangian, but the unique solution which is eventually chosen does not: we say that the true symmetry of the system is hidden by the choice of a specific ground state. This ground state can be expressed as:

$$\phi_0 = \frac{1}{\sqrt{2}} \begin{pmatrix} 0 \\ v \end{pmatrix}. \tag{1.29}$$

The Goldstone theorem states that whenever a continuous symmetry undergoes SSB, each broken generator gives rise to a massless scalar boson (*Goldstone bosons*). When expanding about the minimum for small fluctuations, it is possible to perform a gauge transformation such that the 3 Goldstone bosons associated with $SU(2)_L$ are eliminated from the Lagrangian, and to conveniently express the field in the simpler *unitary gauge* [58, 59]:

$$\phi = \frac{1}{\sqrt{2}} \begin{pmatrix} 0 \\ v + h(x) \end{pmatrix}, \tag{1.30}$$

where the Higgs field $h(x)$ is the only remaining physical field. The 3 degrees of freedom represented by the Goldstone bosons are absorbed into different terms, and turned into the 3 longitudinal degrees of freedom of the mass eigenstates $W^\pm$ and Z^0 which become massive. In other words, expanding the kinetic and potential terms of Eq. 1.27 in the unitary gauge generates mass terms for the $W^\pm$ and Z^0 bosons, as well as for the excitation

of the Higgs field, the Higgs boson H. The masses of the bosons are predicted to be [13]:

$$\begin{aligned} m_W &= \frac{gv}{2}\,, \\ m_Z &= \frac{v\sqrt{g^2+g'^2}}{2}\,, \\ m_H &= \sqrt{2\lambda}v\,, \end{aligned} \tag{1.31}$$

and all depend on v, which has an approximate value of $v = \frac{2m_W}{g} \approx 246$ GeV. The parameter λ was not known before the measurement of m_H.

This procedure also introduces interaction terms representing the coupling of the Higgs boson to the weak gauge bosons, and its self-coupling. The field associated with the photon remains massless in the process, and the photon does not interact at leading order with the electrically-neutral Higgs boson. From Eq. 1.27, it is possible to determine the couplings of the Higgs with other bosons, and all the Feynman diagrams describing its possible interaction vertices.

1.5.2 Yukawa couplings

So far we have seen that the SSB of the electroweak interaction generates the necessary mass terms for the $W^{\pm}$ and Z bosons through their interactions with the Higgs field. The same field can be exploited in order to give masses to fermions in a gauge-invariant way, through what are known as Yukawa interactions [60]. Such interactions couple a Dirac field ψ to a scalar field ϕ, as illustrated in Fig. 1.7.

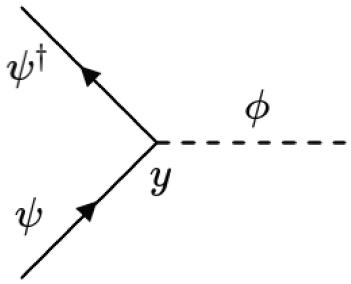

Figure 1.7: Feynman diagram representing a Yukawa interaction vertex of strength y between a Dirac field ψ and a scalar field ϕ.

As the Higgs field acquires a non-zero VEV through spontaneous symmetry breaking, the coupling of the left-handed doublets f_L and right-handed singlets f_R of fermionic fields to the Higgs scalar field ϕ contribute to the Lagrangian as:

$$\mathcal{L}_{Yukawa} = -y_f(\bar{f}_L\phi f_R + \bar{f}_R\phi f_L)\,, \tag{1.32}$$

where the constants y_f represents the *Yukawa couplings* of fermions to the Higgs field. The values of these couplings are not predicted by the theory, but they are directly proportional to the masses of the fermions via the relation:

$$y_f = \frac{\sqrt{2}\, m_f}{v}\,, \tag{1.33}$$

and so they can be inferred from mass measurements. It is considered in the SM that neutrinos are massless and do not exist as right-handed particles, thus they do not have a Yukawa coupling.

To summarise, the Higgs mechanism introduces a scalar Higgs field which permeates the entire universe and has a non-zero vacuum expectation value. This VEV is involved in the couplings of the field, and can be used to generate mass terms in a gauge-invariant way for both the fermions interacting with it, and the bosons of the weak interaction (while the photon remains massless). Thus this mechanism proposes an elegant solution to an important shortcoming of the theory, and leads to new verifiable predictions. Within this framework, it is possible to relate many different quantities (masses, couplings, etc.) through just a small number of free parameters which are left to the experiments to determine.

The physical existence of the Higgs field was successfully established in 2012 both by the ATLAS and CMS experiments at the Large Hadron Collider (LHC), which observed a Higgs boson at a mass of approximately 125 GeV whose properties conform with the SM predictions up to now [24, 61, 62]. The main properties of the Higgs boson are described in Sec. 1.7.

1.6 Top quark physics

The discoveries of the τ lepton [63] and bottom quark (b) [64] in the mid-1970s, which formed a third generation of fermions, led to the prediction of the existence of the top quark (t) in order to restore the symmetry between quark and lepton doublets. Therefore its quantum numbers were inferred from the existing patterns, e.g. $Q_t = +\frac{2}{3}$ and $I_t^3 = +\frac{1}{2}$. Based on the mass ratios of the other quarks, physicists suggested that its mass would be about 3 times that of its down-type counterpart, of the order of 10 GeV. This started a twenty-years international hunt for the observation of this missing piece of the SM, and gave rise to a very fertile research field. Over time the top quark properties have been studied by several experiments from two accelerators, at many different energies and with two beam particle configurations.

1.6.1 Properties

The top quark was discovered in 1995 at the Tevatron collider [65–67], independently by both the CDF [68] and DØ [69] collaborations. A recent combination of Tevatron and LHC measurements [24] estimates its mass to be $m_t = 173.0 \pm 0.4$ GeV, slightly less than

that of a gold nucleus, making it the heaviest known elementary particle. Its mass is of the same order than the Higgs vacuum expectation value, and its Yukawa coupling is close to unity (Eq. 1.33). This results in a strong interplay between the top quark and the Higgs boson.

Since the discovery of the top quark, the measurement of its mass has been an important focus. It is a key free parameter of the SM, which makes a significant impact on several electroweak observables. For example, it contributes quadratically to quantum loop corrections to the masses of the W and Z bosons, while the Higgs boson does so logarithmically (Fig. 1.8 (a)). This made it possible to constrain the possible values for the mass of the Higgs boson through electroweak measurements, even before the LHC was built [70]. The top quark mass also makes the largest contribution to the Higgs boson self-interaction (Fig. 1.8 (b)). From the combination of precision measurements of the masses of these bosons and of the top quark, the magnitudes of these quantum corrections and their consistency with the SM predictions can be probed [24].

Another unique property of the top quark is encoded in the CKM matrix (Eq. 1.25). As a consequence of $|V_{tb}|^2 \sim 1 \gg |V_{ts}|^2, |V_{td}|^2$, the top quark almost does not mix with first- and second-generation quarks. This means that it will decay to an *on-shell* [10] W boson and a bottom quark with a probability close to 100%, as its large mass kinematically allows it. This lone decay mode $t \to W^+ + b$ gives the top quark a distinctive signature, as discussed in Section 1.6.3.

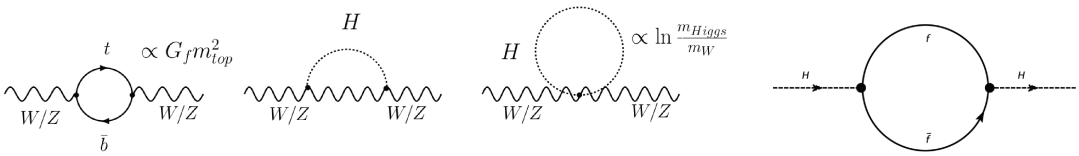

Figure 1.8: Examples of tree-level loop corrections (a) to the masses of the W and Z bosons from the top quark (quadratic) and Higgs boson (logarithmic), and (b) to the Higgs boson self-interaction from virtual fermions, at one-loop level. Due to its large mass, the top quark contributes the most to these corrections.

The top quark has a resonance width $\Gamma_t = 1.41^{+0.19}_{-0.15}$ GeV [24]. This implies a very short lifetime $\tau_t = \hbar/\Gamma \approx 5 \times 10^{-25}$ s, much shorter than the typical timescale for the formation of hadronic bound states ($\tau_{QCD} \approx 3 \times 10^{-24}$ s). Thus the top quark decays before it hadronizes, and as a result is the only quark which exists as a free particle. Another consequence is that the fundamental properties of the top quark are not hidden by hadronization, and the study of its decay products provides access to important information (e.g. about the V-A structure of the charged weak interaction).

[10] Particles "on the mass shell" (or simply *on-shell*) satisfy the energy-momentum relation $E^2 = (pc)^2 + (mc^2)^2$. On the contrary, "virtual" (*off-shell)* particles do not, and are labelled with a star (X^*).

Due to these peculiar properties, the top quark stands out among the other quarks, and has physicists wondering whether it plays a special role in the theory, for instance related to the mechanism of electroweak symmetry breaking.

1.6.2 Production

At hadron colliders, top quarks can either be produced as $t\bar{t}$ pairs via the strong interaction, or as a single top quark via the electroweak interaction.

The pair production mode is dominant at the LHC. Its cross section at $\sqrt{s} = 13$ TeV is currently measured by CMS [71] to be $\sigma_{t\bar{t}} = 888 \pm 2\,(stat)\,^{+26}_{-28}\,(syst) \pm 20\,(lumi)$ pb. At the Tevatron, it mostly proceeded via $q\bar{q}$ annihilation due to the presence of valence antiquarks within the antiprotons. On the other hand, at the LHC the only antiquarks come from the sea, and the centre-of-mass energy is such that their probability densities are exceeded by that of gluons (Fig. 1.4). Thus the dominant process is gluon fusion ($\sim$ 80% at $\sqrt{s} = 7$ TeV and $\sim$ 90% at $\sqrt{s} = 14$ TeV [24]). Both processes are illustrated in Fig. 1.9. Consequently, the pair production is sensitive to the gluon PDF in the large x region, which is currently affected by large uncertainties.

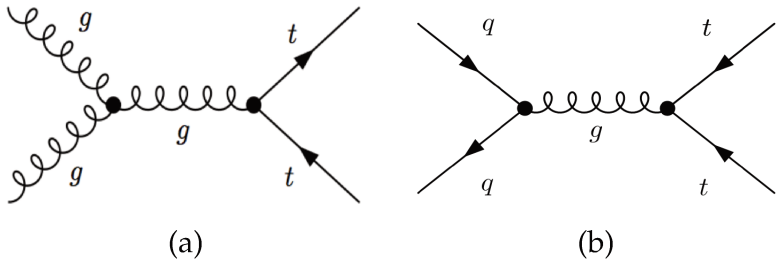

Figure 1.9: Tree-level Feynman diagrams for top quark pair production via (a) gluon fusion and (b) quark-antiquark annihilation.

On the other hand, the top quark can be produced alone via the charged weak interaction as a *single top*. This can proceed through 3 distinct channels at LO, illustrated in Fig. 1.10 (a) : the *t-channel*, the *s-channel* and the *tW-channel*. The predicted NLO cross sections at 13 TeV for each channel are [72]:

$$\begin{aligned} \sigma_{t-channel} &= 217\,^{+9}_{-8}\ pb, \\ \sigma_{tW-channel} &= 60 \pm 6\ pb, \\ \sigma_{s-channel} &= 10.3 \pm 0.2\ pb. \end{aligned} \tag{1.34}$$

The dominant t-channel corresponds to the exchange of a W boson between a light (first- or second-generation) quark and a bottom quark. One interesting signature of this channel is that the light quark in the final state, which "recoils" against the much heavier top quark, is expected to be emitted in the forward region of the detector (i.e. it tends to be collimated with the beams). This feature is used extensively in experimental searches targeting this production mode, such as the ones presented in Chapters 4 and 5.

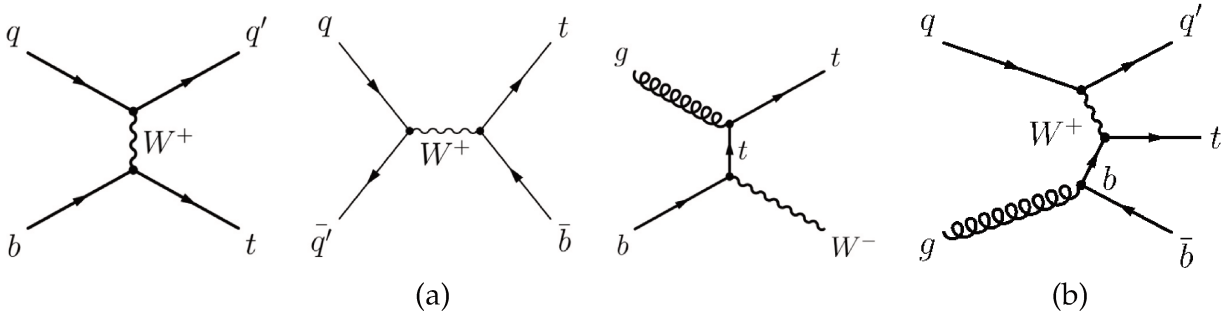

Figure 1.10: (a) LO Feynman diagrams for the production of a single top quark through the t-channel in the 5-flavour scheme (left), s-channel (middle) and tW-channel (right). (b) t-channel production in the 4-flavour scheme.

The parton-level theoretical description of the t-channel production mode suffers from an ambiguity regarding the origin of the incoming b quark. One can either assume that it comes from the sea of quarks within the proton, using a so-called "5-flavour scheme" [73–75] PDF (not 6, because sea top quarks are neglected), or instead that b quarks must originate from gluon splitting (using a "4-flavour scheme" PDF, which also ignores sea bottom quarks). The associated Feynman diagrams are represented in Fig. 1.10 (a) and (b) respectively.

While both valid and properly defined, these two approaches can lead to different predictions for the cross section when computed at finite order (although the agreement is rather good already at the NLO level for single top production [76]), and for the kinematic properties of the spectator b quark from $g \to b\bar{b}$. Precise measurements of t-channel production could provide useful information about the properties of the incoming partons, and favour one scheme over the other. Additionally, since the productions of single top and antitop quarks are initiated by different initial state partons, the ratio of their production cross sections can help to constrain the PDFs in the large x region.

Another interesting property of the single top production modes is their sensitivity to the tWb vertex, which is involved both in the production and the decay. The strength of this interaction depends on the magnitude of the CKM matrix element V_{tb}, hence the single top production cross section is approximately proportional to $|V_{tb}|^2$ [77].

Presently this value is much constrained via the measurements of the other elements, assuming matrix unitarity and the existence of 3 quark generations. If one does not want to make these assumptions, single top production is a privileged way for estimating it [24, 77]. For example, if a fourth family of quark were to mix with the third one[11], V_{tb} could considerably deviate from 1, resulting in a coherent decrease of the cross sections of the 3 single top production channels [82].

[11] Such models have interesting features, but are already much constrained from several measurements, as discussed in Refs. [78–81].

1.6.3 Decay channels

The fact that the top quark only decays through $t \to W^+ + b$ (to a good approximation) leads to a limited number of possible final states. Moreover, the b quark can be *tagged* by a dedicated algorithm due to its particularly long lifetime (see Sec. 2.3.4), and thus the top quark decay possesses a distinctive signature.

The different types of decays of a top quark pair can be grouped into 3 categories: "dileptonic", "semi-leptonic" or "hadronic". Figure 1.11 represents the probability, or *branching ratio*, associated with each channel. In the dominant hadronic mode the two W bosons both decay to quark-antiquark pairs, making this channel hard to detect among the large QCD backgrounds at hadron colliders. In the semi-leptonic channel only one W boson decays hadronically, while the other decays into a lepton and neutrino (with a probability of about 15 % for each generation).

Top quarks decaying leptonically are much easier to identify in the presence of large QCD backgrounds, as they produce an isolated lepton with high momentum as well as a neutrino which escapes the detector. For this reason, the leptonic decay of the top quark was targeted in the analyses presented in Chapters 4 and 5.

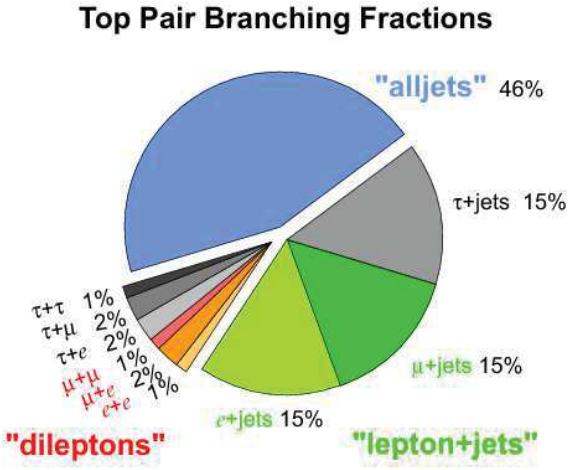

Figure 1.11: Branching ratios for the different decay channels of a top quark pair. Taken from Ref. [83].

1.7 Higgs boson physics

1.7.1 Properties

Since the Higgs boson was discovered at the LHC in 2012 at a mass of 125 GeV [1, 2], its properties have been the subject of an ever-increasing number of experimental searches. The reason is twofold: firstly the Higgs mechanism is at the core of the SM, and the study of its associated particle could reveal a lot about our universe: nature and interactions of fundamental particles, relationship with new physics, role of the Higgs field in the early universe, etc.

Secondly, it is important to ensure that the discovered particle indeed conforms in all respects with the SM Higgs boson. Up to now, all the measurements of its quantum numbers and couplings to other particles agree with the SM predictions. The CMS measurements [84] of several such couplings as a function of the particle's mass are represented in Fig. 1.12. The Higgs boson is expected to have a narrow resonance width of approximately $\Gamma_H \approx 4$ MeV, three orders of magnitude smaller than the current mass resolution reached at the LHC. The corresponding lifetime is $\tau_H = 1.56 \times 10^{-22}$ s.

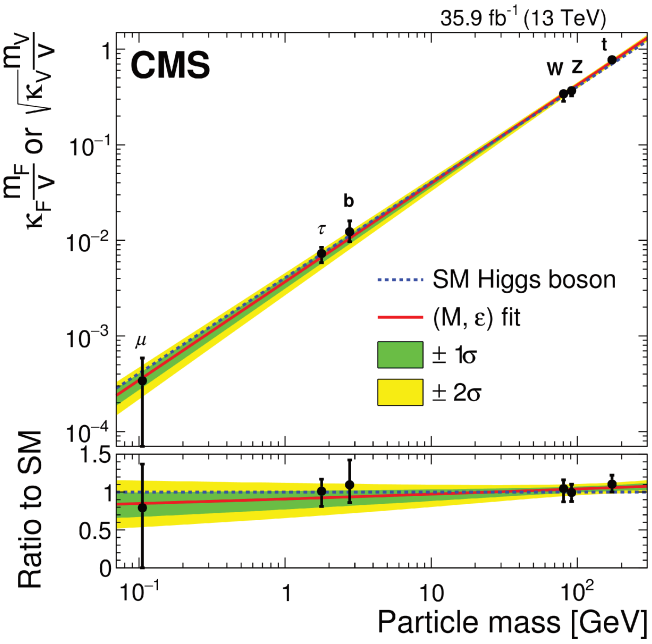

Figure 1.12: CMS measurements of the Higgs boson couplings to several bosons and fermions as a function of their masses. Taken from Ref. [84].

1.7.2 Production

At the LHC, the Higgs boson can be produced in many different ways. Leading-order diagrams for the main processes are represented in Fig. 1.13, and Fig. 1.14 (a) represents their theoretical cross sections as a function of the centre-of-mass energy.

As for top quark pairs, the dominant production mode for the Higgs boson is gluon fusion (ggH). Its cross section of about 50 pb is more than one order of magnitude above that of other modes. Since the Higgs field does not couple to massless particles, this mechanism proceeds through an intermediate loop involving virtual quarks. Due to its very large mass, the top quark contributes the most to this process ($\sim$ 90%), followed by bottom quarks. Because the Higgs boson is produced alone, and depending on its subsequent decay, gluon fusion can lead to rather clean final states containing only few particles.

The second production mode in terms of cross section is vector boson fusion (VBF), wherein the scattering of 2 quarks is mediated by 2 weak bosons which interact (or "fuse")

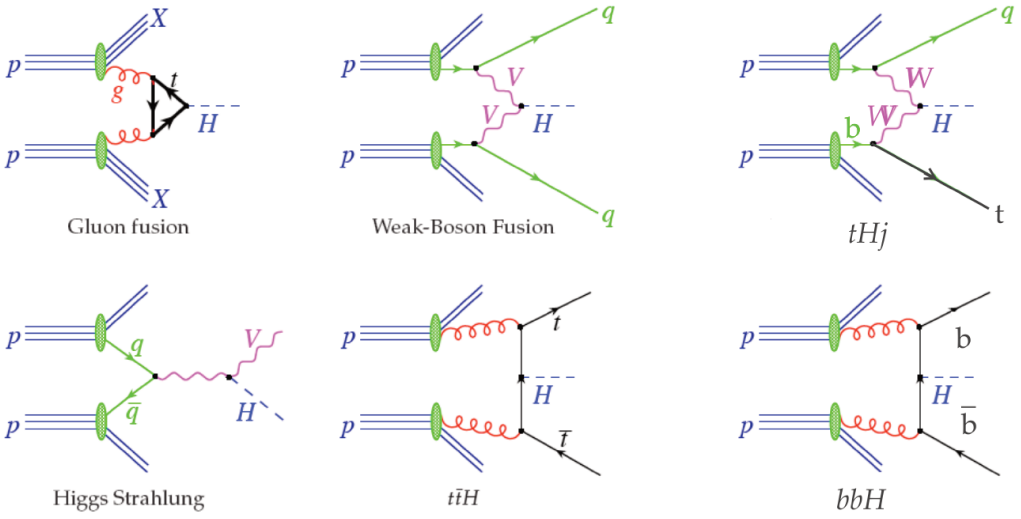

Figure 1.13: LO Feynman diagrams for the main production modes of the Higgs boson. Taken from Ref. [85].

and emit a Higgs boson. The quarks are emitted in the forward region, and the absence of QCD radiation in the central region of the detector give this process a distinctive signature. In the Higgs-Strahlung mechanism (VH), a weak boson originating from quark-antiquark annihilation with sufficient energy radiates a Higgs boson.

The associated production of a top quark pair and a Higgs boson ($t\bar{t}H$) represents about 1% of the total Higgs production rate. This mechanism was recently observed for the first time both by the ATLAS and CMS collaborations [86, 87], thus confirming that the two particles interact strongly with each other. This observation results from the combination of analyses targeting different decay channels, and the use of advanced techniques. This process is particularly interesting to study because it directly probes the magnitude of the Yukawa coupling of the top quark. The similar process involving a pair of bottom quarks ($b\bar{b}H$) has a comparable cross section but leads to final states harder to distinguish from backgrounds [88].

In comparison, the associated production of a single top quark and a Higgs boson (tH) has a cross section smaller by one order of magnitude. The study of this very rare process is part of the work presented in this thesis, and an extensive introduction will be given in Chapter 5.

1.7.3 Decay channels

Due to its short lifetime, the Higgs boson can not reach the detector and must be studied through its decay products. The SM predictions for the branching ratios of the different decay channels depend directly on its mass, as shown in Fig. 1.14 (b). It is fortunate that many of them are sizeable at the observed value $m_H = 125$ GeV. This yields a very rich phenomenology and a wealth of possible final states, allowing to probe many different SM parameters.

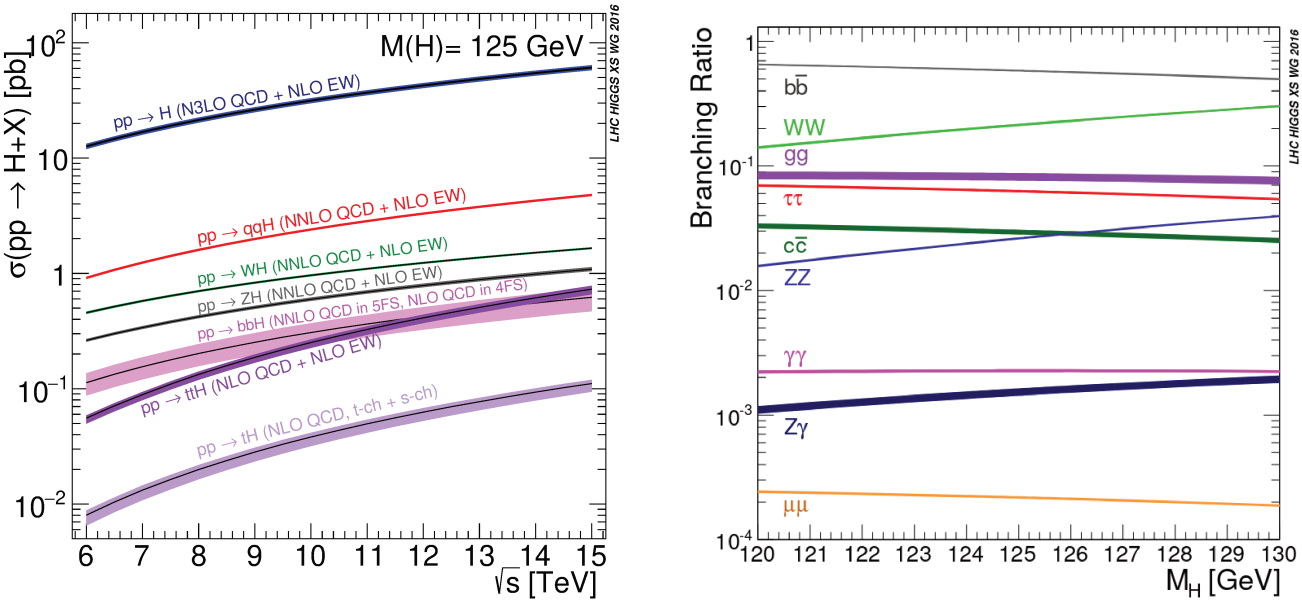

(a) (b)

Figure 1.14: (a) Cross sections of the SM Higgs boson production modes as a function of the centre-of-mass energy $\sqrt{s}$ and (b) main branching ratios ofhe SM Higgs boson for proton-proton collisions. The VBF process is labelled qqH. The theoretical uncertainties are indicated as bands. Figures taken from Ref. [24].

The coupling of the Higgs field to fermions scales with their masses. Since a pair of b quarks is the heaviest possible final state of a Higgs boson decay, the $H \to b\bar{b}$ decay channel is dominant. It is followed by the decays to WW^*, gg, $\tau\bar{\tau}$, $c\bar{c}$, ZZ^* and $\gamma\gamma$. The mass difference between the Higgs and weak bosons implies that one boson must be off-shell in the WW^* and ZZ^* channels. The decay to a pair of top quarks (with one quark off-shell) is heavily suppressed kinematically and is not expected to be observable. As the Higgs field does not couple to gluons nor photons, such decays are loop-induced, with the top quark and W boson contributing the most to these loops.

Interestingly, even though the $\gamma\gamma$ and ZZ^* channels have the tiniest branching ratios (compared to the other decays studied at the LHC), they contributed the most to the discovery of the Higgs boson in 2012. Indeed they both have very clean and distinctive signatures, compensating for their small cross sections. Other channels such as $H \to e\bar{e}$, $\mu\bar{\mu}$ would also have clean signatures, but are inaccessible at the LHC due to their small branching ratios. This is one of the many motivations for the upgrade to the High-Luminosity LHC [89–91] (HL-LHC), or the development of new colliders focused on precision measurements, such as the International Linear Collider [92] (ILC).

1.8 Beyond the standard model

1.8.1 Shortcomings of the standard model

We have described the core components of the standard model and mentioned a few of its major successes. In particular it provides a coherent picture for all the elementary particles known up to now, and for their interactions via the 3 fundamental forces relevant at the considered scales. Its predictive power makes it one of the most stringently tested models in physics, and was again remarkably exemplified by the discovery of the Higgs boson.

But in spite of its important achievements, the SM falls short of explaining several important observations. First of all, it considers neutrinos as massless particles. This is in direct contradiction with the results of a multitude of experiments, which have established the existence of *neutrino oscillations*. This phenomenon whereby the flavour of a propagating neutrino can evolve with a given propability implies a mismatch between its flavour and mass eigenstate, thus requiring a non-zero mass.

Furthermore, a major insufficiency of the theory is its lack of description of *dark matter* and *dark energy*. The first evidence for dark matter came in 1933 [93] from the study of the rotational speed of galaxies, which suggests that they contain a large amount of undetected mass. It could not be related to any SM particle, and the fact that dark matter was never observed directly implies that it must interact only weakly with ordinary matter and radiations. Many experiments are aiming at the direct detection of such *Weakly Interacting Massive Particles* [94, 95] (WIMP), yet without success.

Likewise, dark energy was hypothesised to have a repulsive action and to permeate the universe, in the first place to explain its accelerated expansion. Since then, the existence of these new forms of matter and energy have been supported by cosmology experiments of various kinds. Notably, they could explain the data collected by the Planck spacecraft regarding the *cosmic microwave background* (CMB). This relic radiation dating to an early stage of the universe indicates that the spacetime curvature is close to flat, which presupposes a mass-energy density much higher than what we would expect. Along with other peculiar features of the CMB (such as the pattern of its anisotropies), this can most conveniently be explained by models including dark energy and dark matter. From Planck's data it is estimated [96] that they represent about 68% and 27% respectively of the mass-energy content of the universe, implying that the SM describes no more than 5% of it.

Thirdly, the SM does not provide a satisfactory explanation for the asymmetry between matter and antimatter. Indeed it would be expected that after the Big Bang, the constant production and annihilation of particle-antiparticle pairs would yield similar amounts of both, resulting in a universe dominated by radiations. Instead, the fact that all the large cosmological structures are constituted of matter, rather than antimatter, suggests that some mechanism made their production asymmetric already at the early ages of the universe. An example of such a mechanism within the SM is the violation of

the CP symmetry by the weak interaction [53]. However, the magnitude of this effect has been measured to be tiny, and can not alone account for the observed disproportion.

In addition to these insufficiencies related to experimental observations, the SM also contains some arbitrariness in its construction and a few surprising features. Although they do not invalidate the model, they are strong indications that it is not yet complete, and that new physics is required to understand these features.

The SM possesses 19 free parameters (when neglecting neutrino masses) whose values must be determined experimentally. Moreover the gravitational force could not yet be included in the SM as a gauge theory. Indeed, general relativity, which describes it so accurately, is not perturbatively renormalizable in its quantized version. The associated boson (*graviton*) would introduce ultraviolet divergences in the theory that can not be eliminated, and which make its predictions unphysical. It is also difficult to accomodate the different paradigms wherein gravity is either caused by the deformation of spacetime, or is mediated by the exchange of gauge bosons.

Besides, one could question why the weak force is 10^{24} times stronger than gravity, or why the masses of fermions range across so many orders of magnitude without an obvious pattern. On a related note, the so-called "naturalness" problem [97] arises from the fact that the mass of the Higgs boson is highly sensitive to loop corrections (mainly involving the top quark, the W boson and itself according to the SM). If the theory was to be considered valid up to very high energies such as the Planck scale $\Gamma_P = 10^{19}$ GeV, the magnitude of these corrections would blow up ($\propto \Gamma_P^2$). Since the Higgs boson's mass was measured to have the comparatively tiny value of 125 GeV, it would mean that its bare mass parameter must be fine-tuned extremely precisely to cancel out the divergences, in a way considered artificial by many theorists.

This non-exhaustive list of shortcomings of the SM suggests that it only corresponds to a low-energy approximation to a more fundamental theory *beyond the standard model* (BSM). Various BSM models propose explanations to some of the aforementioned issues or questions, by postulating the existence of new particles or mechanisms.

Among BSM models, *supersymmetry* [98, 99] (SUSY) is regarded as one of the most promising. It exists in different versions which all share a common underlying principle, namely the introduction of a new symmetry beween bosons and fermions. Each fermion would be associated with a supersymmetric boson, and vice-versa. SUSY extensions could for instance solve the naturalness problem, or predict the unification of the gauge interactions at higher energy. They could also provide a stable particle candidate for dark matter. But despite an important research effort led by the ATLAS and CMS experiments at the LHC, no evidence for supersymmetry was found yet.

1.8.2 Effective field theory and indirect search for new physics

Even in the absence of any direct observation, new particles could still manifest themselves indirectly, e.g. through their decay products or via loop corrections. To interpret

deviations in measurements in terms of new physics, one of the main approaches is that of *effective field theory* (EFT) [100]. An EFT corresponds to a low-energy approximation to a more fundamental underlying theory, characterized by an energy scale Λ (e.g. the mass of new particles) well above what can currently be probed experimentally. The validity of an EFT is restricted to a limited energy range, and may not hold in different regimes.

EFTs provide a well-defined framework to interpret deviations from predictions in a model-independent way. They consistently correlate the effects that new physics could potentially have on different observables, and thus allow to distinguish between competing BSM models. There is a wealth of historical examples in which the use of effective theories made it possible to precisely describe phenomenons, before the fundamental mechanisms involved could be unveiled. For example, Classical Mechanics can be considered as an effective theory of special relativity, and the Fermi model of the weak interaction (Sec. 1.4.1) is an EFT which provided precise predictions before the SM was built or the W boson discovered.

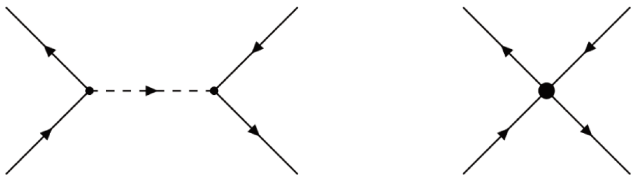

Figure 1.15: Illustration of the basic concept of an EFT. An interaction mediated by a new, yet undiscovered particle (left) is considered as a contact interaction (right) for simplification.

Within the context of EFT, one assumes that a hypothetical new particle is much more massive than the SM particles, and hence its interactions are short-ranged. Consequently, they can be approximated as contact (point-like) interactions, as illustrated in Fig 1.15, much simpler to describe.

In the SM Lagrangian, products of fields (*operators*) are of mass dimension 4. One can introduce new physics effects in the theory by constructing an effective Lagrangian, adding to the SM Lagrangian an infinite sum of higher-order operators:

$$\mathcal{L}_{eff} = \mathcal{L}_{SM} + \sum_i \sum_d \frac{C_i^d}{\Lambda^{d-4}} \mathcal{O}_i^d \,, \tag{1.35}$$

where $\mathcal{O}_i^d$ are the effective operators of dimension d, whose coupling strengths are encoded in the *Wilson coefficients* C_i^d. In this way, the contribution of an operator of dimension n to the effective Lagrangian is proportional to $1/\Lambda^n$. This suppresses the contributions from operators of increasingly high orders, and implies that the effects of new physics can be approximated with a finite set of low-order operators. Moreover, the only valid dimension-five operator violates the conservation of lepton number [101, 102], and is only relevant to test specific BSM models. To probe the existence of new physics in

interactions involving the top quark or the Higgs boson, it is therefore common to only consider the list of dimension-six operators.

CHAPTER 2

The CMS experiment at the LHC

The CERN (*European Organization for Nuclear Research*, formerly known as *Conseil Européen pour la Recherche Nucléaire*) is a European research organisation founded in 1954, dedicated to the advancement of knowledge primarily in the fields of nuclear and particle physics. It is located near Geneva, at the Franco-Swiss border. Besides the numerous scientific breakthroughs that took place at CERN, its constant need for the development of new technologies have had an important impact on the world. Most notably, it is the birthplace of the World Wide Web [103].

The major facility hosted at CERN is the Large Hadron Collider. The Section 2.1 gives an overview of the design, goals and characteristics of this accelerator. In Section 2.2 the CMS detector is presented, which collected the data used in this thesis. The characteristics and performance of its different subsystems are discussed. Finally, physics objects and event reconstruction are introduced in Sections 2.3-2.3.6.

2.1 The Large Hadron Collider

2.1.1 Overview of the LHC

CERN's Large Hadron Collider [3, 4] (LHC) is the world's largest and most powerful accelerator, conceived to cover a broad physics programme. First of all, it was designed as a discovery machine for the Higgs boson, which was observed by the ATLAS and CMS collaborations [1, 2] in 2012. It also aims at revealing new physics, and at favouring or

ruling out BSM scenarios which propose explanations to several shortcomings of the SM (see Sec. 1.8.1). To fulfil these goals, the LHC produces proton and heavy-ion collisions (*events*) at unprecedented energy, notably in order to abundantly produce heavy particles and directly probe the existence of new particles at the TeV scale. Moreover, it provides a high instantaneous luminosity, as discussed in Sec. 2.1.4, allowing to collect data faster than its predecessors. Thus the LHC can be used to perform precision measurements of key parameters of the SM.

Built between 1998 and 2008, its design was largely driven by the desire to take advantage of pre-existing CERN infrastructures. It is installed in the 26.7 km ring tunnel previously used by the Large Electron-Positron (LEP) collider [104]. The LEP was operated from 1989 to 2000, and produced electron-positron collisions at energies ranging from 90 GeV to 209 GeV. Its 4 collaborations published more than a thousand scientific articles, and performed important tests of the SM [105–107]. Notably, a combination of searches for the Higgs boson set a lower bound on its mass and reported a mild excess of data at 115 GeV [108].

The LHC tunnel is located between 45 m and 170 m below ground level and has a diameter of 3.7 m. It now contains 2 adjacent beam pipes, inside which 2 counter-rotating beams travel around the ring. The LHC principally produces proton-proton (p-p) collisions, with a design maximum centre-of-mass energy $\sqrt{s} = 14$ TeV. It can also accelerate heavy-ions, such as lead (Pb) nuclei, both in Pb-Pb or p-Pb configuration. Throughout the year, data-taking periods are interspersed with maintenance breaks. During winter, the LHC is stopped for the year-end technical stop (YETS), in order to spare energy (the peak consumption of the LHC and the detectors alone amounts to as much as 1/5 of that of the city of Geneva) and perform the necessary maintenance and upgrade works.

LHC operations started in September 2008. Only a week later, an incident caused by a faulty electrical connection resulted in an additional 14 months delay and the lowering of the beam energy [109, 110]. During the Run 1 data-taking period, from 2009 to 2013, the LHC produced p-p collisions at the record-breaking centre-of-mass energies $\sqrt{s} = 7$ TeV (2010, 2011) and later $\sqrt{s} = 8$ TeV (2012). The previous record of $\sqrt{s} = 1.96$ TeV was held by Fermilab's Tevatron [65, 66], which was decommissioned in 2011. The LHC was then shut down for 2 years, to upgrade its detectors and allow for an increase of the beam energy. It was restarted in 2015, and produced p-p collisions at $\sqrt{s} = 13$ TeV until the end of the Run 2, in late 2018. The ongoing long shutdown (LS2) period aims at the repair and upgrade of the LHC infrastructures and detectors.

In general, accelerators use charged, stable particles. Electrons, being fundamental particles, are much better suited to perform extremely precise measurements at controlled energies. However, the main rationale for colliding instead composite protons at the LHC is that they undergo much smaller synchrotron radiation losses due to their larger mass (by a factor of about 1836^4, since the synchrotron radiation power is proportional to $1/m^4$, and $m_p/m_e \approx 1836$).

Synchrotron radiations are emitted whenever a charged particle is accelerated radially or moves in a magnetic field on a circular orbit, as is for instance the case in circular accelerators, where particles are forced to travel along a curved path by a magnetic field. Although this is a useful feature used by many experiments to produce radiations at specific energies, in the case of particle physics this represents a loss limiting the maximum beam energy in a circular accelerator. Therefore, a proton collider can reach much higher energies than an electron collider. While the centre-of-mass energy of the LEP was limited by the large synchotron radiation of its electrons, that of LHC is determined by the capacity of its magnets to maintain the massive protons on their circular trajectory.

Furthermore, the energy reached at the LHC is such that an important fraction of the proton's momentum is carried by the sea quarks and gluons. Therefore it is possible to generate interesting physics (e.g. the production of Higgs bosons via gluon fusion) without colliding protons with their antiparticles, which are less affordable and much more difficult to produce in sufficient quantities.

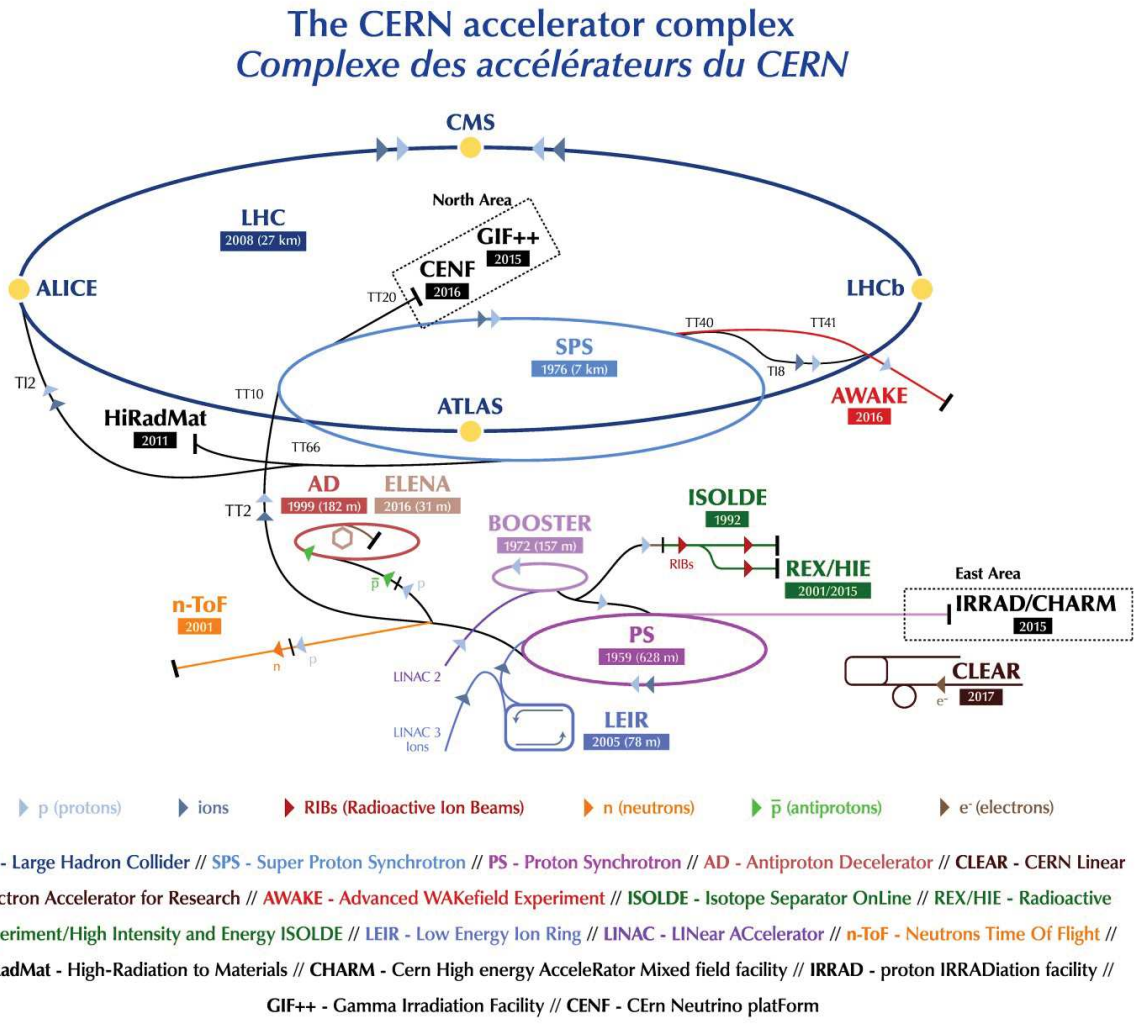

Figure 2.1: Illustration of the accelerator complex at CERN. Taken from Ref. [111].

2.1.2 The accelerator complex

The LHC is the final and major part of a wider accelerator complex illustrated in Fig. 2.1. Before protons enter the LHC ring and get accelerated to their maximum energy, they first pass through a chain of pre-accelerators. These were built well before the LHC, and upgraded to meet its stringent needs. They also provide particles to smaller CERN experiments with different aims.

The very first step of the chain consists in the extraction of protons from a bottle of hydrogen gas. The gas is injected into a metal cylinder called *duoplasmatron* [112], where protons are separated from electrons using an electric field. The protons are then sent to a *Radio Frequency Quadrupole* (RFQ), a type of cavity which allows at the same time to group the protons into bunches, accelerate the bunches, and focus them. After being accelerated to 750 keV, the protons are fed into the Linear Accelerator (Linac 2, currently being replaced by the newer Linac 4) and brought to an energy of 50 MeV.

Following a 80-m-long transfer line, the particles then arrive into the Proton Synchrotron Booster (PSB, 150 m circumference) where they reach an energy of 1.4 GeV. Next, they enter the Proton Synchrotron (PS, 628 m circumference) and later the Super Proton Synchrotron (SPS, 6912 m circumference) which bring them to energies of 26 GeV and 450 GeV respectively. Finally, the proton bunches are provided to the LHC using fast kicker magnets. It takes about 5 minutes to fill the ring with the 2 counter-rotating beams, and they get accelerated for about 20 minutes before they reach their final energy.

Similarly, lead atoms are obtained from a lead sample heated to high temperature. This generates lead ions which are selected depending on their charges, and sent through a carbon foil to turn them into Pb^{54+} ions. Once accumulated, they get accelerated in the Low Energy Ion Ring (LEIR) and sent to the PS. After being fully stripped of their electrons, the resulting Pb^{82+} ions are sent to the SPS, and finally the LHC which accelerates them at an energy of up to 2.76 TeV per nucleon.

2.1.3 The LHC machine

Design

The two rings hosted in the 3.7-m-diameter tunnel of the LHC share the same mechanical structure and cryostat system. A ultra-high vacuum is achieved around the magnets and the cooling system to insulate them, and in the beam pipes to minimize the contamination from gas molecules. About 2 weeks of pumping are required to bring the pressure down to 10^{-13} atm in the beam pipes. With the current optimized filling scheme, the LHC can accelerate and collide as many as 2556 proton bunches per beam, each bunch containing about 115 billion protons. They are spaced at intervals of 25 ns each (50 ns during Run 1), and circle around the ring about 11000 times per second, only 3.1 m/s slower than the speed of light. This corresponds to a bunch collision rate of 40 MHz when the LHC is full.

Each beam is accelerated by its own radio frequency (RF) system comprising 8 cavities. The cavities are operated in a superconducting state, in order to greatly reduce the amount of heat generated by the large electrical power currents. They are cooled with superfluid helium down to a temperature of 4.5 K. Each cavity provides a 2 MV accelerating voltage at a frequency of 400 MHz. The oscillating field is synchronized with the arrival of proton bunches, in order to provide optimal acceleration throughout the cavity length. *Asynchronous* protons, which are early or late with respect to the bunch average, are subjected to fields of different intensities. The resulting acceleration or deceleration forces them back into the bunches.

The LHC comprises a total of 9593 magnets based on niobium-titanium (NbTi) technology, which represent an important fraction of the machine's total cost. Among them, 1232 dipole magnets bend the path of the proton bunches to keep them on a circular trajectory. They are almost 15-m-long and weigh 35 tons each. They generate a magnetic field of 8.3 T, about 10^5 times more than the Earth's magnetic field. 392 quadrupole magnets focus the beams. Their 4 symmetric poles squeeze the beams both horizontally and vertically. Stronger magnets are placed close to the collision points to maximise the luminosity. Additionally, magnets of higher multipole orders (sextupoles, octupoles, decapoles) are used to fine-tune the geometry of the fields at the extremities of the dipoles.

The LHC magnets are cooled down to 1.9 K, colder than outer space. This requires about 120 tons of superfluid Helium-4 with null viscosity, which has excellent heat dissipation properties, making the LHC the largest cryogenic system in the world. This extremely low temperature keeps the wires of the magnets in a stable supraconducting state wherein their electrical resistance vanishes, allowing them to sustain higher electrical currents and generate more intense magnetic fields. As an example, operating the magnets at the slightly higher temperature of 4.22 K (the boiling point of helium) would translate into a decrease of about 3 T of the dipole magnets' magnetic field, corresponding to a decrease of the beam energy by several TeV [113, 114].

As illustrated in Fig. 2.2, the LHC is not perfectly circular. It is composed of 8 independent sectors of 2.45 km each which contain the bending magnets, linked by 545-m-long straight sections. The exact layout of a given straigth section depends on its purpose: namely beam injection, beam dumping, beam cleaning or physics experiment. The beam dump system allows the safe redirection of the beams into a 8-m-long graphite block embedded in concrete, using fast kicker magnets. As the total energy stored in each beam can reach 350 MJ (comparable to the energy of a train of 400 tons moving at 150 km/h), such a system is necessary to protect the infrastructures and the detectors in case of a technical failure. It is also used whenever the proton density in the bunches has decreased below a given threshold, and the beams need to be removed from the machine prior to re-injection.

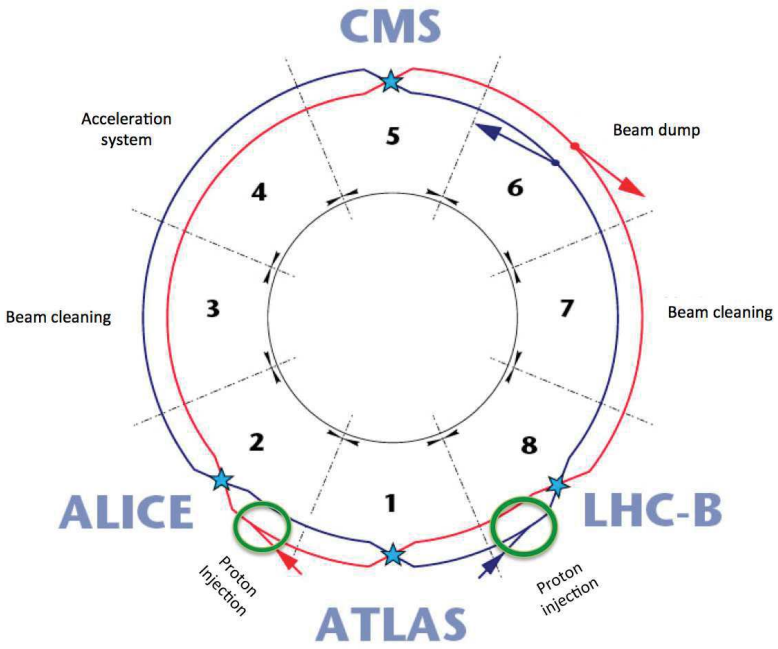

Figure 2.2: Schematic layout of the LHC ring. Taken from Ref. [115].

Experiments

The LHC hosts 4 major experiments, located at the 4 interaction points (IP) where particles collide. ATLAS [116] (*A Toroidal LHC ApparatuS*) and CMS [117] (*Compact Muon Solenoid*) are multi-purposes detectors which can study both protons and heavy-ions collisions. They cover a broad physics programme, from precision tests of the SM to searches for new physics. Their subdetectors use different technologies, making these experiments complementary to each other. Major findings, such as the discovery of the Higgs boson, or the recent observation of the $t\bar{t}H$ process, can thus be verified independently by the 2 collaborations, which increases the credibility of the results. Moreover, analyses performed both by ATLAS and CMS can later be combined to reach better statistical precision.

ALICE [118, 119] (*A Large Ion Collider Experiment*) is a detector optimized to study heavy-ion collisions. One of its primary aims is to explore the *quark-gluon plasma* [120] forming at extreme energy densities, a phase of matter in which quarks and gluons are no longer bound into hadrons. Its study may provide insights on the early state of the universe, as it is speculated that matter existed in this phase up to a few microseconds after the Big Bang (temperature of $\sim$ 100 MeV, or 10^{12} K). It also helps understanding better key QCD mechanisms such as confinement. The ALICE detector comprises a total of 19 subdetectors, and was designed to efficiently cope with the very high particle multiplicities generated by heavy-ions collisions.

LHCb [121] (*Large Hadron Collider beauty*) is a specialized b-physics experiment, focusing on hadrons containing a bottom quark. Among its main goals are the measurement of parameters of the CKM matrix and the search for CP violation [122] and flavour violation [123]. Contrary to the 3 other detectors, which enclose the interaction point, LHCb is an asymmetric single-arm detector. Its layout exploits the fact that at high energies, $b\bar{b}$ pairs are predominantly produced via strongly asymmetric gluon fusion, and are thus boosted together in the same forward (or backward) region.

In addition, smaller experiments are connected to the LHC and use its beams: TOTEM [124–126] (*TOTal cross section, Elastic scattering and diffraction dissociation Measurement at the LHC*) is located in the CMS cavern and notably performs precision measurements of the p-p interaction cross section, as well as in-depth studies of the proton structure; its ATLAS counterpart is called ALFA [127] (*Absolute Luminosity For ATLAS*); MoEDAL [128, 129] (*Monopole and Exotics Detector at the LHC*) searches for magnetic monopoles and shares the same cavern as LHCb; LHCf [130] (*Large Hadron Collider forward*) produces particle cascades akin to those generated in cosmics rays, to understand better this phenomenon.

2.1.4 Luminosity and pileup

Luminosity

Luminosity [24, 131] is a crucial quantity for any particle collider. The number of events $\partial N/\partial t$ produced for a given process with cross section σ, per unit of time, is directly related to the *instantaneous luminosity* $\mathcal{L}$ as:

$$\frac{\partial N}{\partial t} = \mathcal{L} \times \sigma. \tag{2.1}$$

By integrating $\mathcal{L}$ over time, one obtains the *integrated luminosity* $L = \int \mathcal{L}\, dt$, which characterizes the volume of data which has been produced or collected. The instantaneous luminosity is usually expressed in $\mathrm{cm}^{-2}.\mathrm{s}^{-1}$, and the integrated luminosity in inverse picobarns (pb^{-1}) or femtobarns (fb^{-1}) [1].

Alongside the beam energy, the instantaneous luminosity is one of the most important parameters of a collider, and a direct indicator of its performance. This rings particularly true for the LHC, whose physics programme heavily relies both on the highest achievable centre-of-mass energy and luminosity, to study very rare processes and perform the most precise measurements to date of several SM parameters.

In order to achieve a high collision rate, it is necessary to maximise the instantaneous luminosity. In the case of two relativistic beams sharing the same characteristics at a

[1] 1 barn = 10^{-28} m^2, thus 1 fb^{-1} = 10^{39} cm^{-2}.

circular collider, it is defined as:

$$\mathcal{L} = \frac{f\, N_b\, n_p^2}{4\pi\, \sigma_x\, \sigma_y}\, F\,, \tag{2.2}$$

where N_b is the number of bunches per beam, n_p is the number of particles per bunch, f is the revolution frequency of the bunches, $\sigma_{x,y}$ are the transverse beam sizes along the x and y axes, and F is the geometric luminosity reduction factor due to the crossing angle at the interaction point ($F \leq 1$). Although the LHC specifications foresaw that the machine could accelerate up to 2808 bunches in each direction, this number was limited to 2556 during Run 2 to allow for an important reduction of the transverse size of the beam to about 2.5 μm, resulting in a greater beam density and hence luminosity. This optimized filling scheme (called BCMS [132–135]) used during Run 2 made it possible to reach a peak luminosity of 2.1×10^{34} cm^{-2}s^{-1}, more than twice the design value (and almost two orders of magnitude larger than that of the Tevatron [136]).

Figure 2.3 shows the cumulative evolution of the integrated luminosity delivered to the CMS detector during p-p collisions at nominal $\sqrt{s}$, for each year of data-taking. The observed trend illustrates how the continuous improvement of the LHC machine allowed collecting data at an ever-faster rate over the years. The total integrated luminosities collected by CMS during Run 1 and Run 2 amount to 27.4 fb^{-1} and 150.3 fb^{-1} respectively [137].

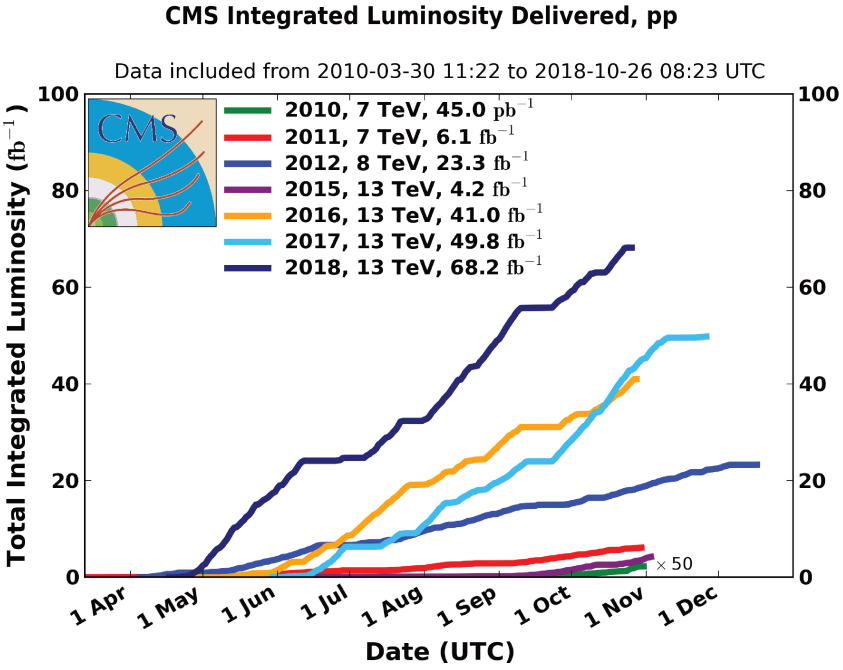

Figure 2.3: Evolution of the cumulative luminosity delivered to CMS over time, during stable beams for p-p collisions at nominal centre-of-mass-energy, for each year of data-taking. Taken from Ref. [137].

Pileup

The *pileup* (PU) represents an important limitation for any collider with high instantaneous luminosity. At the LHC, pileup corresponds to the fact that multiple p-p interactions take place at each bunch crossing, resulting in a higher detector occupancy. As the typical cross sections of the processes of interest at the LHC are many orders of magnitude lower than the p-p interaction cross section, it is unlikely that 2 distinct "hard" (highly energetic) collisions between partons happen in the same bunch crossing and produce physics of interest simultaneously. However, the products of the different interactions must still be disentangled, and this degrades the efficiency and resolution of particle reconstruction.

The PU directly affects the precision of measurements, and can represent an important source of systematic uncertainty for some analyses. Figure 2.4 (a) shows the distributions of the mean number of proton-proton interactions per bunch crossing, for each year of data-taking. It illustrates the increase of the average pileup since the beginning of LHC operations, due to the increase in instantaneous luminosity. In 2018, the average pileup in the CMS detector was measured to be 37 in average. Figure 2.4 (b) shows a CMS event display in which 78 different interaction vertices were reconstructed in the tracker, illustrating the challenges posed by a large pileup.

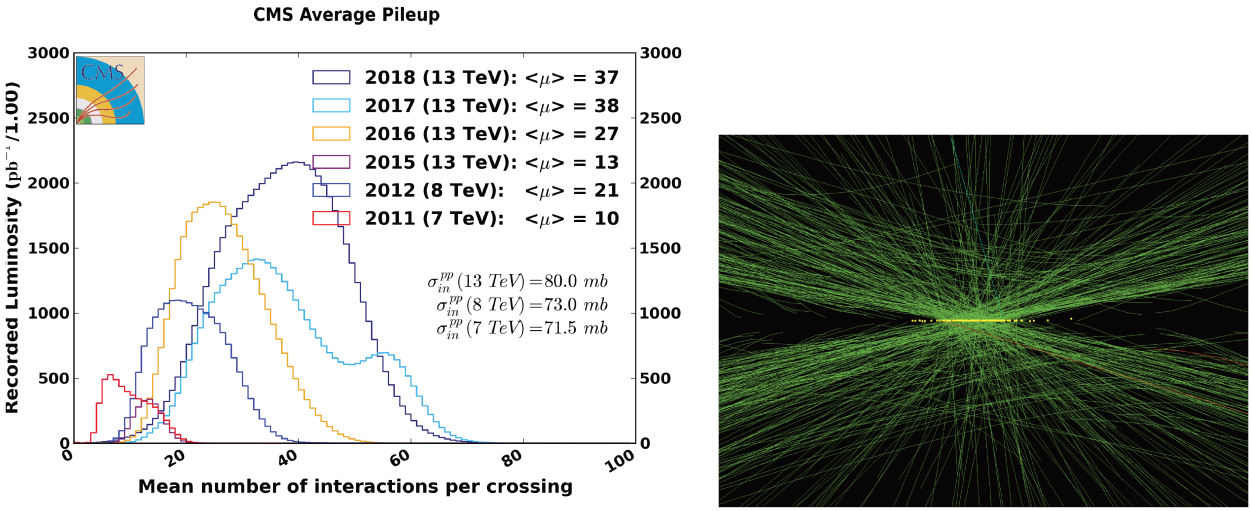

(a) (b)

Figure 2.4: (a) Mean number of interactions per bunch crossing (pileup), for each year of *pp* data-taking. The mean pileup values are indicated. Taken from Ref. [137]. (b) Event display showing 78 different reconstructed vertices (yellow dots) in the CMS Tracker. This event was recorded during a high-pileup run in 2012. Taken from Ref. [138].

A distinction is made between *in-time* PU, corresponding to multiple collisions taking place in the same bunch crossing as the collision of interest, and *out-of-time* PU, corresponding to interactions happenning in the bunch crossings before and after it (other minor sources of PU are listed in [139]). Their effects must be simulated and mitigated

as efficiently as possible [140, 141]. In-time PU interactions may be distinguished by the positions of their respective vertices, which are spread along the beam axis (cf. Fig. 2.4 (b)). As they are also less energetic, the sum of the momenta of the tracks associated with each vertex can be used to identify the primary vertex. As the response times of most detectors exceed 25 ns, out-of-time PU may bias the measurement. In order to reduce the impact of pileup, a detector close to the interaction point with high granularity and satisfying time resolution is thus essential for any LHC experiment.

2.2 The CMS detector

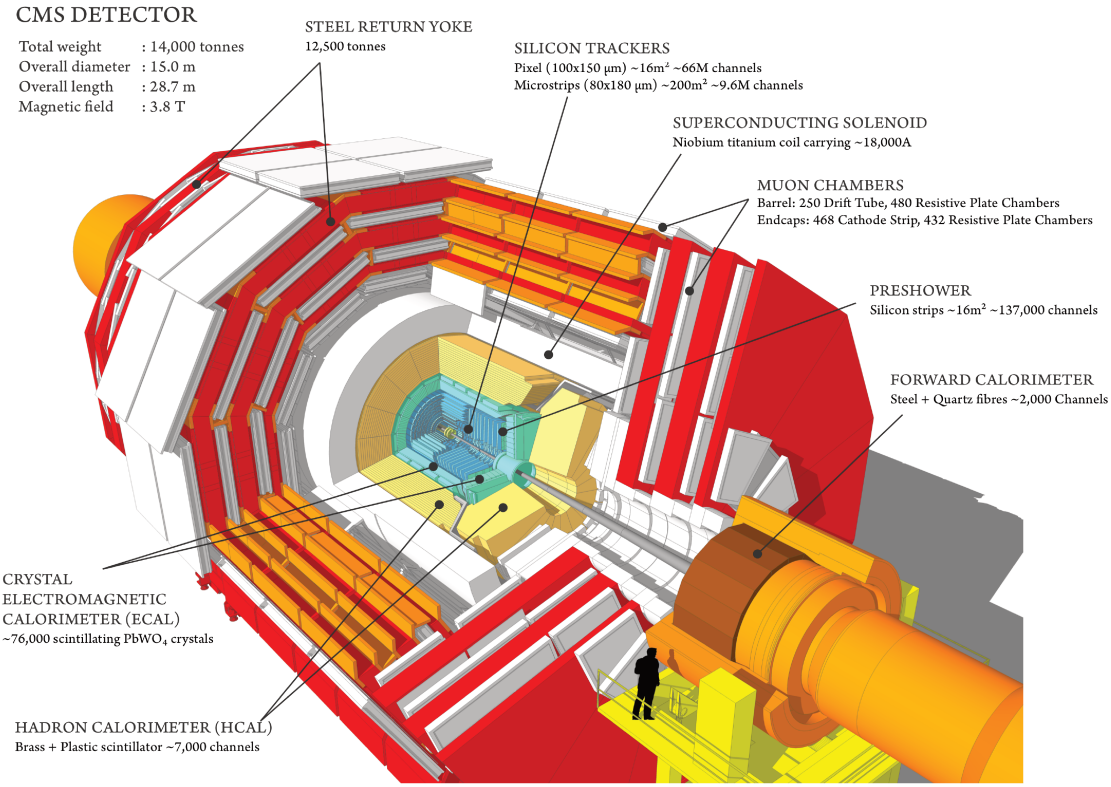

Figure 2.5: Sectional view of the CMS detector, with its main subdectors indicated. Taken from Ref. [142].

CMS [117] (*Compact Muon Solenoid*) is a cylindrical detector, which has a length of 21.6 m, a diameter of 14.6 m, and weighs 14500 tons[2]. It is located in a cavern at the LHC Point 5, near the village of Cessy in France, about 100 m below ground level. The CMS collaboration is one of the largest in the world, with almost 3000 physicists and 1000 engineers, representing 229 institutes from 51 countries and regions [143]. As it was already

[2]The fact that it is labelled as "compact" can be understood when comparing it to the ATLAS detector, which is 46-m-long and 25-m-wide, but weighs 7000 tons.

mentioned, CMS is a general-purpose detector covering a broad physics programme, with a focus on the investigation of the mechanism of electroweak symmetry breaking.

The layout of the detector and its main components is illustrated in Fig. 2.5. One of the distinctive features of CMS is its high field (3.8 T) solenoidal magnet, which in combination with the silicon tracker allows for the precise measurement of the momenta of charged particles. Its also comprises a homogeneous electromagnetic calorimeter with excellent energy and spatial resolutions, a hadronic calorimeter, and a highly-efficient muon detection system. These features allow for the measurement of the momenta of muons, electrons and photons with a precision of about 1% at 100 GeV, and better than 3% for jets above 30 GeV. More details on the design and performance of each subdetector are given in the sections 2.2.3-2.2.5.

Moreover, CMS covers a very wide solid angle (close to 4π for the muon system), and has radiation-hard detectors and electronics which can sustain the extreme radiation levels close to the interaction point. The *trigger system*, is described in Sec. 2.2.6. It uses simple criteria to quickly decide if an event is to be recorded or not, and is rendered necessary by the limitations in computing power, data storage rate and capacity. The algorithm used to reconstruct and identify particles from the detector-level information is introduced in Sec. 2.3.1.

2.2.1 Coordinate system and conventions

The coordinate system used by CMS is sketched in Fig. 2.6 (a). The axis of the CMS detector corresponds to the beam axis, labelled z, and collisions take place in its centre (IP5). The y-axis points vertically upward, while the x-axis points radially toward the centre of the LHC ring.

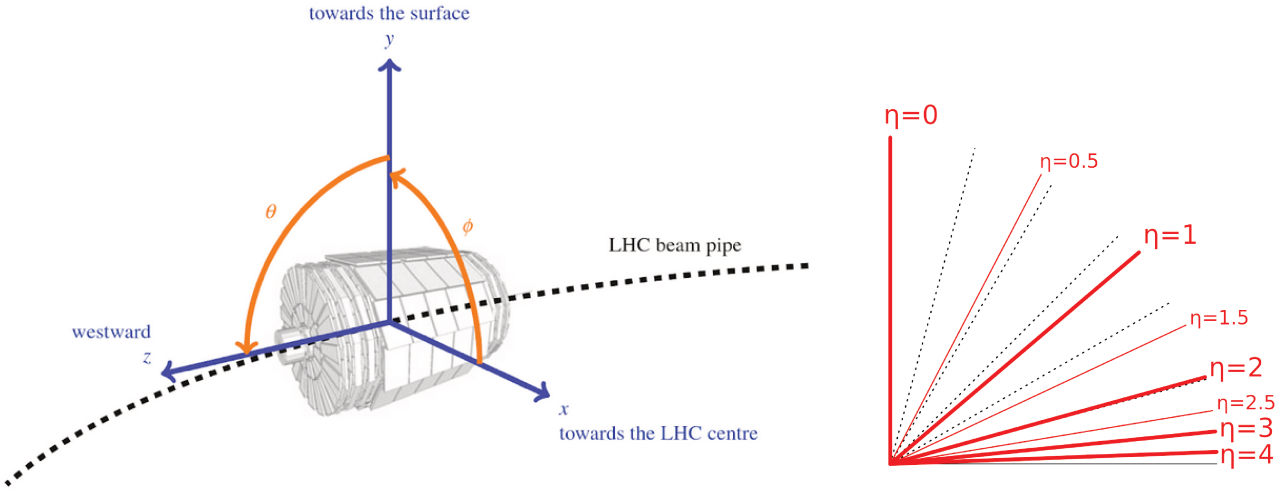

(a) (b)

Figure 2.6: (a) Illustration of the coordinates conventions used at CMS. (b) Examples of corresponding values between the polar angle θ and the pseudorapidity η. As θ approaches zero, η approaches infinity.

The x-y plane is called the *transverse* plane, and is of particular importance for LHC experiments (as explained in Sec. 2.3.5). Within this plane, one can compute transverse quantities such as the *transverse momentum*, defined as $p_T = \sqrt{p_x^2 + p_y^2}$, and the azimuthal angle ϕ starting from the x-axis. In the y-z plane, the polar angle θ is measured from the y-axis. To describe the angle of a particle relative to the beam axis, a very useful spatial coordinate is the pseudorapidity η:

$$\eta \equiv -ln(tan\frac{\theta}{2}) \,. \tag{2.3}$$

The difference in pseudorapidity $\Delta\eta$ between 2 particles is Lorentz-invariant, i.e. it does not depend on the longitudinal boost of the event. This is important because colliding partons have different energies, implying that the longitudinal boost of the event's rest frame differs from one collision to another. As illustrated of Fig. 2.6 (b), a pseudorapidity $|\eta| \to \infty$ corresponds to a trajectory parallel to the beam line.

Another important quantity is the *angular distance*, defined as:

$$\Delta R \equiv \sqrt{\Delta\phi^2 + \Delta\eta^2} \,, \tag{2.4}$$

where $\Delta\phi = |\phi_1 - \phi_2|$ and $\Delta\eta = |\eta_1 - \eta_2|$. This quantity is particularly useful to characterize the solid angle around a particle, and how *isolated* it is. The isolation of electrons and muons is measured relatively to their transverse momentum p_T^l as [144]:

$$I^l = \left(\sum p_T^{charged} + max\left[0, \sum p_T^{neutral} + \sum p_T^{\gamma} - p_T^{PU}\right] \right) / p_T^l \,, \tag{2.5}$$

where $\sum p_T^{charged}$, $\sum p_T^{neutral}$ and $\sum p_T^{\gamma}$ are the scalar sums of the transverse momenta of charged hadrons originating from the primary vertex, neutral hadrons and photons respectively, found within a cone of fixed size. The contribution from pileup p_T^{PU} is estimated differently for electrons and muons [144, 145]. It must be substracted because isolation-related quantities are among the most sensitive to the presence of PU. The isolation is a most useful quantity to identify *prompt* leptons produced in electroweak interactions, as will be explained in Chapter 4.

2.2.2 The solenoidal magnet

The superconducting solenoid magnet of CMS constitutes one of its key components, and is the central apparatus around which the experiment was designed. With its 220 tons and large dimensions (6-m-wide, 12.5-m-long), this device is the largest of its kind ever built. It generates an axial magnetic field of 3.8 T, mostly uniform within its volume, bending the paths of charged particles in the transverse plane through the Lorentz force $\vec{F}_L = q(\vec{v} \wedge \vec{B})$.

The magnet encompasses the tracker and the calorimeters, which prevents that the measurements of these detectors be affected by the particles' interactions with the material of the magnet. Combined with the precise spatial resolution of the tracker, the intense magnetic field aims at providing an unambiguous determination of a particle's charge, as well as a precise measurement of its momentum, based on its reconstructed trajectory. It also enables the use of sharper momenta thresholds for triggering on muon, which directly impacts the muon detection efficiency. For example, for a muon p_T threshold set at 20 GeV, a decrease of the magnetic field from 4 T to 3 T almost results in the doubling of the muon trigger rate [146].

Like for the dipole magnets, the cabling of the solenoid is made of niobium-titanium alloy. It is cooled by a cryostat system using liquid helium, and is operated at a temperature of 4.7 K. Apart from the superconducting coil, the two other main components of the magnet are the vacuum tank, which houses and insulates the coil, and the return yoke.

The return yoke is responsible for the return of the magnetic flux, to reduce the stray field. It makes up most of the mass of the entire experiment, about 10000 tons. It is composed of 5 three-layered dodecagonal wheels, plus 3 endcap disks at each end. Since the iron of the yoke gets magnetized by the field, it increases its strength and improves its homogeneity outside of the solenoid. Furthermore, the yoke serves as the main mechanical structure supporting all the barrel detector components, and provides housing for the muon tracking system. The thick, dense material of the yoke effectively acts as a filter. It stops all the remaining particles which were not absorbed by the calorimeters, with the exception of muons and neutrinos.

The magnetic field must be accurately characterized over the entire volume of the experiment. Dedicated tests were performed to parameterise the magnetic flux density inside the superconducting coil, with a precision of the order of 0.1% [147].

2.2.3 The silicon tracker

The CMS tracker [117, 148–150] is the device closest to the interaction point. It is 5.6-m-long and 2.2-m-wide, and is composed of 2 main parts: the inner pixel tracker, and the outer strip tracker. They both comprise cylindrical *barrel* layers in the central region of the detector, and *end-cap* disks perpendicular to the beam in the forward region, which extend the geometrical acceptance of the tracker up to $|\eta| < 2.5$.

The design requirements regarding its high granularity, quick response time and radiation hardness led to the choice of silicon sensor technologies for the entire tracker. Charged particles deposit energy via ionisation in the silicon semiconductors and create electron-hole pairs, which then drift towards the electrodes and induce a signal. The reconstruction of such *hits* in several consecutive layers determines the particle's trajectory. The physics related to the silicon strip sensors is introduced in more details in Chapter 3.

With an active silicon area of ~ 200 m^2, the silicon tracker is the largest device of its kind ever built, and its challenging construction involved the collaboration of 51 institutes over more than a decade. The general layout of the tracker is shown in Fig. 2.7,

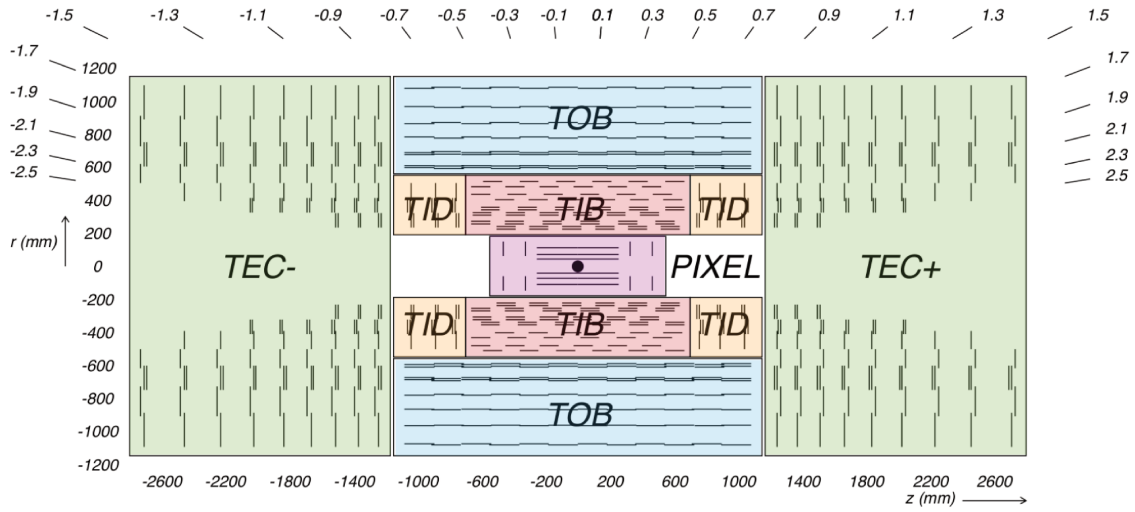

Figure 2.7: Schematic view of a cross section through the CMS tracker. The positions of the pixel tracker and the different parts of the strip tracker are indicated. The lines represent detector modules. The pixel detector was replaced in 2017 and now features one additional layer both in the barrel and endcaps, as explained in the text. Adapted from Ref. [117].

where lines represent detector modules. Double lines indicate *stereo* modules consisting of two strip modules mounted back-to-back and rotated at an angle of 100 mrad, in order to provide 3-D measurements.

A compromise had to be found between providing the best possible services to the detector (high power for electronics, efficient cooling system, precise alignment of the mechanical structure, etc.), and keeping the amount of inactive material as low as possible. Indeed, the passive material generates multiple scattering which degrades the position resolution of the detector modules, and nuclear interactions with hadrons which reduce the tracking efficiency for these particles. Additionally, it causes bremsstrahlung and photon conversions which affect the subsequent energy measurement in the electromagnetic calorimeter. Figure 2.8 shows the simulated material budget of the tracker, in number of hadronic interaction length λ_0, as a function of pseudorapidity.

The primary task of the tracker is the reconstruction of the trajectories of charged particles. As they get bent by the strong magnetic field, this subdetector is able to measure both the electric charge and momentum associated with each reconstructed track. Moreover, its high granularity gives it an excellent spatial resolution, allowing it to precisely reconstruct the *primary* and *secondary* vertices. This is essential to the overall performance of the detector, as it is necessary to identify an interaction of interest in the midst of a high-pileup environment.

The tracker also enables the identification of heavy-flavour quarks or tau leptons produced in many processes of interest. Indeed, their production is characterized by a vertex displaced away from the primary vertex, due to their relatively long lifetimes (i.e. longer

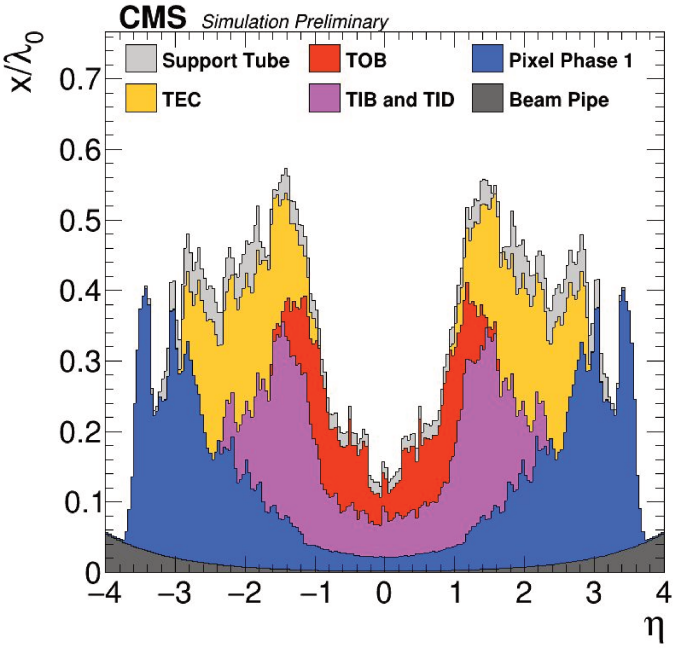

Figure 2.8: Material budget of the CMS tracker in number of hadronic interaction length λ_0 as a function of pseudorapidity η, for the different subdetectors. It is estimated from the simulation with an accuracy better than 10% [151]. Taken from Ref. [152].

flight times before decaying). The information provided by the tracker is used extensively by the trigger system (at HLT level, see Sec. 2.2.6), in order to reduce the rate of potentially interesting events down to reasonable levels.

The pixel inner tracker

The pixel tracker directly surrounds the interaction point, and is subjected to a very high particle flux. This motivated the choice of a silicon pixel technology, which achieves excellent spatial and time resolutions even in such an extreme environment.

The pixel detector plays a very important role, especially regarding the reconstructions of vertices. Its measurements also provide most of the *seeds* for the tracking algorithm, i.e. the starting points from which the full tracks are reconstructed.

Prior to 2017, the pixel barrel (BPIX) contained 3 layers covering the radius range $4.4 \leq r \leq 10.2$ cm from the IP, while the pixel endcaps (FPIX) closing both sides each contained 2 disks located at the distances $|z| = 34.5$ cm and $|z| = 46.5$ cm.

As the pixel detector receives high doses of irradiation, and in order to maintain its excellent performance at an even higher instantaneous luminosity, it was replaced during the extended 2016-2017 winter shutdown. The Phase-1 Upgrade pixel detector [153, 154] features an improved, faster readout chip, as well as an additional tracking layer both in the barrel and forward regions. With the new design, the material budget could be reduced, the innermost layer was moved closer to the interaction point, while the outermost layer was moved further away from it.

The new BPIX now contains 4 layers covering the radius range $3 \leq r \leq 16$ cm, while both sides of the new FPIX contain 3 disks located at distances ranging from $|z| = 29.1$ cm to $|z| = 51.6$ cm. In total this represents 125 million silicon pixels over 1856 modules, with a size $100 \times 150 \mu m^2$ designed for optimal charge sharing between cells. The thickness of the sensitive volume is 285 μm. Beam tests realized with electrons under optimal conditions found that the upgraded pixel detector could reach a tracking efficiency of 99.95$\pm$0.05 %, with intrinsic spatial resolutions of (4.80$\pm$0.25μm) and (7.99$\pm$0.21μm) along the 100 μm and 150 μm directions, respectively [155].

The strip tracker

The strip tracker [117, 156] surrounds the pixel detector and is made of 15148 modules, amounting to a total of 24244 silicon sensors and 9.3 million individual strips. Each module carries either one "thin" 320 μm-thick sensor, or two 500 μm-thick ones. The thicker sensors have correspondingly higher signal, and are used in the outer tracker region to maintain a signal-to-noise ratio well above 10. The sensors come in 15 different geometries, and possess either 512 or 768 strips. The distance between the strips (*pitch*) and the strip length range respectively from 80 μm and 8.5 cm, to 205 μm and 20 cm in the outer regions where the particle flux and occupancy is reduced [117]. A constant ratio $w/p = 0.25$ between the pitch and strip width is used for all sensors.

The strips are wired by groups of 128 to a read-out chip (*APV25* [117, 157], for *Analog Pipeline Voltage*), which samples, shapes and amplifies their signals. Upon a positive decision of the trigger system for a given event, the signal is then propagated via optical fibres to the Front End Driver (FED) boards where it is digitized. A TIB module is shown in Fig. 2.9.

Figure 2.9: Single-sided TIB module. The 512 strips are read-out by 4 APV chips on the right-hand side. Taken from Ref. [158].

The strip tracker has a rather complex design, which reflects the great deal of tradeoffs among resolution, material budget, compactness, cost, etc. It is partitioned into 4 distinct parts. Its innermost barrel detector is the TIB (*Tracker Inner Barrel*) which consists of 4 concentric layers located at radii 25.5 cm, 33.9 cm, 41.85 cm and 49.8 cm respectively,

ranging from -70 cm to +70 cm along the beampipe. The 2 layers closest to the interaction point host *stereo* modules, while the 2 others are made of *mono* modules.

Further from the interaction point in the barrel region is the TOB (*Tracker Outer Barrel*), containing 2 first layers of stereo modules, and 4 additional layers of mono modules. Perpendicularly to the beam, the TID (*Tracker Inner Disks*) close each end of the TIB, providing an hermetical coverage up to $|\eta| \approx 2.5$. Both TID$\pm$ sides (referring to +z or -z) contain 3 parallel *disks*, each of which is made of 3 concentric *rings*. The 2 innermost rings host stereo modules, while the outer one hosts single-sided modules. Similarly, the 2 endcaps TEC+ and TEC- (*Tracker EndCaps*) consist of 9 disks each, made of 4 to 7 rings (equipped with either mono or stereo modules).

2.2.4 The calorimeters

The main purpose of the calorimeters is to measure precisely the energy of the particles. The electromagnetic calorimeter targets electrons and photons, which generate electromagnetic showers, while the hadronic one is primarily aimed at measuring the energy deposited by hadronic jets. They both fit inside the volume of the magnet, and their designs were directly influenced by the need for compactness. They both have high granularities, to avoid that the stacking of multiple particles in a single sensor degrades their measurements. The electromagnetic calorimeter has a much better resolution than its hadronic counterpart.

The electromagnetic calorimeter

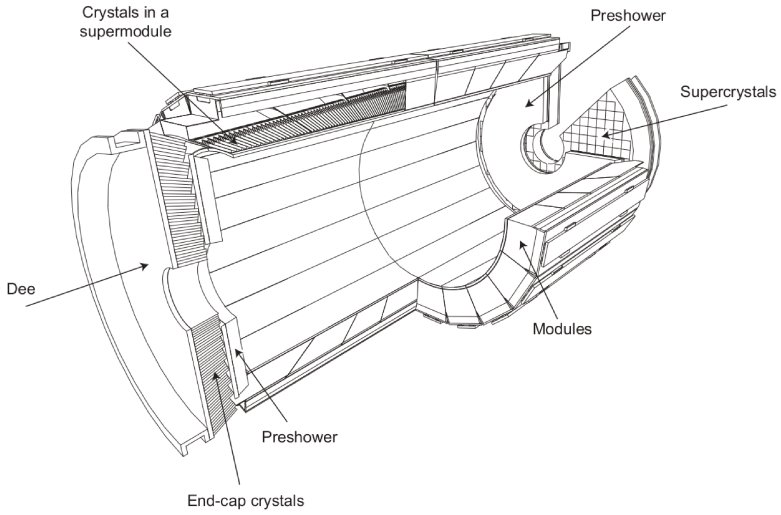

Figure 2.10: Schematic layout of the CMS electromagnetic calorimeter, showing the arrangement of crystal modules, supermodules and endcaps (EE), with the preshower (ES) in front. Taken from Ref. [117].

The homogeneous electromagnetic calorimeter [159] (ECAL) is made of 61200 lead tungstate ($PbWO_4$) crystals in the barrel part (EB, $|\eta| < 1.479$), plus 7324 crystals in both endcaps (EE) which ensure good hermeticity up to $|\eta| < 3$. This high-density material was chosen for its radiation-hardness, fast light emission (80% of the light is emitted within 25 ns) and good sensitivity. Its small radiation length (0.89 cm) and Molière radius [3] (2.2 cm) permitted the design of a finely-segmented and compact detector.

The layout of the ECAL is represented in Fig. 2.10. The barrel is divided into two EB+ and EB- halves, which comprise 18 supermodules each. The preshower (ES) detector is located in front of the endcaps, and provides an improved spatial resolution in the region $1.65 < |\eta| < 2.6$. It contains 2 mm-long silicon strips, to be compared with the $2.2 \times 2.2 \times 23$ cm^3 of the EB crystals. In particular it helps differentiating between single high-energy photons and pairs of collimated, low-energy photons resulting from $\pi^0 \to \gamma\gamma$ decays.

Electromagnetic showers are initiated in the crystals, or the layer of lead radiators in the ES, and use up almost all the energy of electrons and photons. This excites the atoms of the crystals, which relax by emitting an amount of blue light proportional to the deposited energy. This light then reaches photodetectors, namely avalanche photodiodes (APDs) in the EB, and vacuum phototriodes (VPTs) which can sustain a higher particle flux in the EE.

One of the main performance requirements for the ECAL was the precise measurement of diphoton invariant masses, as $H \to \gamma\gamma$ is one of the most sensitive discovery channels of the Higgs boson, and of the energies of energetic electrons and photons in general. Its typical energy resolution σ_E as a function of the electron energy E was initially measured to be [117]:

$$\left(\frac{\sigma_E}{E}\right)^2 = \left(\frac{2.8\%}{\sqrt{E}}\right)^2 \oplus \left(\frac{12\%}{E}\right)^2 \oplus (0.3\%)^2. \tag{2.6}$$

The first term represents stochastic fluctuations in the event-by-event measurements, and is small due to the calorimeter being homogeneous. The second one represents noise contributions (from electronics, digitization and pileup), and the third constant term is due to non-uniformities, miscalibrations and energy leakage. The resolution slightly degraded over time, as radiation damages increase the noise from the leakage current and decrease the transparency of the crystals.

One drawback of this detector is its constant need for calibration. As the response of the numerous channels evolves with radiation, even during a single fill of the LHC ring, it is monitored with a laser system every 40 minutes in order to apply corrections. Light is injected in each ECAL crystal and then read by the standard readout channels. The resulting difference between input and output amplitudes is used to derive correction factors [160, 161].

[3] The radiation length X_0 and Molière radius R_M are constant properties of a material. They represent the distances characterizing the energy loss of a particle interacting electromagnetically, respectively in the longitudinal and transverse directions.

The hadronic calorimeter

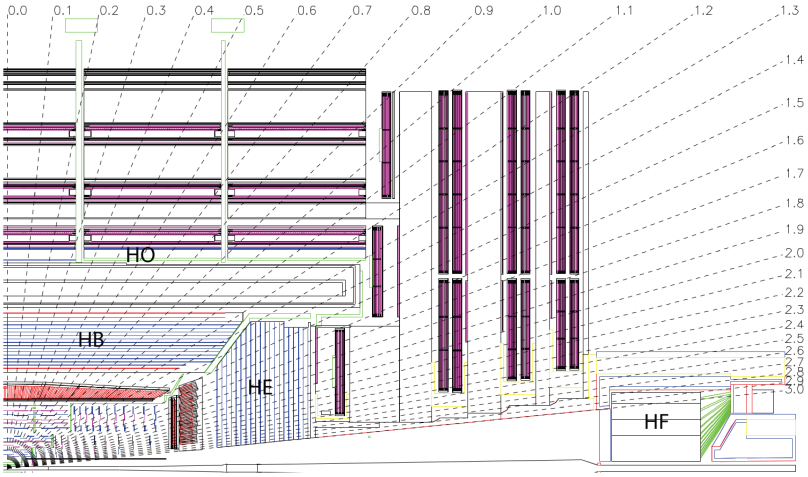

Figure 2.11: Representation of a quarter of the hadronic calorimeter in the longitudinal plane, indicating the locations of the Hadron Barrel (HB), Endcap (HE), Outer (HO) and Forward (HF) subdetectors. Taken from Ref. [117].

The hadronic calorimeter (HCAL) measures the energies of particles interacting mostly via the strong force, after they have passed through the tracker and ECAL. It provides the only measurement for neutral hadrons, and complements the p_T measurement of the tracker for charged hadrons. The HCAL is divided in 4 heterogeneous sampling calorimeters, in which passive layers alternate with active ones. As particles interact in the passive layers, they produce secondary particles which lose energy in cascade. The emitted light reaches the active layer, where it is detected by fibres smaller than 1 mm.

The Hadron Barrel (HB, $|\eta| < 1.4$) and Endcaps (HE, $1.4 < |\eta| < 3$) are located within the volume of the solenoid, and consist of brass absorbers interspersed with plastic scintillators. As the barrels of the electromagnetic and hadronic calorimeters may not provide enough stopping power for highly energetic particles in the central region ($|\eta| < 1.3$), the magnet acts as an absorber for the Outer (HO) scintillators placed immediately after it. The HO extends the depth of the calorimeter system to at least 11.8 interaction lengths[4], except in the barrel-endcap transition region [117]. Finally, the Forward (HF) calorimeter has its front layer located at $|z| = 11.2$ m, and covers the region $2.9 < |\eta| < 5.2$. It is thus exposed to the highest particle fluxes, including neutrons which activate the absorber material, making its design particularly challenging. It uses a radiation-hard Cerenkov technology of quartz fibres as active elements, placed behind plates of steel and borated polyethilene neutron shielding. The layout of the HCAL is represented in Fig. 2.11.

[4]The interaction length λ_I is the mean distance travelled by a hadronic particle before it undergoes an inelastic nuclear interaction.

Its wide pseudorapity coverage makes the HCAL sensitive to most of the particle activity in collisions, and its measurements are thus essential to indicate the production of undetected particles such as neutrinos (as explained in Sec. 2.3.5). During the 2017 winter shutdown, parts of the HCAL were upgraded to improve its segmentation and overall performance. Hybrid photodiodes were replaced with silicon photomultipliers in the HB and HE, single-channel phototubes were replaced with multi-anode phototubes in the HF, and the readout electronics were substantially upgraded. Details on the changes and gains in performance can be found in Ref. [162].

2.2.5 The muon chambers

As the name of CMS suggests, the precise and robust measurement of muons was a core specification already at the early design stage of the experiment. Muons are produced by many interesting physics processes, and their clean distinctive signature makes them well-suited to inform the trigger decision. Furthermore, they undergo smaller energy loss in the tracker material compared to electrons, and their energies can be measured with high accuracy.

The muon system shares most of its mechanical structure with the flux-return yoke. The solenoidal magnet and the yoke serve as hadron absorbers, as their dense material exceeds 16 interaction lengths and prevents hadrons punchthroughs. A dedicated alignment system measures the positions of the muon detectors relatively to each other and to the inner tracker, in order to optimize the muon p_T resolution. Figure 2.12 shows a cross section quadrant of the CMS experiment in the r-ϕ plane, where the positions of the different muon subsystems are indicated.

In the barrel region, the muon system [117, 164] has a radius ranging from 4 m to 7.5 m. The endcap region is located in the range $5.5 < |z| < 11$ m along the beam line. Since the muon system is located far away from the IP and provides a pseudorapidity coverage up to $|\eta| < 2.4$, its detector components must cover a very wide surface area. This led to the choice of gas ionisation chambers, which are reliable and possess satisfying properties for a reduced cost. The muon system is divided into 3 main gaseous detectors, made of a total of 1400 chambers, arranged in layers interspersed with the steel flux-return plates. This "sandwich" design causes a traversing muon to be detected at several points, so that its trajectory can be reconstructed and its momentum determined.

The barrel drift tube (DT) chambers cover the central region with $|\eta| < 1.2$. They consist of 4 cylindric *stations* concentric around the beam line, which contain about 172000 sensitive wires. This central region is characterized by a rather low particle rate and local magnetic field. The tubes have a cross section of 1.3×4.2 cm^2, and a length of 2.4 m. They are filled with a mixture of argon and carbon dioxyde. The smallest unit composing the DT is the *drift cell*. When a muon ionises the gas, it knocks off electrons which drift toward the positively-charged wire at the centre of the cell, generating a signal which is then amplified and collected.

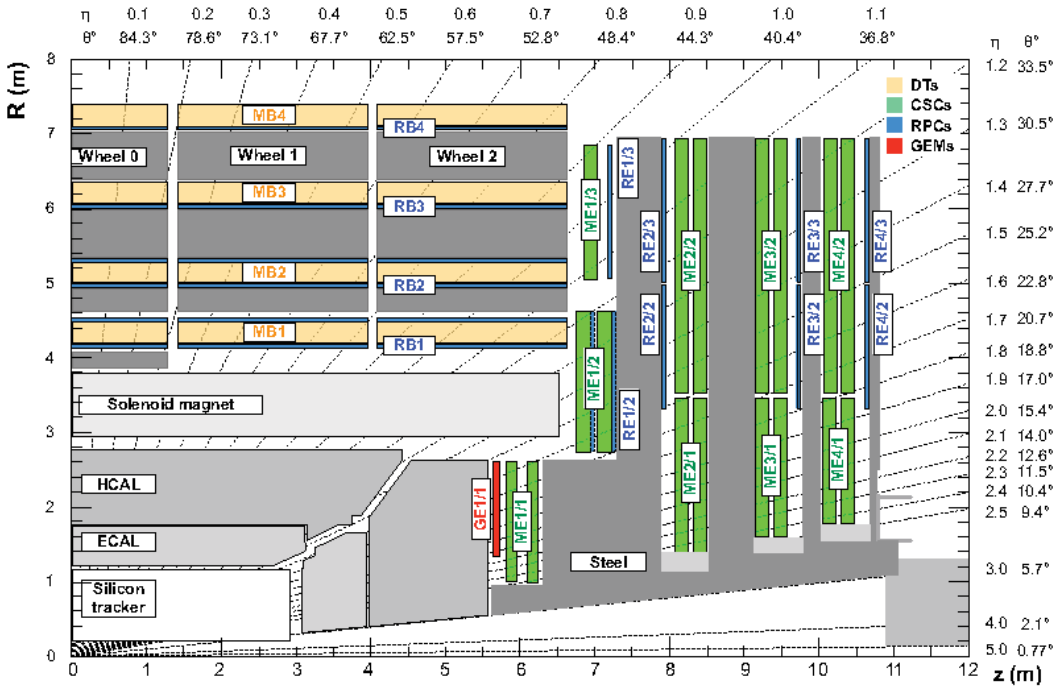

Figure 2.12: Cross section quadrant of the CMS detector in the y-z plane, with the radius R of the barrels increasing upward. The interaction point is located at the origin. The drift tube stations are labelled "MB", the cathode strip chambers "ME", and the resistive plate chambers "RB" (barrel) or "RE" (endcaps). The GEM detector added in 2017 is highlighted in red. The steel flux-return plates are shown as dark areas. Taken from Ref. [163].

Cathode strip chambers (CSCs) are multiwire proportional chambers, in which one of the cathodes is segmented into strips. They represent a sensitive surface area of about 5000 m^2, and a gas volume larger than 50 m^3. They identify muons in the region $0.9 < |\eta| < 2.4$, where the muon and background rates are higher than in the barrel, and the magnetic field becomes large and non-uniform. Among the advantages of CSCs are their fast response time, fine segmentation, reliability and radiation-hardness. The strips provide a precision measurement in the r-ϕ plane in which the muon's track is bended, while the anode provides a pseudorapidity measurement. Four CSC stations are positioned orthogonally to the beam line in each endcap, in alternate layers with the flux-return plates.

Additionally, resistive plate chambers (RPCs) operated in avalanche mode are arranged in the barrel (6 layers) and endcaps (3 layers in each). These parallel-plate detectors are faster than DTs and CSCs, and can detect an ionising event in much less than 25 ns, but have a coarser spatial resolution. They are thus particularly useful to unambiguously identify the exact bunch crossing with whom a track is associated, even in the presence of a high background rate. They provide a fast, independent and granular information to the trigger system, associated with a good estimation of the p_T. The DT, CSC and RPC subsystems can each trigger on the muon p_T independently from the rest of the detector.

During the 2017 winter shutdown, additional detector chambers were included in the region $1.6 < |\eta| < 2.2$ to increase the redundancy of the muon system in the endcaps. They use the gas electron multiplier (GEM) technology [163, 165], which is well-suited due to its excellent rate capability and radiation hardness. This so-called "slice test" comprises 10 single prototype chambers, and preludes the full installation of 144 detectors during the ongoing LS2 [166].

2.2.6 The trigger system and computing grid

Trigger system

The use of a trigger system [117, 167] is rendered necessary by the high collision rate of 40 MHz at the LHC. It is designed to rapidly select events which exhibit a potential physics interest, in order to cope with real-world limitations such as the electronics' time response or the available computing ressources. It consists of a first hardware-based level, followed by a second software-based level.

The first level (L1) trigger takes decisions based on the presence of detector signals consistent with objects such as leptons, photons, jets, etc. It has a fixed latency of 4 μs, during which all the information collected for the event is buffered before they are either discarded or forwarded to the next stage. The L1 uses information from the calorimeters and the muon system. It is controlled via a *trigger menu* containing many different algorithms aimed at spotting the distinctive features of interesting signals. Its composition can be adapted to suit the needs of the physics programme of CMS. Moreover, the trigger thresholds can be adjusted to the instantaneous luminosity delivered by the LHC during data-taking, in order to limit the output rate below the upper limit of ~ 100 kHz imposed by the readout electronics. During the first long shutdown (LS1), the content of the L1 menu was extended from 128 to 256 algorithms, and they were optimized to function at higher pileup and luminosity conditions [168, 169].

Upon positive decision of the L1 trigger, the full information collected in the event is forwarded (but not yet fully reconstructed) to the high-level (HLT) trigger. It consists of a processor farm whose goal is to filter events using offline-quality reconstruction algorithms. This processing is controlled via *HLT paths*, which are algorithms implemented in a series of steps of increasing complexity. Events which successfully pass the trigger decision are then stored on disk locally, before being transferred to an offline computing centre for permanent storage and for distribution.

Computing grid

The LHC experiments require considerable computing ressources for several tasks, such as the processing and reconstruction of the data, the production of Monte Carlo simulations (see Sec. 2.3.6), and their subsequent analysis. Furthermore, a spacious and

reliable storing system is necessary to ensure the safe storage of the data, associated with a high-speed network for worldwide distribution.

The CMS computing system is based on the Worldwide LHC Computing Grid [170] (WLCG), which interconnects computing centres around the world in a tiered distributed architecture. First, the *Tier-0* centres located at CERN and in Budapest are responsible for the storage and distribution of the raw data obtained directly from the CMS Online Data Acquisition and Trigger system (TriDAS). Together, the Tier-0 centres represent a computing power of $\sim$ 230K processor cores and a total storage capacity of about 800 PB ($8 \cdot 10^8$ GB). They transfer both raw and reprocessed data to 13 *Tier-1* sites. These centres with large storage capacity also ensure the storage of both raw and reconstructed datasets, and perform larger-scale data reprocessing. 160 smaller *Tier-2* centres are hosted by universities and scientific institutes around the globe, offering storage space and computing power directly available to users. The WLCG infrastructures provide authorized users around the globe with sufficient computing power to perform demanding tasks related to their physics analyses, independently from their location. More details regarding the WLCG and CMS computing operations can be found in Ref. [171, 172].

2.3 Object and event reconstruction at CMS

2.3.1 The particle flow algorithm

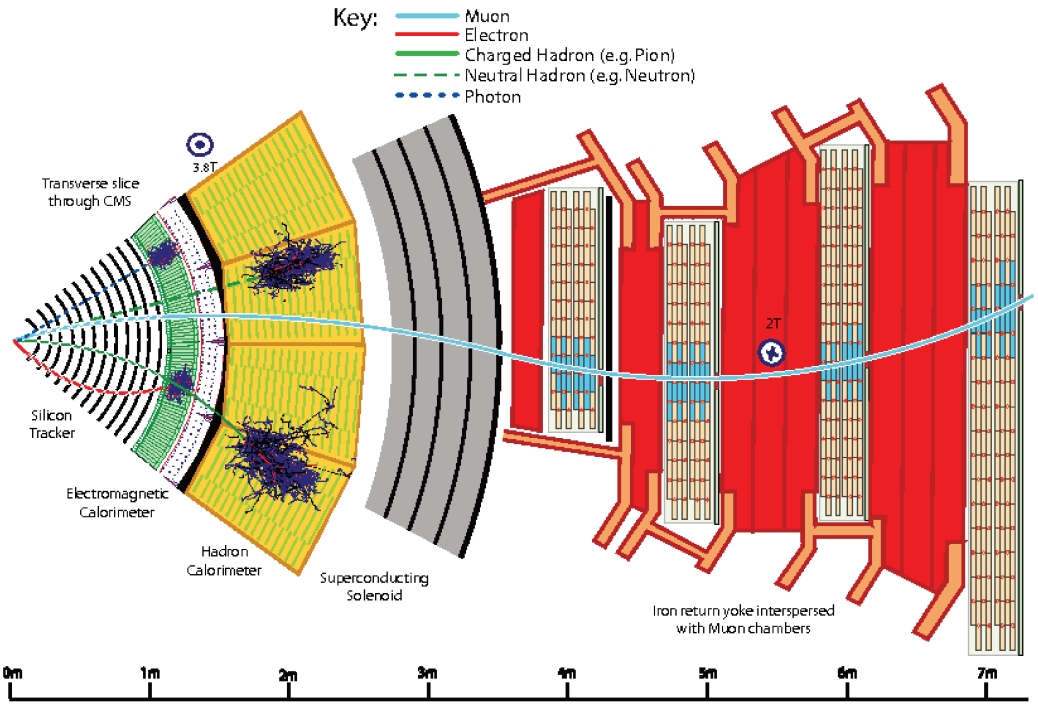

Figure 2.13: Schematic view of a transverse slice of the CMS detector, illustrating the specific signatures left by different kinds of particles. Taken from Ref. [173].

The CMS experiment reconstructs events using the Particle Flow (PF) algorithm [173], designed to optimally combine information from all the subsystems. As can be understood from Fig. 2.13 representing a slice of the CMS detector, different types of particles leave distinctive signatures in the complementary subdetectors.

The PF algorithm starts with low-level information such as tracker hits and calorimeter clusters, and performs iterative steps of increasing complexity to reconstruct final state *physics objects*. These objects provide a complete and unique description of an event, and are the ones used by most physics analyses. The PF algorithm reconstructs objects in the following order : muons, electrons (including photons found to originate from bremsstrahlung), photons (converted to e^+e^- or not), and finally hadrons. More information about their reconstruction is given in the following sections.

In a second step, all these objects may be used to reconstruct composite objects such as hadronic taus and jets. At CMS, the use of a reconstruction algorithm based on the PF concept was rendered possible notably by the highly-segmented tracking system allowing for precise vertexing and p_T measurements, and by the high-granularity calorimeters.

Tracking

The tracks of charged particles are reconstructed from the hits detected in tracker layers, using a software called the Combinatorial Track Finder (CTF) [174] based on Kalman filtering[5] [175, 176]. The seed initiating the track reconstruction can be provided by algorithms using different information. In the first iterations, high-p_T tracks clearly originating from the PV are reconstructed. In the successive iterations, the hits which were already used are not considered anymore. This reduction of the combinatorial complexity allows the progressive loosening of the quality criterions that are applied, and to search for less evident tracks originating from radiating electrons, b-hadrons, etc. The tracking algorithm is able to reconstruct tracks with a p_T as low as 0.1 GeV or produced as far as 60 cm from the PV [150]. The muon tracking is not specific to the PF algorithm, and is presented in Sec. 2.3.2.

Clustering

The other building block used by the PF algorithm is the *cluster*, reconstructed from the calorimetry information. The clustering aims to achieve a high detection efficiency even at low p_T, and to distinguish among closeby energy deposits. It is performed independently in the ECAL and HCAL subsystems. Again, the cluster reconstruction is

[5]The Kalman filter uses a 2-steps recursive procedure. First, it predicts the evolution of a system from a state $\hat{x}_k$ to $\hat{x}_{k+1}$, and then accounts for the measurement performed at the step $k+1$ to update its parameters, using Bayesian inference to form a joint probability distribution. Its low CPU-time and memory-consumption, and its ability to provide informed predictions make this algorithm well-suited for a wide variety of applications, including particle tracking.

initiated from *seeds* corresponding to a local maximum of deposited energy. Neighboring sensor cells with signals larger than twice the noise level are aggregated with the seed into *topological clusters*.

Once reconstructed, the PF elements are connected together to form PF objects, based mostly on topological considerations. The information associated with a reconstructed object, such as the track and the ECAL energy deposit for an electron, is not considered further by the algorithm.

2.3.2 Leptons

Electrons

The material budget in the tracker causes an electron to lose a sizeable fraction of its energy, mostly via the highly non gaussian phenomenon of bremsstrahlung. This motivated the development of the *Gaussian-sum filter* (GSF) algorithm [177], instead of using the same Kalman filter procedure (which relies on single Gaussian PDFs) as for other charged particles. The GSF algorithm models this energy loss with a weighted sum of Gaussians to better capture these effects, resulting in an improved momentum resolution for electrons.

However, this algorithm is quite CPU-intensive and can only be run on seeds which are likely to correspond to initial electron trajectories. This seeding uses both a *tracker-based* and a *ECAL-based* approach. The former uses all the tracks with $p_T > 2$ GeV as potential seeds and is extrapolated outward, while the latter starts from ECAL clusters with $p_T > 4$ GeV and is extended inward. The addition of the tracker-based seeding improves significantly the electron reconstruction and identification efficiency, while reducing the misidentification probability. This is illustrated in Fig. 2.14 (a) for electrons produced in b-hadrons decays (signal) and hadrons misidentified as electrons (background), in different p_T regimes. To account for the fact that bremsstrahlung photons have a high probability to convert into e^+e^- pairs, which get deflected in the azimuthal direction by the magnetic field, clusters are grouped into *superclusters* in a small window in η and an extended window in ϕ.

Electrons can be reconstructed up to $|\eta| < 2.5$ over a large p_T spectrum. The reconstruction and selection efficiency was determined in $Z \to e^+e^-$ data (10<p_T<100 GeV) to range from 88% to 98% in the barrel and from 90% to 96% in the endcaps. The typical momentum resolution varies between 1.7% for well measured electrons in the barrel, and 4.5% for poorly measured electrons in the endcaps [178].

Muons

Muons which are reconstructed from the muon system alone are labelled *standalone muons*. Hits within the DT, CSC and RPC sensors are clustered to form track segments along the muon's trajectory, and a beamspot constraint is applied. A standalone muon track matched to a track in the inner tracker forms a *global muon*, with a p_T resolution

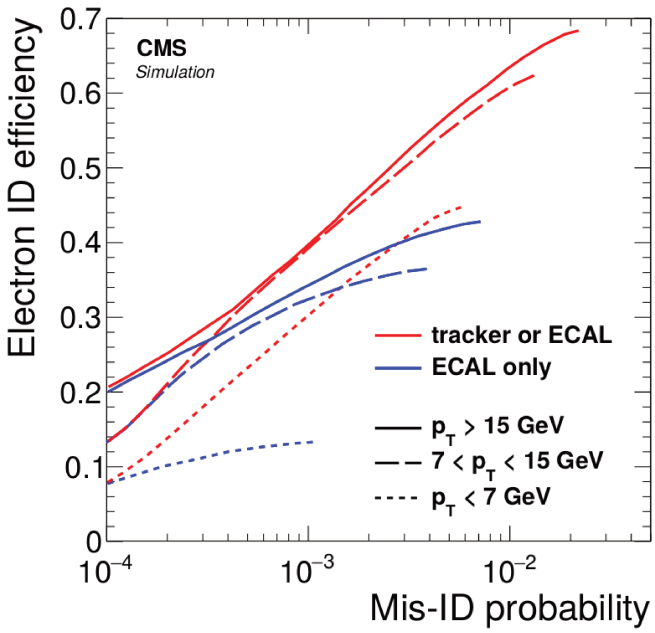

Figure 2.14: Comparison of the efficiency to reconstruct and identify electrons ($p_T > 2$ GeV, $|\eta| < 2.4$) from b-hadrons decays versus the probability to misidentify jets as electrons, using 2 different algorithms on simulated events, motivating the combination of the ECAL and tracker information for the seeding of electrons. Taken from Ref. [173].

improved by the combined fit. *Tracker muons* are seeded by tracks in the inner tracker and extrapolated to match at least one segment in the muon detectors. This reconstruction is useful to identify muons with low transverse momentum ($p_T > 0.5$ GeV and $p > 2.5$ GeV). About 99% of the muons produced within the acceptance of the muon system are reconstructed either as global or tracker muons (most often as both) [173].

Global muons are retained if they are sufficiently isolated. The sum of the p_T of the tracks and the E_T of the calorimeter deposits within a distance $\Delta R < 0.3$ must not exceed 10% of the muon p_T. Nonisolated global muons may for instance originate from b-hadrons, and must meet tighter selection requirements. If they don't, they may still be retained if either their standalone or tracker track is of excellent quality.

The upgrade of the muon system and the improvement of the algorithms resulted in equal or better performance during Run 2 compared to Run 1, despite the higher instantaneous luminosity and pileup. The typical muon reconstruction and identification efficiency is above 96%, with a spatial resolution on reconstructed hits between 50 to 300 μm [164]. The good ability of CMS to identify muons, trigger on them and reconstruct them accurately over an extended p_T range is illustrated by Fig. 2.15. It represents the invariant mass distribution for dimuon events selected in 2015 data by inclusive and specific HLT trigger paths. The expected resonance peaks are clearly visible.

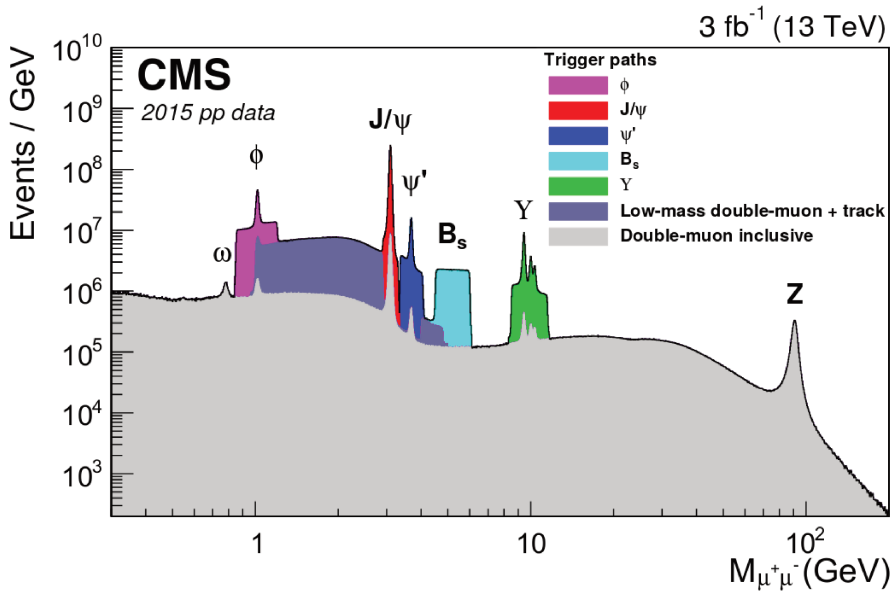

Figure 2.15: Dimuon invariant mass distribution as reconstructed by the CMS HLT in 2015 data. Taken from Ref. [164].

Taus

In about 1/3 of the cases, the τ lepton decays into an electron or muon plus two neutrinos, and the decay lepton can then be reconstructed as explained above. The rest of the time the τ will decay into a combination of neutral and charged hadrons (mostly pions or kaons), accompanied by a tau neutrino. Such hadronically-decaying taus τ_h are reconstructed by the *hadrons-plus-strips* (HPS) algorithm [179]. The main purpose of this algorithm is to distinguish genuine τ_h from the abundant quark and gluon jets. The typical signature of a τ_h comprises a lower particle multiplicity, a different energy deposit topology, and a higher isolation compared to jets from QCD processes.

The HPS algorithm uses the reconstructed PF jets as seeds, and starts by looking for the $\pi^0 \to \gamma\gamma \to \gamma e^+ e^-$ process which is present in a large fraction of τ_h decay chains. The photons and electrons passing given p_T and topological requirements are clustered via an iterative procedure into *strips* of size 0.05×0.20 in the (η, ϕ) plane. For the Run 2, this procedure was optimized as described in Ref. [144]. Strips (π^0) with $p_T > 2.5$ GeV are then combined with the charged constituents ($h^\pm$) of the jet in a combinatorial approach to form several τ_h candidates related to its main decay modes ($h^\pm$, $h^\pm h^\mp h^\pm$, $h^\pm\pi^0$, $h^\pm\pi^0\pi^0$). Mass, isolation, and multivariate-based requirements are further applied to reduce the misidentification of jets and electrons as τ_h.

In the simulation, the correct decay mode is found in about 90% of the cases. The reconstruction and identification efficiency for hadronic taus is of around 50–60% both in data and simulation, with a misidentification probability for QCD jets, electrons, muons and photons as τ_h of around 0.1–1% [144].

2.3.3 Photons

Photon candidates are seeded from ECAL superclusters with $E_T > 10$ GeV which are not related to any GSF track. They must be isolated from other ECAL clusters or any track extrapolated from the tracker, and produce an energy deposit distribution compatible with a photon shower. Neutral mesons decaying to photons constitute a substantial background. Their contamination is reduced using both a *cut-based* approach (requirements on individual variables) and a multivariate-based approach, as described in Ref. [180].

The $\gamma \to e^+e^-$ conversions taking place in the tracker material are reconstructed using dedicated variables (e.g. related to the shape of the electromagnetic shower). The corresponding tracks are either seeded by displaced secondary vertices and extrapolated outward, or by ECAL clusters and extrapolated inward. If these tracks are compatible with the direction of a bremsstrahlung photon, they are associated to the original electron.

The typical energy resolution is of about 1% (1.3–2.5%) in the ECAL barrel and 2.5% (3%) in the endcaps for unconverted or late-converting (converted) photons with $p_T > 25$ GeV [180].

2.3.4 Jets

Jets are reconstructed from the remaining PF elements, after electrons, muons and photons have been removed from the object collections. As hadrons generally deposit energy both in the ECAL and HCAL, links are sought between clusters in each calorimeter. A HCAL cluster reconstructed in the central region ($|\eta| < 2.5$) not linked to any track, or beyond the tracker acceptance where neutral and charged hadrons can not be distinguished, is identified as a photon or neutral hadron depending on whether it is linked to an ECAL cluster or not. The remaining HCAL clusters are linked to one or several tracks, which may themselves be linked to ECAL clusters, and are reconstructed as charged hadrons. Charged hadrons not associated to the primary vertex are removed to reduce the contamination from pileup particles.

The hadronization of quarks and gluons usually generates many collimated hadrons, resulting in an important particle activity in a narrow cone around their barycentres. Therefore, jets are reconstructed by the PF algorithm by clustering closeby particle candidates. There exists a large variety of algorithms to perform this clustering; the CMS collaboration uses the *anti-k_t* algorithm [181, 182] as baseline. It works recursively, and tries to cluster objects within a cone depending on their distance and p_T. It exhibits the important properties of *infrared and collinear safety*, meaning that the emission of *soft* (low-p_T) radiations, or replacing 1 parton by 2 very collimated partons, does not affect its results. The anti-k_t algorithm primarily aims to determine the kinematic properties of the original parton, and discriminate between QCD jets and the instrumental noise.

The rejection of this background was measured to be $> 99.9\%$ in the barrel region, and $> 92\%$ in the forward region where tracking information is not available [183].

The energy of a reconstructed jet differs from that of the original parton, due to theoretical uncertainties on the hadronization process, and experimental uncertainties on the jet reconstruction which bias the measurement. This requires a dedicated *jet energy scale* (JES) calibration of the jet energy. After correcting jets for pileup and calorimeter noise, scale factors are obtained from the simulation for different ranges of p_T and η to account for the response of the detector. Residual corrections are then determined by applying data-driven methods on several samples covering a wide p_T range [184]. Similarly, the discrepancy in the *jet energy resolution* (JER) between data and simulated event is corrected by smearing the jet energy distribution in the simulation. The typical uncertainty on the JES is below 3%. The typical jet energy resolution was measured in data events at central pseudorapidities to be of about 15% at 30 GeV, 10% at 100 GeV and 5% at 1 TeV [184].

B-tagged jets

It was already mentioned that bottom quarks are of great importance since they are produced by a large number of interesting processes, and in particular they are central to top quark physics. Therefore, dedicated *tagging* algorithms are used to idenfify jets originating from b-quarks. They exploit the fact that such jets contain a long-lived B-hadron decaying at a secondary vertex with a rather large particle multiplicity, and with a high probability of leptonic decay ($b \to X + l^{\pm} \sim 20\%$). Thus, these algorithms rely heavily on the good tracking and vertexing abilities of the tracker, and function up to $|\eta| < 2.4$. Jets tagged by such algorithms are hereinafter referred to as *b-tagged jets*, or simply *b-jets*. Different working points of the tagging algorithm, usually defined as "Loose", "Medium" and "Tight", correspond to misidentification probabilities of light jets as b-jets of 10%, 1% and 0.1% respectively. The choice of working point depends on the specificities and needs of each analysis.

B-tagging algorithms have considerably improved over the years of data-taking at the LHC. This is illustrated in Fig. 2.16, comparing the misidentification probability versus b-tagging efficiency for several algorithms. The BDT algorithm *CSV* was superseeded by *CSVv2* for the Run 2, and CSVv2 is outperformed by the newer *DeepCSV* neural network. Since then, the yet more efficient *DeepJet* neural network has been developed, with a more involved architecture and more input variables. Furthermore, there is an ongoing effort to extend the tagging to charm quarks.

2.3.5 Missing Transverse Energy

Missing transverse energy (denoted $\vec{E}_T$) is a crucial quantity at the LHC to infer the production of undetected particles, such as neutrinos or BSM weakly-interacting particles.

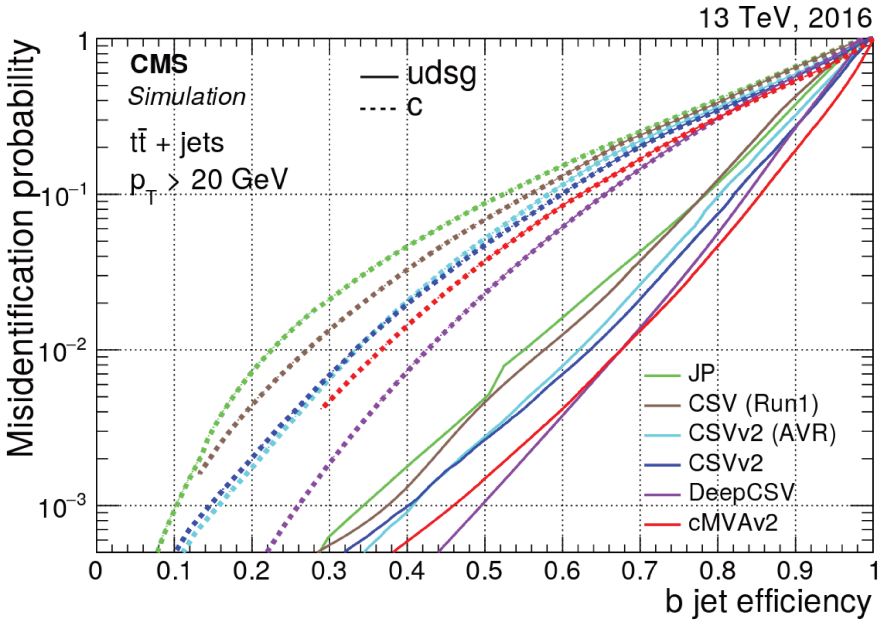

Figure 2.16: Probability to misidentify a c or light-flavour jet as a b-jet, versus b-jet identification efficiency. Different algorithms are compared, using jets with $p_T > 20$ GeV from simulated $t\bar{t}$ events. Taken from Ref. [185].

Colliding partons inside the protons carry unknown fractions of momentum in the longitudinal direction, and therefore the conservation of momentum can only be exploited in the transverse plane since $\vec{p}_T$ is null for all initial state particles. Missing transverse energy is defined as minus the vectorial sum of the transverse momenta of all PF particles:

$$\vec{E}_T = -\sum_i \vec{p}_T(i)\,. \tag{2.7}$$

A precise measurement of the missing energy requires the experiment to cover almost the full solid angle, to ensure that as many visible particles as possible are detected and accounted for. As the biases in the jet reconstruction directly affect this quantity, energy corrections to the jet momenta are propagated to $\vec{E}_T$. The uncertainty attached to $\vec{E}_T$ is evaluated by varying the transverse momentum of each PF particle within its resolution. Distributions of $E_T = \| \vec{E}_T \|$ for $Z \to l^+l^-$ events, in which any missing energy is purely instrumental, show good agreement between data and simulation [186].

Missing transverse energy plays an important role especially in BSM analyses (such as SUSY searches) and in any SM analysis involving W bosons, since they decay into a lepton and neutrino about 30 % of the time. This quantity is used in the two analyses presented in Chapters 4 and 5, since they target the leptonic decay modes of the top quark and the Higgs boson involving W bosons.

2.3.6 Monte Carlo simulations

Simulations are essential to any modern high-energy physics experiment, from conception to final results. The considerable complexity of an experiment such as CMS generally forbids to *directly* compare experimental results to theoretical predictions. Indeed, the former are affected by uncertainties of many different origins, and probe regions of the phase space which are practically impossible to define analytically (related to detector acceptance, imperfect object reconstruction, etc.).

For these reasons, the CMS collaboration generates large simulated samples [187–190] of events in order to reproduce as accurately as possible the behaviours of the processes of interest and their reconstruction by the detector. Simulated events can then be compared directly to the real data. This requires the use of numerical methods to speed up the extremely CPU-intensive computations, among which the most famous and widespread is the *Monte Carlo* (MC) method. This algorithm based on the random sampling of the phase space allows for fast convergence in high-dimensional problems, and is introduced in Ref. [191].

The generation of a simulated event at CMS proceeds in several steps. First, the particles created during the initial collision between partons (*hard process*) are generated with proper kinematics. This may be taken care of by a general-purpose MC generator [24, 192, 193] like PYTHIA [194] or Herwig++ [195] which incorporates all the necessary theoretical ingredients and performs all the steps of the generation.

As these generators provide leading-order predictions in perturbative QCD, dedicated programmes like MADGRAPH5_aMC@NLO [196] or POWHEG [197] are often used to extend the event description to higher-orders of the expansion in α_s. They evaluate the parton-level matrix element up to NLO accuracy, calculate the cross section of the process, and perform the integration over the phase space using advanced MC techniques. The hard event must then be matched with another generator which handles the hadronization of quarks and simulates the effects of higher-order terms in perturbative QCD through *parton showering*, which can be viewed as an evolution in momentum transfer from the hard-scattering down to a low-energy cutoff scale (of order 1 GeV).

Radiations from initial and final state partons (ISR and FSR) develop into showers dominated by soft gluons and photons. The *underlying event*, corresponding to the hadronic activity not originating from the hard scattering, is also simulated. It may be related to multiple parton interactions during a single pp collision, or to interactions between beam remnants. Although the underlying event interactions are generally softer compared to the hard scattering, they may still impact the event in several ways (colour screening, larger particle multiplicity, etc.). A hadronization (or *fragmentation*) model is then used to bound partons into stable hadrons, and the decay of unstable particles is enforced according to known branching ratios. *Minimum bias events*, which do not feature a hard interaction, are generated to mimic the presence of pileup.

This generation procedure results in samples of events containing stable final state particles. The entire event history is saved (*MC truth*) and may be used to study the relations between mother and daughter particles, or the performance of the particle reconstruction. MC generators vary from one another by their choices of simulation models and free parameters such as the cutoff scale for the parton shower. All these parameters must be optimized coherently (*MC tune* [198]) in order to reproduce as accurately as possible the observed data.

The output from the MC generator is then interfaced with the Geant4 toolkit [199], which simulates the passage of particles through the entire detector volume of the CMS experiment. This is done either in the *full simulation* [200] setup with a detailed geometry and detector response, or in the less CPU-intensive *fast simulation* [201] parametric approach ($\sim$ 100 times faster) depending on the purpose of the sample. Once the signal hits have been generated with Geant4, the response of the electronics is simulated during the step of *digitization*, which accounts for the effect of pileup. From there, simulated samples are available in the same raw format as actual data, and the same reconstruction algorithms can be applied. The workflow of the event simulation in the CMS experiment is sketched in Fig. 2.17.

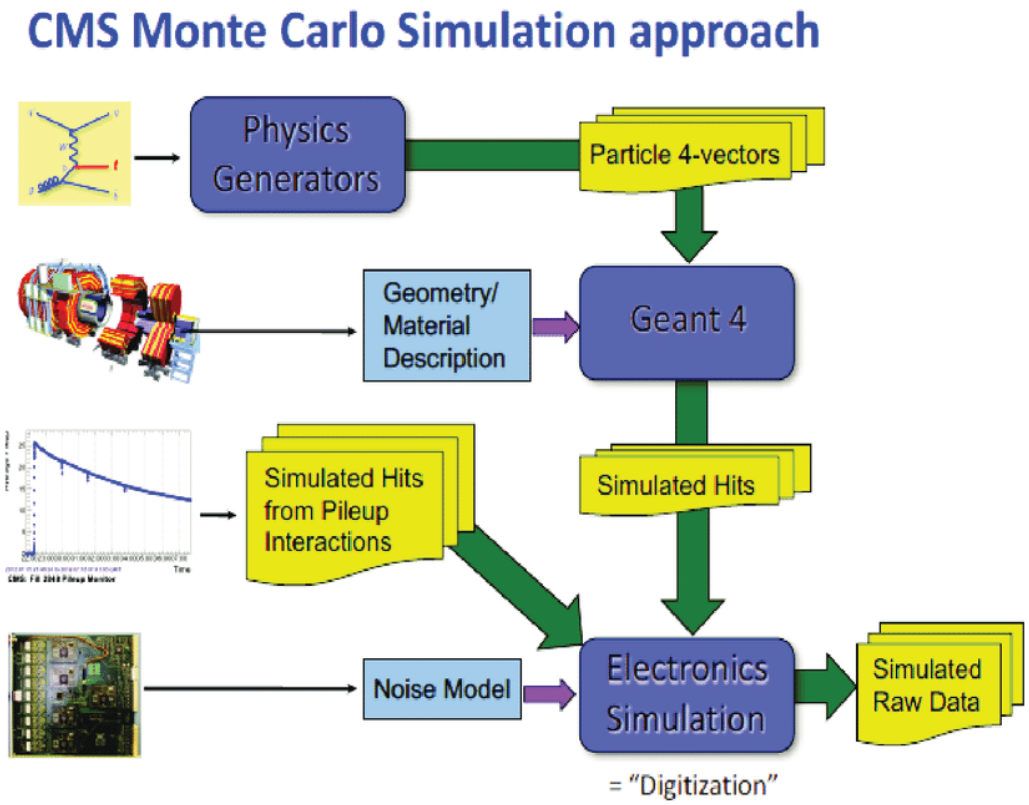

Figure 2.17: Sketch of the simulation workflow in CMS. Each step is introduced in the text. Taken from Ref. [188].

CHAPTER 3

Study of the ageing of the silicon strip tracker under irradiation

Whenever a silicon sensor is irradiated by high-energy particles, its properties evolve due to the accumulation of defects in its crystal lattice. The consequences of these radiation damages are referred to as *ageing*. In this chapter, a study aimed at monitoring the ageing of the CMS strip tracker is presented.

Apart from frequently updating the analysis by including the most recent data, an important fraction of my work was dedicated to the implemention of a more robust and reliable algorithm to extract the results. Thanks to this improved algorithm, the analysis could be extended from the barrel inner layers to the whole strip tracker. Several different results [202–204] were approved by the CMS collaboration to be made public. I was also involved as "on-call shifter" for the strip tracker several weeks per year, during which I was responsible for the coordination of tracker activities and the monitoring of detector parameters.

First, we recall the working principle of semiconductor sensors, and present the main characteristics of the CMS strip tracker sensors in Sec. 3.1. Then, we motivate the study of the full depletion voltage of the sensors to monitor their ageing in Sec. 3.2. The procedure followed to obtain the data is described in Sec. 3.3. Finally, the method and results are presented and discussed in Sec. 3.4-3.8.

3.1 The strip tracker sensors

3.1.1 Elements of semiconductor physics

The electrical conductivity of any solid is determined by its electronic band structure. A semiconductor has a rather small band gap separating its valence and conduction bands. When supplied with sufficient energy, for instance from thermal excitation or the passage of an ionising particle, an electron e can cross the band gap to enter the conduction band, leaving behind a vacancy (or hole h) which represents a positive charge in the valence band. The motion of free electrons and holes induces a current in the semiconductor.

For an *intrinsic* (pure) semiconductor, the concentration n of excited electrons in the conduction band is equal to that of holes p in the valence band. In order to increase the conductivity of a semiconductor, impurities can be purposedly added to its material. This introduces new energy levels in its band structure, making it easier to generate free charge carriers. This process is called *doping* and makes the semiconductor *extrinsic*. This can be done using either *donor* atoms (usually phosphorus) which introduce excess electrons, or *acceptor* atoms (usually boron) which introduce excess holes.

Such "n-type" or "p-type" semiconductors can not be used directly for particle detection, as their concentrations of free charge carriers exceed by several orders of magnitude the number of $e^- - h^+$ pairs generated by an ionising particle, thereby rendering its detection impossible. It is necessary to form a *p-n junction*, by joining together both types of semiconductors, causing holes from the p-side to diffuse towards the n-side, and vice-versa for electrons. This creates a *depleted zone* without free charge carriers in the bulk of the semiconductor, near the interface between the n and p regions. The fixed, charged ions which are left behind generate a "built-in" electric field at the interface, whose effect counters that of diffusion. The two opposing flows eventually reach an equilibrium, with the net flow of charge carriers accross the junction being zero. The depleted zone thus represents a potential barrier preventing the current to flow through the semiconductor, which acts as a diode.

This potential barrier can be increased by *reverse biasing* the p-n junction: it consists in applying an external voltage with the anode connected to the p-side and the cathode to the n-side. As the applied bias voltage V_{bias} increases, so does the electric field which pulls further away the electrons and holes from the junction towards the cathode and anode respectively. This increases the width of the depleted zone and further suppresses the diffusion of free charge carriers across the junction, which results in a reduced background noise for the sensor even at room temperature.

In practice however, a small residual *leakage current* (or reverse current) still exists due to the presence of trapped impurities, introducing new energy levels into the band structure of the semiconductor (near the mid-gap). It is a source of noise which must be

kept as low as possible. It also leads to a larger heat dissipation, which at some point may cause *thermal runaway*[1].

The depleted zone represents the active volume of the detector. When an ionising particle passes through, it generates $e^- - h^+$ pairs which drift towards the electrodes under the action of the electric field. This induces a current which can be determined from the Shockley-Ramo theorem [205, 206]. Charges created outside the depleted zone immediately recombine with the majority charge carriers and do not contribute to the signal.

It is therefore of crucial importance to ensure that the bias voltage V_{bias} applied to a sensor always exceeds its *full depletion voltage* V_{FD}, at which the bulk is entirely depleted, in order to maximise the width of the active volume. This makes V_{FD} one of the most important design parameters of a sensor, and it can be expressed as [207]:

$$V_{FD} = \frac{D^2}{2 \cdot \epsilon_0 \cdot \epsilon_{Si} \cdot \mu_e \cdot \rho}, \tag{3.1}$$

where D is the thickness of the bulk, ϵ_0 and ϵ_{Si} are the vacuum and silicon dielectric constants, μ_e is the electron mobility, and ρ is the substrate resistivity.

Following several major developments in the late 1970's [208, 209], silicon sensors have played an increasingly important role in modern particle physics experiments. Among their numerous advantages are their cost-effectiveness, as silicon semiconductors are massively produced by the microelectronics industry, and their superior physical properties. For instance it only takes 3.6 eV to ionise a silicon atom, about 10 times less than for a gas molecule in a gaseous detector [207], hence the passage of an ionising particle may generate a large number of charges.

Moreover silicon is a high-density material, which means that ionising particles deposit more energy per unit length. The mobility of charge carriers is high even at room temperature, allowing a fast collection time for the signal ($\sim$ 10 ns). Silicon sensors can be very finely segmented and operated in a high-flux environment. This makes them particularly well-suited for particle tracking, and motivated the design of the all-silicon CMS tracker.

3.1.2 Properties of the CMS strip tracker sensors

Figure 3.1 illustrates the design of the silicon semiconductors used in the CMS strip tracker, which consist in single-sided "p-on-n" microstrip sensors. They are formed by a n-type bulk which has an uniform n^+ implantation[2] on its backplane, covered with aluminium to form a contact with the cathode. On the other side, strip-shaped diodes are

[1] Thermal runaway occurs when the leakage current becomes large or the cooling of the module is faulty. The temperature then increases locally, which in turn increases the leakage current, and so on (uncontrolled positive feedback).

[2] The '+' sign indicates a higher concentration of dopants. Typical concentration levels are 10^{12} cm^{-3} for the silicon n-bulk, and $10^{14} - -10^{16}$ cm^{-3} for the implant dopping [207].

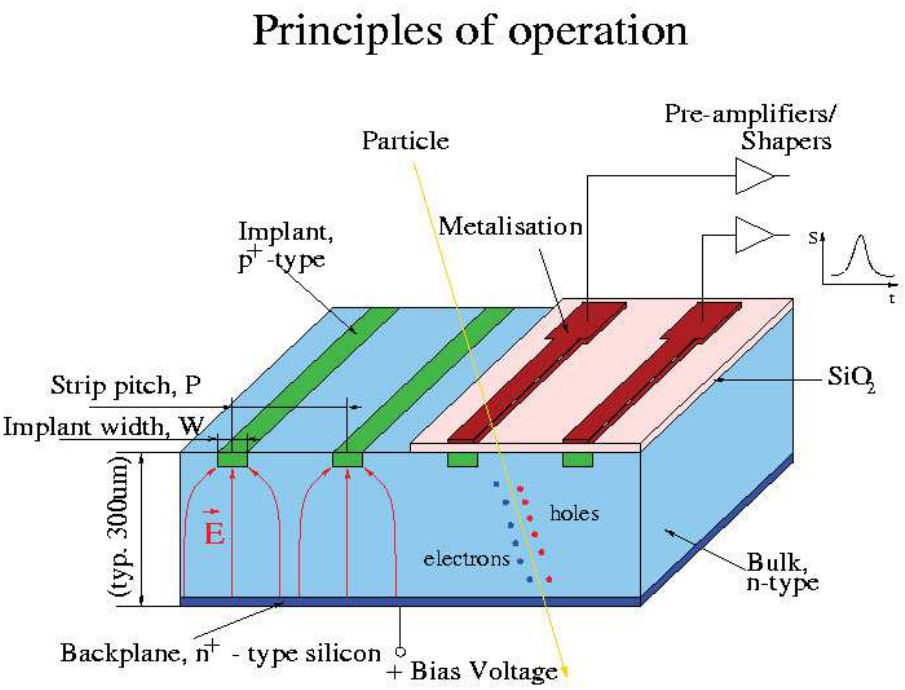

Figure 3.1: Typical layout of a silicon sensor of the CMS strip tracker. The reverse bias is connected to the n^+-type backplane. The passage of a particle generates $e^- - h^+$ pairs along its trajectory which drift towards the electrodes. The induced current is collected on p^+-type strips implanted in the n-type bulk material. They are coupled capacitively to aluminium strips, from which they are insulated by a thin layer of silicon oxide and nitride. The metal strips are connected to the readout electronics. Taken from Ref. [210].

formed by p^+ implants. They are electrically insulated by thin layers of silicon oxide and nitride (SiO_2, Si_3N_4) from aluminium strips placed on top. This forms integrated capacitors, which are used to induce the current via capacitive (AC) coupling in the aluminium strips. This coupling filters out the direct current (DC) component of the signal, which reduces the leakage current. Each metal strip is wire-bonded to the readout electronics, where the signal is shaped and amplified.

For the 320 μm-thick sensors used in the innermost layers of the strip tracker, which have resistivities in the range $1.55 < \rho < 3.25$ kΩ·cm, V_{FD} can be determined from Eq. 3.1 to range approximately within 122–244V. The 500 μm-thick sensors would in principle have higher depletion voltages, but were produced with a higher resistivity ($4 < \rho < 8$ kΩ·cm) so that they lie in the same range.

Therefore, to ensure that sensors are properly *over-depleted*, the operation voltage of the strip tracker modules is set to 300V. As the width of the n^+ and p^+ implants are negligible compared to that of the bulk, the entire volume of the sensors can be considered as active.

Prior to the tracker assembly, initial V_{FD} measurements were performed by measuring the bulk capacitance C of the strips for different bias voltages. A sensor can be seen as a planar capacitor with the silicon acting as a dielectric inside. The bulk capacitance decreases linearly with $\sqrt{V_{bias}}$ below V_{FD}, and is constant above it [207]:

$$C = \begin{cases} A \cdot \sqrt{\frac{\epsilon_0 \cdot \epsilon_{Si}}{2 \cdot \rho_{Si} \cdot \mu \cdot V_{Bias}}} & , V_{bias} \leq V_{FD} \\ A \cdot \frac{\epsilon_0 \cdot \epsilon_{Si}}{D} = const & , V_{bias} > V_{FD} \end{cases} \tag{3.2}$$

where A is the surface of the p-n junction. These C-V curves exhibit a kink signaling the change of regime, making it possible to infer the value of V_{FD}. More details about the setup and measurements are given in Ref. [211].

Figure 3.2 shows the initial V_{FD} values measured in this way, for all the modules of the strip tracker. All the sensors were verified to have initial values of V_{FD} below 300V. For reasons which will be made clear in the following sections, sensors having the highest initial full depletion voltages were placed in the regions expected to be the most irradiated (innermost layers and rings). Although some thin sensors were observed to have an initial value of V_{FD} below the specified requirement of 100V, dedicated studies concluded that they could still be operated in the outer TIB layers subjected to lower levels of irradiation [211].

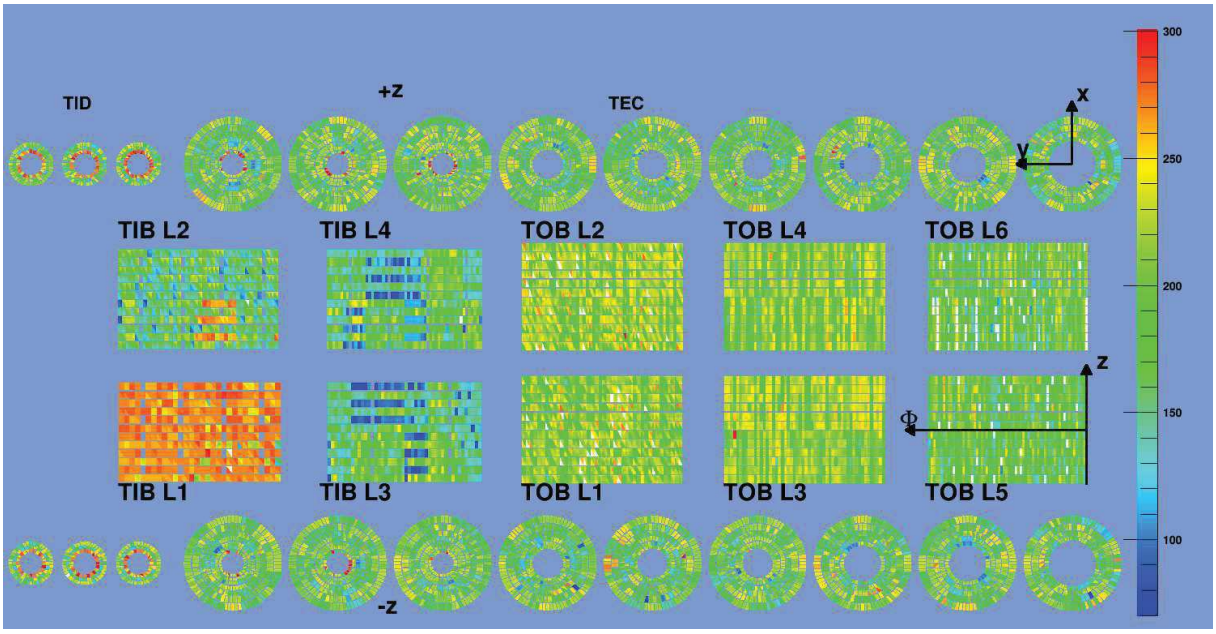

Figure 3.2: Initial values of the full depletion voltage for all the strip tracker modules, as measured prior to the tracker assembly from C-V measurements. This type of plot layout is called a *tracker map*, and is used to represent a quantity for each and every module of the strip tracker. The different layers of the barrel detectors are represented as flat, and all the disks of the endcap detectors are shown separately. For stereo modules, the value corresponding to each module is represented as a triangle instead of a rectangle. For TOB and TEC modules including 2 sensors, the lowest value is shown. This figure was made public [203].

3.2 Radiation damage and annealing

Radiation damage

Tracker sensors are subjected to extreme levels of irradiation, which cause damages both to their surfaces and bulk lattices. Traversing particles do not only ionise the material, but also displace its atoms via the electromagnetic and strong forces, introducing defects in the lattice. These defects can take different forms [212–214], such as:

- Vacancy (V): when an atom is removed from its lattice position;
- Interstitial (I): when an atom is introduced in a normally unoccupied site (interstice);
- *Frenkel pair*: the combined effects of a vacancy and an interstitial, which may result from a *primary knock on atom* (PKA) removed from its site.

There also exist more complex defects, e.g. di- or triple-vacancies, di-interstitials, etc. Figure 3.3 illustrates the impacts of such defects on the lattice. A distinction is made between *intrinsic* defects (e.g. vacancies), and *extrinsic* defects due to impurities (e.g. the substitution of an atom of the material by an impurity atom).

The PKAs will lose their energy via ionisation and the displacement of other atoms. As this energy loss is usually dominated by non-ionising processes towards the end of the recoil path, the initial *point defects* tend to create dense agglomerations of defects called *clusters*.

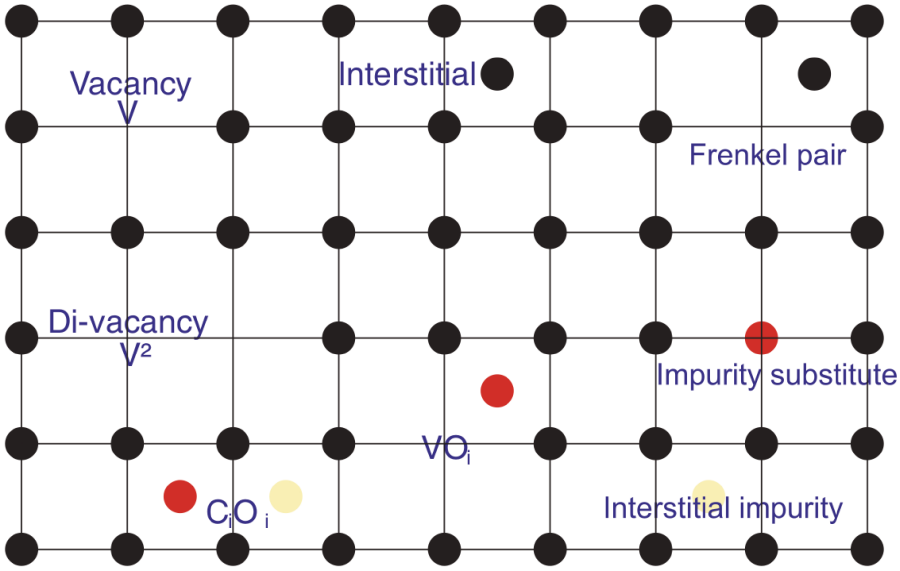

Figure 3.3: Examples of lattice deformations due to radiation damages, which impact the macroscopic properties of the sensor. The main types of defects are introduced in the text. Impurities are labelled with their atomic symbols; the index *i* refers to "interstitial". Taken from Ref. [207].

Both point and cluster defects are responsible for the changes in the semiconductor properties. Such changes were found to scale with the non-ionising energy loss up to some approximation (the so-called NIEL hypothesis [207]). This hypothesis can be used to relate the damage caused by different particles of different energies. It is conventional to refer to a 1 MeV neutron equivalent fluence [n_{eq}/cm^2], labelled Φ_{eq}. In the scenario where the LHC will collect an integrated luminosity of 500 fb^{-1} in about 10 years of operation, the strip tracker sensors are expected to be subjected to fluences of the order of $0.5 \cdot 10^{14}$–$1.8 \cdot 10^{14}$ n_{eq}/cm^2 depending on the tracker region [117].

The microscopic defects make the lattice less ordered and populate new levels in the band structure of the semiconductor. This modifies its macroscopic properties, making it less stable when it is used as a detector. The main changes of macroscopic properties due to bulk damages are:

- (a) **an increase of the leakage current**. The irradiation constantly introduces defects (energy levels) close to the middle of the band gap of the semiconductor, which generate charge carriers and are responsible for an increase of the leakage current. This increase is linear with fluence to a good approximation;
- (b) **a change of the full depletion voltage**. Taking a CMS strip sensor with n-type bulk as example, its effective doping concentration N_{eff} evolves with irradiation. While donors and acceptors may get removed, e.g. by reacting with mobile defects, the dominant effect is the introduction of acceptor-like levels in the bulk material. An example of such a reaction is the recombination process $V + V + O \rightarrow V_2O$, where V is a radiation-induced vacancy, O is an oxygen atom and V_2 is a di-vacancy. As a consequence, the semiconductor will progressively evolve towards becoming intrinsic, before the relative concentration of acceptors finally exceeds that of donors. The bulk then turns into p-type material, and the semiconductor is said to undergo *type inversion*. The full depletion voltage progressively decreases until it is close to zero at type inversion, and then starts increasing again;
- (c) **a decrease of the charge collection efficiency (CCE)**. As defects accumulate in the bulk, more and more deep-level traps are introduced. Such defects have long trapping times because the energy required to remove a charge from the trap is greater than the thermal energy kT. They interfere with the drift of charge carriers and degrade the charge collection efficiency. This effect evolves approximately linearly with fluence. It may reach the point where the trapping time becomes larger than the integration time of the electronics, and part of the charge does not contribute to the signal anymore.

In addition, radiation-induced surface damages in the SiO_2 insulating layer increase the inter-strip capacitance, thus increasing the noise [148]. They also decrease the inter-strip resistance, which increases the cross-talk[3]. Figure 3.4 illustrates the impact of radiation defects on the band structure of a semiconductor and on its properties.

[3]The cross-talk corresponds to the coupling of strips due to the inter-strip capacitance. It causes neighboring strips to share part of their charge.

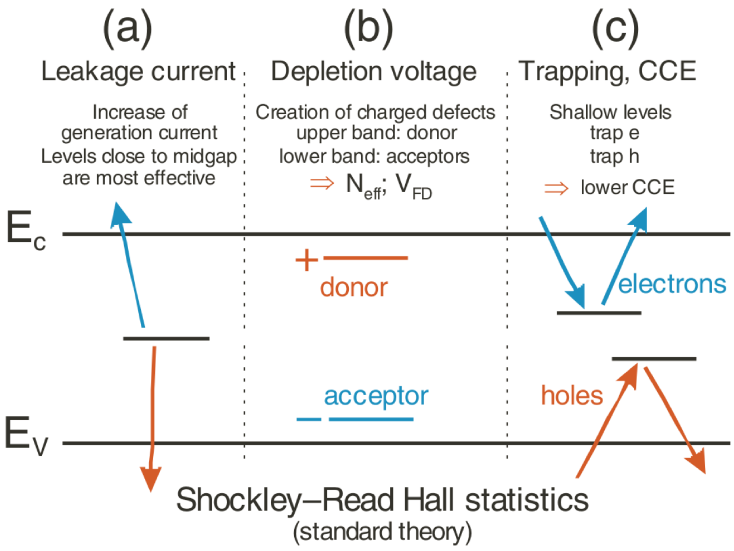

Figure 3.4: Illustration of different types of energy levels introduced by irradiation, and their effects on macroscopic properties of the semiconductor. (a) Energy levels located near the mid-gap contribute the most to the increase of the leakage current. (b) Energy levels located near the valence and conduction bands have the most impact on the modification of the full depletion voltage. (c) Energy levels with long trapping time compared to the read-out time reduce the charge collection efficiency (CCE). Figure originally from Ref. [207], adapted in Ref. [214].

According to Ref. [207], the aforementioned effects on the macroscopic properties of the sensor rank in the following order, in terms of thresholds at which they start limiting the sensor operation:

- from $\sim 10^{14}$ n_{eq}/cm^2, the main issue is the increase of the leakage current;
- from $\sim 10^{15}$ n_{eq}/cm^2, the large increase of the full depletion voltage becomes problematic;
- from $\sim 10^{16}$ n_{eq}/cm^2, the degradation of the CCE becomes problematic.

Annealing

Even after a semiconductor has been irradiated, defects continue to take part in different processes, making some properties of the sensor unstable over time. For example, interstitials and vacancies are very mobile at temperatures above 150 K, and will therefore mostly recombine, migrate, reconfigure, etc., at different speeds depending on the process. Part of this phenomenon is beneficial to the sensor and is called *annealing* (self-repair). On the other hand, the counter-acting *reverse annealing* may further degrade the sensor's properties when it is kept at room temperature [212]. Beneficial annealing is mostly a short-time effect, while reverse annealing operates on longer timescales and may continue after several months. The amount of reverse annealing is proportional to the fluence.

In order to mitigate the reverse annealing, it is necessary to permanently keep the sensor at a controlled, low temperature. The CMS tracker was initially operated at a temperature of +4°C during Run 1, instead of the design value of -10°C. This was due to abnormally high levels of humidity, which may damage the delicate electronics [214]. During the LS1 period, the insulation of the tracker volume was improved, and the capacity of the plant supplying dry gas to the detector was increased. The nominal temperature was set to -15°C from 2015 to 2017, to -20°C in 2018, and it will be set to -25°C at the beginning of the upcoming Run 3. However, the temperature distribution is not uniform across the tracker regions, due to faulty cooling loops, degraded cooling contacts, and the density variations of active material.

In addition to the temperature, it is believed that the deliberate addition of specific impurities to a silicon sensor (*defect engineering*) could help controlling the evolution of its macroscopic parameters [212].

Several searches have investigated these phenomena and their causes (see e.g. Ref. [215, 216]), but no definitive explanation was found yet. Studies focusing on silicon sensors similar to the ones used in the CMS tracker are still being conducted [217].

Although the knowledge regarding complex phenomenons like radiation damage and annealing is yet incomplete, these effects could still be parameterised and simulated to some extent. For instance, the *Hamburg model* [213] aims to describe the evolution of the full depletion voltage with irradiation, and accounts for annealing. Technical details regarding this model are out of the scope of this work, but simulations based on this model were compared with the data obtained in this analysis (see Sec. 3.7).

Motivations for the study

The CMS strip tracker is an all-silicon detector of unprecedented size, which must operate in extremely harsh conditions of irradiation. The radiations alter the sensors by degrading their performance and making their properties unstable over long periods of time. This study aims at monitoring the evolution of the full depletion voltage V_{FD} of the sensors under irradiation.

It is of the utmost importance to control and understand this evolution. Indeed, in case the sensors would undergo type inversion prior to what is expected, the full depletion voltage would increase faster than anticipated, potentially until it exceeds the capacity of the power supplies. This would result in the operation of under-depleted sensors with reduced detection efficiency.

Even if V_{FD} would not exceed the operational voltage of the tracker modules, the increase of this parameter could still impact the performance of the detector. Indeed, irradiation studies carried out prior to the tracker assembly showed that the signal-to-noise ratio reaches an asymptotic, maximal value for values of V_{bias} sensibly larger than V_{FD} [148]. For this reason, it is preferable to operate modules at a voltage well above V_{FD}. This further motivates the careful monitoring of the full depletion voltage, since the precise knowledge of V_{FD} may help us anticipating better the evolution of the crucial signal-to-noise ratio parameter.

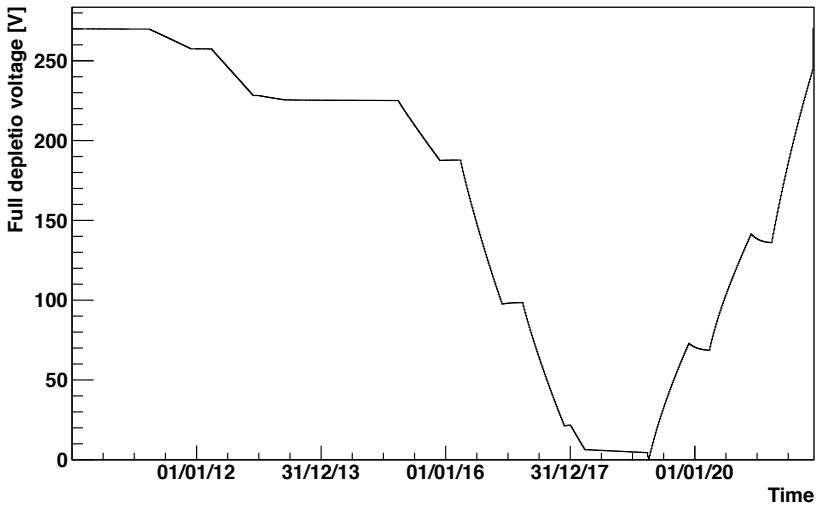

Figure 3.5: Simulated evolution of the full depletion voltage V_{FD} for one example module in the TIB innermost layer (L1). After the module reaches type inversion, V_{FD} will increase continuously until it exceeds the bias voltage applied to the module (set at 300V). At this point, the sensor will become under-depleted. Taken from Ref. [214].

Tests carried out prior to the tracker assembly concluded that the strip sensors could remain fully operational for at least 10 years of LHC running [212]. Figure 3.5 shows the simulated evolution of V_{FD} for one module in the TIB innermost layer (L1). The simulation is based on the Hamburg model. It uses a luminosity and temperature scenario as input, and accounts for the effects of annealing (both beneficial and reverse). It can be seen that after a bit more than 10 years of LHC operation, the V_{FD} values of the most irradiated strip sensors are expected to reach the threshold of 300V, still well within the 600V capacity of the power supplies [218].

Such simulations are known to rely on approximations and hypotheses, and have a limited predictive power regarding the radiation damages of sensors. Therefore this study is strongly motivated both by the need to anticipate the evolution of the tracking performance, and to improve our understanding of the complex phenomena at play. This study, alongside other works which focus on the evolution of other parameters such as the leakage current, may provide insights to improve the reliability of the predictions, and thus support the design of future detectors.

3.3 Signal bias scans

Bias scans

It is not possible to perform *in-situ* measurements of the strip capacitance of the tracker sensors, as was done prior to the modules assembly. Fortunately, there exist other quantities which can be measured and are sensitive to the full depletion voltage, as explained

in Sec. 3.4. Similarly to C-V curves, they exhibit different behaviours in cases where the sensor is under- or over-depleted, and so can be used to estimate V_{FD}.

This study uses data collected in dedicated *bias scans* during pp collision runs. In what is called *full scans*, the bias voltage is varied at once for all the modules of the strip tracker. These scans allow the estimation of V_{FD} over the entire detector. However, for the scanning points corresponding to low values of V_{bias}, most of the sensors are under-depleted. This severely degrades the hit efficiency and the quality of reconstructed tracks, and hence such scans are only performed once to twice a year during low-luminosity periods, to limit the loss of data for other analyses.

In order to collect scans more frequently without degrading the quality of the data, *small scans* are taken on a monthly basis, in which the bias voltage is varied only for a few power supplies (PS) providing power to a small subset of modules. Seven PS are impacted in total, among which 1 is connected to TIB+, 1 to TIB-, 2 to TOB+ and 2 to TEC-. Their positions were chosen so as to avoid missing more than 1 hit along a particle's trajectory, which would prevent the track from being reconstructed. In the TIB, the 2 PS were selected in the L1 layer which is the most exposed to irradiation. One is located in a region with higher temperature (due to degraded cooling contacts), hence larger annealing effects can be expected in this region.

Voltage steps

From mid-2011 up to the end of 2016, the bias voltage was scanned from 30V to 350V, by steps of 15V up to 240V, and steps of 25V above. However, as the full depletion voltage of the sensors decreased with irradiation, it became necessary to adapt the scheme so that more measurements would be taken at low bias voltage, in the range of interest. This is especially important because the hit efficiency is degraded at low bias voltage, and less statistics can be collected in the same amount of time. Focusing on this range thus improves the sensitivity of the analysis at low V_{FD}.

The current scheme ranges from 10V to 300V, with steps of 5V up to 40V and steps of 10V up to 90V. The typical duration of a scan is of about 2h (about 3 minutes per step). It is run from the CMS Control Room at P5 by the on-call tracker shifter.

3.3.1 Data quality

The bias scans used to obtain the results were collected between mid-2011 and the end of 2018. Among them are 9 full scans and 17 small scans. A few scans were not included in the final results because they were not properly completed. The statistics collected for a given module depends on many parameters: for instance the instantaneous luminosity, the centre-of-mass energy, the pileup, the kind of trigger used to fill the dataset (most often minimum bias triggers), etc. When needed and possible, several datasets were combined to increase the statistics.

In this analysis, a charge cluster[4] in a sensor is considered only if it allowed the reconstruction of a track (*on-track cluster*). The corresponding track must contain at least 5 hits, and have a normalized χ^2 score below 5.

3.4 Cluster charge and cluster width observables

Two observables are considered for this analysis: the cluster charge and the cluster width. Both are sensitive to the width of the depleted zone, and thus studying the behaviours of these quantities during bias scans allows the estimation of V_{FD}.

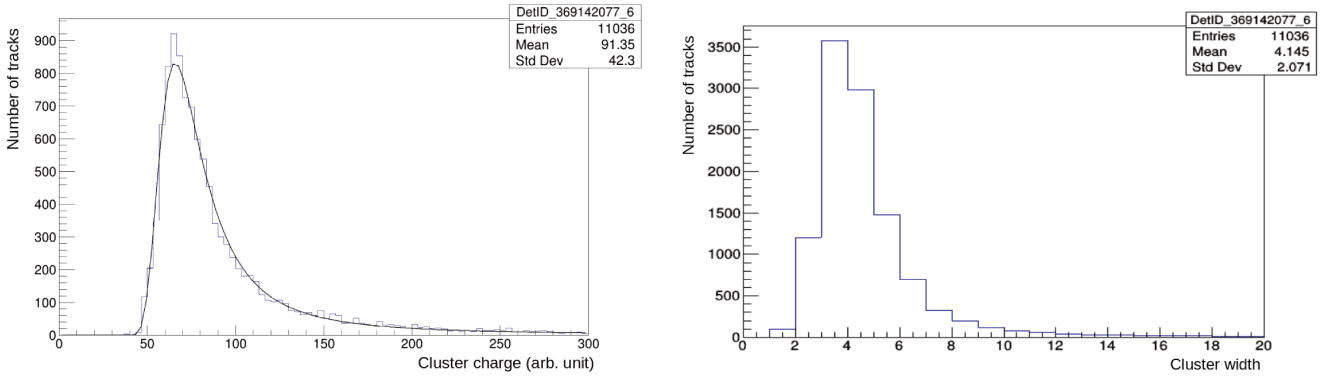

(a) (b)

Figure 3.6: Examples of distributions of (a) the cluster charge and (b) the cluster width observables, for a given sensor and voltage step. The values used for the analysis are extracted (a) from the MPV of a fit with a Landau function and (b) from the mean.

3.4.1 Cluster charge

The cluster charge, or signal amplitude, was the first observable to be used for this study. The amplitude of a cluster is corrected for the path length of the particle through the sensor (normalized to an orthogonal path, i.e. the sensor's width).

For a given voltage step, an histogram is constructed for each sensor included in the scan, from the numbers of ADC counts associated with all clusters reconstructed in that sensor. Each distribution is then fitted with a Landau function to estimate the most probable value (MPV) of the distribution, as illustrated in Fig. 3.6 (a). By repeating this procedure for each voltage step included in the bias scan, we obtain a curve representing the evolution of the cluster charge versus the bias voltage for all sensors.

Examples of such curves are shown in Fig. 3.7 (a), corresponding to the same sensor but several consecutive bias scans. The plateaus of the curves are normalized to the same value, to facilitate the visual comparison. It can be clearly seen that these curves exhibit two different regimes: in the first regime at low values of V_{bias}, the sensor is

[4] A cluster corresponds to the collection of strips which are associated with the same single energy deposit.

under-depleted and hence the signal increases with V_{bias}. Above V_{FD}, the sensor is over-depleted and the curve is expected to saturate.

As expected, the most recent curves tend to shift towards lower voltage values, indicating that the V_{FD} of the sensor has decreased during the considered period of time. The shape of the curve depends on the thickness of the sensor and on the value of V_{FD}. For thicker sensors the turn-on of the curve is less sharp, making it more difficult to clearly define the position of the saturation point. This motivates the use of alternative observables.

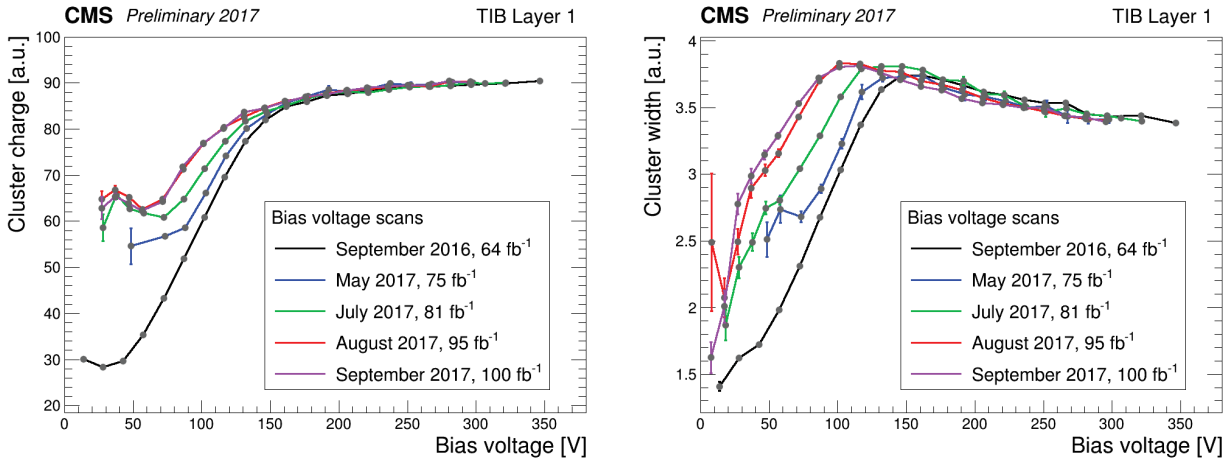

(a) (b)

Figure 3.7: Comparison of curves for the same sensor but different consecutive bias scans of (a) the cluster charge and (b) the cluster width, as a function of the bias voltage. The plateaus of the curves are superimposed. The integrated luminosity values comprise the Run 1 and 2 periods. The most recent curves tend to shift toward lower values as expected for this period, indicating that the V_{FD} of the sensor is decreasing over time. In the left plot, the constant regime at low voltage for the curves from 2017 scans is due to the introduction of a minimum threshold for the signal (*cluster charge cut*). These figures were made public [202].

3.4.2 Cluster width

The cluster width corresponds to the number of activated strips associated with the same cluster. A strip is activated if the collected signal exceeds a minimal threshold. The cluster width depends on many parameters such as the track's incidence angle, the sensor's width, the magnitude of the magnetic field, the cross-talk, etc. As the width of the depleted zone increases, so does the range travelled by charge carriers in the sensor's plane, which results in wider clusters until V_{FD} is reached. Therefore, similarly to the signal amplitude, the cluster width increases with bias voltage, until V_{FD} is reached and the observable saturates. For each sensor and voltage point, the mean width of the selected clusters is extracted, as shown in Fig. 3.6 (b).

Figure 3.7 (b) shows curves of the cluster width versus V_{bias}, corresponding to the same sensor but several consecutive bias scans. As the full depletion voltage of the sensor decreases, the curves may exhibit decreasing slopes instead of flat plateaus. This is

mainly due to surface damage, which increases the inter-strip capacitance and hence the cross-talk (see Sec. 3.2). Irradiation studies performed on strip sensors showed that this damage-induced coupling between neighboring strips can be reduced by substantially over-depleting the devices [148]. This explains why, for irradiated sensors, increasing the bias voltage leads to a decrease in the cluster width.

In comparison with Fig. 3.7 (a), it can also be seen that the cluster width observable exhibits a sharper change of regime compared to the cluster charge, which is beneficial to this analysis as will be explained in Sec. 3.6.

3.5 Voltage drop corrections

Due to the presence of resistors in the front-end electronics and in the powering system [218], the voltage which is effectively applied to the sensors is lower than the nominal value set at the PS level. This may bias this analysis by artificially shifting the curves towards higher voltage values. To compensate for this effect, voltage drop corrections estimated as a function of the bias voltage are applied.

The voltage drop can be measured in two different ways: at the level of the PS, and directly at the level of the module via DCU [219] (*detector control unit*) readings. A PS channel is common to several modules, and the main cable splits to power individually each module. Taking into account the resistivities and resistances at each end of the cable, the voltage drop can then be estimated as:

$$V_{drop} = I_{PS} \cdot 1k\,\Omega + I_{DCU} \cdot 13.8\,k\Omega\,, \tag{3.3}$$

where I_{PS} and I_{DCU} are the currents at the PS and DCU levels respectively. The first term corresponds to the voltage drop which is common to all the modules connected to the same main cable. The main contribution to the voltage drop arises from the second term, which requires a separate measurement for each individual module.

Ideally, I_{DCU} is obtained individually for each module from DCU readings. However, the default frequency of these measurements is approximately one every 5 minutes, which is often longer than the duration of the voltage step itself. Alternatively, the measurement of I_{PS} can be used to approximate I_{DCU}. The DCU current measurements are used to compute V_{drop} in case at least 8 such measurements were collected during the bias scan. If fewer measurements were taken, they are only used to estimate the fraction of the total current I_{DCU}/I_{PS} powering each individual module. Finally, if less than 2 DCU measurements were collected, the ratio I_{DCU}/I_{PS} is taken to be $\frac{1}{N_{mod}}$, with N_{mod} the number of modules connected to the PS (i.e. I_{PS} is assumed to be shared equally among the modules).

For each scan, the voltage drop for each module can be parameterised with the function:

$$V_{drop} = a + b \cdot V_{bias}^{1/2} + c \cdot V_{bias}^{3/2} \ . \tag{3.4}$$

This parameterisation was empirically found to be robust and to provide a satisfying description of the shape of V_{drop} versus the bias voltage. It is then used to correct the values of the bias voltage in all the plots, as illustrated in Fig. 3.8.

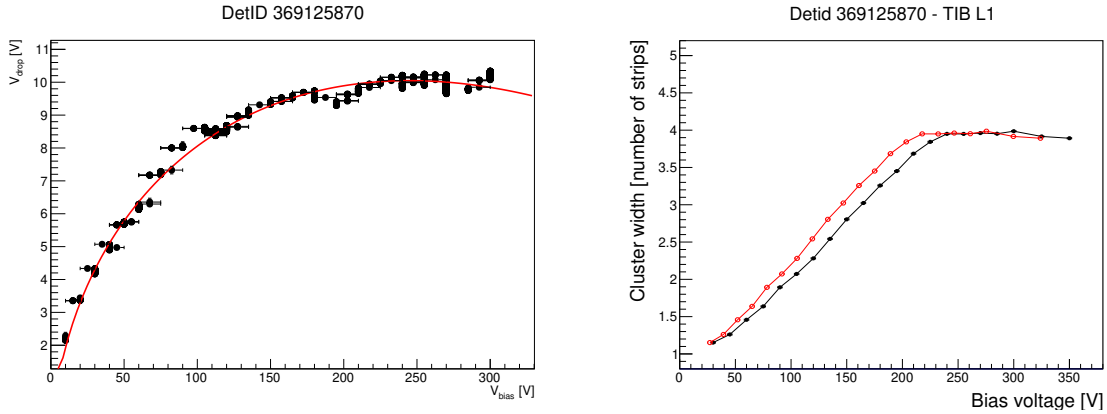

(a) (b)

Figure 3.8: (a) Curve of the voltage drop as a function of the bias voltage. The data points (black dots) are fitted with the function given in Eq. 3.4. The voltage drop is parameterised in this way for each sensor and bias scan, and corrected for in the analysis. Horizontal error bars indicate that the measurement was taken in-between 2 voltage steps. (b) Comparison of curves of the cluster width for a TIB L1 sensor, before (black curve) and after (red curve) correcting the bias voltage for the voltage drop.

3.6 Estimation of the full depletion voltage V_{FD}

This section introduces the different methods which were tested to estimate the value of V_{FD} from the cluster charge and cluster width curves. The emphasis is put on the method which was improved during this thesis, with which the results were obtained.

3.6.1 Simulation method

A first method used to extract the value of V_{FD} relies on the simulation of the signal charge as a function of the bias voltage. A simplified model is used which describes the charge deposition, the generation and drift of electron-hole pairs, and the shaping of the signal by the read-out electronics. The function has only 2 free parameters, namely the full depletion voltage of the sensor and the amplitude of the curve's plateau. Although it was found to properly describe the signal curves for thin sensors during the earliest bias scans taken in 2011 (a good example is shown in Fig. 3.9 (a)), it is not the case for thick sensors nor for later scans. This method was not used to produce results.

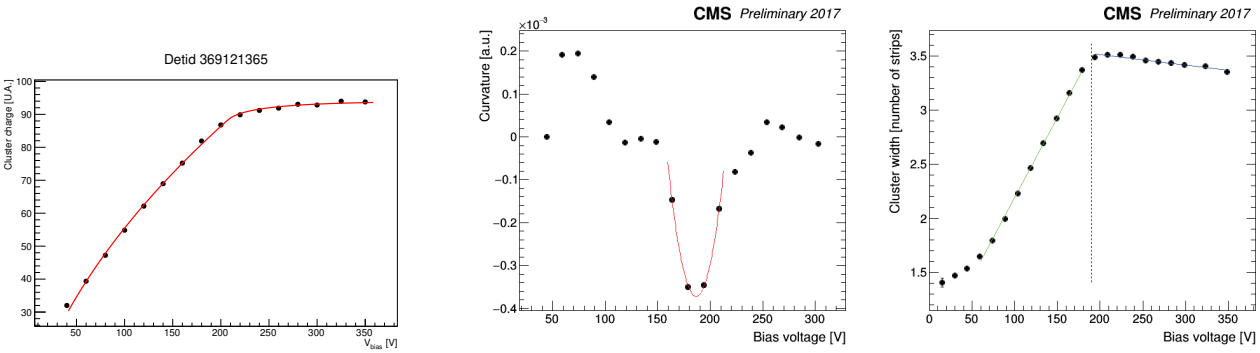

(a) (b) (c)

Figure 3.9: Examples illustrating the methods used to estimate the full depletion voltage, in curves of the cluster width versus bias voltage. (a) The curve is fitted using a set of curves obtained with a simplified model. (b) The curvature can be computed at each point of the curve, and a minimum is extracted. (c) The linear fits of the two regimes and their intercept are superimposed on the curve. Figures (b) and (c) were made public [202].

3.6.2 Leakage current as a possible estimator of V_{FD}

The magnitude of the leakage current depends on the integrated fluence received by the sensor and is impacted by the temperature. It also depends on the width of the depleted zone, and hence varies with the bias voltage. Like for the cluster charge and width, curves representing the leakage current versus the bias voltage exhibit 2 distinct regimes in the cases where the sensor is under-depleted (steep increase) or over-depleted (saturation). In the regime $V_{bias} > V_{FD}$, the leakage current increases linearly with the bias voltage, which is indicative of a resistive behaviour[5].

An example of I_{leak} curve is shown in Fig. 3.10. It can be fitted with analytic functions in order to extract V_{FD}. The first regime can be fitted with a sigmoid or arctangent function, and the saturated regime with a straight line. Depending on the choice of the first function, the results can vary significantly. Generally it is found that the sigmoid under-estimates V_{FD} while the arctangent over-estimates it, as illustrated in Fig. 3.10.

The main drawback of this approach is that we often only have access to leakage current measurements performed at the level of the power supply channel, as mentioned previously. A single PS channel being common to 3 to 6 modules (i.e. 3 to 12 sensors), the curves which are obtained are averaged over several sensors which may have different individual values of V_{FD}. Therefore this variable was only used for cross-checks.

3.6.3 Curvature method

To cope with the large variety of curves to analyse, more ad hoc methods were developped to estimate V_{FD} regardless of the evolution of the curves' shapes over time. The

[5]The linear behaviour continues until the *avalanche breakdown*, at which point the leakage current increases dramatically. This occurs when the electric field is strong enough that charge carriers have enough speed to knock out bound electrons, thus generating more charge and causing an avalanche. All tracker sensors have a breakdown voltage exceeding 500V [117].

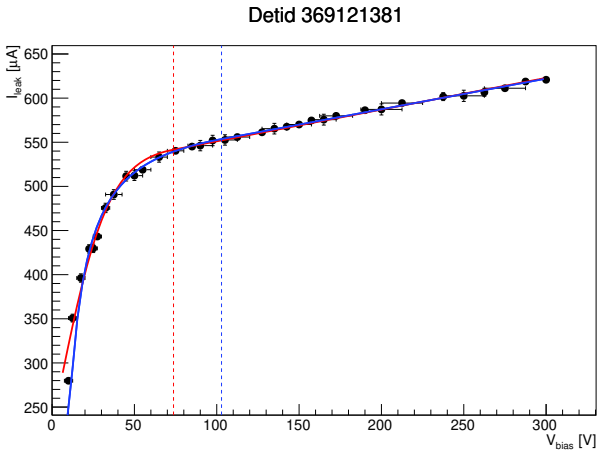

Figure 3.10: Evolution of the leakage current with bias voltage, as measured at the level of the power supply channel (black dots) for 1 TIB module. Analytic functions can be used to fit the data. The red curve corresponds to a sigmoid function, and the blue curve to an arctangent function. The vertical dashed lines indicate the estimated positions of the transition point between the two regimes, taken as V_{FD}.

"curvature method" aims at locating the transition between the two regimes by finding the point in the graph where the negative curvature[6] is minimal, as illustrated in Fig. 3.9 (b). As this method is rather sensitive to fluctuations, the curves are first smoothed with robust filters which preserve their overall shapes. This method was found to provide satisfying results but lacks robustness, as there may be several local minima in the curves. It was mostly used for comparison with the default method.

3.6.4 Crossing lines method

A more straightforward way of estimating the value of the saturation point was developped, which uses the intercept of linear fits of the two expected regimes in the curves. I re-implemented and significantly improved this algorithm, with the aim to make it as robust and adaptive as possible.

The algorithm was optimized on cluster width curves. An example illustrating the procedure is shown in Fig. 3.9 (c). The first line fits the steeply increasing regime, while the second one fits the saturated regime. Both regimes can be assumed as linear over limited ranges only. The free parameters to determine are the bounds of the 2 linear fits, which are optimized based on their χ^2 scores.

Although the problem at hand is rather basic, the difficulty to properly adress it comes from the great variety of shapes which are encountered, and the fact that the final result can be highly sensitive to the bounds of the fits. This required the implementation of many protections and the tuning of the algorithm, so that it could deal with non-ideal shapes. Figure 3.11 shows a few examples of cluster width curves with shapes which are

[6] The signed curvature for the graph of a function $y = f(x)$ is: $k = \frac{y''}{(1+y'^2)^{3/2}}$.

quite different from one another. The linear fits and their intercept are superimposed, and illustrate the capacity of the algorithm to provide meaningful estimates for a wide variety of configurations.

In a first step, the first few points of the graph are used to perform the fit of the increasing regime. The higher bound of the fit is then extended as long as its χ^2 score stays below a given threshold. When it does exceed it, the lower bound of the fit is moved towards higher bias voltage values (by 1 voltage step). If it makes the χ^2 score decrease below the threshold, we proceed with extending the higher bound of the fit, and stop there otherwise. The same procedure is applied to obtain the range of the other fit (but reversed).

From this starting point the fits are further refined, this time considering both of them at the same time. Their lower and upper bounds are moved, provided that some conditions are fulfilled. For example it is forbidden for a given data point to be used by both fits, or conversely for too many points in-between the two fits to be ignored.

Several requirements, for instance on the slopes of the fits, aim at ensuring that the two regimes of interest were correctly identified. Among the relevant configurations satisfying all the conditions, the one with the lowest combined χ^2 score is selected to extract the bias voltage value at which the two fits intersect.

In more recent bias scans, for which the full depletion voltage is getting close to zero in parts of the tracker and there are not enough points that can be used in the first regime of the curves, the algorithm estimates the position of the turning point based on the y-value of the first data points alone. An example is shown in the bottom right of Fig. 3.11.

Unless explicitly stated, the results presented in this chapter were obtained using the cluster width as observable and the crossing lines method.

3.7 Results

This section presents the main results which were obtained. Several results have been approved and shown at public conferences [202–204].

3.7.1 Evolution of V_{FD} for individual sensors

The evolution of V_{FD} as a function of the integrated luminosity and simulated fluence is shown in Fig. 3.12, for different sensors located in the barrels and the endcaps. The FLUKA Monte Carlo code [220] is used to simulate the fluence in the whole tracker volume, depending on the positions of the sensors and the centre-of-mass energy of the collisions. The simulated fluence can then be computed independently for each sensor and each bias scan, using the integrated luminosity as a simple multiplicative factor.

It can be seen that the measurements (black dots) are much more fluctuating for TEC and especially TOB sensors (bottom), than for TIB sensors (top) which exhibit a more stable trend. This is mostly due to the fact that the TIB receives a higher flux of particles

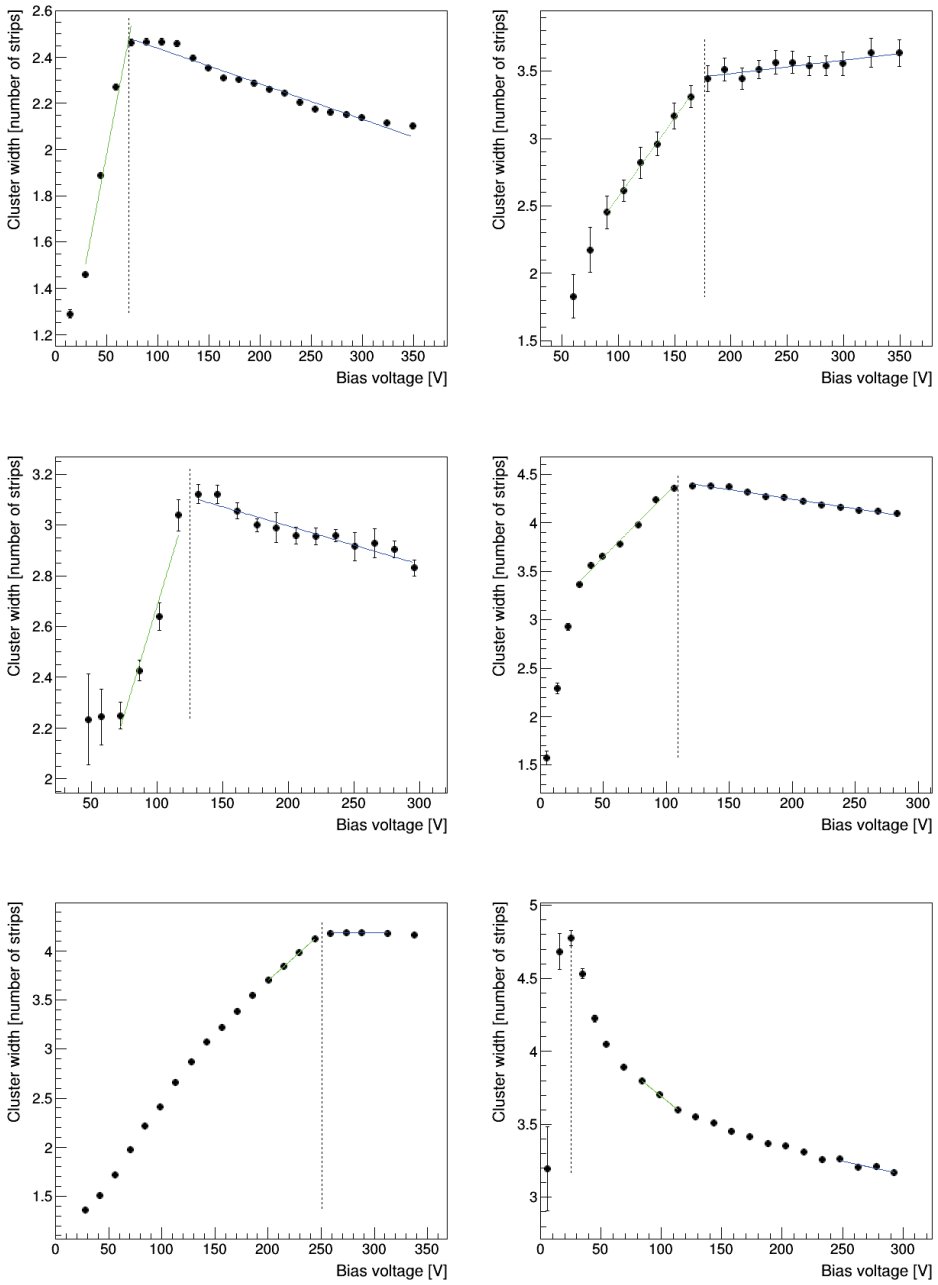

Figure 3.11: Examples of cluster width curves for different sensors and bias scans, with linear fits and their intercept superimposed. In the bottom right figure, the position of the maximum of the curve is used instead to estimate V_{FD}, as explained in the text. This illustrates the large diversity of shapes which are considered in this analysis, and the need for a robust algorithm to estimate V_{FD}.

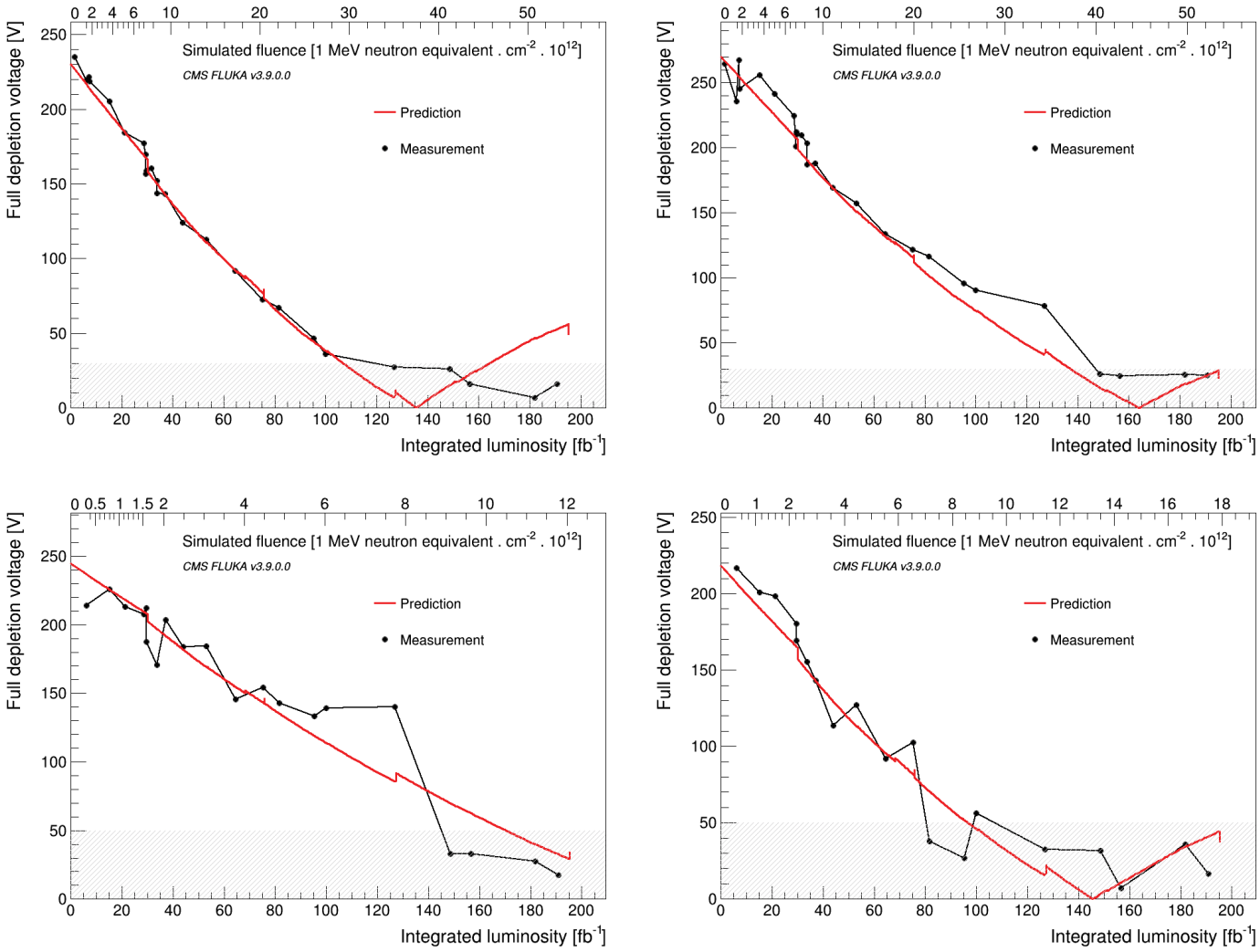

Figure 3.12: Evolution of V_{FD} as a function of the integrated luminosity delivered to CMS, for different sensors. The correspondance with the simulated fluence received by the sensor is shown on the top horizontal axis. The measurements (black dots) are compared to the simulation (red line). The top plots correspond to TIB L1 sensors, the bottom left plot to a TOB sensor, and the bottom right plot to a TEC sensor. The sensitivity of the analysis degrades at low V_{FD} values, as illustrated by the grey bands. The break around 30 fb^{-1} is due to annealing in the LS1 extended maintenance period, during which the tracker was at room temperature. Previous versions of similar figures were made public [202, 203].

compared to the TOB and TEC, hence its sensors gather more statistics during the bias scans. Although the larger pitch and strip width in the outer layers reduces the difference in terms of occupancy and irradiation per sensor, the reconstruction inefficiency for on-track clusters is also larger in the outer region. Explanations for the absence of error bars in these results are given in Sec. 3.8.1.

Simulated curves are superimposed for comparison with the measurements. They were obtained based on the Hamburg model (see Sec. 3.2), taking into account several parameters such as the initial value of V_{FD} and the temperature and fluence history of the sensor. The overall agreement of the measurements with the simulation is rather satisfying, especially for TIB sensors.

As the sensors approach type inversion, the analysis loses its sensitivity. This is partly because the sensors get over-depleted even at low bias voltage, and hence the curves do not feature a clear, steeply increasing regime anymore. Furthermore, the signal-to-noise ratio degrades at low bias voltage, hence there are more fluctuations in the data and the method becomes less precise. The sensivity threshold is approximately 30V in the TIB, and 50V for the rest of the strip tracker.

3.7.2 Evolution of V_{FD} averaged per layer

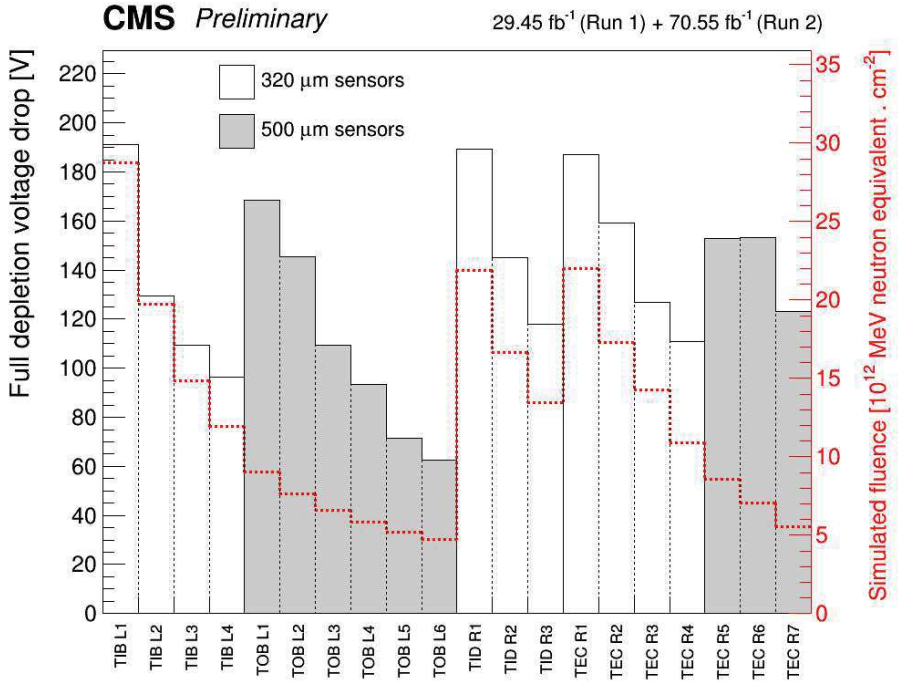

Figure 3.13: Average decrease of V_{FD} for each layer of the strip tracker, computed as the difference between the values measured at the time of the tracker construction and the values obtained by the analysis of a full scan performed in September 2017. The average fluence for each layer is shown by the red line. This figure was made public [203].

The magnitude of the average decrease of the full depletion voltage for each layer of the strip tracker is represented in Fig. 3.13. It is computed as the difference between the initial V_{FD} values measured prior to the tracker assembly, and the V_{FD} values measured by the analysis of a full bias voltage scan performed in September 2017. This particular scan was chosen because no part of the tracker was yet expected to be close to inversion at this time, making it relevant to average over an entire layer. The average fluence received by each layer is superimposed.

It is observed that the decrease of V_{FD} is more important for layers closer to the interaction point, which correlates with the larger fluence received by the sensors. Moreover, the evolution rate of the full depletion voltage of a sensor is proportional to its thickness squared (since $V_{FD} \propto N_{eff} \cdot D^2$), which explains the transitions between the TIB and TOB layers, and between TEC rings 4 and 5.

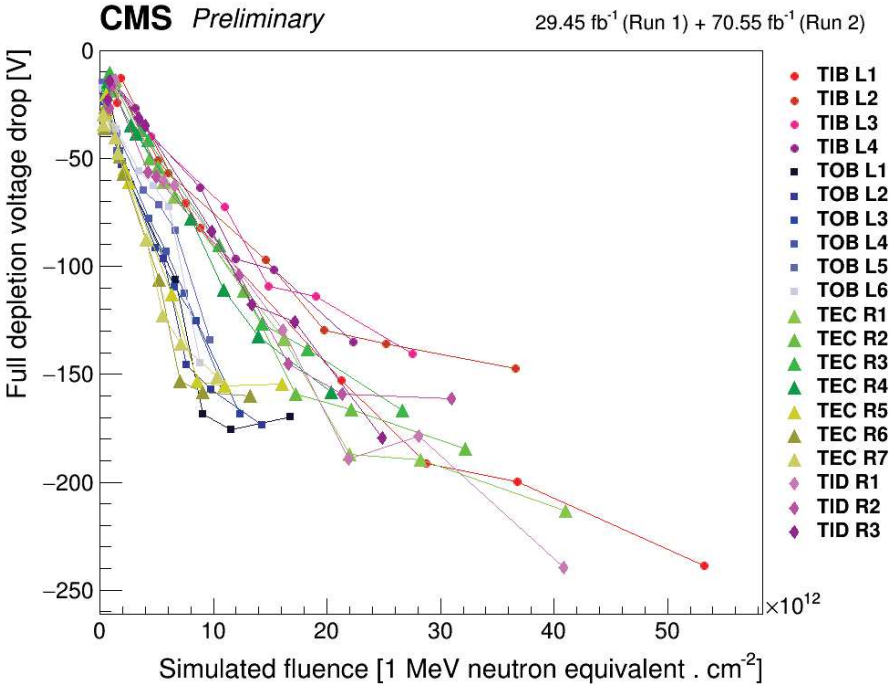

Figure 3.14: Evolution of V_{FD} with fluence, averaged for each layer of the strip tracker, using the initial laboratory measurements as reference values. This figure was made public [203].

Similarly, the relative evolution of the full depletion voltage averaged for each layer is shown as a function of fluence in Fig. 3.14. Only bias scans involving all the strip tracker modules are included. As expected, it is observed that for a given amount of irradiation, the ageing of the different layers is comparable with one another.

Two distinct populations can be distinguished, which corresponds to layers and rings which feature either thin or thick sensors. The change of trend in the latest bias scans indicates that parts of the tracker are approaching type inversion. The analysis becomes mostly insensitive in this regime, until the point where V_{FD} will increase sufficiently to exceed the minimal sensitivity threshold again.

3.8 Discussion

3.8.1 Limitations of the analysis

The results obtained in this analysis, some of which were presented in Sec. 3.7, are found to be in rather good agreement with the simulation and confirm several predictions: quasi-linear dependance of the evolution of V_{FD} with the fluence, dependance on the sensor's thickness, impact from annealing during shutdown periods, etc. However, there are also limitations to the analysis which should be kept in mind when interpreting the results, discussed in this section.

Firstly, an obvious limitation is the absence of error bars in the results. The data points which are used to extract the results come with errors (see e.g. Fig. 3.7), which are taken as the uncertainty on the MPV for the cluster charge, and as the error of the mean for the cluster width. Altough these errors directly impact the estimation of V_{FD}, since they are taken into account in the χ^2 minimization, they could not be propagated trivially to the final results.

This can be understood by looking for instance at the top right plot of Fig. 3.11, where the sizeable error bars reflect that less statistics were collected, but the algorithm was nonetheless able to extract a relevant value of V_{FD}. On the contrary, for some curves exhibiting tiny error bars, it may be difficult to estimate visually the precise value of V_{FD} within a range of e.g. 30V, for instance because the change of regime is not sharp enough. In other words, there is an ambiguity on the determination of V_{FD} due to the design of the analysis itself.

Moreover, although special care was taken to make the algorithm as robust as possible, it still relies on several ad-hoc criteria, such as arbitrary thresholds for the χ^2 scores. As a result, on rare occasions, it may be sensitive to peculiar features in the curves and provide incorrect estimates even in some cases in which the kink is clearly visible.

Since this analysis is primarily aimed at providing quantitative estimates and trends, the emphasis was put on the development of a robust method which yields relevant results rather than the precise estimation of the errors. In the future however, several ideas could be tested in order to improve the analysis in this direction. For instance, one could imagine varying artificially the error bars on the data points, and then run the algorithm again to determine lower and upper bounds on V_{FD}. To better quantify the intrinsic bias of the method, one could also run the algorithm on simulated curves to compare the true value of V_{FD} with the estimate, and try to correlate the bias with different parameters. For this purpose, more realistic simulations for the cluster width would be required.

An additional limitation comes from the limited statistics collected during a bias scan. Since bias scans must be run manually from the CMS control room, and the collected data can not be used for physics analyses in the case of full scans, a compromise had to

be found regarding their duration. Even with a robust method, the study of the TOB and TEC sensors often suffer from the low available statistics, resulting in rather imprecise estimates.

During the upcoming Run 3, the voltage scheme may need to be further adapted, e.g. to collect more data at specific values of V_{bias}. Regarding full scans, it was proposed that the scanning procedure could be improved by varying the voltage separately for the different layers of the tracker. This would avoid under-depleting all the layers at the same time, as it degrades the tracking efficiency at low V_{bias} and reduces the available statistics.

3.8.2 Comparison between methods and observables

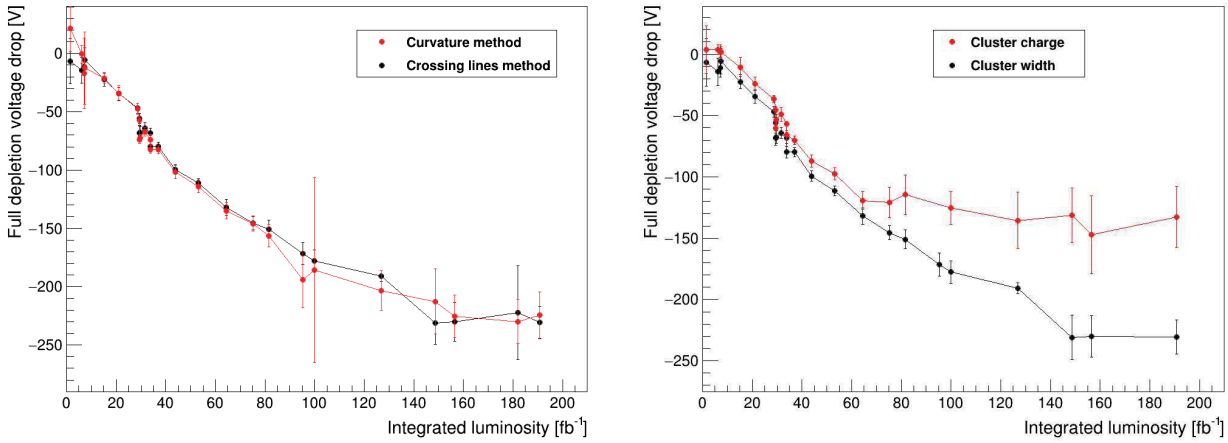

(a) (b)

Figure 3.15: Relative evolution of V_{FD} averaged over 9 TIB modules included in small bias scans, compared when using either (a) the curvature and crossing lines methods (with the cluster width observable), and (b) the cluster charge and width observables (with the crossing lines method). The reference point corresponds to the laboratory measurements. The error bars correspond to the RMS.

In order to roughly assess the bias of our default procedure, we compared the relative evolution of the full depletion voltage, averaged over 9 TIB L1 modules included in small bias scans, using different observables and methods. The laboratory measurements of V_{FD} are used as reference. Results obtained with the curvature and crossing lines methods (using the cluster width as observable) are compared in Fig. 3.15 (a), while Fig. 3.15 (b) compares the results obtained using either the cluster charge or cluster width observable (with the crossing lines method). The error bars correspond to the RMS of the values of the 9 sensors.

Figure 3.15 (a) shows that both methods provide very similar results for the TIB L1 when using the cluster width observable. This does not hold true for other parts of the tracker for which the statistics is lower: the curvature method is not robust enough in

these cases, and large fluctuations in the trend occur even when averaging over many modules.

It can be seen from Fig. 3.15 (b) that the results provided by the crossing lines method when using either the cluster charge or width as observable follow the same trend up to an integrated luminosity of about 60 fb^{-1}. The measured values differ by about 10V, with the cluster charge providing the upper estimates. Then, the cluster charge observable begins to lose its sensitivity to the full depletion voltage. This evolution can be mostly understood from Fig. 3.16, which shows simulated distributions of the cluster charge as a function of V_{bias} , for sensors having different full depletion voltages (indicated by the vertical lines). Even when neglecting higher-order effects which may degrade the shapes of the curves, it can be seen that the position of the kink becomes an increasingly biased proxy for the actual value of V_{FD} as this parameter decreases. This is mostly due to the convolution with effects from the readout electronics, and it makes the cluster charge observable rather insensitive in the low V_{FD} regime.

The smaller error bars of the measurements obtained with the cluster width also indicate that this observable provides more stable and consistent estimates. This is somewhat expected, since the crossing lines method was developped specifically for this observable.

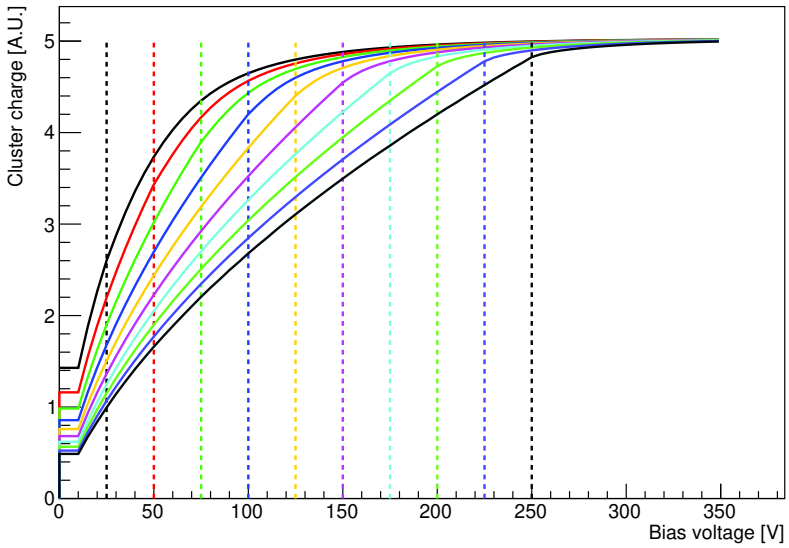

Figure 3.16: Simulated curves of the cluster charge observable, for different values of the full depletion voltage. The model is the same as the one mentioned in Sec. 3.6.1. The true V_{FD} values are indicated by the vertical dashed lines.

3.8.3 An alternative: noise bias scans

An alternative way to monitor the full depletion voltage of the sensors is to collect *noise bias scans*. In this case the observable of interest is the average noise at sensor level,

which is measured while the bias voltage is varied. The noise mostly depends on the bulk capacitance, hence it exhibits different behaviours in the under- and over-depleted regimes (cf. Eq. 3.2). The curves of the noise versus bias voltage can be fitted for instance with a rather simple function of the form:

$$N(V) = \begin{cases} C + \beta(\sqrt{\frac{1}{V_{bias}} - \frac{1}{V_{FD}}}) & , V_{bias} \leq V_{FD} \\ C & , V_{bias} > V_{FD} \end{cases} \tag{3.5}$$

where β, the constant C and V_{FD} are free parameters, determined by the fit for each curve. Above V_{FD}, the noise is expected to be constant and minimal. An example of a "good" curve is shown in Fig. 3.17, with the fit superimposed.

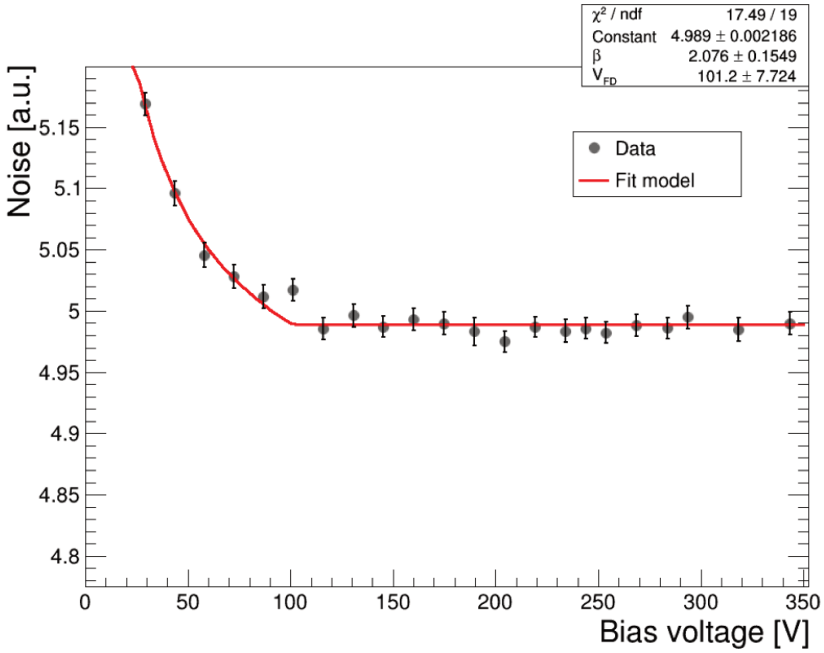

Figure 3.17: Average noise of a TIB L1 sensor as a function of bias voltage. The parameterisation from Eq. 3.5 is used to fit the curve and extract a value of V_{FD} for the sensor.

The major advantage of this approach is that noise scans can be taken during down-times of the LHC, and do not use beam time. They become particularly valuable during long shutdown periods, as signal scans can not be collected anymore, and noise scans remain the only option to monitor the evolution of V_{FD}. However, this approach is currently less accurate, as the transition between the regimes is rather subtle and difficult to identify.

Moreover, new features were observed in recent scans, such as a slightly decreasing slope replacing the saturated regime, which would require investigations and further work related to the choice of the fitting function.

I restarted this analysis, which was on hold for several years, in prevision of the ongoing long shutdown period during which only noise scans could be collected. The entire chain of codes was re-implemented, to obtain V_{FD} estimates from raw data. The full procedure includes the automated production of jobs to retrieve the noise information for all strips and voltage steps, the computation of the mean noise per APV, and the production of the final curves which are fitted to estimate V_{FD}. Investigations on the choice of the fitting function were carried out, based on data and simulation.

However, given that the analysis of the signal bias scans was set as the priority, and the fact that improving the noise analysis to a similar precision would require important work, investigations had to be stopped at the stage of preliminary results. Future work will be needed to find a more robust parameterisation of the curves, to allow for a direct comparison of the results obtained with the two analyses.

CHAPTER 4

Search for the associated production of a single top quark and a Z boson at $\sqrt{s}$ =13 TeV

This chapter presents a search for the associated production of a single top quark and a Z boson, denoted tZq. The study uses a data sample of proton-proton collisions at $\sqrt{s}$ = 13 TeV recorded in 2016 by the CMS experiment, and targets final states with three leptons (either electrons or muons, potentially arising from leptonic τ decay).

I took in charge most of the analysis, from the event selection up to the final results. In particular, an important fraction of my work was dedicated to the estimation of the nonprompt background using data-driven techniques, and the design and optimization of the multivariate analysis. Colleagues from the CIEMAT laboratory handled the processing of data and MC simulation samples, the estimation of event scale factors and the implementation of systematic uncertainties.

The first section introduces the tZq process and motivates its study. Then the main sources of background are presented, as well as the datasets and simulated samples used in the analysis. Section 4.4 details the object reconstruction and identification. Section 4.5 defines the *signal and control regions*, i.e. the phase space regions used in this analysis, enriched either in signal or background events. Section 4.6 describes the data-driven

procedure for the estimation of the nonprompt background. The design of the multivariate analysis is described in Sec. 4.7, and the sources of systematic uncertainty which are accounted for are listed in Sec. 4.8. The procedure for signal extraction is presented in Sec. 4.9, and the final results are given in Sec. 4.10. Finally, we conclude with a discussion of the results in Sec. 4.12. Most of the concepts introduced in this chapter will also be used in the analyses presented in Chapter 5.

4.1 Introduction

The large centre-of-mass energy and luminosity at the LHC provide an outstanding playground for studying rare SM processes involving the top quark, such as the associated production of a single top quark and a Z boson (tZq).

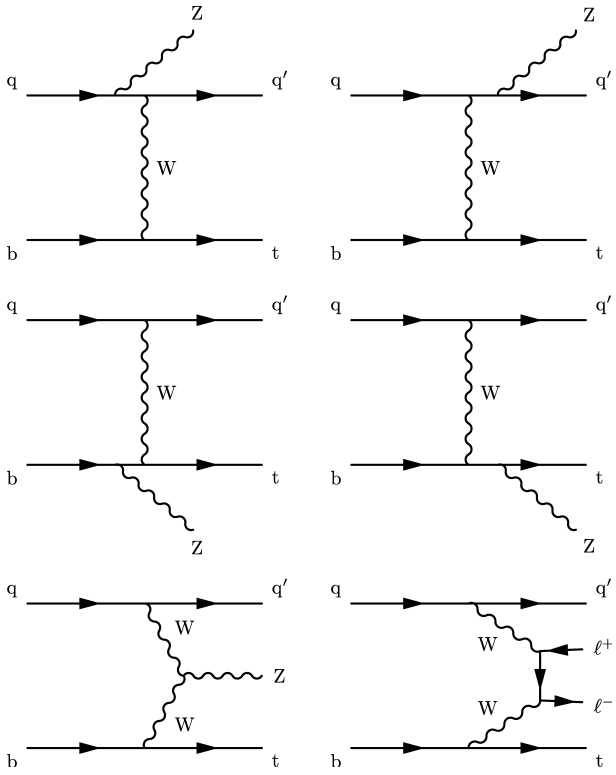

Figure 4.1: Leading-order Feynman diagrams for tZq production. The lower right-hand diagram represents the non-resonant contribution to the tZq process. The quarks labelled q and q' are predominantly first-generation quarks.

Leading-order Feynman diagrams for the tZq process are shown in Fig. 4.1. In this process, the top quark is produced via the dominant t-channel mechanism (while the tW-channel is considered as a background, and the s-channel is comparatively negligible). The associated light quark, labelled *recoiling* quark, is emitted preferentially in the same direction as the incoming proton, in the forward region of the detector. The Z boson is either radiated off one of the quarks (top and middle diagrams) or is produced via

trilinear gauge coupling (lower left-hand diagram). The study of the tZq process thus probes the top quark coupling to the Z boson as well as the WWZ coupling. This production mechanism also includes a contribution from non-resonant lepton pairs (lower right-hand diagram).

Moreover, similar final states could be produced via BSM mechanisms, such as flavour-changing neutral currents (FCNCs) or the production of vector-like quarks [221–223] decaying as $T' \to tZ$. Therefore, measuring the cross section of tZq production probes the standard model in a unique way, and can help constraining BSM models. In particular, a significant deviation from the expected SM tZq production cross section would constitute a clear indication of the presence of new physics.

This analysis targets events in which both the top quark (via $t \to bW \to b\ell\nu_\ell$) and Z boson decay to electrons or muons. There is also a small signal contribution from τ leptons decaying into electrons or muons. Therefore the distinctive signature of the signal process consists in 3 isolated leptons, a forward light jet, a jet originating from a b quark, and missing transverse energy arising from the undetected neutrino.

This leads to four possible final states depending on the flavours of the leptons: $\mu\mu\mu$, $\mu\mu e$, $e\mu\mu$ and eee. Although the trilepton channel has a low branching ratio of only $\sim 2\%$, it offers the best signal-to-background ratio and the possibility to efficiently separate the rare signal from much larger backgrounds.

For pp collisions at a centre-of-mass energy $\sqrt{s}$ =13 TeV, the next-to-leading order cross section is computed with MADGRAPH5_aMC@NLO [196] for the $tZq \to t\ell^+\ell^-q$ process, where the symbol ℓ stands either for an electron, muon or τ. Although τ leptons are not explicitly targeted by this analysis, electrons or muons arising directly from the decay of a W boson can hardly be distinguished from those involving an intermediate τ; thus the cross section calculation and event generation must also account for τ leptons. As this analysis is not sensitive to final states in which a τ lepton decays hadronically, the measured cross section will be extrapolated to include all decay modes of the τ lepton.

The calculation considers the leptonic decay of the Z boson, any decay of the top quark, and includes lepton pairs from off-shell Z* and γ^* bosons having invariant masses $m_{\ell^+\ell^-} > 30$ GeV. It results in the prediction $\sigma^{SM}(pp \to t\ell^+\ell^-q) = 94.2^{+1.9}_{-1.8}$ (scale) ± 2.5 (PDF) fb. The calculation is performed in the 5-flavour scheme, which accounts for the PDF of the b quark and treats it as massless in the proton, as it is expected to be more precise [73–75]. The scale uncertainty was estimated by varying the QCD renormalization and factorization scales by factors of 0.5 and 2 (see Sec. 1.2.3 and Ref. [224] for instance). The PDF uncertainty corresponds to the 68% confidence level (CL) uncertainty on the NNPDF3.0 PDF set [225].

This is a blind analysis, which means that the design of its strategy and the optimization studies were performed based on the MC simulation, and that the data-to-prediction agreement was first assessed in background-enriched control regions. This procedure avoids the unintended biasing of the results in a particular direction [226].

A previous search for SM and FCNC signatures at $\sqrt{s} = 8$ TeV with the CMS experiment had found an observed significance[1] of 2.4σ [227] for the tZq process. Contemporaneously with this analysis, the ATLAS collaboration also reported evidence for tZq production at $\sqrt{s} = 13$ TeV corresponding to an observed significance of 4.2σ [228]. Since then, a new CMS analysis combining the 2016 and 2017 datasets reported the first observation of the tZq process, with an observed significance of 8.2σ [229]. The results from the latter two analyses will be compared to those of the present study as part of the discussion in Sec. 4.12.

4.2 Sources of background

Backgrounds consist of all events which have final states similar to the targeted signal, and may be mistaken for signal events, but which actually originate from different physics processes.

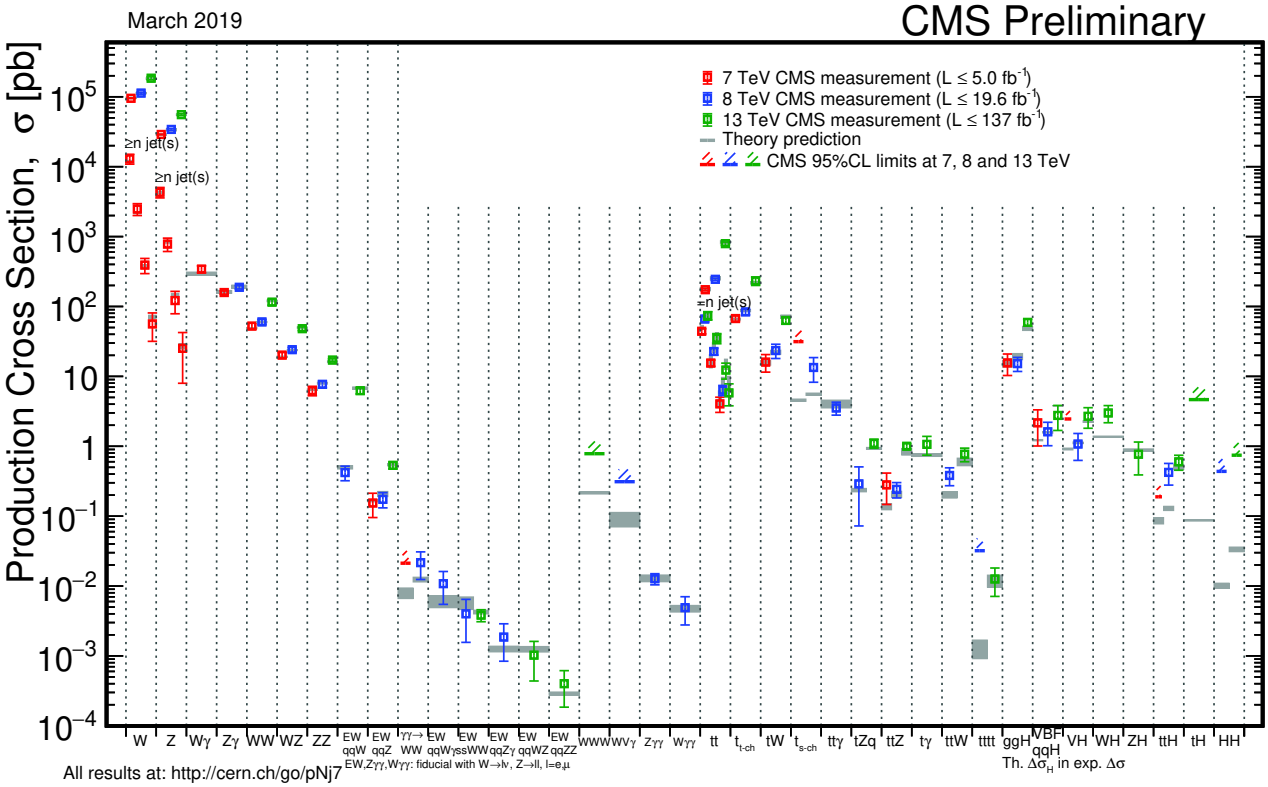

Figure 4.2: Summary plot of the CMS measurements of several SM processes. Taken from Ref. [230].

[1]The higher the statistical significance of the result, the more we are confident that the searched signal exists. A mathematical definition will be given in Sec. 4.9. Note that a significance is commonly expressed in number of Gaussian standard deviations denoted by the symbol σ, which is not to be confused with a cross section.

A distinction is made between *irreducible* backgrounds which contain 3 *prompt* leptons[2], and *reducible* backgrounds which contain at least 1 *nonprompt* lepton. A prompt lepton is defined as a lepton originating from the decay of a W or Z boson, potentially with an intermediate τ lepton; it is most often produced isolated and with high p_T. Most often, leptonic analyses aim at selecting only prompt leptons.

On the other hand, nonprompt leptons not produced via such decays are an important source of background and must be reduced as much as possible, as explained below. The figure 4.2 summarises the predicted cross sections for several SM processes and their measurements by the CMS collaboration. It illustrates how this analysis targets a rare signal in the presence of much larger backgrounds ($t\bar{t}Z$, $t\bar{t}W$, $t\bar{t}H$, $t\bar{t}$, Z+jets, etc.).

4.2.1 Irreducible backgrounds

Several SM processes have final states similar to the tZq signal and contain 3 prompt leptons. Among these irreducible backgrounds, the largest contributions arise from $t\bar{t}Z$ and WZ+jets production. Both these processes have final states which feature an opposite-sign same-flavour (OSSF) pair of leptons from the Z boson decay, and a third high-p_T lepton coming from W boson decay.

Although the $t\bar{t}Z$ process is expected to feature 2 jets arising from the hadronization of b quarks (b-jets), one of them may not be reconstructed or may be misidentified as a light jet due to the inefficiency of the b-tagging algorithm, resulting in a topology close to that of the signal. Likewise, one of the jets produced via gluon splitting in the WZ+jets final state may be b-tagged. Example Feynman diagrams for these 2 processes in the trilepton final state are shown in Fig. 4.3. The MC simulation samples used to model the signal and the irreducible backgrounds are listed in Table 4.1 with their input cross sections.

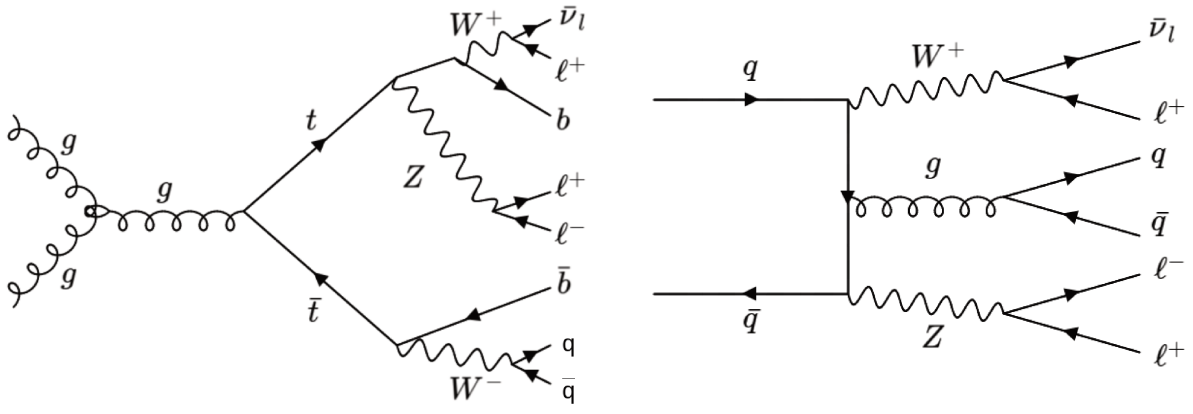

(a) (b)

Figure 4.3: Example Feynman diagrams for the (a) $t\bar{t}Z$ and (b) WZ+jets irreducible backgrounds, in the trilepton channel.

[2]Unless stated otherwise, from now on the term "lepton" is used to refer exclusively to electrons and muons. This holds in the next chapter.

In order to improve the modelling of the heavy-flavour content of the WZ+jets process, the contributions from the WZ+b, WZ+c and WZ+light-flavour jets are treated as independent processes throughout the analysis and are ultimately measured in the data. This splitting is done using the generator-level truth information. The WZ+b, WZ+c and WZ+light-flavour samples are respectively composed of WZ+jets events containing at least 1 b-jet, the remaining events containing at least 1 c-jet, and from all remaining events. This procedure avoids relying on the rather imprecise flavour content of the MC simulation for this process. In this way, the respective normalizations of these processes may vary independently in the final fit to better reproduce the data.

Table 4.1: Simulated samples used in the analysis, with their MC generator information and normalization cross sections. All the cross sections are calculated at NLO, except for that of tWZ calculated at LO.

Dataset	MC generator	Cross section [pb]
$pp \to tZq, Z \to \ell\ell$	MADGRAPH5_aMC@NLO, NLO	0.0942
$pp \to t\bar{t}Z, t\bar{t} \to 2\ell 2\nu 2b$ ($m_{\ell\ell} > 10$ GeV)	MADGRAPH5_aMC@NLO, NLO	0.253
$pp \to t\bar{t}W + jets, W \to \ell\nu$	MADGRAPH5_aMC@NLO, NLO	0.204
$pp \to WZ + jets$	MADGRAPH5_aMC@NLO, NLO	5.26
$pp \to Z\bar{Z} \to 4\ell$	POWHEG, NLO	1.21
$pp \to t\bar{t}H, H \nrightarrow b\bar{b}$	POWHEG, NLO	0.215
$pp \to tWZ, Z \to \ell\ell$	MADGRAPH5_aMC@NLO, LO	0.0112

4.2.2 Nonprompt background

Nonprompt leptons (NPLs) can have different origins. A first source corresponds to the production of genuine leptons from the leptonic decay of a heavy-flavour hadron, a pion or a kaon. For example, charged pions within jets decay to muons with the probability $\mathcal{B}(\pi^{\pm} \to \mu^{\pm}\nu_{\mu}) \sim 100\%$ [24]. Several B mesons also have sizeable branching ratios to semileptonic decays, such as the one illustrated in Fig. 4.4 (a). An additional source of NPLs is the conversion of a photon $\gamma \to e^{+}e^{-}$, which may produce isolated electrons. On the other hand, NPLs may correspond to jets misidentified as leptons, often referred to as *fake* leptons.

While nonprompt muons are principally produced by the leptonic decays of hadrons, the dominant sources of nonprompt electrons are the misidentification of jets and photon conversions. Indeed, a jet may deposit most of its energy into the ECAL, but it is unlikely to punch through and contaminate the muon system. Hence, nonprompt electrons and muons are quite different objects which it is natural to treat separately.

The major background to this analysis consists of events containing 2 prompt leptons plus 1 NPL, hereinafter referred to as the "nonprompt background" or "NPL background". In comparison, the probability for an event to contain 2 NPLs identified as

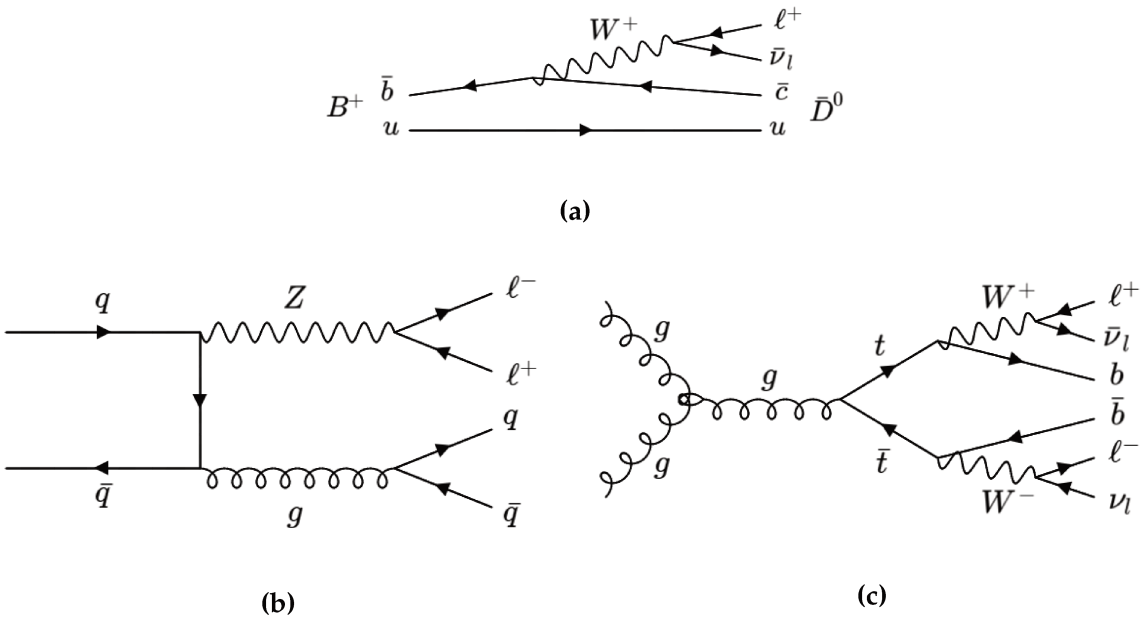

Figure 4.4: Example Feynman diagrams for (a) the semileptonic decay of a B meson, (b) the DY+jets background in the dilepton channel, and (c) the $t\bar{t}$ background in the dilepton channel.

prompt leptons is negligible and is not considered. The NPL background is mostly composed of DY+jets events ("Drell-Yan", corresponding to Z/γ^*) and $t\bar{t}$ events, which contain 2 prompt leptons from W or Z boson decay, in association with 1 NPL. A smaller contribution is due to the WW and tW processes. Example Feynman diagrams for the $t\bar{t}$ and DY+jets processes in the dilepton final state are shown in Fig. 4.4 (b) and (c).

Although the probability for a NPL to be identified as a prompt lepton is relatively small, the cross sections of the DY+jets and $t\bar{t}$ processes exceed that of the tZq signal by several orders of magnitude (see Fig. 4.2), resulting in abundant contributions. Another important issue is the fact that the NPL background is of instrumental origin. It represents a reducible background in the sense that its contamination could be removed using an ideal detector, which would never misidentify objects, and would be able to exploit the specific features of leptonic hadron decays or photon conversion to reject the associated leptons with 100% efficiency.

In reality however, nonprompt leptons result from a complex interplay of detector-related parameters and limitations, and are known to be very difficult to reproduce with MC simulation. For these reasons, as is common in analyses wherein the NPL background has a major impact, it was estimated directly from the data. The corresponding procedure is explained in Sec. 4.6.

4.3 Datasets and simulated samples

Datasets and trigger selection

This analysis uses the full dataset of pp collisions collected in 2016 with the CMS detector, which corresponds to an integrated luminosity of 35.9 fb^{-1}. Events are selected by triggers relying on the presence of either 1, 2 or 3 high-p_T leptons. The lowest p_T thresholds of the 3l (2l) triggers are 16, 12 and 8 GeV (23 and 12 GeV) for electrons, and 12, 10 and 5 GeV (17 and 8 GeV) for muons.

For events passing the trilepton baseline selection defined in Sec. 4.5, a trigger efficiency of nearly 100% is achieved by also including single-lepton triggers with thresholds of 32 and 24 GeV for electrons and muons respectively. The efficiency in the data was estimated based on a sample collected using $\vec{\not{E}}_T$ triggers uncorrelated with lepton triggers, in which we expect the presence of leptons. In the simulation, it was estimated in the signal sample. The trigger efficiencies in the data and the MC simulation are estimated as the ratios:

$$\begin{aligned} \epsilon_{data} &= \frac{N(\text{events passing lepton \& } \not{E}_T \text{ triggers})}{N(\text{events passing } \not{E}_T \text{ triggers})} \,, \\ \epsilon_{MC} &= \frac{N(\text{events passing lepton triggers})}{N(\text{total events})} \,. \end{aligned} \tag{4.1}$$

Since the trigger efficiency is measured to be $\sim$ 100% both in the data and simulation, no correction is applied for it.

Monte Carlo samples

The signal sample is generated using MADGRAPH5_aMC@NLO at next-to-leading order (NLO) QCD accuracy. The WZ+jets, $t\bar{t}Z$ and $t\bar{t}W$ processes are simulated with the same event generator, with up to 1 additional jet at NLO. The signal sample is generated in the 4-flavour scheme, which is expected to better model the kinematics of the recoiling jet and of the spectator b quark from $g \to b\bar{b}$ [231], and normalized to its cross section computed in the 5-flavour scheme (see Sec. 4.1). Other minor backgrounds are ZZ and $t\bar{t}H$ production, which are generated at NLO accuracy with MADGRAPH5_aMC@NLO and POWHEG respectively, and tWZ production generated at LO accuracy with MADGRAPH5_aMC@NLO. The MC generators used to simulate irreducible backgrounds are summarised in Table 4.1.

Apart from tWZ, all processes are normalized to their predicted NLO cross sections. All generated events are interfaced with PYTHIA for the parton showering and hadronization. Minimum bias events are overlaid to mimic the presence of pileup, corresponding to the CMS recommended value for the pp inelastic cross section of 69.2 mb.

In order for the simulation to properly reproduce the efficiencies, resolutions and energy scales measured in data, several scale factors are applied to simulated events. First of all, the distribution of the expected number of pileup events is reweighted separately for each simulated sample to match that observed in the data. Scale factors depending on

the p_T and η of the selected leptons account for differences in identification and isolation efficiencies. The electron energy is scaled and its resolution smeared to match those in the data (corrections obtained from $Z \rightarrow ee$ events).

Likewise, JES and JER corrections are applied to the jet 4-momenta. The shape of the b-tagging discriminant is later used in the multivariate analysis, and its value is corrected for differences in b-tagging efficiency and purity between data and simulation. These corrections depend on the p_T, η and score of the b-tagging discriminant for each jet.

4.4 Object reconstruction

The leptons, jets and $\vec{\not{E}}_T$ used in this analysis all correspond to PF objects, which result from the optimal combination of the information from all the subdetectors, as described in Sec. 2.3.1. This section presents the additional object selection criteria used in this analysis.

Lepton reconstruction and identification

Following official recommendations at the time of this work, electrons and muons are identified with different categorisations based on the sequential application of requirements (*cut-based* approach). The *loose* and *veto* categories are used for the purpose of the estimation of the NPL background, and the *tight* category is the standard used to identify prompt leptons.

While loose muons are simply required to be either PF global or tracker muons, tight muons correspond to global muons which satisfy additional quality requirements, related for instance to the number of hits in the pixel detector and muon system, or the distance of the track to the primary vertex. All muons must satisfy $p_T > 10$ GeV and $|\eta| < 2.4$.

Similarly, electrons are identified either as veto (95% identification efficiency) or tight electrons (70% identification efficiency), using requirements aiming to select objects compatible with electromagnetic showers in the ECAL arising from the primary vertex. All electrons must satisfy $p_T > 10$ GeV and $|\eta| < 2.5$. Some requirements were optimized separately for the barrel and endcap regions.

The concept of relative isolation I_{rel} defined in Eq. 2.5 is used to quantify the particle activity around leptons, in a cone of radius $\Delta R < 0.3$ for electrons and $\Delta R < 0.4$ for muons. This variable is corrected for the pileup. In the case of electrons, it is estimated from the median energy density per area of PU contamination [145]. In the case of muons, it was determined in multijet events to be roughly equal to the half of the energy from charged hadrons not coming from the primary vertex. Tight leptons are required to pass the isolation thresholds $I_{rel} < 0.15$ for muons, and $I_{rel} < 0.06$ for electrons (as recommended by the dedicated CMS working groups).

On the contrary, NPLs are expected to be poorly isolated, as they are most often related to jets. Therefore, NPLs are identified using the same variables, but with the isolation requirement inverted. Suitable candidates are loose muons satisfying $I_{rel} > 0.25$, and veto electrons satisfying $I_{rel} > 0.17$. In addition, in order to remove the large fraction of misidentified photons with $I_{rel} \sim 1$, and of DY events containing a soft jet misidentified as a high-I_{rel} electron, nonprompt electrons must verify $I_{rel} < 1$. For both prompt and nonprompt electrons, tight criteria are applied to reject photon conversions [178].

Jet reconstruction

Jets are reconstructed using the anti-k_T algorithm and must have a transverse momentum $p_T > 30$ GeV. Following official CMS recommendations, they must satisfy several quality requirements related to the multiplicity of particles, the relative fractions of charged and neutral particles, the angular distance to any selected lepton, etc. Since the signal process is expected to feature a light jet in the forward region, jets are selected within an extended pseudorapidity range up to $|\eta| < 4.5$.

It was noticed that the pseudorapidity distribution of jets exhibits a large discrepancy between data and simulation around $|\eta| \sim 3$, even after applying the necessary jet energy corrections (JEC). This problem could be related to a known issue, namely the imprecise measurement of the p_T of soft jets in the calorimeter transition region around $2.7 < |\eta| < 3$. This was supported by the observation of a much larger discrepancy in the NPL background sample, which is expected to contain softer jets compared to prompt lepton samples. Although the large uncertainties associated with the JEC in this noisy region approximately cover the discrepancy, it remains a problem as it would bias the estimation of the NPL background from the data. Moreover, background events containing a jet in the noisy region are more likely to be mistaken as being signal-like. The solution found consists in removing all events containing a jet within $2.69 < |\eta| < 3$ and having $30 < p_T < 50$ GeV, both in data and simulated samples. This veto solves the problem, at the cost of a moderate loss in statistics.

Jets originating from a bottom quark (b-jets) are identified using the CSVv2 algorithm [232, 233]. It uses a multivariate technique to construct a discriminating variable within the tracker acceptance $|\eta| < 2.4$, by combining various track-based variables with the information of secondary vertices associated with a jet. In this analysis, a jet is considered "b-tagged" if its CSVv2 discriminant is above the standard loose operating point, which corresponds to an average identification efficiency $\epsilon_{btag} \sim 83\%$ and a misidentification rate $\epsilon_{mis} = 10\%$ (not considering jets originating from c quarks). Otherwise, the jet is considered "light".

High-level variables

Once the main objects are reconstructed and selected, higher-level variables can be designed. The W boson transverse mass is a most useful variable to discriminate processes which contain a W boson, from processes which do not. It is used in this analysis both to

determine the normalization of the NPL background, and for the final signal extraction (see Sec. 4.6 and 4.9 respectively). It is defined as:

$$m_T(W) = \sqrt{2 \cdot p_T^l \cdot \not{E}_T [1 - cos(\Delta\phi)]}\,, \tag{4.2}$$

where p_T^l is the transverse momentum of the lepton produced in the W boson decay, and $\Delta\phi$ is the azimuthal difference between the direction of the lepton and that of the transverse missing energy (expected to arise from the undetected neutrino, $W \to l\nu_l$).

In addition, to better discriminate the signal from processes which do not contain a top quark, such as the WZ+jets and NPL backgrounds, the top quark is reconstructed from the final state objects associated with its decay ($t \to Wb \to l\nu b$). First, the pair of opposite-sign same-flavour (OSSF) leptons in the event is considered to originate from the Z boson decay. In case there exist 2 such possible combinations (in the eee and $\mu\mu\mu$ channels), the OSSF pair having the invariant mass most compatible with m_Z is selected.

The remaining lepton is then associated with the decay of the W boson from the top quark, and is hereinafter referred to as the "additional lepton". Assuming the transverse momentum of the undetected neutrino to be equal to $-\vec{\not{E}}_T$, and enforcing the constraint $m_{l\nu} = m_W$, the longitudinal component of the neutrino momentum p_ν^z can be calculated by solving a quadratic equation. In case the event does not contain a b-tagged jet, the b-jet candidate is taken as the leading (highest-p_T) jet. If 2 solutions are found for p_ν^z or if more than 1 jet is b-tagged, the $l\nu b$ system yielding the invariant mass closest to that of the top quark is selected. The remaining jet with highest p_T is referred to as the recoiling jet.

4.5 Event selection and control regions

This search targets tZq event candidates in the decay mode:

$$tZq \to (t \to b\, l\, \nu_l)\, (Z \to l' l')\, q,$$

where l and l' are either electrons or muons. Events are pre-selected if they pass any of the lepton triggers included in this analysis.

Selected events must contain exactly 3 tight leptons with transverse momenta p_T > 25 GeV. They must possess an OSSF pair of leptons having an invariant mass compatible with that of the Z boson within 15 GeV ($|m_{ll} - m_Z| < 15$ GeV). In order to reduce the contaminations from backgrounds which may have final states with $\geq$ 4 leptons, events containing an additional loose muon or veto electron with p_T > 10 GeV are not considered.

Since we aim to extract a rare signal in the presence of much larger backgrounds, large uncertainties related to these backgrounds may severely impact the precision of the measurement. To mitigate this impact, 3 independent regions enriched in signal and the main background processes are designed. Ultimately, distributions in the 3 regions will be fitted simultaneously to extract the signal, while constraining the normalizations of the main backgrounds, as described in Sec. 4.9. The regions are defined based on their jet contents, and labelled according to their b-tagged jet multiplicities:

- **1bjet signal region** *(tZq enriched):* this is the main signal region, which targets events from tZq production containing 1 b-tagged jet and 1 recoiling jet. To increase the signal acceptance, events with an additional light jet are also included, to account for the presence of initial- or final-state radiations;
- **2bjets control region** *(t$\bar{t}$Z enriched):* this region contains events with at least 2 jets, among which at least 2 are b-tagged. This mainly enhances the contribution from the t$\bar{t}$Z process, while still retaining a sizeable fraction of signal events;
- **0bjet control region** *(WZ+jets and DY+jets enriched):* this region includes events with at least 1 jet, of which none is b-tagged. This enhances the contribution from the WZ+jets process and strongly suppresses that of signal. Since most DY+jets do not contain a b-jet neither, this region is also rich in NPL background.

Table 4.2: Summary of the selection requirements defining the 3 regions used to extract the results.

Common requirements	Pass trigger selection Exactly 3 tight leptons p_T(l) > 25 / 25 / 25 GeV OSSF lepton pair with $\lvert m_{ll} - m_Z \rvert < 15$ GeV No 4^{th} lepton with $p_T > 10$ GeV		
Total jets	2, 3	≥ 2	≥ 1
b-tagged jets	1	≥ 2	0
Region	**1bjet**	**2bjets**	**0bjet**

Table 4.2 summarises the selection requirements in each region. Figure 4.5 shows distributions of several kinematic variables in each region, both for the data and the sum of the samples modeling the signal and backgrounds. Such *control plots* were used to verify that the data and simulation are in good agreement in all the regions, when accounting for uncertainties. In order to stay blind to signal contributions, only events classified as being sufficiently background-like were originally considered in the 1bjet and 2bjets regions, by applying requirements on the values of the multivariate discriminants described in Sec. 4.7.

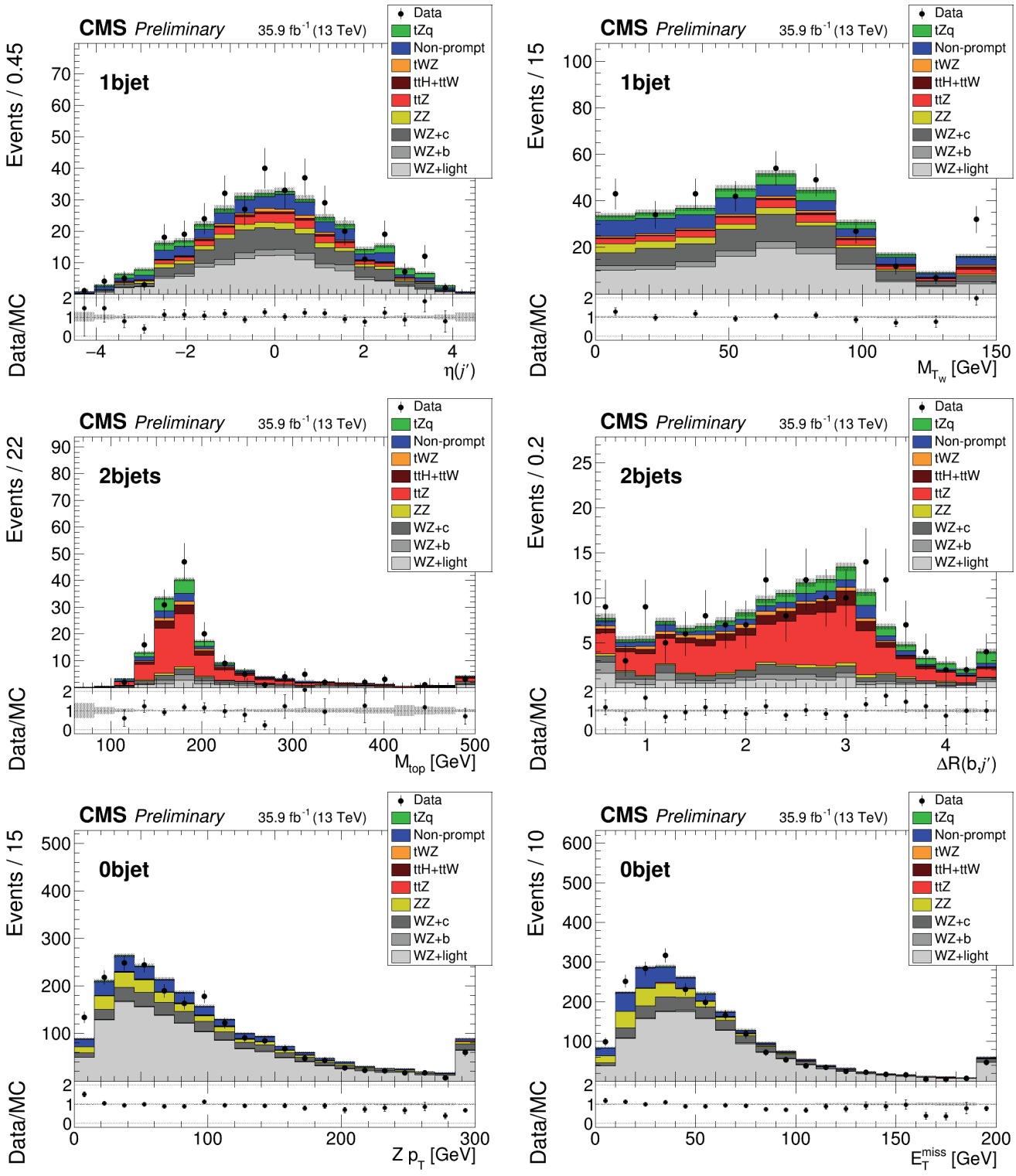

Figure 4.5: Distributions of several kinematic observables in the 1bjet signal region (top), 2bjets control region (middle) and 0bjet control region (bottom). The 4 channels are summed. The MC simulations of SM processes (stacked histograms) are compared to the data (black dots). The grey shaded areas represent the MC statistical uncertainty only, and do not include systematic uncertainties. From top to bottom and left to right, the following quantities are represented: η of the recoiling jet; m_T(W) ; the mass of the reconstructed top quark; ΔR separation between the b-tagged jet associated with the top quark decay and the recoiling jet; p_T of the Z boson; $\not{E}_T$.

4.6 Data-driven estimation of the nonprompt background

This section describes the data-driven procedure followed to estimate the NPL background. It is one of the key points of the analysis, and has been the focus of rather extensive studies, some of which are mentioned in Sec. 4.11.

4.6.1 Construction of the nonprompt sample

The NPL background sample is obtained from the 2016 data, using exactly the same selections as in the signal and control regions, except that events are required to contain exactly 1 lepton fulfiling the NPL criteria instead of tight criteria (as described in Sec. 4.4). Contrary to what was done in the previous CMS analysis [234], the NPL is not necessarily associated to the additional lepton (least compatible with the Z decay), but may be any of the 3 leptons. This procedure is more accurate, as it was seen in simulation studies that the hypothesis of the additional lepton always being the NPL only holds for the DY+jets process in the $\mu\mu e$ and $ee\mu$ channels. It does not hold for $t\bar{t}$ events, which make up an important fraction of the NPL background, and in the eee and $\mu\mu\mu$ channels.

NPL background samples are obtained separately for nonprompt electrons and muons. They are treated as independent throughout the analysis, for the reasons mentioned in Sec. 4.2. In this way, the correlations between the different channels are properly taken into account by construction. These samples are used to model the contribution of NPLs in all the kinematic observables used in the analysis.

4.6.2 Normalization

The NPL background samples obtained from the data with this procedure have quite large statistics. Since they are estimated without relying on the simulation, their initial normalizations are arbitrary. Therefore it is necessary to set their input normalizations to reasonable values, both to help the final fit converging, and to get expected results which are sensible. These normalizations are determined from the data following a two-steps procedure.

The first step is illustrated in Fig. 4.6. Prior to the final simultaneous fit, a "pre-fit" to the m_T(W) distribution is performed in the 0bjet control region alone. This fit exploits the fact that this region is dominated by the WZ+jets and DY+jets processes, which exhibit very different shapes in the distribution of $m_T(W)$. Since the former process contains a genuine W boson, its m_T(W) shape is expected to have its maximum around $m_W \sim 80$ GeV. On the other hand, DY+jets events do not, and any missing transverse energy is of instrumental origin. This results in a m_T(W) distribution with a maximum around zero. The use of the 0bjet control region to determine the pre-fit normalization of the NPL background is justified because the DY+jets is the dominant process in the NPL background, in all regions.

The normalizations of all the processes are fixed to their predicted values, except that of the NPL samples which are let floating (i.e. constrained between 0% and 100% of the

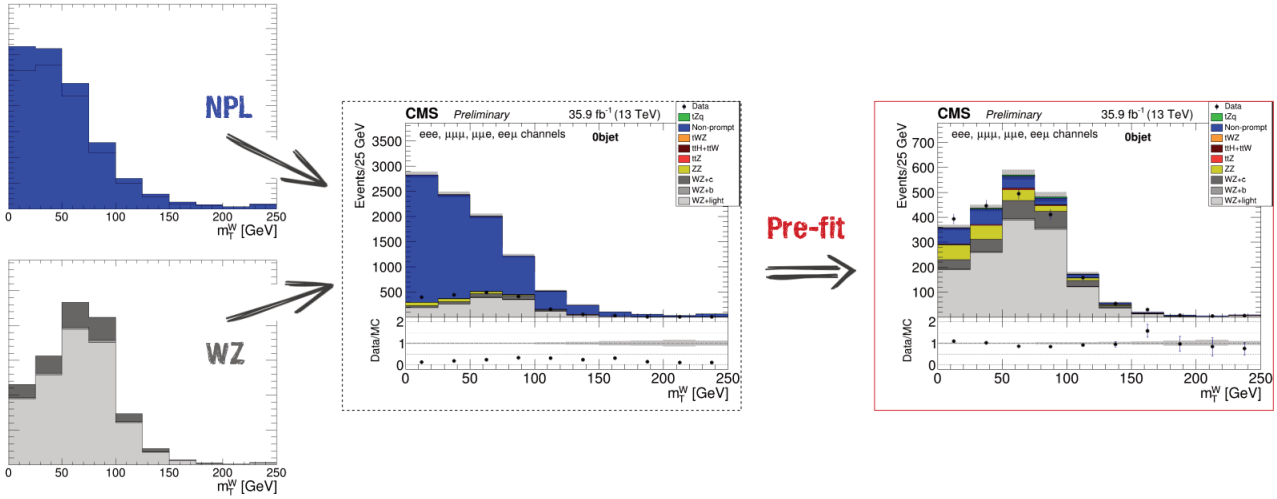

Figure 4.6: Sketch of the procedure used to obtain the "pre-fit" normalizations of the NPL samples. The fit is performed in the 0bjet control region dominated by the WZ+jets process (split depending on the jet flavour) and DY+jets events in association with a NPL. A fit is performed to the m_T(W) variable, and only the normalizations of the NPL backgrounds may vary.

observed yields). The nonprompt electron and muon contributions are summed in this step, and the fit is performed separately in the 4 lepton channels. As a result, a single scale factor is obtained per channel to rescale both the nonprompt electron and muon samples. The initial relative proportions of the 2 components are thus preserved.

The second step corresponds to the final simultaneous fit in all the regions, which provides the results and is described in Sec 4.9. There, the nonprompt electron and muon yields are treated as 2 completely independent parameters. They are let freely floating in the fit, and are properly correlated between each channel: there is 1 nuisance parameter related to the nonprompt electron sample correlated in the eee, eeμ and $\mu\mu$e channels, and 1 nuisance parameter related to the nonprompt muon sample correlated in the $\mu\mu\mu$, eeμ and $\mu\mu$e channels.

4.7 Multivariate analysis with boosted decision trees

In this analysis, we trained *boosted decision trees* (BDTs) both in the 1bjet signal region and 2bjets control region. In this way, we obtain a discriminating variable with good signal-to-background separation power in each of these regions, which is then used for the signal extraction. In the 0bjet control region, the m_T(W) distribution is used because it provides a good separation between the main processes, and this region contains almost no signal.

In the following, we motivate the use of machine-learning (ML) techniques in this analysis and introduce the concept of BDTs. Then, we give details regarding the implementation and training of the BDTs, and how their performance is improved by the

inclusion of variables obtained with the matrix element method. Both these techniques are also used in the analysis presented in Chapter 5.

4.7.1 Introduction to multivariate analysis

High-energy physics (HEP) abounds with binary classification problems, where the goal is to separate signal from background. Modern HEP experiments such as the LHC experiments represent considerable investments both in time and money, which makes it ever more important to make the most out of the collected data. Besides, the data collected by such experiments are becoming increasingly complex and high-dimensional. Many analyses such as the present one target extremely rare signals in the presence of overwhelming backgrounds.

This motivated the introduction of ML techniques in HEP analyses, which became largely accepted during the 1990s following several successful applications. Thanks to continuous advances and regular breakthroughs in ML (most notably the so-called "Deep Learning revolution" in the early 2010s), they are becoming ubiquitous in HEP, from the online trigger-level decision up to the extraction of final results [235, 236].

Within HEP, the use of a ML algorithm to exploit simultaneously multiple variables is referred to as *multivariate analysis* (MVA). This is in opposition with the straightforward *cut-and-count* approach. The latter consists in the sequential application of binary criteria on variables which discriminate the signal and background ("cut"), followed by a straightforward statistical analysis of the selected data ("count"). This approach is very suboptimal in the case of the present analysis for instance, as there is no simple set of variables which allow rejecting a large fraction of background while retaining most signal. Indeed, our regions are very background-dominated, and background processes may possess characteristics very close to that of the signal (see Sec. 4.2).

Instead, greater sensitivity can be achieved by using algorithms which learn the representation of the signal and background in multidimensional space. They take advantage of complex features and correlations between many variables, in order to best infer the origin of a given event.

4.7.2 Introduction to boosted decision trees

A Decision Tree (DT) [238–240] is a rather straightforward predictive model which can be used to classify an event as signal- or background-like (S or B), based on the values of *input variables* for this event. It is a supervised learning algorithm, trained with simulated events for which the *class* (S or B) is known *a priori*. A DT is based on sequential, binary decisions. However, instead of immediately rejecting (or classifying as background) events which fail a given cut, the algorithm proceeds recursively with the partitioning of the dataset based on further cuts, until a stopping criterion is satisfied. Hence these events may still be classified as signal-like in the end.

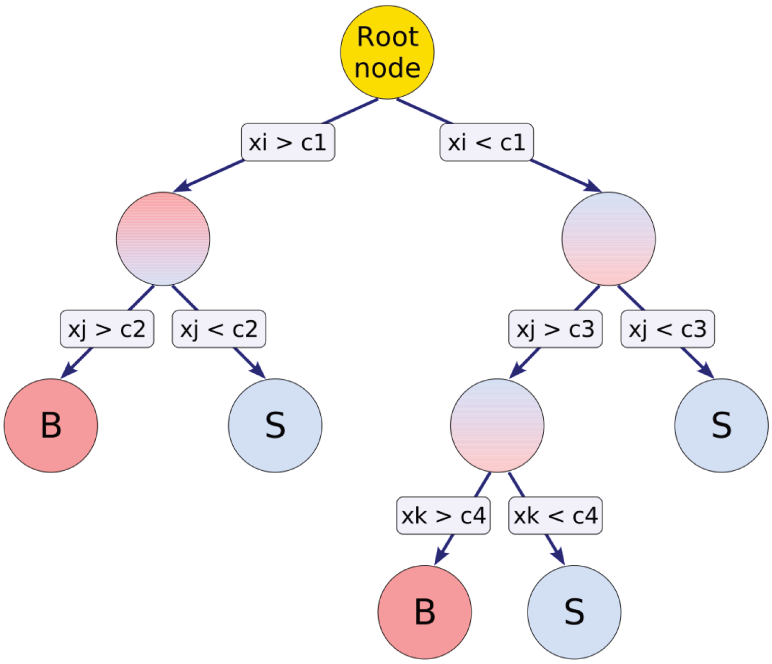

Figure 4.7: Schematic view of a single decision tree. Starting from the full samples (root node), a series of binary splits based on the variables x_i providing the best separation of the signal and background is performed. This proceeds until a stopping condition is matched. Events eventually belong to a signal or background partition, depending on the majority of events it contains. Taken from Ref. [237].

The figure 4.7 illustrates the working principle of a DT. The algorithm starts at the *root node* with the complete training dataset, which must comprise events from both classes. It searches for the cut providing the best separation between the classes among all input variables, and splits accordingly the dataset into 2 separate nodes. For each iteration of the algorithm, the same procedure is repeated at each node. In the process, the same input variable can be re-used many times, and some may not be used at all. The algorithm finishes once a stopping criterion is matched: for instance when the maximum *depth* (number of nodes) is reached, if a node contains too few events, or if the signal purity can not be further improved. In the tree structure, the final nodes are labelled *leaf nodes*, and represent a class (S or B) depending on the majority of events they contain.

After the training phase, the predictive model must be tested to evaluate its performance. To avoid biases, the testing sample must contain events which are not part of the training sample, while respecting the same class proportions. A common procedure is to randomly shuffle the initial dataset, and then split it in halves. The testing phase serves to verify that the model achieves very similar performance both on the training and testing samples, hence that it is not *overtrained*. Overtraining indicates that the model has learnt features which are specific to the training sample, due to fluctuations related to limited statistics, which adversely affects its ability to generalize to new events.

Finally, the model is used to predict the classes of the events of interest (*application* phase), which in the present analysis are the data and simulated events entering the 1bjet and 2bjets regions.

In the geometrical representation, whereas a cut-based analysis only selects events contained in a single hypercube (the n-dimensional analogue of a cube) in the phase space, a DT is able to split the phase space into many such hypercubes.

This algorithm is very popular for many reasons. First of all, it is straightforward and has a human-readable structure, which makes its interpretation rather transparent. It is based on only few *hyperparameters* (maximum depth, number of grid points to find the optimal cuts, etc.), hence it is rather easy to tune. Furthermore, since each step only involves a 1-dimensional cut optimization, the training phase is usually fast compared to more involved algorithms like deep neural networks (DNNs) [241, 242]. It is also insensitive to very correlated or irrelevant variables, as only the best variables are considered in the procedure. And it is insensitive to monotonous transformations of the input variables, which makes the preprocessing of data unnecessary.

However, the algorithm also suffers from several limitations. Firstly, it may be significantly impacted by statistical fluctuations in the training sample. An example is the case in which 2 variables have comparable separation powers, and the DT decides to split on 1 variable instead of the other because of a fluctuation in the sample. This alters the entire tree structure below this particular node, and can lead to substantially different classifier response when applied to new datasets. Secondly, all events entering the same leaf node are attributed the same result. Thirdly, due to the recursive splitting, fewer and fewer events are effectively available to train the final nodes. Finally, as is the case for all supervised ML techniques, the training sample must have sufficiently large statistics, and must be representative of the application dataset.

Several of these limitations could be overcome with the use of *ensemble learning* techniques. The most widespread is *boosting*, whose main idea is to train a *forest* of many "weak" DTs instead of one single high-performance classifier. Events which are misclassified by a DT are assigned larger weights, and hence the subsequent DTs will focus on events increasingly difficult to properly classify. The final decision for a given event is obtained from the combination of the votes from all the DTs, weighted by their classification errors.

The resulting BDT has increased statistical stability and improved separation power with respect to a single DT. It provides a quasi-continuous response usually bound between -1 (background-like) and +1 (signal-like). More details about common techniques to improve the stability and performance of BDTs can be found in the references.

4.7.3 Training of the BDT classifiers

The implementation of the multivariate analysis is based on the TMVA [237] package. The BDTs are trained using the simulated tZq sample as signal, and the simulated samples for the $t\bar{t}Z$, WZ+jets and ZZ processes as backgrounds. Other processes are not included, in particular the NPL background, due to a lack of statistics.

Eight BDTs are trained in total, 1 per channel in the 1bjet and 2bjets regions. The hyperparameters of the BDTs are optimized to maximise their performance while avoiding overtraining. Relatively small forest of 200 DTs are trained, using a maximum depth parameter of 2.

Table 4.3: Description of the input variables used in the BDTs. A cross indicates that the variable is included in the corresponding region. The last variables are obtained with the matrix element method described in Sec. 4.7.4.

	Variable description	1bjet	2bjets
1	CSVv2 algorithm discriminant	x	x
2	ΔR separation between the b-jet and the recoiling jet	x	x
3	η of the recoiling jet	x	x
4	p_T of the recoiling jet	x	x
5	η of the Z boson	x	x
6	Top quark mass	x	x
7	ΔR separation between the top quark decay lepton and the closest jet	x	x
8	Top quark decay lepton asymmetry	x	x
9	$\Delta\phi$ separation between the top quark decay lepton and the Z boson	x	x
10	$\Delta\phi$ separation between the top quark decay lepton and the b-jet	x	
11	η of the top quark decay lepton	x	
12	η of the leading jet	x	
13	ΔR separation between the top quark decay lepton and the recoiling jet		x
14	ΔR separation between the Z boson and the top quark		x
15	p_T of the Z boson		x
16	Total number of jets	x	x
17	Log of the MEM score associated with the most probable tZq kin. config.	x	x
18	Log of the MEM score associated with the most probable $t\bar{t}Z$ kin. config.	x	
19	Log-likelihood ratio of the weights under tZq vs $t\bar{t}Z$ & WZ+jets hyp.	x	
20	Log-likelihood ratio of the weights under tZq vs $t\bar{t}Z$ hyp.	x	x

The input variables used to train the BDTs in each region are listed in Table 4.3. They include the kinematics and angles of the reconstructed top quark and Z boson, and of their decay products. The CSVv2 discriminant and the multiplicity of b-tagged jets are also included.

One of the most distinctive signature of the tZq process is its recoiling jet at large $|\eta|$, and this feature is used extensively to discriminate the backgrounds. The top quark decay lepton asymmetry $q_l|\eta(l)|$ corresponds to the lepton's charge times its absolute pseudorapidity, and exploits the production asymmetry between single top and anti-top quarks. Several high-level variables obtained with the matrix element method are included, which are described in the following section.

The lists of input variables were optimized separately in each region, based on their individual impacts on the expected significance of the analysis, estimated by removing them one at a time. A total of 17 variables are used in the signal region, and 15 in the 2bjets control region.

Figure 4.8 represents the normalized distributions of all the input variables used to train the BDT in the signal region in the $\mu\mu\mu$ channel, both for the signal and background samples. Their discrimination power is clearly visible.

Figure 4.9 shows the correlation matrices for the same BDT, both for the signal and background. While a few variables are correlated with others to a significant extent, this does not adversely affects the performance of the BDT. Correlations, or more precisely different correlations for the signal and background, may even improve the BDT performance. As part of the optimization, it was verified that each and every variable improves the overall performance.

The performance of the BDT trained in the signal region in the $\mu\mu\mu$ channel is illustrated in Fig. 4.10. The left-hand figure represents the BDT outputs for the simulated signal and background samples. Firstly, it shows that the BDT achieves good performance, since it clearly discriminates signal from background events. Secondly, it can be seen that this BDT shows no sign of overtraining, as its response is equivalent for both the training and testing samples.

Figure 4.10 (b) represents the ROC (*Receiver Operating Characteristic*) curve associated with the same BDT, which is a common graphical way to estimate the performance of a classifier. The x-axis represents the signal efficiency, and the y-axis represents (1 - background efficiency). Each point represents a different requirement on the value of the classifier output.

In this representation, at worst, a classifier which assigns events a class at random would correspond to a diagonal line joining the bottom-right and top-left corners (equal rejection of signal and background). As the performance of a classifier improves, its ROC curve tends towards the top-right corner, corresponding to optimal signal efficiency and background rejection. Here for example, by applying a requirement on the value of the BDT discriminant, it would be possible to retain 80% of the signal events while rejecting more than 85% of background events ($t\bar{t}Z$, WZ+jets , ZZ). However, in the approach which is followed here, all selected events are retained to perform the final signal extraction, and we are only interested in separating the backgrounds as well as possible from the signal.

4.7.4 The matrix element method

The matrix element method (MEM) [236, 243–245] is a powerful technique first introduced in a pioneering measurement of the top quark mass by the DØ collaboration [246]. It has since been used extensively both at the Tevatron and the LHC, notably in analyses in the top quark and Higgs boson sectors [247–251].

The MEM allows quantifying the compatibility of an event with a given process *hypothesis*, encoded by its matrix element. The event weight is computed as the normalized cross section of the process at a given phase space point, which corresponds to the reconstructed kinematic configuration of the event. For a hypothesis α, the weight is defined

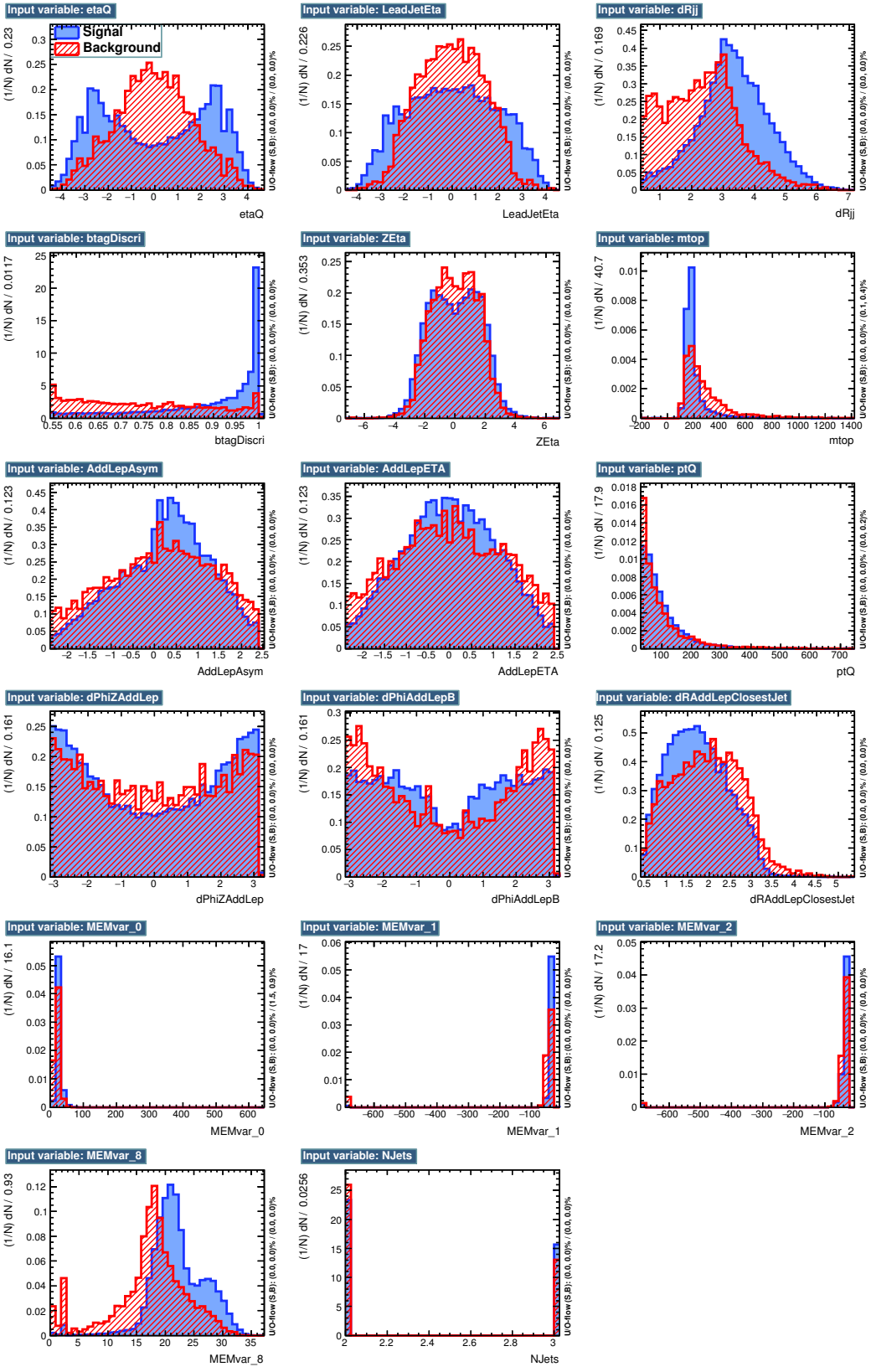

Figure 4.8: Normalized distributions of the input variables used to train the BDT in the signal region in the $\mu\mu\mu$ channel, for the signal (blue) and background (red) samples. From left to right and top to bottom, the correspondance with variables listed in Tab. 4.3 is as follows : (3,12,2), (1,5,6), (8,11,4), (9,10,7), (20,17,18), (19,16).

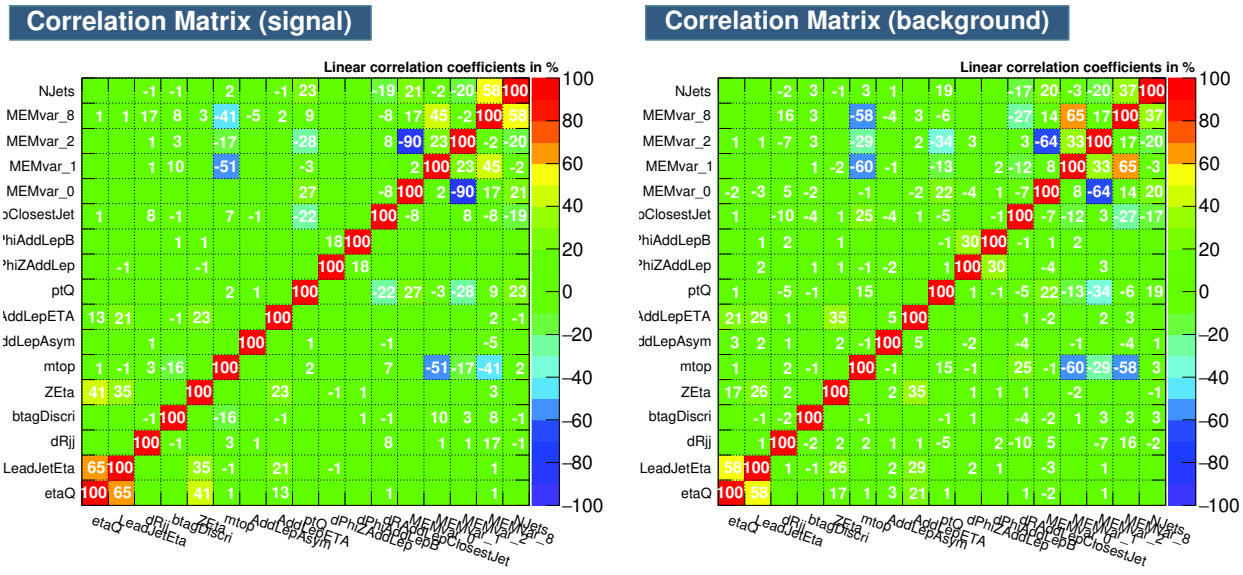

(a) (b)

Figure 4.9: Correlation matrices for (a) the signal and (b) the backgrounds, for the input variables of the BDT trained in the signal region in the $\mu\mu\mu$ channel.

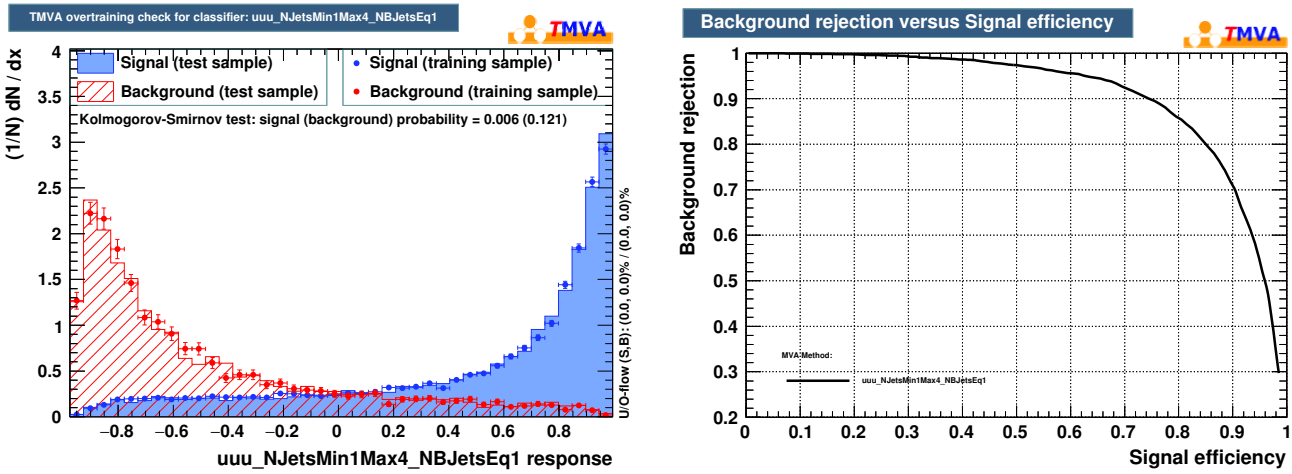

(a) (b)

Figure 4.10: (a) Normalized output of the BDT trained in the signal region in the $\mu\mu\mu$ channel, for the simulated signal (blue) and backgrounds (red). The BDT response to the training and testing events are represented as points and histograms respectively. (b) ROC curve for the BDT trained in the signal region in the $\mu\mu\mu$ channel.

as:

$$w_{i,\alpha}(\Phi') = \frac{1}{\sigma_\alpha} \int d\Phi_\alpha \cdot \delta^4\left(p_1^\mu + p_2^\mu - \sum_{k\geq 3} p_k^\mu\right) \cdot \frac{f(x_1,\mu_F) f(x_2,\mu_F)}{x_1 x_2 s} \cdot \left|\mathcal{M}_\alpha(p_k^\mu)\right|^2 \cdot W(\Phi'|\Phi_\alpha)\,, \tag{4.3}$$

where σ_α is the cross section of the process; Φ' are the 4-momenta of the reconstructed

particles in the event; $d\Phi_\alpha$ is the element of phase space corresponding to unmeasured quantities for all final state particles; the δ function enforces the momentum conservation between initial and final state particles; $f(x, \mu_F)$ are the proton PDFs; x_1, x_2 are the fractions of proton energy carried by the incoming partons; $\left|\mathcal{M}_\alpha(p_k^\mu)\right|^2$ is the matrix element squared; and W are the transfer functions for the jet energy and $\not{E}_T$, evaluated from the simulation.

The transfer functions $W(\Phi'|\Phi_\alpha)$ encode the probability density of reconstructing a set of quantities Φ', given a phase space point Φ_α at the matrix element level. They take into account showering and hadronization effects, and the experimental resolution and reconstruction. The energies of leptons, and the directions of leptons and jets are assumed to be perfectly measured, and are not associated with transfer functions.

The MEM presents several unique advantages [236]. Firstly it does not require any training and can provide good discrimination irregardless of the available statistics. It can be applied to a wide variety of processes and analyses, and incorporates all the available kinematic information with proper correlations. Most importantly, it makes the best use of the theoretical information related to the processes. And it is properly defined within QFT in terms of transition probability, hence it has a clear physical meaning.

On the other hand, the major drawback of this technique is that it is extremely computationally intensive because it involves high-dimensional integration. Moreover, it is usually relying on leading-order matrix elements, although it is often applied to events generated at NLO containing additional jets. In our case, the transverse momentum of the tZq system is forced to zero. This "inverse boost" is applied to all final state particles, and corrects for any additional jet not present in the LO matrix element. Other methods exist to properly handle the presence of additional radiations [252].

The MEM is implemented as a custom C++ code [253] developed at the IPHC laboratory. The phase space implementation follows that outlined in Ref. [254]. The code is interfaced with the VEGAS adaptive algorithm [255] to perform the integration. Matrix elements are obtained at leading order from the MADGRAPH generator, and PDF sets are taken from LHAPDF6 [256].

MEM weights were computed under 3 different hypotheses: tZq, $t\bar{t}Z$ and WZjj (WZ plus 2 jets). The top quark mass is fixed to 173 GeV, the b quark mass to 4.7 GeV, and the masses of other quarks and leptons are neglected. For the method to work, reconstructed particles must be associated with particles at the matrix element level. For each hypothesis, weights are computed for all possible permutations of the selected leptons and jets, and averaged. In case expected jets are missing in the reconstructed event, the phase space integration is extended to additional variables, so that MEM weights can be computed for all events entering the 1bjet and 2bjets regions.

Several variables computed with the MEM are included as input variables to the BDTs to increase their separation power, 4 in the 1bjet signal region and 2 in the 2bjets control region:

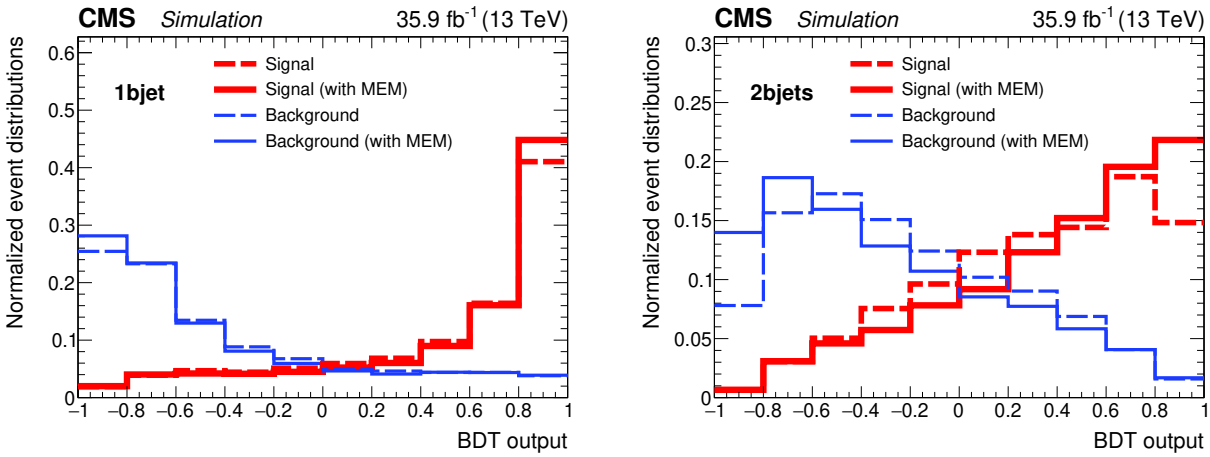

(a) (b)

Figure 4.11: Normalized distributions of the BDT output for simulated signal (thick red lines) and background (thin blue lines), in the 1bjet (left) and 2bjets (right) regions. The discriminants corresponding to the cases where the MEM variables are included or excluded are shown respectively as solid and dashed lines. The 4 channels are summed.

- The log-likelihood ratio of MEM weights computed under the tZq versus $t\bar{t}Z$ hypotheses (in both regions);
- The highest integrand value during the integration process under the tZq hypothesis. This is equivalent to a kinematic fit, as it corresponds to the phase space point with most probable kinematic configuration (in both regions).
- As above, under the $t\bar{t}Z$ hypothesis (in the 1bjet region).
- The log-likelihood ratio of MEM weights computed under the tZq versus $t\bar{t}Z$ + WZjj hypotheses (in the 1bjet region).

Figure 4.11 compares the normalized BDT outputs for simulated signal and background events in both regions. It is clearly visible that the addition of input variables obtained with the MEM increases the separation powers of the BDTs, by making the output distributions more peaked. The separation power of MEM variables can also be assessed by looking at the 5 downmost sub-figures of Fig. 4.8 (but the last one). Including the MEM variables improves the expected significance of the analysis by about 20%.

4.8 Systematic uncertainties

Various sources of systematic uncertainty are considered, related to the incomplete knowledge of detector- and theory-related effects. Both the event yields and the shapes of the observables used in the final fit may be impacted. These systematic uncertainties are listed and described in this section. Correlations between the channels are taken into account.

Experimental uncertainties

- **Luminosity:** An uncertainty of 2.5% on the integrated luminosity of the 2016 dataset is propagated as a normalization-only uncertainty to all predicted yields [257].
- **Pileup:** The central value of the pp inelastic cross section used to simulate pileup events is varied by $\pm$4.6% following recommendations. This impacts both the shapes of the distributions, and the phase space acceptance.
- **Trigger efficiency:** Although the trigger efficiency is estimated to be close to 100% (see Sec. 4.3), the predicted yields are varied by $\pm$1% ($\pm$2%) in the $\mu\mu\mu$ and $\mu\mu$e (eeμ and eee) channels to account for residual differences in trigger efficiency between data and simulation.
- **Lepton selection:** The scale factors used to correct differences in lepton isolation and identification are varied within their $\pm 1\sigma$ uncertainties. This affects both the shapes and normalizations.
- **Jet energy scale and resolution:** The JES and JER scale factors are varied independently within their $\pm 1\sigma$ uncertainties, and the changes are propagated to all kinematic quantities. These uncertainties affect both the shapes and normalizations.
- **B-tagging:** Eight independent variations by $\pm 1\sigma$ are considered for the scale factors related to b-tagging and mistagging efficiencies. They correspond to 2 types of statistical uncertainty on the b-, c-, and light-flavour components in samples, and the estimated contamination from light-flavour (heavy-flavour) jets in heavy-flavour (light-flavour) measurement regions. They affect both the shapes and normalizations.

Theoretical uncertainties

The scale and PDF uncertainties affect the shape of the signal, as well as the shapes and normalizations of the background distributions. The tWZ sample is generated at LO and does not contain all the necessary information, hence normalization-only theoretical uncertainties are considered for this sample.

- **Renormalization and factorization scales at matrix element level:** At the matrix element level, both the renormalization and factorization scales μ_R and μ_F are set to the same value, which depends on the process and the choice of event generator. As is common, the uncertainties attached to the particular choices of scales are assessed by varying these parameters independently by factors of 1/2 and 2, and taking the uncertainty envelope [224].
- **Renormalization and factorization scales at parton shower level:** The impact of the variations of μ_R and μ_F by factors or 1/2 and 2 on the parton showering is also evaluated, from a comparison with a dedicated sample. This uncertainty only affects the shape of the tZq process.

- **PDF:** The uncertainty attached to the choice of PDF set is estimated based on the PDF4LHC recommendations [258], and taken as the root-mean-square (RMS) of 100 variations of the NNPDF set.

Background estimation

- **Normalization of irreducible backgrounds:** The input normalizations of all the simulated backgrounds are attached a relative uncertainty of 30%. This corresponds to an inflation by a factor 2 or more of the theoretical uncertainties on their cross sections, to account for possible mismodeling in the phase space targeted by the present analysis.
- **Shape of NPL backgrounds:** The uncertainties on the shapes of the nonprompt electron and muon samples are estimated independently, by increasing the isolation requirement respectively for nonprompt electrons and muons. This provides an alternative shape for each NPL sample.

4.9 Signal extraction

The tool [259–261] used for the statistical analysis is based on the RooStats framework [262]. This section presents an overview of the statistical model used for signal extraction. Extensive descriptions of the concepts can be found in the references.

Nuisance parameters

The parameter of interest (POI) we measure in this analysis is the signal strength μ, which simply corresponds to the ratio of the estimated cross section of the signal process divided by its SM prediction:

$$\mu = \frac{\sigma(pp \to t\ell^+\ell^- q)}{\sigma^{SM}(pp \to t\ell^+\ell^- q)} \,. \tag{4.4}$$

All the other parameters which must be included in the statistical model in order to describe the observed data are represented by a set of *nuisance parameters* θ. In this case, they correspond to the various sources of uncertainty.

A nuisance parameter is associated with a probability density function (p.d.f), or *prior*, which can generally be expressed in terms of 2 parameters: its *estimate* $\hat{\theta}$ (*central value*) and uncertainty $\pm\delta\theta$[3]. The prior usually consists of a pre-existing measurement which characterizes the nuisance parameter (e.g. a luminosity measurement), a theoretical insight or a physical constraint. Nuisance parameters which are not *a priori* constrained by any measurement or consideration are assigned uniform priors.

[3]The interval $[\hat{\theta} - \delta\theta; \hat{\theta} + \delta\theta]$ forms a 68% CL interval, constructed in a way such that it will contain the true parameter value 68% of the time, corresponding to a $\pm 1\sigma$ interval under a Gaussian distribution.

For parameters which can take either negative or positive values, a Gaussian p.d.f often provides a reasonable model for one's degree of belief regarding the nuisance parameter. For positively-defined quantities such as the ones we are considering (efficiencies, NPL rates, etc.), a log-normal p.d.f is generally prefered rather than a Gaussian truncated at zero. It also has useful properties which make it better suited in these cases where the nuisance parameter describes a multiplicative correction.

Using the method described below, nuisance parameters can be handled by estimating their central values and uncertainties from the data. In this analysis, normalization uncertainties on the NPL backgrounds are assigned a uniform prior with quasi-infinite range, as we explicitly want these parameters to be inferred and constrained from the data.

Other normalization-only uncertainties are assigned a log-normal prior. Uncertainties which distort the shapes of the distributions are evaluated by providing the tool with "shifted" distributions obtained after varying the corresponding nuisance parameter by $\pm 1\sigma$, and according to the method described in Ref. [263].

Statistical uncertainties related to the finite MC statistics are treated with the Barlow-Beeston method, detailed in Ref. [263, 264]. This method represents the overall statistical uncertainty on the predicted number of events from all sources by assigning a single nuisance parameter to each bin of the fitted distributions, with a Poisson or Gaussian prior depending on the statistics.

Maximum likelihood estimation

In order to estimate the POI and its uncertainty, we start by constructing a binned likelihood function which incorporates all known information regarding the different parameters of the model.

The likelihood function $\mathcal{L}(data|\mu,\theta)$ quantifies the compatibility between the observed data and the prediction, for given values of the POI and nuisance parameters. In our case, it can be expressed as the product of the Poisson probabilities (counting experiments) associated with all the bins i included in the fit, as:

$$\begin{aligned}\mathcal{L}(data|\mu,\theta) = &\prod_i \frac{\mu\cdot s_i(\theta) + b_i(\theta) + \alpha_e\cdot B_i^e(\theta) + \alpha_\mu\cdot B_i^\mu(\theta)]^{N_i}}{N_i!} \\ &\times e^{-\mu\cdot s_i(\theta) - b_i(\theta) - \alpha_e\cdot B_i^e(t\theta) - \alpha_\mu\cdot B_i^\mu(\theta)} ,\end{aligned} \tag{4.5}$$

where N_i is the observed number of events in each bin; s_i and b_i are the expected signal and background yields in each bin; θ is the set of nuisance parameters associated with log-normal priors; $B_i^{e,\mu}$ are the yields of the nonprompt electron and muon backgrounds in each bin; $\alpha_{e,\mu}$ are the parameters which determine the normalization of the NPL backgrounds and are left free in the fit (flat priors).

The prevalent *maximum likelihood estimation* (MLE) method is then used to estimate the parameters. It consists in finding the point in the parameter space which makes the likelihood function maximal, i.e. for which the observed data are the most "probable". For computational simplicity, it is more common to instead minimize $-2\ln(\mathcal{L})$. This is solved numerically using the Minuit tool [265].

Profiled likelihood ratio

In order to draw conclusions from the data, a *test statistic* quantifying the compatibility between the data and a given hypothesis $\mathcal{H}$ must be defined. It condenses the signal-to-background discrimination information into a single value.

A common test statistic to test the hypothesised signal strength μ corresponds to the ratio of *profiled*[4] likelihood functions:

$$\mathcal{Q} = \frac{\mathcal{L}(data|\mu, \hat{\theta}_\mu)}{\mathcal{L}(data|\hat{\mu}, \hat{\theta})}. \tag{4.6}$$

The numerator corresponds to the case where the signal strength is fixed to a given value, while in the denominator it is treated as a free parameter. The values of the nuisance parameters maximising the likelihood are profiled separately in each case. $\hat{\theta}_\mu$ is the profiled *conditional* estimator for a specific value of μ, while $\hat{\mu}$ and $\hat{\theta}$ are global maximum likelihood estimators. By construction, as the numerator of the ratio can not exceed the denominator, this *profile likelihood ratio* (PLR) is bounded between 0 and 1, with higher values indicating better compatibility between the data and the hypothesised value of μ.

In the present case, we are interested in determining whether the observed data supports the background hypothesis $\mathcal{H}_0$ (*null hypothesis*, $\mu = 0$) or not, i.e. whether the following PLR is compatible with zero or significantly differs from it:

$$\lambda_0 \equiv -2\ln(\mathcal{Q}) = -2\ln\Big(\frac{\mathcal{L}(data|\mu = 0, \hat{\theta}_0)}{\mathcal{L}(data|\hat{\mu}, \hat{\theta})}\Big). \tag{4.7}$$

Significance and p-value

The *significance* of the observed result is obtained from the *p-value* p_0, corresponding to the probability of getting a result at least as "unlikely" as the observed value, assuming the background hypothesis $\mathcal{H}_0$ to be true:

$$p_0 = \int_{\lambda_{obs}}^{\infty} f(\lambda_0|\mathcal{H}_0)d\lambda_0\,, \tag{4.8}$$

where $f(\lambda_0|\mathcal{H}_0)$ is the p.d.f of the test statistic under the assumption of $\mathcal{H}_0$. The hypothesis is then rejected if p_0 is found less or equal to a fixed threshold specified before carrying out the test. The p-value can be directly translated into the significance $Z = \Phi^{-1}(1 - p_0)$,

[4] "Profiling" a likelihood function amounts to maximising it with respect to all but one parameter.

expressed in units of Gaussian standard deviations σ, where Φ^{-1} is the inverse of the cumulative distribution (or *quantile*) of the standard Gaussian.

In HEP, the standard thresholds for claiming an *evidence* or a *discovery* are set to $Z = 3$ and $Z = 5$, corresponding to p-values of 1.4×10^{-3} and 2.9×10^{-7} respectively for the background hypothesis. For the purpose of excluding a signal hypothesis, a threshold p-value of 0.05 is often used, which corresponds to $Z = 1.64$. More details about the procedure for determining upper limits are given in Chapter 5.

Asymptotic limit

In many cases, the complete distribution of the likelihood-ratio statistic is difficult to determine. Besides, calculating the expected significance may require the generation of a large number of simulated pseudo-experiments (commonly referred to as "MC toys"), which is very computationally intensive.

These problems can be overcome by the application of Wilks' theorem [266, 267] and approximate formulae from Wald [268], which hold in the *asymptotic* regime (large sample limit $n \to \infty$). It is one of the reasons why the MLE method is among the most used for statistical inference. Wilks' theorem [266, 267] states that the likelihood-ratio statistic λ_μ is asymptotically distributed following a χ^2 distribution, with n degrees of freedom corresponding to the number of POIs.

As a result, the significance can be computed very quickly by simply comparing the value of the test statistic to the value of the χ^2 function for a given confidence level. For example, a test statistic $\lambda_\mu > 3.84$ corresponds to a p-value $p_\mu = 5\%$ and allows the rejection of $\mathcal{H}_0$ at 95% CL[5].

Another important consequence is that the median expected significance for a given hypothesis can be asymptotically approximated using an *Asimov dataset* [261] instead of MC toys. The Asimov dataset is a representative dataset, in which the estimates of all parameters are set to their expected values, and statistical fluctuations are suppressed.

In this analysis, the signal strength is extracted from a profiled likelihood scan in all the regions and channels simultaneously, representing a total of 12 distributions. The BDT discriminants are used in the 1bjet and 2bjets regions, while the m_T(W) distribution is used in the 0bjet control region.

4.10 Results

The observed tZq signal strength is measured to be:

$$\mu = 1.31^{+0.35}_{-0.33}\,(stat)\,^{+0.31}_{-0.25}\,(syst)\,. \tag{4.9}$$

The reference NLO cross section is $\sigma^{SM}(pp \to t\ell^+\ell^- q) = 94.2^{+1.9}_{-1.8}$ (scale) ± 2.5 (PDF) fb, for $m_{\ell^+\ell^-} > 30$ GeV. The measurement is thus extrapolated from the considered phase

[5] 3.84 is the 95^{th} percentile of the χ^2 distribution with 1 degree of freedom (μ).

space (see Sec. 4.5), which requires the presence of 3 leptons (electrons or muons) and constrains $m_{\ell^+\ell^-}$ to be within 15 GeV of the Z boson mass, to express the measured cross section:

$$\sigma(pp \to t\ell^+\ell^- q) = 123^{+33}_{-31}\,(\text{stat})\,^{+29}_{-23}\,(\text{syst})\,\text{fb}\,, \tag{4.10}$$

where ℓ stands either for electrons, muons, or τ leptons. The overall impact of systematic uncertainties is estimated by taking the difference in quadrature of the 68% CL intervals derived in the nominal fit, and in a separate fit where the corresponding nuisance parameters are not considered.

The corresponding observed significance against the null hypothesis is 3.7σ, and thus this measurement represents the first evidence for the tZq process. The expected significance estimated from an Asimov dataset is 3.1σ, and the associated 68% CL interval is $\mu \in [1.4, 5.9]$.

The measurement was repeated separately in each channel, and the corresponding results are listed in Table 4.4. The most sensitive channel is the $\mu\mu\mu$ channel. This is rather expected because muons are typically reconstructed with better precision compared to electrons at CMS. Moreover, the rate of nonprompt electrons being larger than for muons, tighter requirements must be applied to electrons at the cost of lower statistics. The observed and post-fit expected yields for all the considered processes in the 1bjet signal region are given in Table 4.5.

Table 4.4: Observed signal strength, and expected and observed significance in each separate channel.

Channel	Signal strength	Expected signif. (σ)	Observed signif. (σ)
eee	$1.32^{+1.14}_{-0.99}$	1.2	1.6
eeμ	$0.66^{+0.78}_{-0.63}$	1.3	1.1
$\mu\mu$e	$0.01^{+0.97}_{-0.01}$	1.2	0.0
$\mu\mu\mu$	$1.22^{+0.75}_{-0.63}$	2.2	2.1

The figure 4.12 shows the post-fit data-to-prediction comparisons of several input variables, after the POI and nuisance parameters have been constrained by the data, for each of the 3 regions. From the distributions and their *pulls*[6], it can be seen that the data and MC simulation are in very good agreement.

The post-fit data-to-prediction comparisons of the distributions used to perform the signal extraction are shown in Fig. 4.13. It is clearly visible that the signal significance is primarily driven by the signal-like bins of the BDT output in the 1bjet signal region, where the signal is concentrated. The main background contamination in these bins is due to the NPL background, which represents the main limiting factor for the sensitivity of this analysis.

[6]The pull [269] of a random variable x following a Gaussian distribution of mean μ and width σ is defined as $g = \frac{x-\mu}{\sigma}$. It quantifies the difference between the observation and expectation in number of standard deviations.

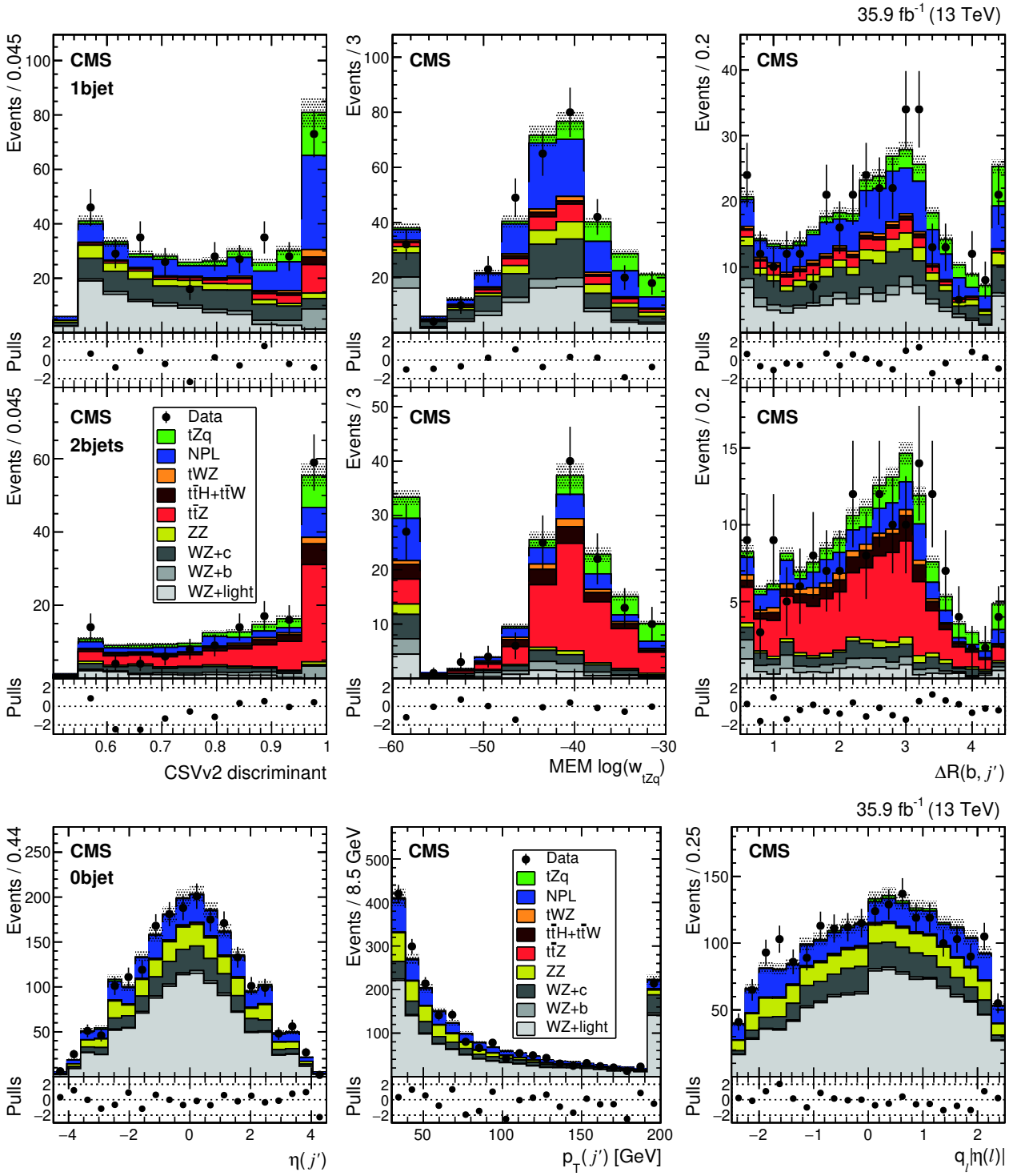

Figure 4.12: Post-fit data-to-prediction comparisons in the 1bjet signal region (top), 2bjets control region (centre) and 0bjet control region (bottom) for several input variables used to train the BDTs. From left to right, the variables are ranked 1^{st}, 17^{th}, 2^{nd} (top and middle) and 3^{rd}, 4^{th}, 8^{th} (bottom) respectively in the descriptive Table 4.3. The 4 channels are summed. The hatched bands represent the total uncertainty on the prediction.

Table 4.5: Observed and post-fit expected yields for each considered process in the 1bjet signal region, for each individual channel and their sum. The total uncertainties on the predictions are indicated.

Process	eee	eeμ	e$\mu\mu$	$\mu\mu\mu$	All channels
tZq	5.0 ± 1.5	6.6 ± 1.9	8.5 ± 2.5	12.3 ± 3.6	32.3 ± 5.0
$t\bar{t}Z$	3.7 ± 0.7	4.7 ± 0.9	6.1 ± 1.2	8.0 ± 1.5	22.4 ± 2.2
$t\bar{t}W$	0.3 ± 0.1	0.3 ± 0.1	0.7 ± 0.2	0.6 ± 0.2	1.9 ± 0.3
ZZ	4.8 ± 1.3	3.2 ± 0.9	9.0 ± 2.5	7.8 ± 2.2	24.7 ± 3.6
WZ+b	3.0 ± 0.9	3.4 ± 1.1	4.6 ± 1.4	5.5 ± 1.7	16.6 ± 2.6
WZ+c	9.0 ± 2.4	13.7 ± 3.7	18.0 ± 4.9	24.2 ± 6.5	64.8 ± 9.3
WZ+light	12.2 ± 1.6	16.6 ± 2.0	22.4 ± 2.8	29.1 ± 3.4	80.3 ± 5.1
$t\bar{t}H$	0.6 ± 0.2	0.9 ± 0.3	1.0 ± 0.3	1.5 ± 0.4	4.0 ± 0.6
tWZ	1.0 ± 0.3	1.3 ± 0.4	1.7 ± 0.5	2.4 ± 0.7	6.5 ± 1.0
NPL: electrons	19.2 ± 3.1	0.6 ± 0.1	17.9 ± 2.8	-	37.7 ± 4.2
NPL: muons	-	7.2 ± 2.3	31.1 ± 9.9	15.3 ± 4.9	53.6 ± 11.3
Total	58.8 ± 4.8	58.4 ± 5.5	121 ± 12	107 ± 10	345 ± 18
Data	56	58	104	125	343

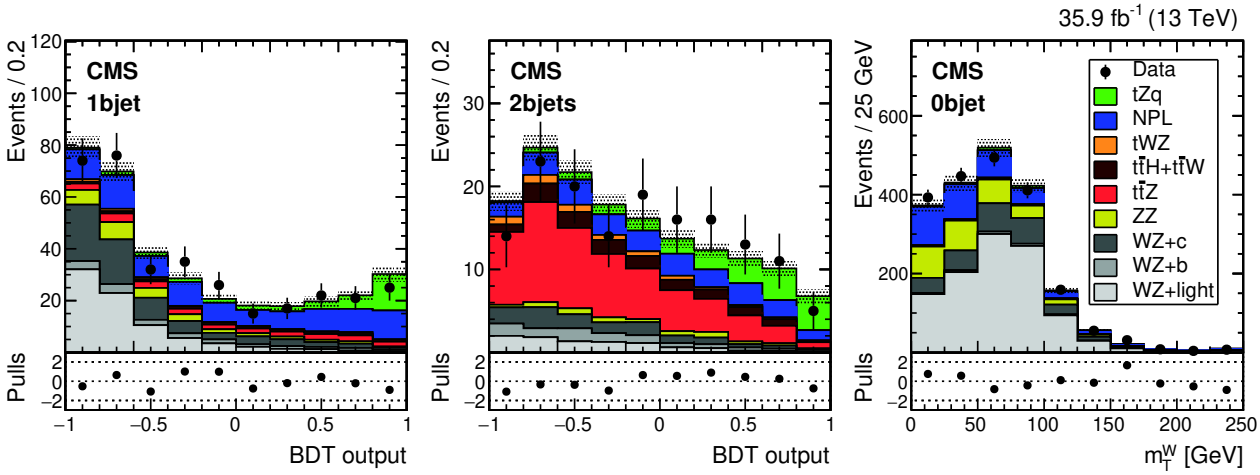

Figure 4.13: Post-fit data-to-prediction comparisons of the distributions used for signal extraction. Left: BDT output in the 1bjet signal region; middle: BDT output in the 2bjets control region; right: m_T(W) distribution in the 0bjet control region. The 4 channels are summed. The hatched bands represent the total uncertainty on the prediction.

The figure 4.14 shows the post-fit central values and uncertainties of all the nuisance parameters included in the MLE. Nuisance parameters are ranked in decreasing order, based on the impact of a $\pm 1\sigma$ variation of their central values on the signal strength. The uncertainties related to the normalizations of the nonprompt muon and electron backgrounds have the largest impact on the final result, and contribute the most to the total systematic uncertainty. Other major sources of uncertainty are related to the choice of scale at parton shower level (2^{nd}), the light-flavour contamination in the derivation of b-tagging scale factors (4^{th}), the normalization uncertainty on the $t\bar{t}Z$ process (5^{th}), and the PDF uncertainty (6^{th}).

The nuisance parameter related to the normalization of the WZ+light-flavour jets

(ranked 21^{st}) has its central value shifted by about -1σ and its input uncertainty constrained by about half after the fit. This corresponds to a $\sim$ 30% decrease of the corresponding yield. A comparable deficit was observed for some jet multiplicities by a dedicated CMS measurement [270] of the WZ+jets production cross section, using the same dataset (see Fig. 2 of the reference). It was verified that this feature does not affect the results. First, as a simple cross check, the relative uncertainty on the WZ+light-flavour normalization is increased to 50%, and the final fit is repeated to verify that this does not impact its convergence. In addition, the pre-fit to the m_T(W) distribution in the 0jet control region (see Sec. 4.6) is repeated, with the WZ+light-flavour yield being fitted simultaneously with the NPL background yields. This results in a scale factor for this process (0.73 ± 0.11) very compatible with that obtained in the final fit. Finally, as can be seen in Fig. 4.8, it was verified that the data are well described in the WZ+light-flavour enriched region.

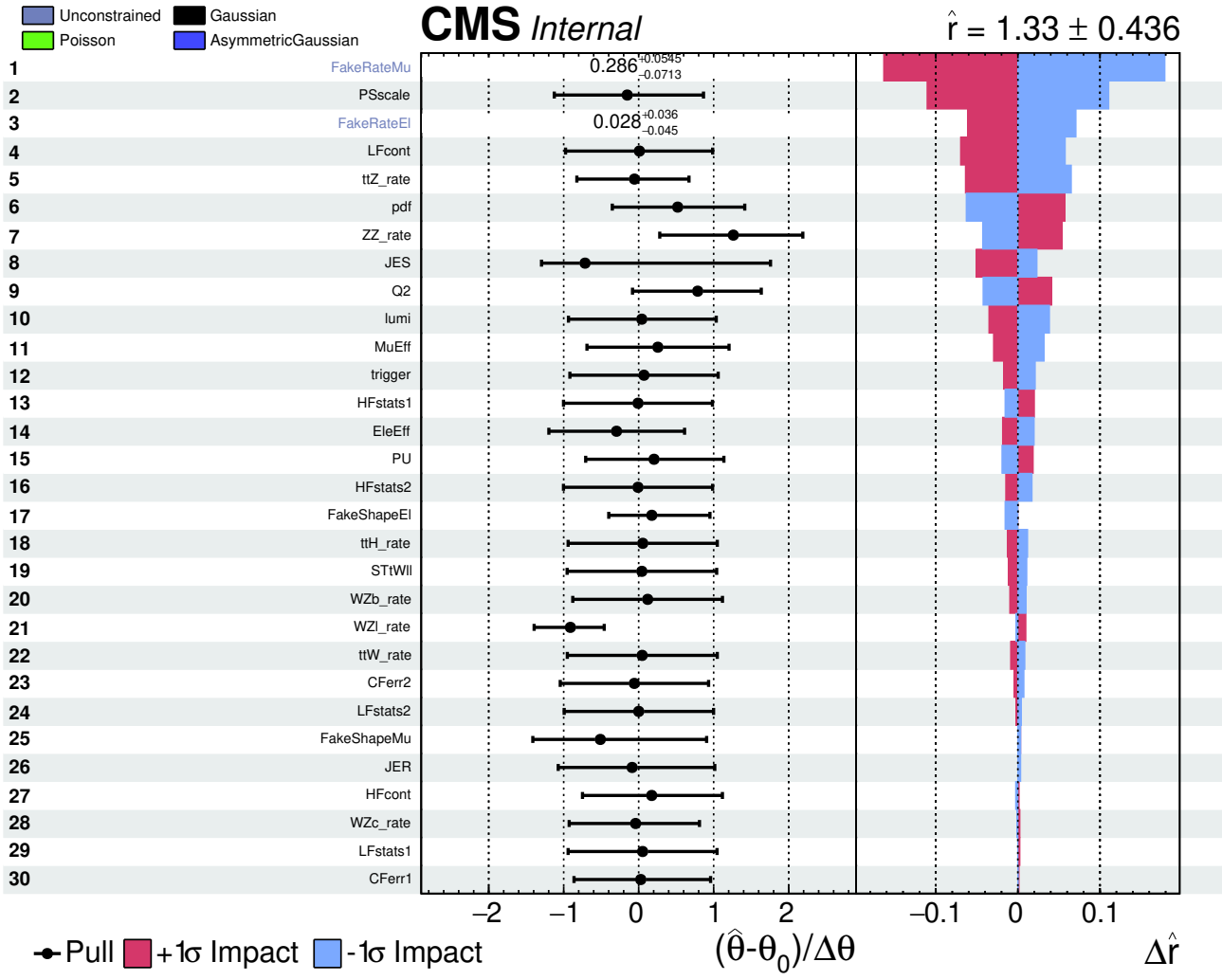

Figure 4.14: Post-fit central values (black dots) and uncertainties (error bars) of the nuisance parameters, compared to their pre-fit values. On the right-hand side, the impact $\Delta\mu$ of the variation of the central value of each nuisance parameter by $\pm 1\sigma$ on the signal strength is shown.

4.11 Cross-check and optimization studies

This section presents a selected subset of cross-check and optimization studies which I carried out to verify that the fit is robust and stable, and to try to improve the sensitivity of the analysis.

Cross-checks

As it was already mentioned, extensive studies were performed to guide the strategy regarding the NPL backgrounds, and verify its robustness. After the 2-steps procedure described in Sec. 4.6 was adopted, the analysis was repeated several times with different settings to quantify their impacts on the results. For instance:

- Alternative variables were used in the 0bjet region to obtain the pre-fit normalizations of the NPL backgrounds, while retaining the m_T(W) variable for the final fit. The invariant mass of the trilepton system m_{3l} and the $\not{E}_T$ variables were tried out, since they are expected to provide good separation between the WZ+jets and DY+jets processes as well;
- The use of single pre-fit renormalization scale factors per channel and NPL background was compared to the use of single scale factors per NPL background;
- In the pre-fit, it was tried to remove the constraints on the normalizations of the WZ+jets processes, or those of all backgrounds;
- In the final fit, instead of leaving the NPL normalizations freely floating, several fixed log-normal uncertainties were tried out. In particular, it was found that setting instead a large log-normal uncertainty of 100% independently for the nonprompt electrons and muons rates increased the observed signal strength by $\sim$ 10%, and its uncertainty by $\sim$ 5%. This is somewhat expected, as the signal and NPL backgrounds have similar BDT responses (see Fig. 4.13), and hence constraining (reducing) the normalizations of the NPL backgrounds increases that of the signal.

Overall, all these verifications confirmed that the adopted strategy regarding the NPL backgrounds is robust, and that the final results are very stable once the NPL backgrounds are reasonably under control.

Moreover, to investigate a possible bias of the fitting procedure related to the $t\bar{t}Z$ process, the analysis was repeated to measure simultaneously the tZq and $t\bar{t}Z$ cross sections. This leaves the observed results for the tZq signal unchanged within 1%.

Finally, the results were verified by a cut-and-count analysis carried out by CMS colleagues. It is based on the yields observed in regions close to those defined in the present analysis, and uses the same strategy to obtain the NPL background samples and their pre-fit normalizations. The results from both analyses are in agreement.

Optimization

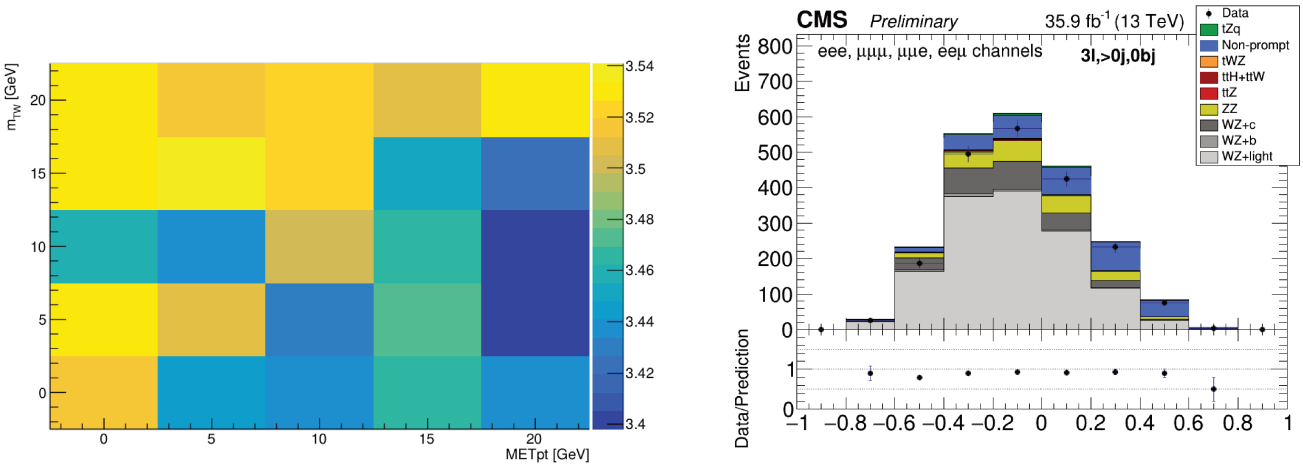

(a) (b)

Figure 4.15: (a) 2D scan of the expected significance as a function of minimum thresholds for $\not{E}_T$ and m_T(W). (b) Output of the BDT trained against NPL backgrounds in the 0bjet region, with the 4 channels summed.

The following is a succinct list of ideas which were tried out, but not adopted, with the aim of improving the analysis' sensitivity. The figure of merit which is to be maximised is the expected signal significance.

- **BDT design:** As was mentioned in Sec. 4.7.3, the lists of input variables of the BDTs trained in the 1bjet and 2bjets regions were optimized based on the final expected significance, as well as their hyperparameters. Moreover, the impact of the binning of the final distributions on the results is scanned independently in the 3 regions, from 10 to 40 bins. While some improvement is achieved, it was decided to keep on using 10 bins to avoid any issue related to low statistics. In addition, to try to better disentangle the NPL backgrounds (not included in the BDT training) from other processes in the signal region, it was tried to combine the BDT output and m_T(W) variable into a single discriminant. Events with low m_T(W) were then fitted using the m_T(W) distribution, while the other events were fitted using the BDT output.

- **$\not{E}_T$ and m_T(W) requirements:** To try to reduce the contaminations from NPL backgrounds, requirements are applied on the values of $\not{E}_T$ and m_T(W) in the 1bjet and 2bjets regions (not in the 0bjet region, since we want it to be populated with NPL backgrounds to constrain them). The result of a 2-dimensional (2D) scan of the expected significance is shown in Fig. 4.15 (a), with requirements on these variables ranging from > 0 to > 20 GeV by steps of 5 GeV. Since this is very CPU-intensive, only the dominant sources of systematic uncertainty are included.

- **BDT against NPLs in 0bjet region:** Contrary to the signal region, whose contamination by NPL backgrounds is not large enough to include them in the BDT training, the 0bjet region contains a sizeable number of events containing a NPL. Thus, a BDT dedicated to the discrimination of the NPL backgrounds (against all other processes) is trained in this region, to replace the m_T(W) variable. The list of input variables is the same as in the signal region, except those from the MEM (since it is not computed in this region), and those involving a b-tagged jet (since there is none). The figure 4.15 (b) shows the resulting distribution.

- **Split signal regions:** The 1bjet signal region is split into 2 categories, based on the presence of either 2 or 3 jets in the events, and BDTs are trained separately in each sub-category. The corresponding BDT responses can be seen in Fig. 4.16, for the sum of the 4 channels.

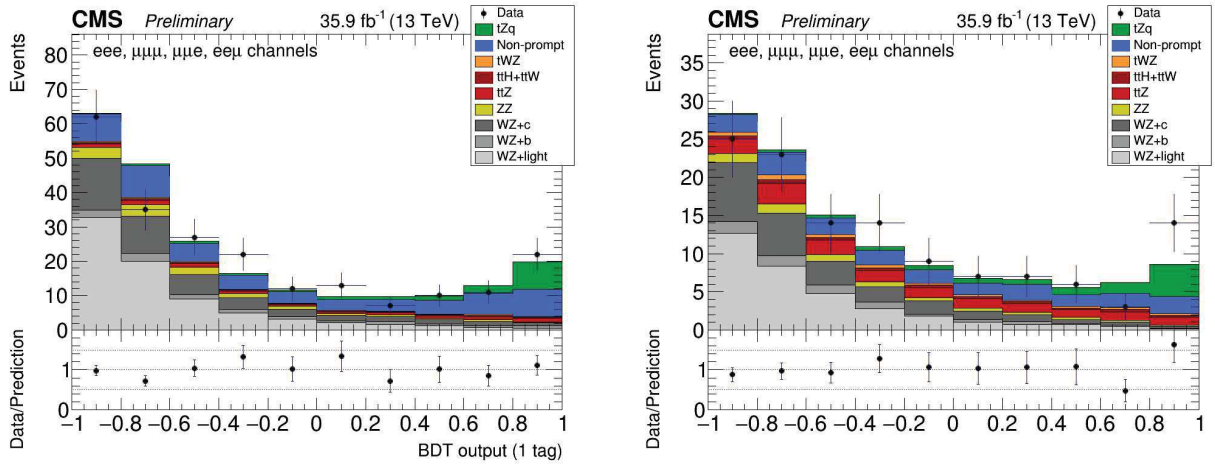

(a) (b)

Figure 4.16: Outputs of the BDTs trained with signal region events containing either (a) 2 or (b) 3 jets. The 4 channels are summed.

- **Additional jet category:** In order to try and retain a larger number of signal events, at the cost of a lower S/B ratio, an additional category containing a single jet which must be b-tagged (1j,1b) is included into the fit. Dedicated BDTs are trained in this category, using the same input variables as in the signal region, except those requiring the presence of at least 2 jets, or obtained from the MEM.

- **Lower lepton p_T thresholds & BDT against NPLs in signal region:** In order to verify whether the analysis could benefit from the use of looser requirements, the expected significance is computed for different p_T thresholds. Thresholds as low as 20/20/10 GeV were tested, resulting in an enhancement of the signal statistics by $\sim$ 40%, at the cost of a much larger NPL yield. As this modification impacts significantly the yields of the different processes in each region, different configurations are compared. For example the treatment of the NPL background is varied (use of a BDT instead of m_T(W) in the 0bjet region, including the NPL backgrounds in the

BDT trainings, etc.), and a tighter b-tagging working point is compared to the default. Moreover, since the NPL statistics increases significantly in the signal region, a BDT is trained specifically to separate the signal from the NPL backgrounds in this region. Then, only events which are sufficiently signal-like according to this BDT are retained for the final, default fit. To avoid overtraining, only a small subset of 5 input variables are used. One BDT was trained per channel, plus 1 in all channels. Figure 4.17 shows the output of the default BDT in the 1bjet signal region, before and after imposing a requirement on the value of the BDT trained against NPLs.

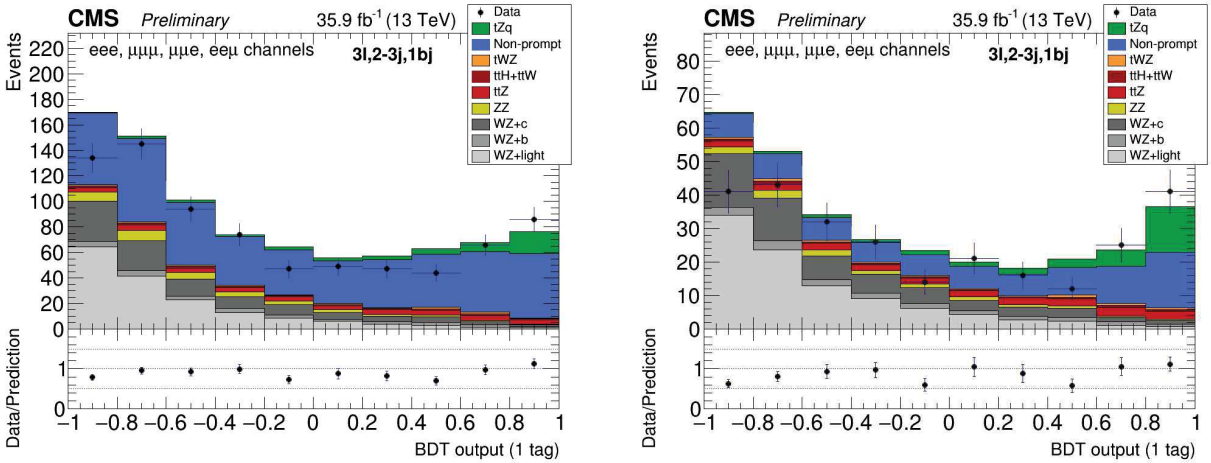

Figure 4.17: Output of the BDT in the signal region (a) before and (b) after imposing a requirement on a dedicated BDT trained to reject the NPL backgrounds, as explained in the text. The p_T requirements are loosened. The 4 channels are summed.

Overall, these studies did not yield any significant improvement on the expected significance, or decreased it, thus confirming that the design of the default analysis is already satisfying. The most promising idea was found to be the use of looser lepton p_T thresholds, associated with a requirement on the value of an additional BDT trained to separate tZq from the NPL backgrounds in the signal region ($\sim$ 10% gain). However, this modification to the analysis was not adopted because of time constraints and the need for MEM reprocessing.

4.12 Discussion

This analysis found the first evidence for the rare tZq process, corresponding to an observed (expected) significance of 3.7σ (3.1σ). The observed tZq signal strength $\mu = 1.31^{+0.35}_{-0.33}\,(stat)\,^{+0.31}_{-0.25}\,(syst)$ is compatible with the SM NLO prediction, and the sensitivity is mainly statistically-limited. The reference and observed cross sections are $\sigma^{SM}(pp \rightarrow$

$t\ell^+\ell^-q) = 94.2^{+1.9}_{-1.8}$ (scale) $\pm$2.50 (PDF) fb and $\sigma(pp \to t\ell^+\ell^-q) = 123^{+33}_{-31}$ (stat) $^{+29}_{-23}$ (syst) fb respectively. These results were published in the journal Physics Letter B [271].

Around the same period, an analysis [228] from the ATLAS collaboration targeting the same final state also reported an evidence for tZq production, with an observed (expected) significance of 4.2σ (5.4σ). This analysis uses a reference cross section $\sigma(pp \to tZq) = 800^{+6.1}_{-7.4}\%$ fb including all tZq final states. The reported measured cross section is $\sigma(pp \to tZq) = 600 \pm 170$ (stat) $\pm$140 (syst) fb, compatible with the prediction.

Apart from the difference due to the consideration of the $Z \to \ell\ell$ branching ratio ($\sim$ 10%) or not, the ATLAS reference cross section is computed in the 4-flavour scheme (instead of the 5-flavour scheme at CMS). Moreover, it does not account for non-resonant production (see Fig. 1.2.3) and interferences with off-shell Z/γ^* (and hence does not include the $m_{ll} > 30$ GeV requirement). Different renormalization scales were also adopted. For all but the latter point, regarding which more theoretical guidance is needed, numerous discussions within the LHC top quark community tended to validate the CMS approach. When accounting for all these differences, the cross sections of both analyses were found to be consistent.

Both analyses follow comparable strategies, based on MVA techniques to discriminate the signal and a binned MLE for signal extraction. While the present analysis uses BDTs and extracts the signal from 12 separate categories, the ATLAS analysis extracts the signal from a neural network (NN) discriminant in a single category. This category contains events with 3 electrons or muons having $p_T > 28/25/15$ GeV, among which an OSSF pair with $|m_{ll} - m_Z| < 10$ GeV. Events must contain exactly 2 jets with $p_T > 30$ GeV, among which exactly 1 b-tagged jet, and must satisfy $m_T(W) > 20$ GeV. Several reasons may explain the difference in expected significance between the 2 analyses, as summarised in the following.

First of all, an important difference is that the ATLAS analysis uses a leading-order signal sample rescaled to a NLO cross section, while the present analysis uses a sample generated at NLO accuracy. Since a sample generated at LO does not include additional QCD radiations, all signal events are generated with exactly 2 jets at matrix element level (i.e. the b-jet and the recoiling light jet). On the other hand, when using a NLO sample, a significant fraction (up to 30%) of signal events feature a 3^{rd} reconstructed jet, which is why the present analysis had to extract the signal from both the 2- and 3-jets categories. The "artificial" concentration of signal events in the 2-jets category may result in an overestimation of the expected significance, because it has a much larger S/B ratio than its 3-jets counterpart. Moreover, it is easier to correctly assign the jet coming from the top quark decay and the recoiling jet, which are used to build the most powerful input variables to the MVA.

The treatments of the NPL backgrounds also differ. In the ATLAS analysis, the contributions from the $t\bar{t}$ and DY+jets processes are separated. The shape of the $t\bar{t}$ process is taken from the MC simulation, and a renormalization scale factor is extracted from

a dedicated control region, with an uncertainty of $\sim$ 40%. The DY+jets process is estimated with a data-driven technique, and rescaled with a scale factor from a sideband region differing from the signal region only by the inversion of the m_T(W) requirement. Furthermore, this process is included in the training of the NN. This has a direct effect on the results, since the signal-like bins of the MVA discriminant are then much less contaminated by NPL backgrounds. On the contrary, the present analysis considers the flavour of the NPL rather than the process, leaves the NPL rates free in the fit, and does not include the NPL backgrounds in the training (low statistics).

Finally, the ATLAS analysis benefits from a better b-tagging algorithm, which achieves a comparable performance for a mistag rate about 10 times lower ($\epsilon_{btag} = 77\%$, $\epsilon_{mis} = 1\%$). This was at least the case in 2016, as ATLAS had already upgraded its pixel detector with an additional detection layer closer to the interaction point, while CMS did the same during the 2016–2017 winter shutdown. This comparative advantage contributes to the reduction of backgrounds with several b-jets such as $t\bar{t}Z$ or $t\bar{t}$, and in turn allows for looser lepton p_T thresholds and a tighter window on the Z boson mass. This results in increased signal statistics and purity.

A newer CMS analysis [229] combining the 2016 and 2017 datasets reported the first observation of the tZq process, with an observed (expected) significance of 8.2σ (7.7σ). While following closely the strategy of the present analysis, several improvements led to an important gain in sensitivity.

Most importantly, the cut-based approach for lepton identification (see Sec. 4.4) was replaced by the use of the BDT-based "lepton MVA" discriminant. It was developed in the context of searches for $t\bar{t}H$ and SUSY processes in multilepton final states, and allows for a much better rejection of NPLs. In addition, the use of a state-of-the-art DNN-based b-tagging algorithm leads to a more efficient background rejection.

These newer tools are used in the analyses presented in Chapter 5, and are described there. Although their use had been considered and advertised at the time by the authors of the present analysis, they could not be incorporated due to tight time constraints.

CHAPTER 5

Search for the associated production of a single top quark and a Higgs boson at $\sqrt{s}$ =13 TeV

This chapter presents a search for the associated production of a single top quark and a Higgs boson, denoted tH. The study uses a data sample of proton-proton collisions at $\sqrt{s}$ = 13 TeV recorded in 2017 by the CMS experiment, and targets the Higgs boson decays H $\to$ WW*, $\tau\bar{\tau}$ and ZZ*, in multilepton final states. Upper limits are derived on the combined tH + t$\bar{\text{t}}$H production cross section, and constraints are placed on the value of the top quark Yukawa coupling.

I implemented and performed the entire analysis, from the processing of the data up to the final results. This study is directly inspired by a previous CMS analysis based on the 2016 dataset [272], and follows closely the strategy and tools used by the t$\bar{\text{t}}$H search in multilepton final states based on the 2017 dataset [273]. This close connection between the tH and t$\bar{\text{t}}$H analyses will be emphasised throughout this chapter, and is desirable mainly for two reasons: firstly, the present analysis greatly benefits from state-of-the-art ingredients developped by the t$\bar{\text{t}}$H group; secondly, this will facilitate the planned combination of the two analyses, as discussed in Sec. 5.11.

A CMS colleague also performed this analysis as part of her PhD, using another independent framework developped by the $t\bar{t}H$ group. A considerable effort was dedicated to synchronize my framework with theirs. I have re-implemented all the selections of the tH and $t\bar{t}H$ analyses, so that I could also contribute to the latter. After verifying that all our results are in very good agreement (at %-level), we derived a single set of final results.

In addition, I re-adapted the main tH study in order to search for new physics in the associated production of a single top quark and a Higgs boson via flavour-changing neutral current (FCNC) interaction. I performed the entire analysis up to the final results, which represent the most stringent upper limits to date on the process under study.

These analyses and their results were reviewed and approved in the context of thesis endorsements carried out by the CMS Higgs and Top groups respectively. Both analyses were made blind, i.e. they were designed based on the MC simulation, and the data-to-simulation agreement was first verified in background-enriched control regions.

The first section consists in a broad introduction of the context and motivations for the study of the tH process. Next, the data and simulation samples are listed. The object identification and selection is described in Sec. 5.3, and the event selection in Sec. 5.4. Distributions obtained in the signal and control regions are shown in Sec. 5.5. Section 5.6 details the procedure for the estimation of reducible backgrounds. The signal discrimination based on a multivariate analysis, the treatment of systematic uncertainties and the signal extraction are described in Sec. 5.7-5.9. The results are presented in Sec. 5.10 and discussed in Sec. 5.11.

Finally, a search for FCNC interactions is presented in Sec. 5.12. After introducing its context and motivations, its differences with respect to the main analysis are highlighted. To conclude, the results are presented and discussed.

5.1 Introduction

Context

As was mentioned in the first chapter, the study of the Higgs boson is a core focus of the LHC physics programme. Precise measurements of its properties represent a crucial step towards the deeper understanding of the electroweak symmetry breaking mechanism and the underlying physics.

The Higgs boson discovered at a mass of 125 GeV has its couplings to gauge bosons and fermions precisely specified by the SM (see Fig. 1.14). The measurements of these couplings are usually expressed within the "κ-framework" [274]. This theoretical framework introduces a set of dimensionless *coupling modifiers* $\vec{\kappa}$ to parameterise possible deviations of the Higgs boson couplings to other particles with respect to SM predictions. For instance, the coupling modifier for a given production process i is defined as: $\kappa_i^2 = \sigma_i/\sigma_i^{SM}$. Hence, by construction, the current best available SM predictions on these parameters are recovered when all κ_i are equal to 1.

The absolute sign of κ_i does not have a physical meaning, while its *relative* sign compared to another coupling modifier κ_j does. Sensitivity to the relative sign of two couplings may only occur through interference terms. In the context of this work, the following coupling modifiers are of particular interest:

- The top quark to Higgs boson (or simply "top-Higgs") coupling modifier κ_t, defined from the ratio of the top quark Yukawa coupling with respect to its SM prediction: $\kappa_t^2 \equiv y_t / y_t^{SM}$;
- The vector boson to Higgs boson coupling modifier κ_V, defined such that $\kappa_V = \kappa_W = \kappa_Z$;
- The fermion to Higgs boson coupling modifier κ_F, defined such that $\kappa_F = \kappa_t = \kappa_b = \kappa_\tau$ (couplings of the Higgs boson to other fermions are negligible in the context of this work).

By convention, and without any loss of generality, this parameterisation assumes that κ_V is positive.

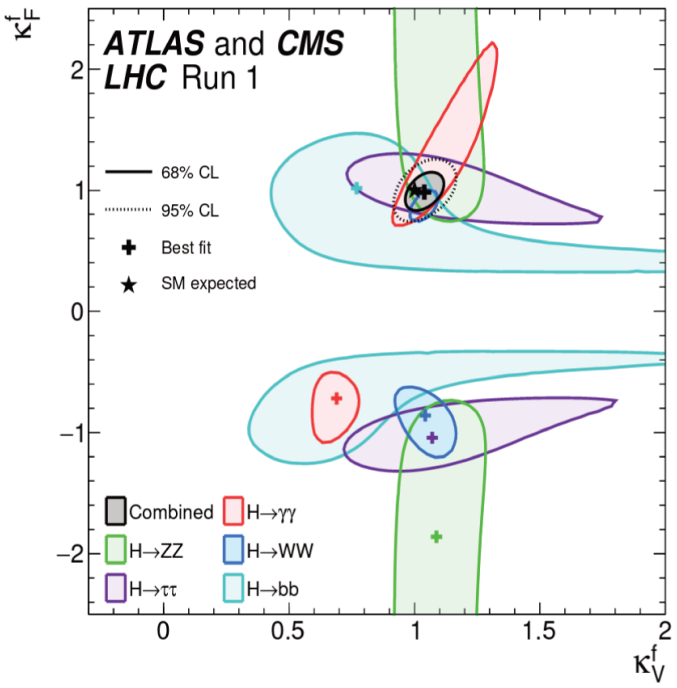

Figure 5.1: Negative log-likelihood contours at 68% and 95% CL in the (κ_V, κ_F) plane from the combination of ATLAS and CMS Run 1 results, in individual decay channels of the Higgs boson and their combination. Taken from Ref. [274].

Figure 5.1 shows the negative log-likelihood contours at 68% and 95% CL in the (κ_V, κ_F) plane, as obtained from the combination of ATLAS and CMS results at $\sqrt{s} = 8$ TeV in individual decay channels of the Higgs boson and their combination. Each channel provides a degenerate result, corresponding to the cases where $\kappa_F > 0$ and $\kappa_F < 0$.

The most useful decay channel to lift this degeneracy is $H \to \gamma\gamma$, due to the fact that this decay arises via loops which mostly involve top quarks and W bosons, creating a negative interference between the 2 coupling modifiers. Due to this interference, if the sign of $\kappa_F^{\gamma\gamma}$ were opposite to that of $\kappa_V^{\gamma\gamma}$, the branching ratio $\mathcal{B}(H \to \gamma\gamma)$ would be substantially larger than predicted in the SM.

The combination of all decay channels allows the exclusion of the opposite sign scenario by almost 5σ [274]. However, these results rely on the assumption that there exist no new particles entering the loops, and neglect any BSM decay. For example the $H \to \gamma\gamma$ decay channel is only sensitive to a *combination* of coupling modifiers, and any deviation in their individual values could be masked in the presence of BSM interactions impacting photon vertices. While the data collected by both experiments currently favour the SM scenario ($\kappa_F = \kappa_V = 1$), the anomalous case of a negative sign is still allowed if new physics contributions are considered.

Motivations

The study of the top quark Yukawa coupling y_t to the Higgs boson, predicted in the SM to be close to unity, is well motivated and could provide valuable insights regarding possible BSM extensions [275, 276]. The recently observed [86, 87] $t\bar{t}H$ process represents a privileged channel to probe y_t directly, without making any assumption about new physics. However, the $t\bar{t}H$ process is only sensitive to the magnitude $|y_t|^2$, not to the sign of this parameter.

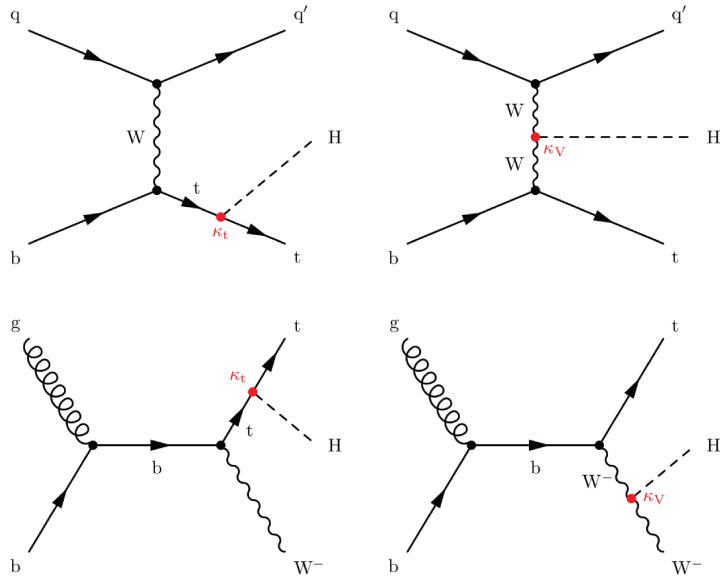

Figure 5.2: Leading-order Feynman diagrams for tHq (top) and tHW (bottom) production. It is indicated whether the κ_t or κ_V coupling modifier is involved. Taken from Ref. [277].

On the contrary, the associated production of a single top quark and a Higgs boson, denoted tH, is the only process sensitive at leading order to the magnitudes, relative sign and phase of the κ_t and κ_V coupling modifiers. Depending on whether the single top quark is produced via the t-channel or tW-channel (see Sec. 1.6.2), the process is referred to as tHq or tHW respectively. The s-channel has a negligible cross section and is not considered. The Higgs boson may couple either to the top quark or the W boson. Figure 5.2 shows leading-order Feynman diagrams corresponding to these processes, with the contributions from the coupling modifiers indicated.

In each channel, the diagrams involving κ_t and κ_V share the same final states, which yields a destructive interference term in the LO amplitude of the form $\mathcal{A} \propto (\kappa_t - \kappa_V)$. A qualitative formulation of the $Wb \to tH$ scattering amplitude is given in Ref. [278].

Within the SM ($\kappa_t = \kappa_V = 1$), both processes have small cross sections due to this destructive interference. However, a deviation from this point may result in an important increase of these cross sections. This is illustrated in Fig. 5.3, representing the dependence of the production cross sections of the tHq and tHW processes on the values of κ_t and κ_V. In particular, in the *inverted top coupling* (ITC) scenario wherein the Higgs boson coupling to vector bosons is equal to 1, but the sign of the top quark Yukawa coupling is flipped ($\kappa_t = -\kappa_V = -1$), the cross sections of the tHq and tHW processes are expected to increase tenfold.

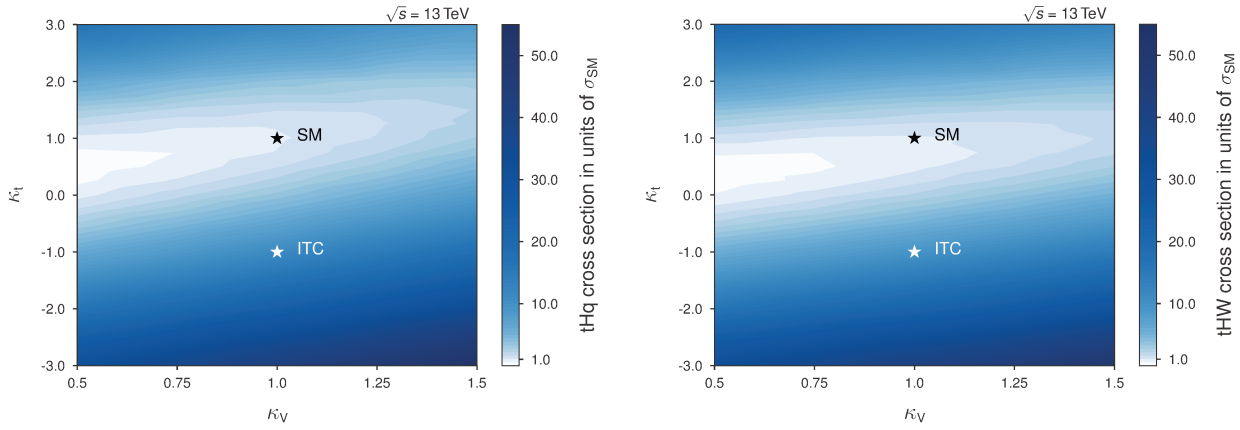

Figure 5.3: NLO production cross sections at $\sqrt{s} = 13$ TeV for the tHq (left) and tHW (right) processes in the κ_t -κ_V plane, expressed in terms of a multiplicative factor to the SM prediction. The points corresponding to the SM and inverted top coupling (ITC) scenarios are indicated. Taken from Ref. [277].

Table 5.1 lists the cross sections of the tHq, tHW and $t\bar{t}H$ processes in the SM and ITC scenarios at $\sqrt{s} = 13$ TeV. As the $t\bar{t}H$ process is not sensitive to the sign of the top quark Yukawa, its cross section is the same in both scenarios. It is noteworthy that in the ITC scenario, the tHq cross section would exceed that of $t\bar{t}H$ production and be well within reach of the current experimental sensitivity. The branching ratios of the different decay modes of the Higgs boson also vary with κ_t and κ_V.

Table 5.1: NLO productions cross sections at $\sqrt{s}$ = 13 TeV for the tHq, tHW and $t\bar{t}H$ processes, both in the SM and inverted top coupling (ITC) scenarios. The values are computed with MADGRAPH5_aMC@NLO and expressed in fb.

[fb]	SM	ITC
tHq	70.96	793
tHW	15.61	147
$t\bar{t}H$	507	507

Likewise, tH production is also sensitive to the possible CP-violating nature of the coupling between the top quark and the SM scalar Higgs boson (i.e. with spin-0, as supported by the current data), which can be encoded in the effective Lagrangian [279–281]:

$$\mathcal{L}_{CP}^{t} = -\bar{\psi}_t \left(\cos(\alpha)\, \kappa_{Htt}\, g_{Htt} + i\, \sin(\alpha)\, \kappa_{Att}\, g_{Att}\, \gamma^5 \right) \psi_t\, X_0 \ , \tag{5.1}$$

where X_0 labels a generic spin-0 particle with CP-violating couplings, α is the CP-mixing phase, $\kappa_{Htt,Att}$ are real dimensionless parameters rescaling the magnitudes of the CP-even and CP-odd couplings, and $g_{Htt} = g_{Att} = m_t/v$ with $v \sim 246$ GeV. In particular, for $\kappa_t = \kappa_V = 1$, the case $\alpha = 0$ corresponds to a pure CP-even (scalar) coupling and recovers the SM cross section, while the case $\alpha = \pi/2$ corresponds to a pure CP-odd (pseudoscalar) coupling. Any intermediate value signals CP violation, and $\alpha = \pi/4$ corresponds to a maximally CP-violating angle. A continous rotation in the scalar-pseudoscalar plane up to $\alpha = \pi$ recovers the tH cross section prediction of the ITC scenario.

Finally, similarly to the tZq process, the tH process is sensitive to the production of some FCNC processes which share similar final states. This is the focus of the analysis presented in Sec. 5.12. Therefore, the tH process possesses unique features, and the measurement of its cross section represents an important test of the SM as well as a possible gateway to new physics.

This analysis follows closely the strategy of the search for $t\bar{t}H$ in multilepton final states using 2017 data [273], and benefits from many ingredients developped by the $t\bar{t}H$ group. It is also directly inspired by the previous CMS tH analysis based on the 2016 dataset [272], which restricted the range of κ_t to [-1.25, 1.60] at 95% CL, assuming κ_V=1. Its combination with other CMS analyses targeting different decay modes of the Higgs boson allowed excluding values of y_t below about $-0.9 \times y_t^{SM}$ at 95% CL. This is assuming κ_V=1, and assuming no contribution from BSM physics in the other channels (e.g. H$\to \gamma\gamma$).

Signals and backgrounds

This analysis is specifically designed to have maximal sensitivity to the tHq process. Indeed, it has a cross section significantly larger than that of tHW, and it features a forward recoiling jet in its final state (like all t-channel processes) which can be used to discriminate backgrounds efficiently. On the opposite, the tHW process has kinematics

which resemble that of the $t\bar{t}H$ process, making it difficult to isolate. Ultimately, as described in Sec. 5.9, the tHq, tHW and $t\bar{t}H$ signals are fitted together in order to maximise the sensitivity to y_t.

The final states considered in this analysis contain either 2 same-sign leptons ($2\ell SS$) or 3 leptons (3ℓ), where ℓ stands either for electron or muon. Like in the tZq analysis, a smaller contribution is due to leptonically-decaying τ leptons. These final states target the leptonic decay of the top quark and the Higgs boson decays to WW^*, $\tau\bar{\tau}$ or ZZ^*, which respectively represent about 76%, 20% and 3.5% of the selected signal events.

The main irreducible backgrounds are the $t\bar{t}W$, $t\bar{t}Z$ and WZ+jets processes. As in the tZq analysis, all irreducible backgrounds containing prompt leptons are estimated from the MC simulation. The contribution from photon conversions to e^+e^- pairs is also estimated from simulated samples.

The $2\ell SS$ signature is quite rare among SM processes. The contamination from irreducible backgrounds is relatively limited in this channel, but nonprompt lepton backgrounds contribute substantially. In this channel, an additional background arises from the possible misidentification of the charge of a final state lepton. It is mostly due to the strongly asymmetric conversions of hard bremsstrahlung photons radiated by the initial lepton. This process is much more likely for electrons than muons.

In case the initial electron loses most of its energy to a radiated photon converting into an e^+e^- pair, and if the electron having a charge opposite to that of the initial electron carries most of the initial momentum or is the only one to be reconstructed, the resulting track will have a curvature opposite to that of the initial electron. As a result, its charge is misidentified. The nonprompt and charge misidentification reducible backgrounds are estimated from the data, with the procedures described in Sec. 5.6.

5.2 Datasets and simulated samples

Datasets and trigger selection

This analysis uses the full dataset collected in 2017 by CMS, which represents an integrated luminosity of 41.5 fb^{-1}. Events are selected by trigger algorithms relying on the presence of either 1 or 2 high-p_T leptons. In the 3ℓ channel, trilepton triggers are also included in the combination.

Differences in efficiency to pass the triggers for data and simulated events are corrected by reweighting simulated events with the corresponding ratio $\epsilon_{data}/\epsilon_{MC}$. These scale factors (SFs) are derived using samples of $Z/\gamma^* \rightarrow ee$ and $Z/\gamma^* \rightarrow \mu\mu$ events, recorded with $\vec{E}_T$ triggers uncorrelated with lepton triggers. Their values and uncertainties are listed in Table 5.2, as provided by the $t\bar{t}H$ group.

Table 5.2: Trigger efficiency scale factors applied to simulated events, and their uncertainties related to the limited statistics of the data and simulated samples.

Channel	Leading lepton p_T	Scale factor
eμ	< 35 GeV	0.952 ± 0.008
	$35 < p_T \leq 50$ GeV	0.983 ± 0.003
	≥ 50 GeV	1.000 ± 0.001
$\mu\mu$	< 35 GeV	0.972 ± 0.006
	≥ 35 GeV	0.994 ± 0.001
ee	< 30 GeV	0.937 ± 0.027
	≥ 30 GeV	0.991 ± 0.002
3ℓ	–	1.000 ± 0.050

Monte Carlo samples

The tHq, tHW and $t\bar{t}H$ samples are generated with a set of per-event weights corresponding to different values of the κ_t and κ_V coupling modifiers and the CP-violating angle α. The tHq and tHW signal events are generated with MADGRAPH5_aMC@NLO at LO precision, and are normalized to NLO cross sections. The $t\bar{t}H$ process and the major $t\bar{t}Z$ and $t\bar{t}W$ backgrounds are generated with MADGRAPH5_aMC@NLO at NLO precision, and are normalized to NLO cross sections. The tHq and $t\bar{t}H$ samples are generated in the 4FS, while the tHW sample is generated in the 5FS to avoid interferences with $t\bar{t}H$ at LO[1] [280]. The NNPDF3.0 [225] PDF set is used.

Other minor backgrounds are simulated at NLO or LO precision using the POWHEG, MADGRAPH or PYTHIA generators, and scaled to their NLO cross sections when available. All generated events are interfaced with PYTHIA for the parton showering and hadronization. The MC simulation samples used to model the signal and the irreducible backgrounds are listed in Table 5.3 with their input cross sections and generators indicated.

5.3 Object identification and reconstruction

5.3.1 Leptons

The aim of the object identification and reconstruction is to select prompt electrons and muons originating from the decay of a W boson, Z boson or τ lepton, while rejecting nonprompt leptons (NPLs) and electrons arising from photon conversion. Following the approach used by the $t\bar{t}H$ group, leptons are categorised as *loose*, *fakeable* or *tight* leptons. These lepton categories are used respectively for preselection, estimation of the NPL background, and for final results. By construction, tight leptons are also fakeable, and fakeable leptons are also loose.

[1]For example, a singly-resonant $t\bar{t}H$ diagram produces the final state $t(bW)H$. This would interfere with a LO Feynman diagram for tHW production in the 4FS featuring a spectator b quark, producing the equivalent final state $tHW(b)$.

Table 5.3: Simulated samples used in the analysis with the corresponding generators and normalization cross sections, accounting for the relevant branching ratios.

Process	MC generator	σ [pb]
$pp \to tHq$	MADGRAPH5_aMC@NLO	0.071
$pp \to tHW$	MADGRAPH5_aMC@NLO	0.016
$pp \to t\bar{t}H$	MADGRAPH5_aMC@NLO	0.51
$pp \to t\bar{t}Z, t\bar{t} \to 2\ell 2\nu 2b$		
$m_{\ell\ell} > 10$ GeV	MADGRAPH5_aMC@NLO	0.25
$1 < m_{\ell\ell} < 10$ GeV	MADGRAPH5_aMC@NLO	0.053
$pp \to t\bar{t}W + jets, W \to \ell\nu$	MADGRAPH5_aMC@NLO	0.20
$pp \to t\bar{t}WW$	MADGRAPH	0.012
$pp \to WZ \to 3\ell\nu$	MADGRAPH5_aMC@NLO	5.06
$pp \to Z\bar{Z} \to 4\ell$	POWHEG	1.26
$pp \to tZq, Z \to \ell\ell$	MADGRAPH5_aMC@NLO	0.076
Rares		
$pp \to ggH, H \to Z\bar{Z} \to 4\ell$	POWHEG	0.012
$pp \to VH, H \nrightarrow b\bar{b}$	MADGRAPH5_aMC@NLO	0.96
$pp \to t\bar{t}t\bar{t}$	MADGRAPH5_aMC@NLO	0.0091
$pp \to t\bar{t}tW$	MADGRAPH	0.00073
$pp \to t\bar{t}WH$	MADGRAPH	0.0011
$pp \to tWZ, Z \to \ell\ell$	MADGRAPH	0.011
$pp \to WW$ (Double scattering)	MADGRAPH	1.92
$pp \to WW + jj$ (EWK)	MADGRAPH	0.037
$pp \to WWW$	MADGRAPH5_aMC@NLO	0.21
$pp \to WWZ$	MADGRAPH5_aMC@NLO	0.17
$pp \to WZ\gamma$	MADGRAPH5_aMC@NLO	0.043
$pp \to WZZ$	MADGRAPH5_aMC@NLO	0.056
$pp \to ZZZ$	MADGRAPH5_aMC@NLO	0.014
γ-conversions		
$pp \to t\bar{t}\gamma + jets$	MADGRAPH5_aMC@NLO	4.09
$pp \to t\gamma + jets$	MADGRAPH5_aMC@NLO	1.02
$pp \to tW + jets, W \to \ell\nu$	MADGRAPH	14560
$pp \to Z + jets, Z \to \ell\ell$	MADGRAPH	1343

Loose leptons are preselected first, before more stringent criteria are applied to identify fakeable and tight leptons. Electrons found within a cone of radius ΔR< 0.3 around any preselected muon are removed. The same applies for hadronic taus reconstructed within ΔR< 0.3 of any preselected lepton. Hadronically-decaying τ leptons are only reconstructed in this analysis for the purpose of removing closeby jets, as mentioned later in this section. They are required to satisfy a very loose working point of a MVA-based discriminant, following official CMS recommandations.

Selection criteria

Muons are considered if they have $p_T > 5$ GeV and $|\eta| < 2.4$, and electrons if they have $p_T > 7$ GeV and $|\eta| < 2.5$. The selection criteria corresponding to the loose, fakeable and tight categories are listed in Tables 5.4 and 5.5, for muons and electrons respectively. The categorisation is based on several variables such as: the longitudinal and transverse impact parameters of the lepton's track relative to the primary vertex (d_z and d_{xy}); the significance of the 3-dimensional impact parameter of the lepton's track relative to the primary vertex (SIP_{3D}); the lepton relative isolation I_{rel} with p_T -dependent cone size and pileup mitigation (see Sec. 4.4); the ratio of the lepton p_T divided by the p_T of the closest jet ($p_T^{ratio} = p_T^{\ell}/p_T^{j}$); the discriminant value of the DeepCSV b-tagging algorithm for the closest jet.

Table 5.4: Selection criteria used to identify and categorise muons, as described in the text. Criteria marked with a † are only applied to muons failing the lepton MVA cut, introduced later in this section.

Requirement	Loose	Fakeable object	Tight
$\|\eta\| < 2.4$	✓	✓	✓
p_T	> 5 GeV	> 10 GeV	> 10 GeV
$\|d_{xy}\| < 0.05$ (cm)	✓	✓	✓
$\|d_z\| < 0.1$ (cm)	✓	✓	✓
$I_{rel} < 0.4$	✓	✓	✓
Loose PF muon	✓	✓	✓
p_T^{ratio}	–	> 0.6† / –	–
Jet CSV	–	< 0.07† / < 0.4941	< 0.4941
Segment compatibility	–	> 0.3† / –	–
Medium PF muon	–	–	✓
Lepton MVA > 0.90	–	–	✓

Furthermore, muons may be required to be associated with track segments in the muon system compatible with the expected pattern for a minimum ionising particle ("segment compatibility"). Electrons may be required to satisfy quality criteria regarding the width in η of the corresponding ECAL cluster ($\sigma_{i\eta i\eta}$), the ratio of the HCAL and ECAL energies associated with the electron (H/E), the difference between the reciprocal of the cluster energy of the electron and the reciprocal of its track momentum (1/E - 1/p), the response of a BDT trained to separate electrons from jets ("MVA ID", provided by the CMS e-γ group), and a photon conversion veto.

Table 5.5: Selection criteria used to identify and categorise electrons, as described in the text. Values given in the form (a,b,c) correspond to the ranges $|\eta| \leq 0.8$, $0.8 < |\eta| \leq 1.479$, and $1.479 < |\eta| \leq 2.5$.

Requirement	Loose	Fakeable	Tight
$\lvert\eta\rvert < 2.5$	✓	✓	✓
p_T	> 7 GeV	> 10 GeV	> 10 GeV
$\lvert d_{xy}\rvert < 0.05$ (cm)	✓	✓	✓
$\lvert d_z\rvert < 0.1$ (cm)	✓	✓	✓
$SIP_{3D} < 8$	✓	✓	✓
$I_{rel} < 0.4$	✓	✓	✓
MVA ID	$> (-0.86, -0.81, -0.72)^1$	$> (-0.86, -0.81, -0.72)^2$	$> (-0.86, -0.81, -0.72)^2$
$\sigma_{i\eta i\eta} < (0.011, 0.011, 0.030)$	–	✓	✓
H/E < 0.10	–	✓	✓
$-0.04 <$ 1/E-1/p	–	✓	✓
Conversion rejection	–	✓	✓
p_T^{ratio}	–	> 0.6† / –	–
Jet CSV	–	< 0.07† / < 0.4941	< 0.4941
Number of missing hits	< 2	$== 0$	$== 0$
Lepton MVA > 0.90	–	–	✓

[1] : $> (-0.13, -0.32, -0.08)$ if $p_T < 10$ GeV
[2] : > 0.50 if electron MVA ID > 0.90

In the $2\ell SS$ final state, additional "tight charge" criteria related to the quality of the charge measurement are applied to reduce the contribution from the charge misidentification background. For electrons, the independent charge measurements provided by the ECAL and the tracker must be consistent, while muons are required to have a well-measured p_T ($\Delta p_T / p_T < 0.2$). To reduce the contribution from electrons originating from photon conversions, electrons are rejected if they miss hits in the innermost tracker layers, or if they are associated with a successfully reconstructed conversion vertex [282].

In order to reduce potential biases of the NPL background estimation described in Sec. 5.6, the p_T of leptons which fail the tight criteria while satisfying the fakeable criteria is set to 0.9 times the p_T of the closest jet; in case the lepton and jet are separated by $\Delta R > 0.4$, the p_T of the fakeable lepton is instead set to $p_T^{\ell} = p_T^{\ell}/(p_T^{\ell} + I_{rel}^{\ell})$, cf. Eq. 2.5, and other variables depending on the closest jet are set to 0. This procedure mitigates the dependence of the NPL estimation on the p_T of the parent of the NPL, and thereby improves the accuracy of the method.

Lepton MVA discriminator

The most important criterion to identify prompt leptons is a BDT-based multivariate discriminant, referred to as *lepton MVA*. It was developed by the $t\bar{t}H$ group and is now also used in the CMS Top quark working group, notably in the tZq and $t\bar{t}Z$ analyses. It optimally combines different variables to discriminate prompt leptons from nonprompt leptons (NPLs).

The training is performed separately for electrons and muons. The BDT is trained using "signal" prompt leptons from an inclusive $t\bar{t}H$ LO sample, and "background" leptons from semileptonic $t\bar{t}$ decays. Signal leptons must be matched to prompt leptons at the generator-level, while background leptons must not be matched to a prompt lepton. The input variables of this BDT are:

1. The lepton p_T ;
2. The lepton η;
3. SIP_{3D};
4. d_z;
5. d_{xy};
6. The lepton isolation with respect to charged particles (within a cone of variable radius $0.05 \leq \Delta R \leq 0.2$, depending on the lepton p_T);
7. The lepton isolation with respect to neutral particles (idem);
8. The response of the DeepCSV b-tagging algorithm for the closest jet;
9. The number of charged particles within the closest jet;
10. The component of the lepton momentum transverse to the direction of the closest jet;
11. p_T^{ratio};
12. (a) For electrons only: the MVA ID discriminant;
    (b) For muons only: the segment compatibility.

The very good performance of the lepton MVA algorithm is illustrated in Fig. 5.4. In particular, it can be noted that it outperforms the standard recommended cut-based (CB) approach, whose tight working point (WP) was used in the tZq analysis presented in Chapter 4.

For instance, for a signal efficiency comparable to that of the CB tight WP, the lepton MVA algorithm achieves a lower misidentification rate by a factor 3 to 4. For muons, contrary to the CB tight WP which corresponds to a high signal efficiency but also a high misidentification rate, the lepton MVA algorithm is typically used at a WP corresponding to a signal efficiency around 80% for a low misidentification rate of about 1%.

Lepton selection efficiency

The efficiency for leptons to pass the loose and tight selection criteria were measured by the $t\bar{t}H$ group in samples of $Z/\gamma^* \rightarrow ee$ and $Z/\gamma^* \rightarrow \mu\mu$ events. They are parameterised as a function of the lepton p_T and η, separately for electrons and muons. In a first step, the efficiency for leptons to pass the loose pre-selection is measured. Then, the conditional probability for loose leptons to also pass the tight selection is measured. In each step, the ratio of the efficiency measured in data divided by the efficiency in the MC simulation yields a scale factor:

$$\rho(p_T, \eta) = \frac{\epsilon_{data}(p_T, \eta)}{\epsilon_{MC}(p_T, \eta)} \, . \tag{5.2}$$

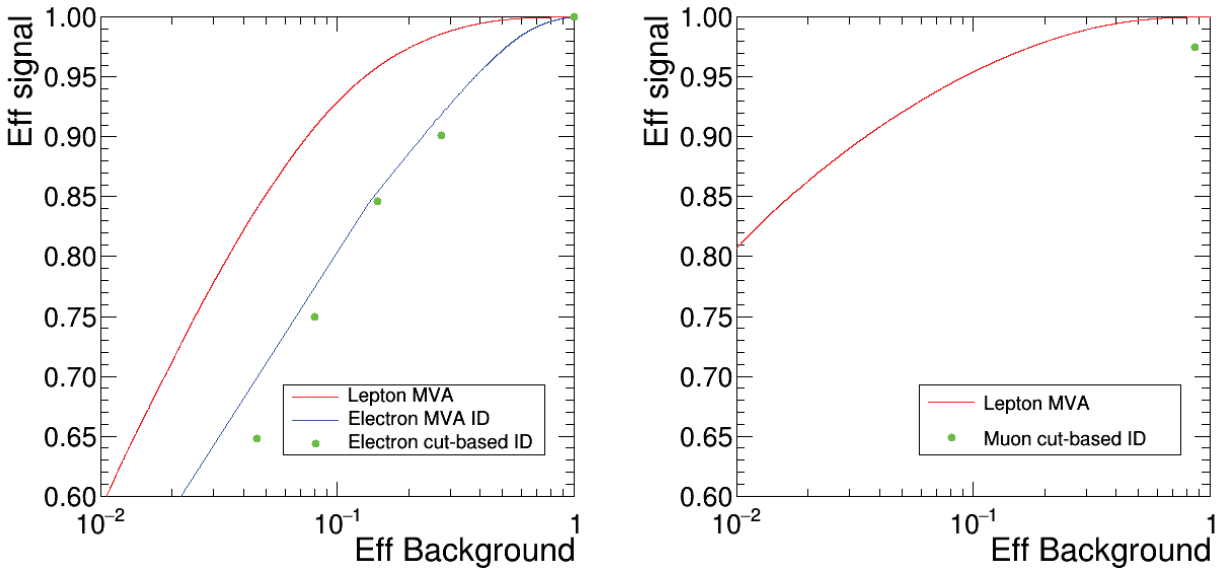

Figure 5.4: Comparison of the performance of several prompt lepton identification algorithms, for electrons (left) and muons (right). The BDT-based lepton MVA algorithm is used in this analysis, and includes the electron MVA ID discriminant as input variable. The *veto*, *loose*, *medium* and *tight* working points of the cut-based approach are indicated for electrons; its tight working point is indicated for muons. The y and x axes represent the identification efficiency for prompt leptons and the misidentification rate for NPLs respectively, in the simulation. Only leptons passing the *loose* requirements are considered. Figures produced by S. Sanchez Cruz.

The scale factors related to the loose selection are applied both to loose and fakeable leptons. Finally, simulated events are reweighted by the product of all scale factors for each selected lepton:

$$\rho = \prod_{j}^{leptons\ eff.} \prod_{i} \rho_i(p_T^j, \eta^j). \tag{5.3}$$

5.3.2 Jets and b-tagging

Selection

This analysis uses jets reconstructed with the anti-k$_T$ algorithm (ΔR = 0.4). Selected jets must satisfy $p_T > 25$ GeV and $|\eta| < 5.0$. Large-η jets are considered due to the expected presence of a forward jet in the tHq final state. For the purpose of matching jets to leptons, a lower threshold $p_T > 15$ GeV is used. Jets are required to satisfy officially-recommended tight identification criteria, listed in Table 5.6. Selected jets must be separated from any fakeable lepton and hadronic τ candidate by $\Delta R > 0.4$.

To mitigate the noise issue already mentioned in Chapter 4, jets found in the calorimeter transition region $2.7 < |\eta| < 3.0$ with $p_T < 60$ GeV are rejected. This veto criterion was found to significantly improve the data-to-MC agreement, while retaining most signal events.

Table 5.6: Recommended selection criteria applied to jets. They are related to the multiplicities and energy fractions of neutral and charged constituents of the jets.

Variable	$\|\eta\| \leq 2.4$	$2.4 < \|\eta\| \leq 2.7$	$2.7 < \|\eta\| \leq 3.0$	$\|\eta\| > 3.0$
Neutral hadron fraction	< 0.90	< 0.90	–	> 0.02
Neutral EM fraction	< 0.90	< 0.90	$0.02 < x < 0.99$	< 0.90
Number of constituents	> 1	> 1	–	–
Number of neutral particles	–	–	> 2	> 10
Charged hadron fraction	> 0	–	–	–
Charged multiplicity	> 0	–	–	–

B-tagging

Jets originating from a b quark are tagged using the DeepCSV algorithm [185]. This algorithm achieves significantly better performance than previous algorithms like CSVv2 (see Fig. 2.16), which was used in the tZq analysis. While using the same input variables, the DeepCSV algorithm is based on a deep neural network (DNN) and takes advantage of important advances in this field.

Thanks to this newer algorithm and the upgrade of the CMS pixel detector during the 2016–2017 shutdown, an improvement of about 10–15% is obtained with respect to the b-tagging efficiency of the 2016 analysis presented in Chapter 4, for a similar misidentification rate. This is comparable to the b-tagging performance achieved by ATLAS [283]. Since then, the newer DeepJet algorithm has been developed, which further improves the b-tagging efficiency by about 5–10% [284].

Jets are considered as b-tagged jets if they satisfy the medium working point (WP) of the algorithm and have $|\eta| < 2.4$, or as light jets if they fail the loose WP. These working points correspond to misidentification probabilities of 1% and 10% respectively.

Corrections

Differences in the b-tagging performance between data and simulation are corrected by applying per-jet weights to simulated events, depending on the jet p_T, η, flavour (from MC truth) and score of the b-tagging discriminant. The per-event weight corresponds to the product of all per-jet weights, including those of the jets matched to leptons.

Moreover, corrections are applied to simulated events to mitigate the so-called *L1 trigger prefiring* issue in the 2017 dataset, following official recommandations. This issue, not accounted for in the MC simulation, notably resulted in a lower efficiency for events containing forward jets depositing a significant amount of energy in the ECAL region $2 < |\eta| < 3$.

5.4 Event selection

The figure 5.5 shows Feynman diagrams for tHq production in the 3ℓ and $2\ell SS$ final states. In both cases, the distinctive signature for the signal consists in isolated leptons mostly from W boson decays, missing energy arising from the undetected neutrino(s),

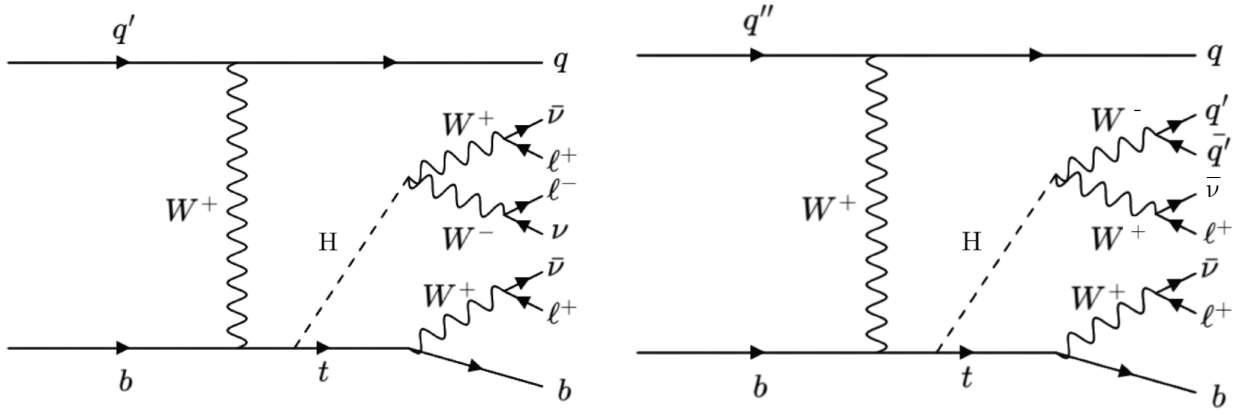

Figure 5.5: Leading-order Feynman diagrams for tHq production in the 3ℓ (left) and $2\ell SS$ (right) final states.

a light jet emitted preferentially in the forward region, and a b-jet from the top quark decay.

Provided that they pass the trigger selection, signal region (SR) events are required to satisfy the following criteria:

- Any pair of loose leptons must have an invariant mass larger than 12 GeV (to reject low-mass resonances);
- The event must contain ≥ 1 b-tagged jet(s);
- The event must contain ≥ 1 light jet(s).

Three leptons (3ℓ)

In the 3ℓ signal region, events must additionally satisfy the following criteria:

- The event contains exactly 3 tight leptons;
- The sum of the tight leptons' charges equals ± 1;
- The leading, sub-leading and trailing tight leptons must have p_T above 25, 15 and 10 GeV respectively;
- The event must not contain any opposite-sign same-flavour (OSSF) pair of loose leptons having an invariant mass within 15 GeV around the Z boson mass ($|m_{\ell\ell} - m_Z| > 15$ GeV, mostly to reduce the $t\bar{t}Z$ and WZ+jets backgrounds).

Two same-sign leptons (2ℓss)

In the $2\ell SS$ signal region, events must additionally satisfy the following criteria:

- The event contains exactly 2 tight same-sign leptons;

- The leading and sub-leading tight leptons must have p_T above 25 and 15 GeV respectively;
- The tight leptons must satisfy tight charge criteria.

Depending on the flavours of the tight leptons, the $2\ell SS$ channel is further split into the $\mu\mu$ and μe channels. The dielectron channel is neglected due to its low sensitivity, and the 3ℓ channel is not split due to its lower statistics.

5.5 Control regions

Control regions (CRs) are defined with selections similar to the signal regions, but with some criteria modified in order to enhance the contributions from specific background processes. They are used to inspect the data-to-MC agreement for the main backgrounds, and the modeling of the input variables used in the MVA. The CRs are defined as follows:

- ***ttZ* CR:** This region is enriched in $t\bar{t}Z$ events. It differs from the 3ℓ SR by the requirement for events to contain an OSSF lepton pair within 10 GeV around the Z boson mass. In addition, events must contain $\geq$ 2 jets within $|\eta| < 2.4$, among which $\geq$ 2 jets are tagged with the loose WP of the b-tagging algorithm or $\geq$ 1 is tagged with the medium WP;
- **WZ CR:** This region is enriched in WZ+jets events. It differs from the 3ℓ SR by the requirement for events to contain an OSSF lepton pair within 10 GeV around the Z boson mass. In addition, events must contain $\geq$ 2 jets within $|\eta| < 2.4$, among which $\leq$ 1 jets is tagged with the loose WP of the b-tagging algorithm and none is tagged with the medium WP;
- **Same-sign dilepton CR:** This region differs from the $2\ell SS$ SR by vetoing events containing a light jet beyond $|\eta| > 2$, to enhance the contribution from the $t\bar{t}$ background. To blind the signal region of the $t\bar{t}H$ search, events with $\geq$ 4 central jets are also rejected.

A summary of the main differences between the signal and control regions is given in Table 5.7. Data-to-MC comparison for different variables are shown in each CR in Fig. 5.5.

5.6 Data-driven estimation of the reducible backgrounds

This section describes the data-driven procedures for the estimation of the nonprompt and charge misidentification reducible backgrounds. Both these contributions are estimated based on the so-called "ABCD method", which relies on the application of appropriately chosen per-event weights, as described below. The design of these procedures and the parameterisation of the event weights were carried out by the $t\bar{t}H$ group. I used these weights to estimate the reducible backgrounds in the specific regions of this analysis.

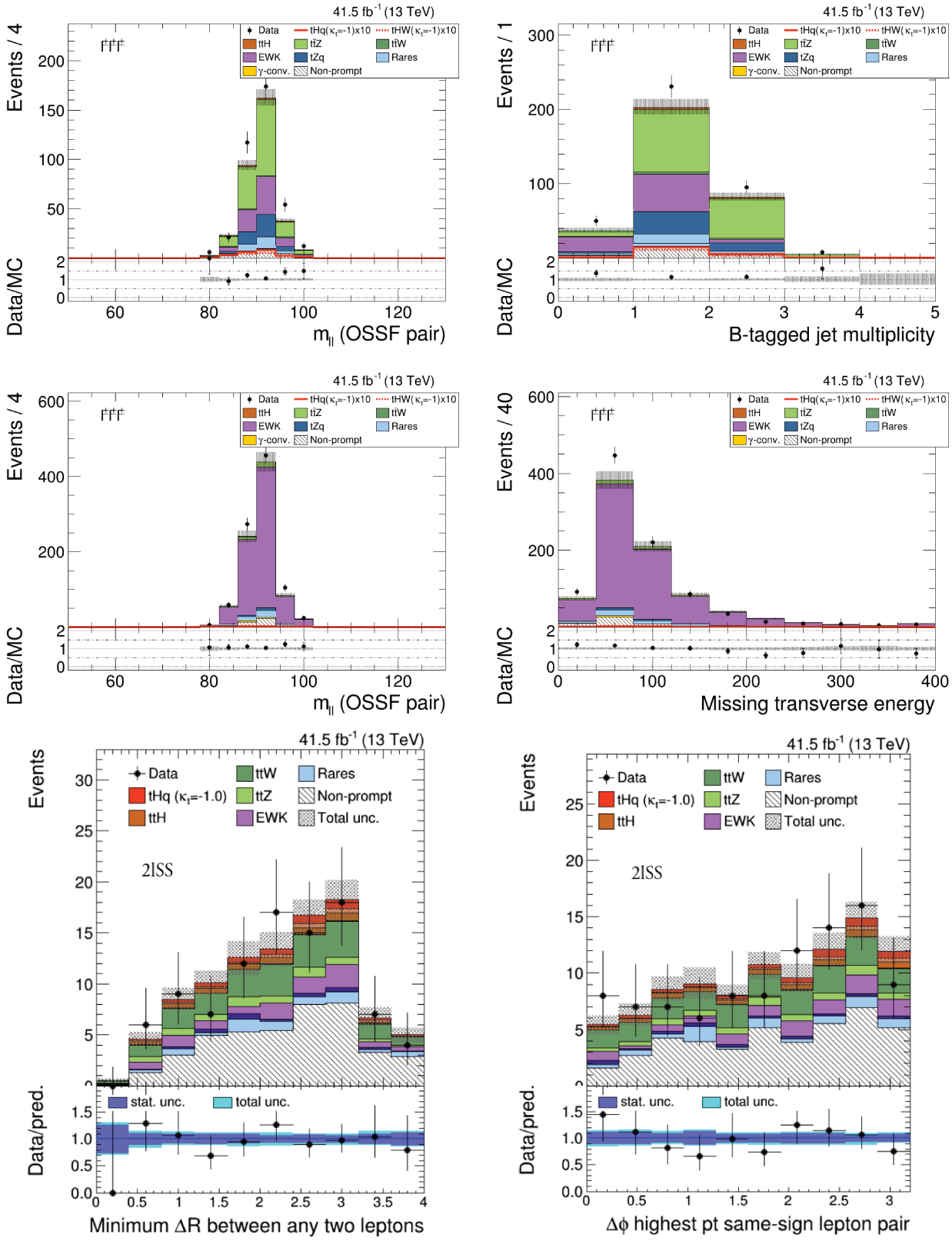

Figure 5.6: Pre-fit data-to-prediction comparisons in the $t\bar{t}Z$ CR (top), WZ CR (middle) and same-sign dilepton CR in the $\mu\mu$ channel (bottom) for different variables. Throughout this chapter, the hatched bands represent the total uncertainty on the simulation. The WZ and ZZ backgrounds are denoted "EWK" (electroweak). The 2 bottom figures were produced within the framework of the $t\bar{t}H$ group.

Table 5.7: Summary of the different requirements between signal and control regions.

Region	Description
$2\ell SS$ SR	2 same-sign leptons $\geq$ 1 b-jet, $\geq$ 1 light jet
3ℓ SR	3 leptons $\geq$ 1 b-jet, $\geq$ 1 light jet $\lvert m_{\ell\ell} - m_Z \rvert > 15$ GeV
$t\bar{t}Z$ CR	3 leptons $\geq$ 2 central jets, $\geq$ 2 loose b-tagged jets or $\geq$ 1 medium b-tagged jet $\lvert m_{\ell\ell} - m_Z \rvert < 10$ GeV
WZ CR	3 leptons $\geq$ 1 central jet, $\leq$ 1 loose b-tagged jet and no medium b-tagged jet $\lvert m_{\ell\ell} - m_Z \rvert < 10$ GeV
$2\ell SS$ CR	2 same-sign leptons $\geq$ 1 b-jet, $\geq$ 1 light jet $\leq$ 4 jets, no light jet with $\lvert\eta\rvert > 2$

5.6.1 Nonprompt background

The basic principle of the ABCD method is illustrated in Fig. 5.7. It relies on the definition of 4 regions in the 2-dimensional plane spanned by orthogonal variables: the *application region* (AR) A, the signal region B, and the *measurement regions* (MR) C and D. The variables must be chosen such that the AR and MR are enriched in the background of interest.

Then, the number of events N_B due to this background in the SR can be estimated by measuring a given "transfer factor", which relates the yields of this background in the regions C and D, and extrapolating it to the AR: $N_B = N_A \times (N_D / N_C)$. This data-driven method has the advantage that, while the AR and SR are analysis-dependent, the transfer factors measured in the MR can be used in many different analyses. There is a separate application region defined for each signal and control region.

In the present case, the transfer factor of interest corresponds to the probability for NPLs to be misidentified as tight leptons, commonly referred to as *fake rate* (FR). It is measured in a sample enriched in QCD multijet events, which are required to contain exactly 1 fakeable lepton and at least 1 jet separated by ΔR$>$ 0.7. The FR is measured separately for electrons and muons in bins of p_T and η. For each bin, the FR is calculated from the number N_{pass} of multijet events whose fakeable lepton satisfies the tight criteria, and the number N_{fail} of remaining multijet events:

$$\mathrm{FR}(p_T, \eta, \text{flavour}) = \frac{N_{pass}}{N_{pass} + N_{fail}}. \tag{5.4}$$

The number of multijet events N_{pass} and N_{fail} are inferred by performing a maximum likelihood fit to the data with several simulated templates (QCD multijet, Z+jets, W+jets,

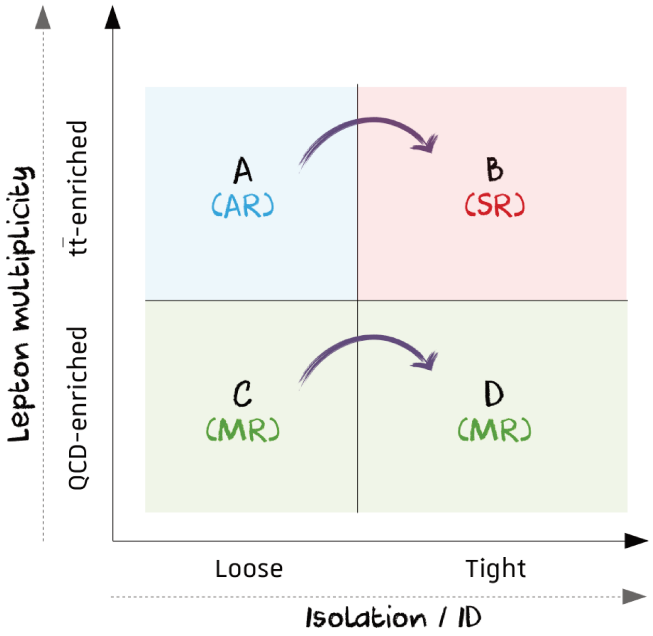

Figure 5.7: Illustration of the ABCD method, described in the text. The variable on the y-axis is chosen such that it defines different regions enriched with different physics processes. Rescaling weights are derived in the measurement region (MR), and then applied to events in the application region (AR) in order to estimate the background of interest in the signal region (SR).

diboson, $t\bar{t}$) of the m_T(W) distribution. Small contributions from other processes are substracted using the MC simulation. The numbers are corrected for the contamination from electrons from photon conversions, based on the MC truth information.

Then, the FRs are applied to events entering the application regions. They are defined exactly in the same way as the $2\ell SS$ and 3ℓ signal regions, except that at least 1 of the final state leptons must fail the tight criteria while passing the fakeable criteria. The reweighting of data events with FRs in the application regions provides samples which model the contributions of the NPL background in the signal regions. To reduce the contamination from genuine prompt leptons in these samples, their contribution is substracted using the MC simulation.

In the $2\ell SS$ channel, most of the NPL background consists in events from the semileptonic $t\bar{t}$ process in association with a NPL. Although the proportion of DY+jets events is larger in the 3ℓ channel, it is still much lower than in the tZq analysis, since the present analysis rejects events having a pair of leptons compatible with a Z boson decay.

The extrapolation from the MR to the AR relies on a few assumptions: for instance that kinematics are similar between the 2 regions, idem for the relative proportions of the sources of NPLs, etc. Several *closure tests* are performed to verify these assumptions and ensure the correctness of the procedure, and to estimate uncertainties impacting the shape and normalization of the NPL background.

A first comparison is done in the MC simulation between FRs obtained with either a QCD multijet or $t\bar{t}$ sample. Small discrepancies reflect differences in the origins of NPLs

between both processes (there are more light jet misidentifications in QCD multijet, and more heavy-flavour hadron decays in $t\bar{t}$). In addition, a closure test is performed in which the NPL sample obtained with the default data-driven procedure is compared to a NPL sample taken directly from the MC simulation ($t\bar{t}$ sample).

5.6.2 Charge misidentification background

The charge misidentification probability was found to be negligible for muons and does not impact the 3ℓ channel, hence this background is only considered in the μe channel. It mostly comprises events from the $t\bar{t}$ and DY+jets processes containing a pair of opposite-sign leptons, but in which the charge of 1 lepton is misidentified.

The charge misidentification background is also estimated with an ABCD method. The probability for an electron to have its charge mismeasured, or "flipped", is determined in a sample of $Z/\gamma^* \rightarrow ee$ data events containing exactly 2 tight leptons. All pairs of leptons with an invariant mass close to the Z boson mass are assumed to originate from its decay, independently of their charges.

The "flip rate" is measured in bins of p_T and η from a maximum likelihood fit to several simulated templates. This allows predicting the rates of the $Z/\gamma^* \rightarrow ee$ and background processes. Finally, the flip rates are defined as: $r = N_{SS}/(N_{SS} + N_{OS})$, where N_{SS} is the number of DY events containing 2 same-sign leptons, and N_{OS} is the number of DY events containing 2 opposite-sign leptons. As it is not possible to know which electron has its charge misidentified, the flip rates are parameterised based on the 2 electrons in the event.

5.7 Multivariate analysis

Multivariate (MVA) techniques are used to design a discriminating variable in each channel. These variables are the ones which are ultimately fitted to the data to extract the signal. Two BDT classifiers are trained both in the $2\ell SS$ and 3ℓ channels to separate the signal from the 2 major backgrounds: the $t\bar{t}W$ and $t\bar{t}Z$ processes, referred to as the $t\bar{t}V$ background, and the $t\bar{t}$ process in association with NPLs. The 4 BDTs are correspondingly labelled BDT-$t\bar{t}V$-$2\ell SS$, BDT-$t\bar{t}$-$2\ell SS$, BDT-$t\bar{t}V$-3ℓ and BDT-$t\bar{t}$-3ℓ . They are trained with the TMVA package [237], using dedicated leading-order simulated samples with higher statistics. In the $2\ell SS$ SR, the same BDTs are used in the $\mu\mu$ and μe channels.

The descriptions of the input variables are given in Table 5.8. Most input variables are related to the kinematics and angular distances of final state particles. Several of them exploit the forward light jet expected in the tHq process, which is a unique and most valuable feature for its discrimination.

Although the design of the BDTs is directly inspired from the previous analysis, I performed optimization studies regarding their hyperparameters and input variables to improve their performance. For instance, I added 2 variables in the BDTs in the $2\ell SS$ channel with respect to the 2016 analysis. The first variable corresponds to the sum of the p_T of

Table 5.8: Description of the input variables used in the BDTs. The MEM-related variables are only used for the training of the BDT-t$\bar{t}$V-3ℓ . The 12^{th} and 13^{th} variables are only used in the 2ℓSS channel.

Variable	Description
1	Number of jets having $p_T > 25$ GeV and $\|\eta\| < 2.4$
2	Maximum $\|\eta\|$ of any light jet with $p_T > 25$ GeV
3	p_T of the most forward light jet
4	Sum of leptons' charges
5	Number of light jets with $\|\eta\|$ >1.0
6	$\Delta\eta$ of most forward light jet and hardest b-tagged jet (loose WP)
7	$\Delta\eta$ of most forward light jet and 2^{nd} hardest b-tagged jet (loose WP) (set to -1 in events with only 1 b-tagged jet)
8	$\Delta\eta$ between the most forward light jet and closest lepton
9	$\Delta\phi$ between the 2 hardest leptons
10	Minimum ΔR between any two leptons
11	p_T of sub-leading lepton
12	Hadronic Top Tagger
13	Total sum of p_T of all selected jets
14	Log-likelihood of MEM weights under the 3 hypotheses
15	Log of MEM weight under tHq hypothesis
16	Log of MEM weight under t$\bar{t}$W hypothesis
17	Log of MEM weight under t$\bar{t}$Z hypothesis

all the jets selected in an event. The second corresponds to the score of the "Hadronic Top Tagger" discriminant developped by the t$\bar{t}$H group [273]; it is a BDT-based algorithm designed to identify hadronic top quark decays, and is especially useful against the t$\bar{t}$ background.

In addition, I included 4 variables obtained with the matrix element method (MEM) described in Sec. 4.7.4. These variables are included in the BDT-t$\bar{t}$V-3ℓ only, as motivated by dedicated studies showing the largest improvement for this BDT. Moreover, the MEM is not much efficient against the t$\bar{t}$ background, and the large statistics in the 2ℓSS channel prevented the use of this very CPU-intensive technique. Logarithms of the MEM weights computed under the tHq, t$\bar{t}$Z and t$\bar{t}$W hypotheses are included as input variables of the BDT, as well as their log-likelihood ratio (see Table 5.8).

The figure 5.8 (a) illustrates the gains in performance due to the addition of all these variables. The figure 5.8 (b) compares the ROC curves of the 4 final BDTs. The responses of all BDTs to the signal and backgrounds are presented in Fig. 5.9; they show no clear sign of overtraining.

I also investigated deep neural network (DNN) alternatives for the MVA, and implemented different DNN architectures using both the TMVA and Keras [285] libraries. A performance comparable to that of the BDTs was achieved. Due to time constraints and the interest for other studies (MEM variables, etc.), a DNN-based MVA was not retained.

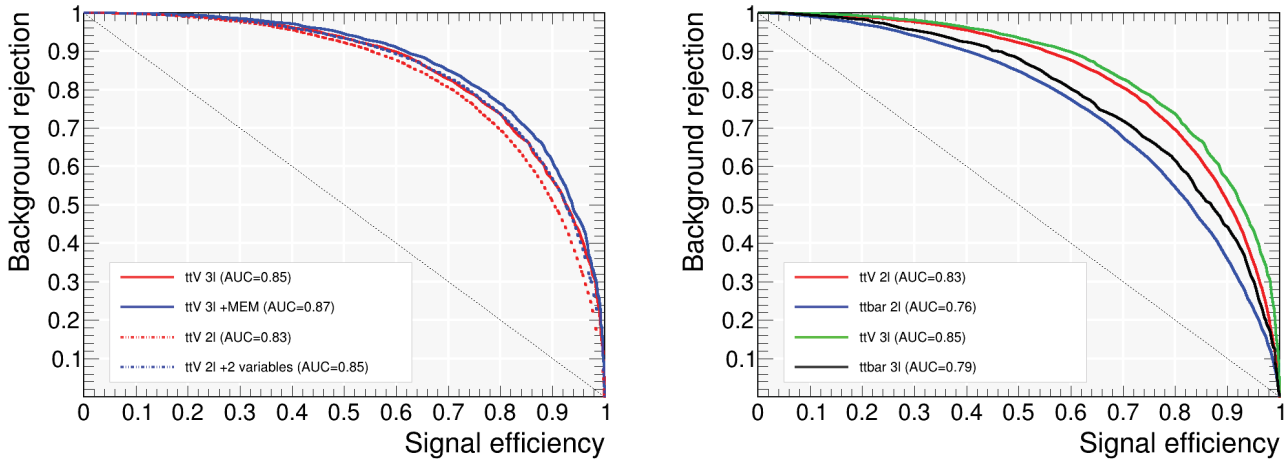

(a) (b)

Figure 5.8: (a) Comparison of ROC curves for the BDT-tt̄V-3ℓ and BDT-tt̄V-2ℓSS , before and after including input variables from the MEM and from the optimization. (b) Comparison of the ROC curves of the 4 final BDTs. The *areas under curves* (AUCs) correspond to the integrals under the ROC curves and are to be maximised.

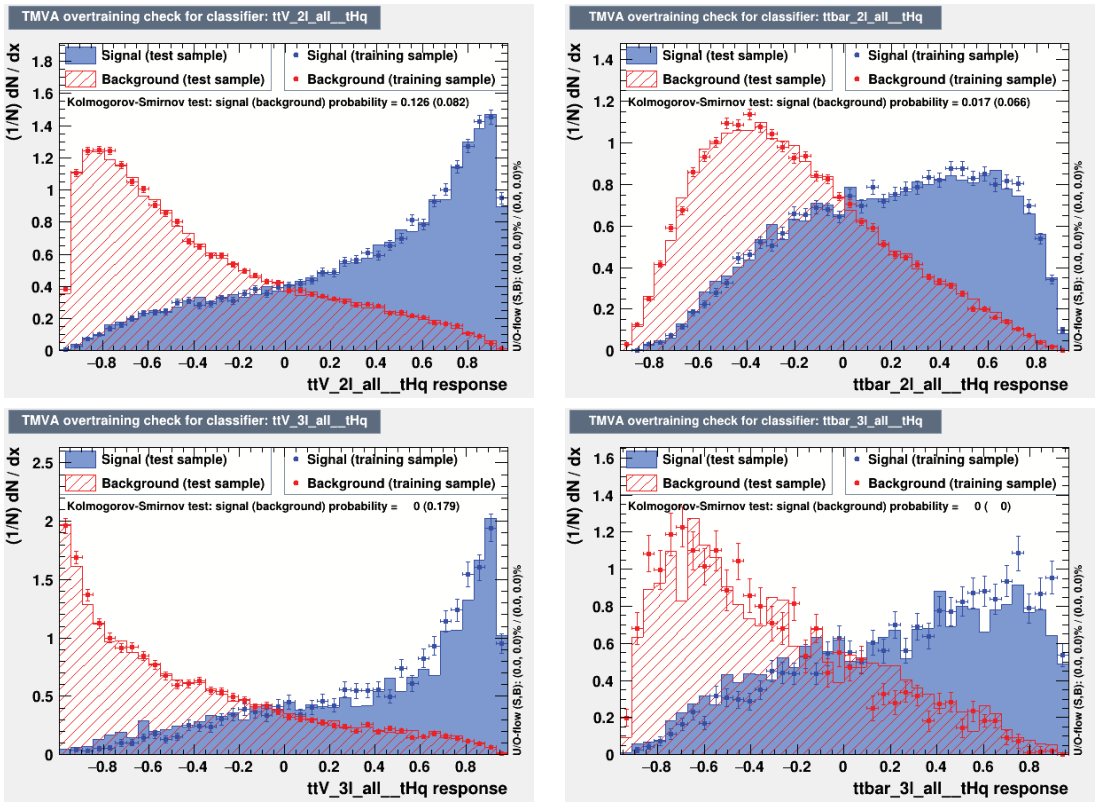

Figure 5.9: Normalized outputs of the BDT-tt̄V-2ℓSS (top left), BDT-tt̄-2ℓSS (top right), BDT-tt̄V-3ℓ (bottom left) and BDT-tt̄-3ℓ (bottom right), for the simulated signal (blue) and backgrounds (red).

5.8 Systematic uncertainties

Various sources of systematic uncertainty are considered, which impact both the event yields and the shapes of the final observables included in the fit. The sources of uncertainty can be grouped as follows:

Experimental uncertainties

- **Luminosity:** An uncertainty of 2.3% on the integrated luminosity of the 2017 dataset is propagated as a normalization-only uncertainty to all predicted yields [286].
- **Pileup:** The central value of the pp inelastic cross section used to simulate pileup events is varied by $\pm$4.6% as recommended. This impacts both the shapes of the distributions, and the phase space acceptance.
- **Trigger efficiency:** The scale factors correcting for differences in trigger efficiency between data and simulation are varied within their uncertainties, listed in Table 5.2.
- **Lepton identification efficiency:** The scale factors correcting for differences in the probabilities for electrons and muons to pass the loose selection criteria are varied within their uncertainties (statistical uncertainty of the DY sample used to derive the SFs). This affects both the shapes and normalizations. The uncertainty on the probability for loose electrons to be reconstructed as tight electrons was determined to be 3% for electrons with $p_T > 25$ GeV and 5% for electrons with $p_T < 25$ GeV. The corresponding value for muons is 2%; in the 3ℓ channel, an average per-event value of 3 % is used.
- **B-tagging efficiency:** Eight independent variations by $\pm 1\sigma$ are considered for the scale factors related to b-tagging and mistagging efficiencies (see Sec. 4.8). These uncertainties are provided by CMS as a function of the jet p_T , η and flavour. They affect both the shapes and normalizations.
- **Jet energy scale:** The JES scale factors are varied within their uncertainties, and the changes are propagated to all kinematic quantities. These uncertainties are provided by CMS as a function of the jet p_T and η. They affect both the shapes and normalizations.
- **L1 prefiring probability:** The officially-recommended per-event weights applied to simulated events to account for this effect are provided with uncertainties by the CMS e-γ working group. They affect both the shapes and normalizations.
- **Forward jet modeling:** In order to further improve the modeling of forward jets, data-to-simulation scale factors are derived in a dedicated control region enriched in the $t\bar{t}$ process, as a function of the η of the jet. Simulated events are then weighted

with these scale factors to obtain an alternative distribution. The difference between the default and the variation is then treated as a systematic uncertainty related to forward jets. The opposite variation is obtained from the "mirror" distribution of the alternative shape with respect to the default. This step was carried out by the other PhD working on the tH analysis.

Theory uncertainties

- **PDF, α_s, scale (cross section normalization):** Normalization-only uncertainties are applied to the predicted yields of the $t\bar{t}H$, $t\bar{t}W$, $t\bar{t}Z$, tHq, tHW and $t\bar{t}WW$ processes, to account for uncertainties related to the PDF, α_s, and missing higher orders on the NLO theory calculations [287]. The input uncertainties on the PDF and scale are of the order of 1–4% and 10% respectively.

- **PDF, α_s, scale (shape and acceptance):** Uncertainties on the PDF, α_s, and Q^2 scale affect the shape and acceptance of the distributions used for signal extraction. Part of this effect is assessed by varying the renormalization scale μ_R and factorization scale μ_F between 1/2 and 2 (with the constraint $1/2 < \mu_R/\mu_F < 2$), and taking the envelope of the difference between the nominal shape and the varied shapes. The resulting shape is then fitted linearly. This procedure was used in the main $t\bar{t}H$ analysis [273]. I performed dedicated studies in the context of the present analysis, to ensure that the overall effect is indeed small and mostly captured by this procedure. Figure 5.10 shows the nominal distributions of the 4 BDTs which are combined to extract the signal, as well as the varied shapes corresponding to shifted values of μ_R and μ_F. This study confirmed that neglecting higher orders indeed has, to a good approximation, a linear impact on the shape of the observables, and that the acceptance effect is of the order of 0.5% on the total yields. Additionally, I investigated the impact of the choice of PDF set on the acceptance by comparing different PDF sets and estimating their average impacts on the total yields. The following PDF sets were compared: *NNPDF31_nnlo_hessian_pdfas*, *NNPDF30_nlo_nf_4_pdfa*, *CT14nnlo* and *PDF4LHC15_nnlo_100i_pdfas* (descriptions can be found in Ref. [288]). The impacts on the acceptance were found to range between 0.2-0.7%.

Background estimation

- **Irreducible backgrounds:** The normalization uncertainties are taken to be 30% for the diboson backgrounds (WZ, ZZ), 50% for rare SM processes, 5% for the tZq process, and 30% for the photon conversion background.

- **NPL background:** Several sources of uncertainty are attached to the NPL background to account for statistical uncertainties in the measurement and application regions, the substraction of the prompt MC contribution, and from the closure tests described in Sec. 5.6.1. The input uncertainty on the yield of this background amounts to about 30%.

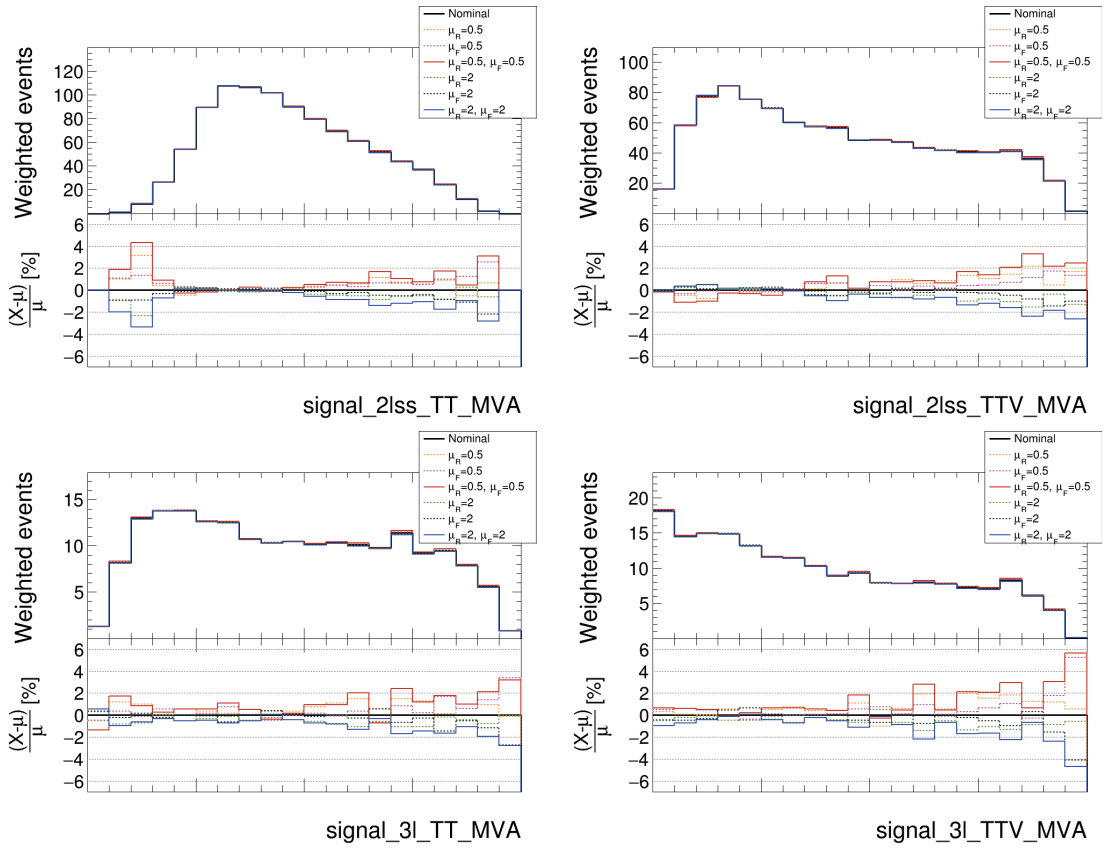

Figure 5.10: Comparison of the nominal BDT distributions with distributions corresponding to variations of the renormalization and factorization scales. This is shown for the BDT-t$\bar{t}$ (left) and BDT-t$\bar{t}$V (right), in the 2ℓSS (top) and 3ℓ (bottom) signal regions. Larger fluctuations in the outermost bins can be attributed to statistical fluctuations.

5.9 Signal extraction

5.9.1 Upper limits

In case the signal process has a small cross section below experimental sensitivity, or may not exist, it is common to quote an upper limit on the signal cross section at 95% CL [24, 261]. Using the test statistic defined in Eq. 4.6, it is possible to compute p-values p_μ for all values μ of the signal strength, under the signal plus background hypothesis, and to reject those that have $p_\mu \leq 0.05$. The impact of statistical fluctuations in the data on upper limits is usually assessed by quoting $\pm 1\sigma$ and $\pm 2\sigma$ ranges for the expected limit, obtained by replacing the median of the test statistic by its value varied accordingly.

However, in case the number of observed events fluctuates substantially below the expectation of the background-only hypothesis, or if the analysis' sensitivity to a given hypothesis is low, the resulting upper value on the signal strength may be anomalously low. This can happen for instance if the signal cross section is small, if the backgrounds are too dominant, or if the experimental resolution is not sufficient, resulting in almost identical distributions of the test statistic under both the null and alternative hypotheses.

In order to adress this issue, the CL_s *method* [289–291] was designed at the LEP, and then its usage slightly evolved at the Tevatron and later at the LHC. This method was used at the LEP and at the Tevatron to set limits on the mass of the Higgs boson [292, 293], and is the standard test statistic to set limits at the LHC (in the asymptotic limit, see Sec. 4.9). It alters the threshold for rejecting a model (or excluding a value of μ) by defining:

$$CL_s \equiv \frac{p_{s+b}}{1 - p_b} \ , \tag{5.5}$$

where p_{s+b} is the p-value of the test statistic computed under the signal plus background hypothesis, and p_b is its p-value computed under the background-only hypothesis (see Eq. 4.7). The largest value of μ which can not be excluded at the desired significance level represents the CL_s upper limit.

Since the denominator is always lower or equal to unity, the CL_s criterion is more conservative than the usual requirement $p_{s+b} \leq 0.05$. This can be quantitatively understood from Fig. 5.11: in case the experiment does not have sufficient sensitivity to discriminate 2 competing hypotheses, like in the sub-figure (c), a small value of p_{s+b} is counter-balanced by a small value of $1 - p_b$, which prevents the exclusion of the signal plus background hypothesis.

5.9.2 Binning optimization

The responses from the 2 BDTs trained against the $t\bar{t}V$ and $t\bar{t}$ backgrounds yield a two-dimensional (2D) discriminant. A *bin mapping* is defined in order to transform this initial 2D distribution into the final 1D distribution used to extract the signal. As the analysis' performance partly depends on the bin mapping, the sizes and boundaries of the bins in the 2D plane are optimized based on the expected significance.

I performed this optimization in the 3ℓ channel, wherein MEM variables are included. First, the x and y axes are divided into 3 bins, which represents a total of 4 free parameters corresponding to free bin boundaries. Then, the bin boundaries are varied independently by steps ($\sim$ 500 configurations tested). For each configuration, distributions are reproduced including all systematic uncertainties, and the one yielding the highest expected significance is retained. Finally, the bins are slightly fine-tuned and ranked by increasing signal-to-background ratio.

A similar procedure was followed to define the bin mapping in the $2\ell SS$ channel. The final bin mappings used in the $2\ell SS$ and 3ℓ channels are sketched in Fig. 5.12. Eight and ten bins are used for the 2D$\rightarrow$1D mapping in the $2\ell SS$ and 3ℓ channels respectively.

5.9.3 Extraction

The tHq, tHW and $t\bar{t}H$ processes are all treated as signals, since they are all sensitive to the κ_t parameter. A common signal strength modifier is let floating in the fit. Simulated tHq, tHW, and $t\bar{t}H$ signal events are reweighted with per-event weights which reflect the impacts of the couplings on kinematic distributions. A total of 51 values of the κ_t and

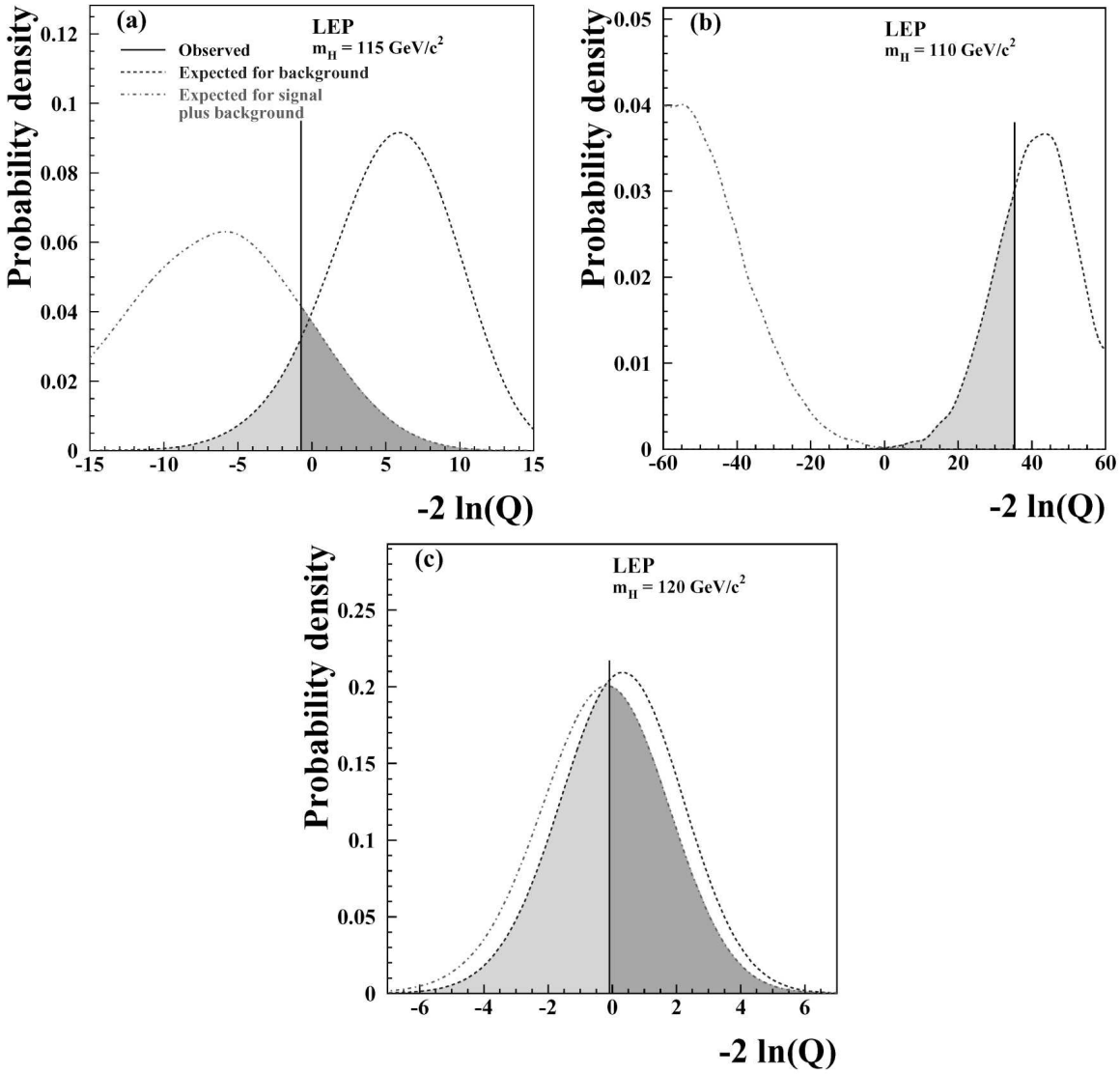

Figure 5.11: Probability density functions of the test statistic $-2\ln(Q)$ for the LEP-wide combination, corresponding to different test masses m_H of the Higgs boson, for the background and signal plus background hypotheses. The observed values of the corresponding test statistic are indicated by the vertical lines. The light shaded areas, $1 - CL_b$, measure the confidence for the background hypothesis, and the dark shaded areas, CL_{s+b}, the confidence for the signal plus background hypothesis. Accounting for $1 - CL_b$ prevents the exclusion of a hypothesis in cases where the experiment does not have sufficient sensitivity, like in Fig. (c). Taken from Ref. [292].

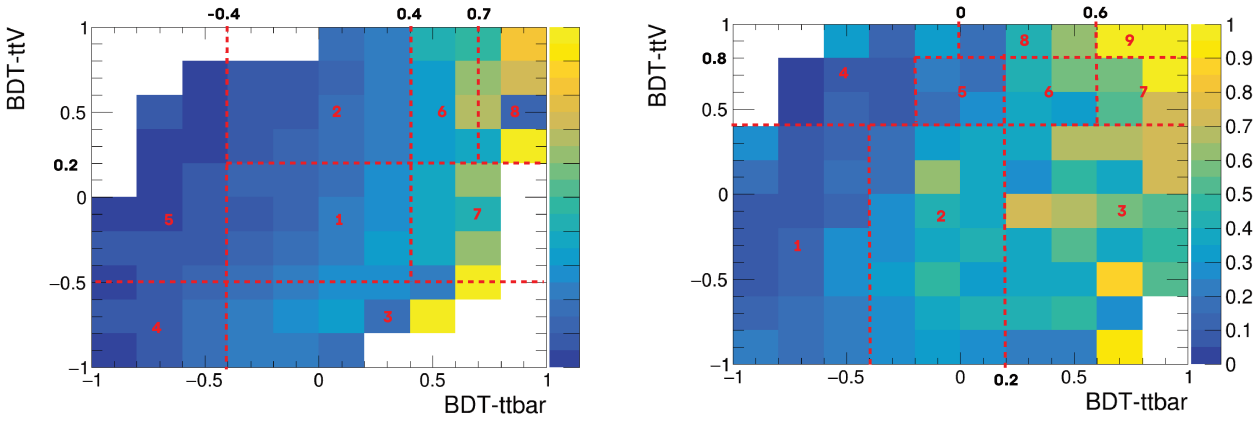

Figure 5.12: Sketches of the bin mappings used in the $2\ell SS$ (left) and 3ℓ (right) channels to obtain the final 1D distributions from the 2 BDT discriminants against the $t\bar{t}$ and $t\bar{t}V$ backgrounds. The distribution of the signal-to-background ratio in the 2D plane is overlaid.

κ_V coupling modifiers (κ_V =0.5, 1, 1.5, $-3 \leq \kappa_t \leq 3$), and 21 values of the CP mixing angle α ($-\pi \leq \alpha \leq \pi$) are probed.

Apart from the κ_t -κ_V interference impacting the tH production cross section, the cross section of the $t\bar{t}H$ process scales with κ_t^2. At each point, the tH and $t\bar{t}H$ production cross sections and the Higgs boson decay branching ratios are varied depending on the κ_t and κ_V coupling modifiers. All other parameters are assumed to take the values predicted by the SM. Upper limits at 95% CL are set on the observed tH + $t\bar{t}H$ cross section times the combined branching ratio of H$\rightarrow$WW* + $\tau\bar{\tau}$+ZZ*, for different values of κ_t and κ_V .

Results are obtained from a simultaneous fit to all 3 channels (3ℓ , $\mu\mu$, μe). Upper limits are obtained with the aforementioned CL_s procedure, while signal strength estimates are obtained from MLEs (see Sec. 4.9).

In order to constrain the range of κ_t for the fixed value $\kappa_V = 1$, a scan of the likelihood ratio $-2\ln\left(\mathcal{L}(\kappa_t)/\mathcal{L}(\hat{\kappa}_t)\right)$ is performed, where $\hat{\kappa}_t$ corresponds to the best fit value of the parameter. First, the profiled likelihood ratio (see Eq. 4.6) is estimated for the cases $\mu = 0$ and $\mu = 1$, for each value of κ_t. Then, we take the difference:

$$\begin{aligned} \Delta\ln\mathcal{L} &= \ln(\mathcal{L}_{\mu=1}/\mathcal{L}_{\hat{\mu}}) - \ln(\mathcal{L}_{\mu=0}/\mathcal{L}_{\hat{\mu}}) \\ &= \ln(\mathcal{L}_{\mu=1}) - \ln(\mathcal{L}_{\mu=0})\,, \end{aligned} \tag{5.6}$$

where the likelihood functions $\mathcal{L}$ depend on κ_t.

Substracting for the minimum value corresponding to $\kappa_t = \hat{\kappa}_t$, and taking advantage from the fact that $\mathcal{L}$ is independent of κ_t for $\mu = 0$, we obtain:

$$\begin{aligned} \Delta\ln\mathcal{L}(\kappa_t) - \Delta\ln\mathcal{L}(\hat{\kappa}_t) &= \left(\ln(\mathcal{L}_{\mu=1,\kappa_t}) - \cancel{\ln(\mathcal{L}_{\mu=0,\kappa_t})}\right) - \left(\ln(\mathcal{L}_{\mu=1,\hat{\kappa}_t}) - \cancel{\ln(\mathcal{L}_{\mu=0,\hat{\kappa}_t})}\right) \\ &\rightarrow -2\ln\left(\mathcal{L}(\kappa_t)/\mathcal{L}(\hat{\kappa}_t)\right)\,, \end{aligned} \tag{5.7}$$

which corresponds to a scan of the κ_t parameter, independently of the signal strength.

5.10 Results

After applying the event selection on the dataset, 193 events are observed in the 3ℓ channel, 352 in the $\mu\mu$ channel, and 668 in the μe channel. Data-to-simulation comparisons for the BDT-based discriminants are shown in Fig. 5.13, before and after the maximum likelihood fit used to extract the results.

For the SM scenario ($\kappa_t = \kappa_V = 1$), the observed (expected) 95% CL upper limit on the combined tH + t$\bar{\text{t}}$H signal strength is $r < 2.87$ ($r < 1.11$), which translates into an upper limit on the combined tH + t$\bar{\text{t}}$H production cross section times branching ratio of 0.52 pb. The observed (expected) best fit signal strength is $\mu^{obs}_{SM} = 1.60^{+0.70}_{-0.64}$ ($\mu^{exp}_{SM} = 1^{+0.62}_{-0.58}$), corresponding to a significance of 2.7σ (1.7σ) for the signal under the background-only hypothesis. In comparison, the 2016 analysis found an observed (expected) significance of 2.7σ (1.5σ), and an observed upper limit of 0.56 pb. The search for t$\bar{\text{t}}$H in final states with electrons, muons and hadronically-decaying τ leptons found an observed (expected) significance of 1.7σ (2.9σ) in the 2017 dataset.

For the ITC scenario ($\kappa_t = -\kappa_V = -1$), the observed (expected) 95% CL upper limit on the combined tH + t$\bar{\text{t}}$H signal strength is $r < 1.81$ ($r < 0.67$) which translates into an upper limit on the combined tH + t$\bar{\text{t}}$H production cross section times branching ratio of 0.80 pb. The observed (expected) best fit signal strength is $\mu^{obs}_{ITC} = 0.97^{+0.44}_{-0.41}$ ($\mu^{exp}_{ITC} = 1^{+0.41}_{-0.38}$), corresponding to a significance of 2.5σ (2.8σ) for the signal under the background-only hypothesis. In comparison, the 2016 analysis found an observed (expected) significance of 1.7σ (2.5σ), and an observed upper limit of 0.64 pb.

For both scenarios, the observation is in agreement with the SM prediction within the uncertainties.

The post-fit central values and uncertainties of all the nuisance parameters included in the MLE are shown in Fig. 5.14, both for the SM and ITC scenarios. For both scenarios, the sensitivity of the analysis is predominantly limited by systematic uncertainties affecting the normalizations of the main background components (NPL background estimation, scale uncertainties on the t$\bar{\text{t}}$W and t$\bar{\text{t}}$Z cross sections), as well as uncertainties related to the JES and to trigger and lepton identification efficiencies. No large deviation from the pre-fit values of the nuisance parameters is observed.

The result of the likelihood ratio scan as a function of the κ_t parameter is shown in Fig. 5.15 (left), both for the data and for an Asimov dataset wherein tH and t$\bar{\text{t}}$H are set to their SM expectations. The expected performance for a SM-like signal is to favour $\kappa_t = 1$ over $\kappa_t = -1$ by about 1.5σ, and to exclude values outside the range of about [-1.1, 1.6] at 95% CL. The data favour a positive value of κ_t by about 1.5σ, and exclude values of κ_t outside the ranges of about [-1.4, -0.7] and [0.7, 1.9] at 95 % CL. The local maximum

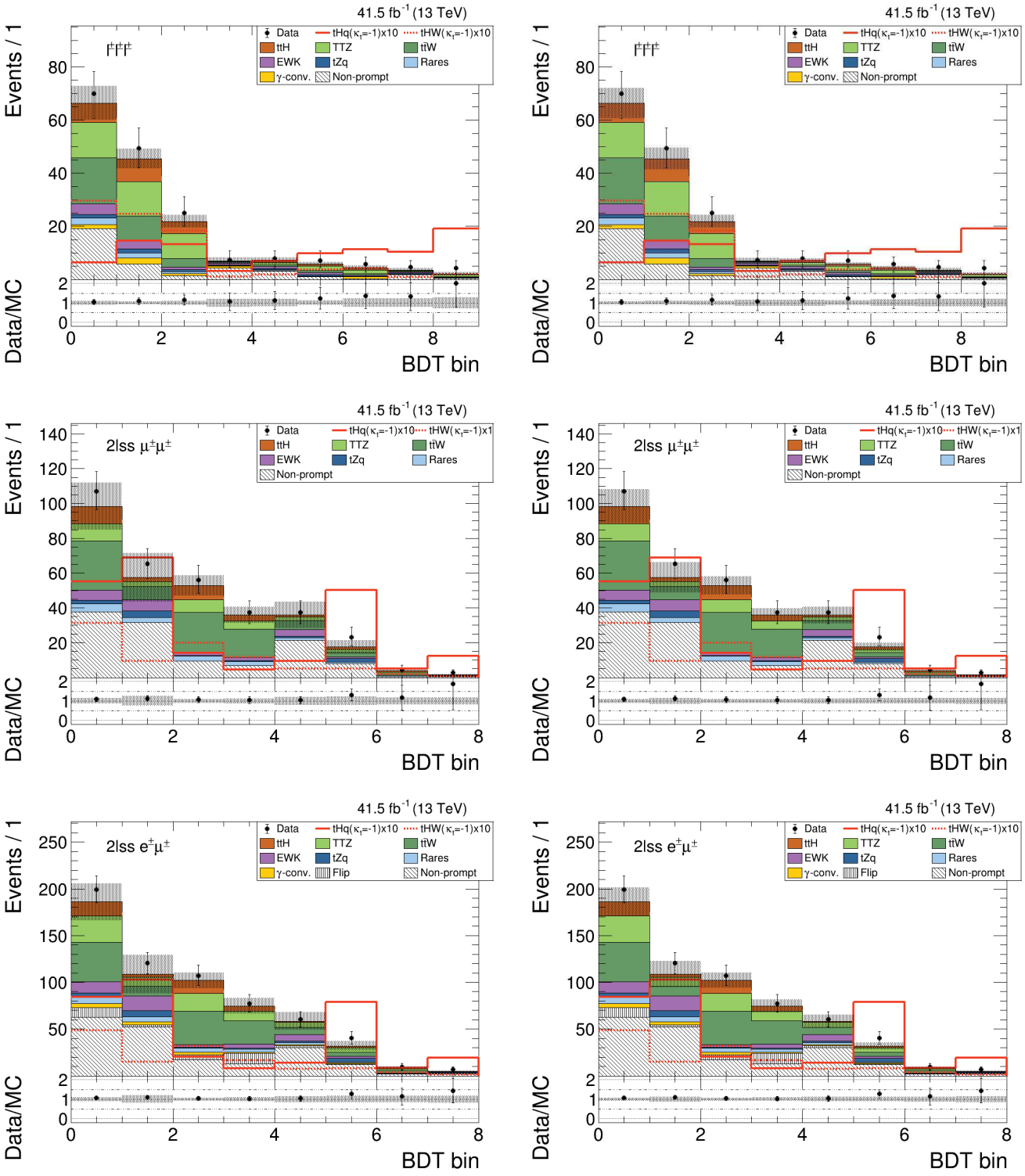

Figure 5.13: Pre-fit (left) and post-fit (right) data-to-prediction comparisons for the BDT-based discriminants in the 3ℓ (top), $\mu\mu$ (centre) and μe (bottom) channels. The signal kinematics correspond to the ITC scenario, and the normalizations of the tH processes are scaled up by a factor 10.

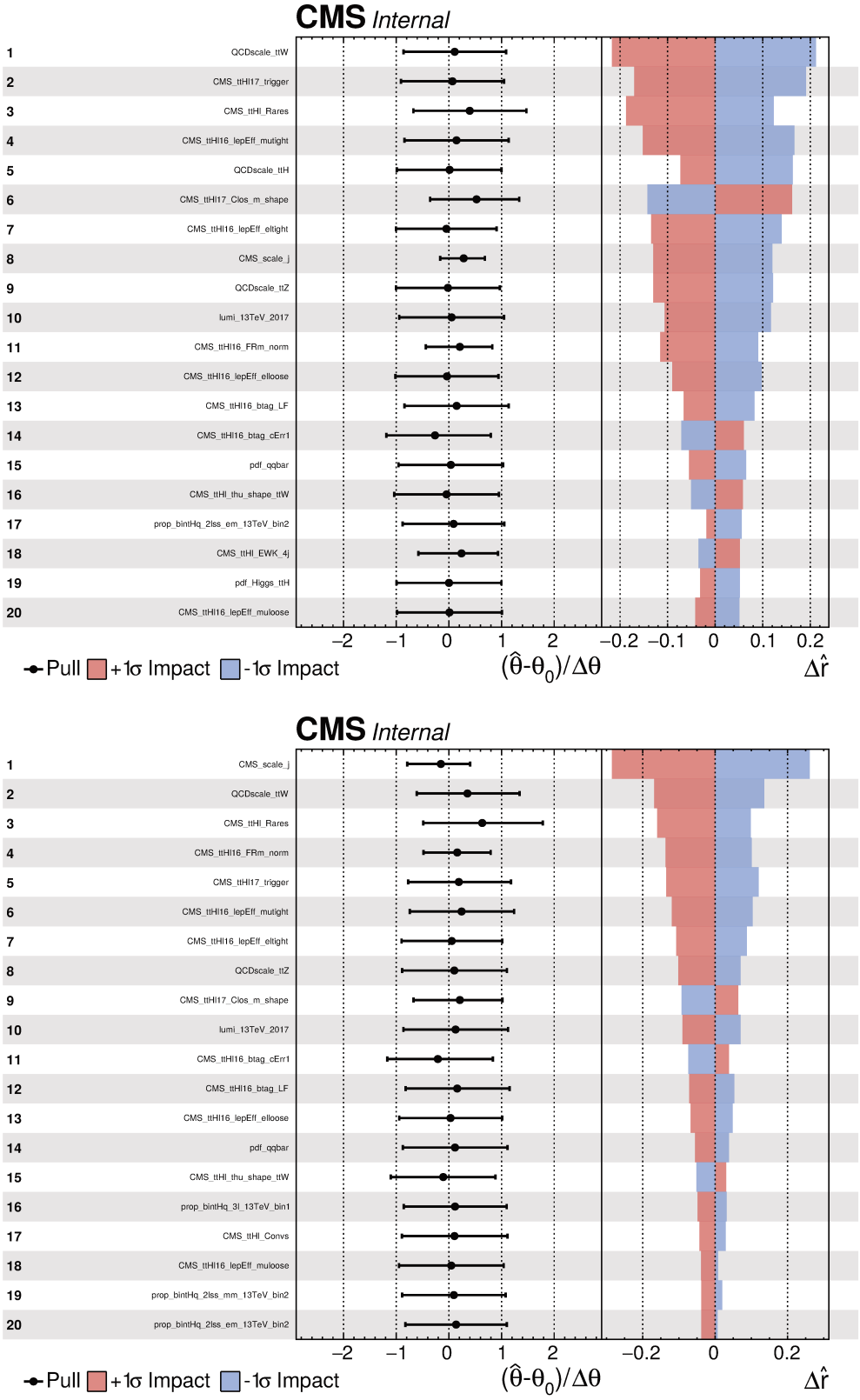

Figure 5.14: Post-fit central values (black dots) and uncertainties (error bars) of the nuisance parameters, compared to their pre-fit values. On the right-hand side, the impact $\Delta\mu$ of the variation of the central value of each nuisance parameter by $\pm1\sigma$ on the signal strength is shown. The fit is performed both in the SM (top) and ITC (bottom) scenarios.

at $\kappa_t = 0$ is due to the fact that the $t\bar{t}H$ component is expected to vanish at this point, which is not supported by the observation. Driven by a small excess of data (visible in Fig. 5.13 and compatible with SM predictions within uncertainties), the observed test statistics is minimal for a value of κ_t slightly larger than 1, corresponding to augmented cross sections for the tH and ttH processes which accomodate the data better.

Likewise, a scan of the likelihood ratio as a function of $\cos(\alpha)$ is performed and shown in Fig. 5.15 (right). The data favour a purely CP-even coupling ($\cos(\alpha) = 1$) of the Higgs boson to the top quark over a purely CP-odd coupling ($\cos(\alpha) = 0$) by about 2σ. This allows excluding values of the mixing angle α corresponding to $\alpha \sim \pi/2$ at 95% CL. Again, a local maximum is found around $\cos(\alpha) = 0$ because the $t\bar{t}H$ component is expected to vanish at this point.

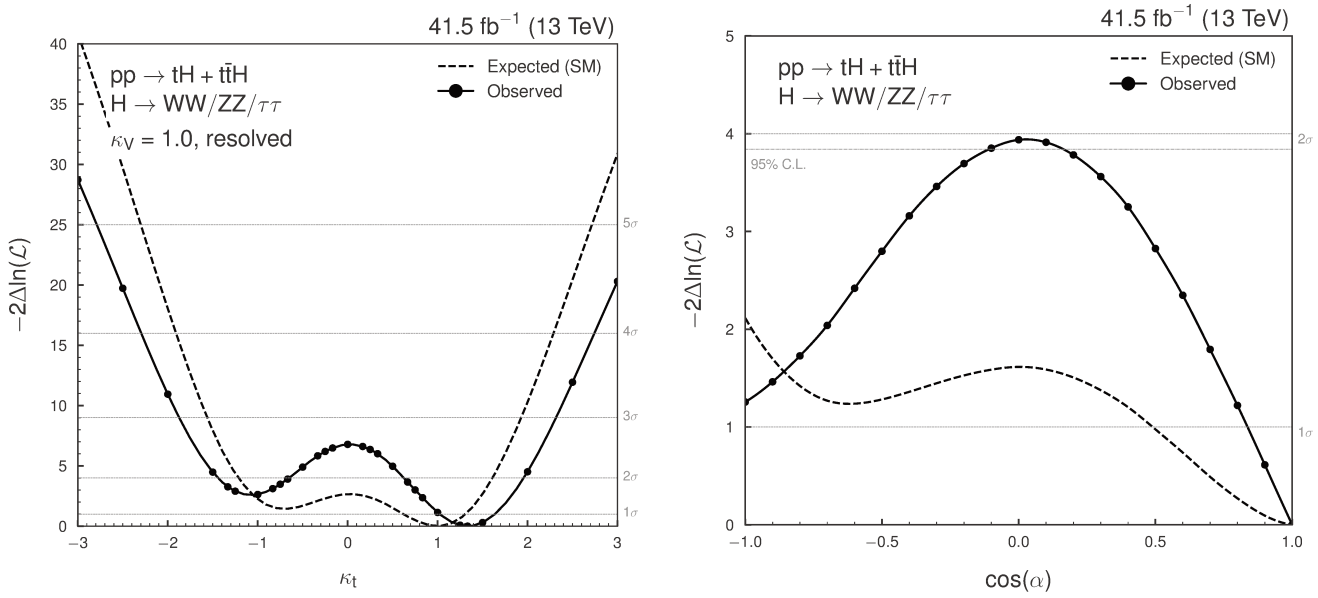

Figure 5.15: Scan of $-2\Delta\ln(\mathcal{L})$ as a function of (a) κ_t and (b) $\cos(\alpha)$ for the data (solid line) and an Asimov dataset (dotted line). Both the tH and $t\bar{t}H$ signals are considered. These figures were produced by the other PhD within the framework of the $t\bar{t}H$ group, using templates I provided.

Finally, expected and observed 95% CL upper limits are set on the tH cross section times the relevant branching ratios, as a function of κ_t. The results are shown in Fig. 5.16 (a). To establish limits on the tH cross section, a different signal strength modifier is introduced for the combination of tHq and tHW only. The κ_t-dependent contribution of the $t\bar{t}H$ process is included as a background with fixed normalization, while the tH signal strength is allowed to float in the fit. An upper limit for the fiducial cross section for SM-like tH production is set to about 0.74 pb, with an expected limit of 0.6 pb.

Figure 5.16 (b) shows the expected and observed 95% CL upper limits set on the combined tH + $t\bar{t}H$ cross section times the relevant branching ratios, as a function of $\cos(\alpha)$. The tH and ttH signals are not included in the background-only Asimov dataset, which explains why the observed limits are consistently higher than the expectation.

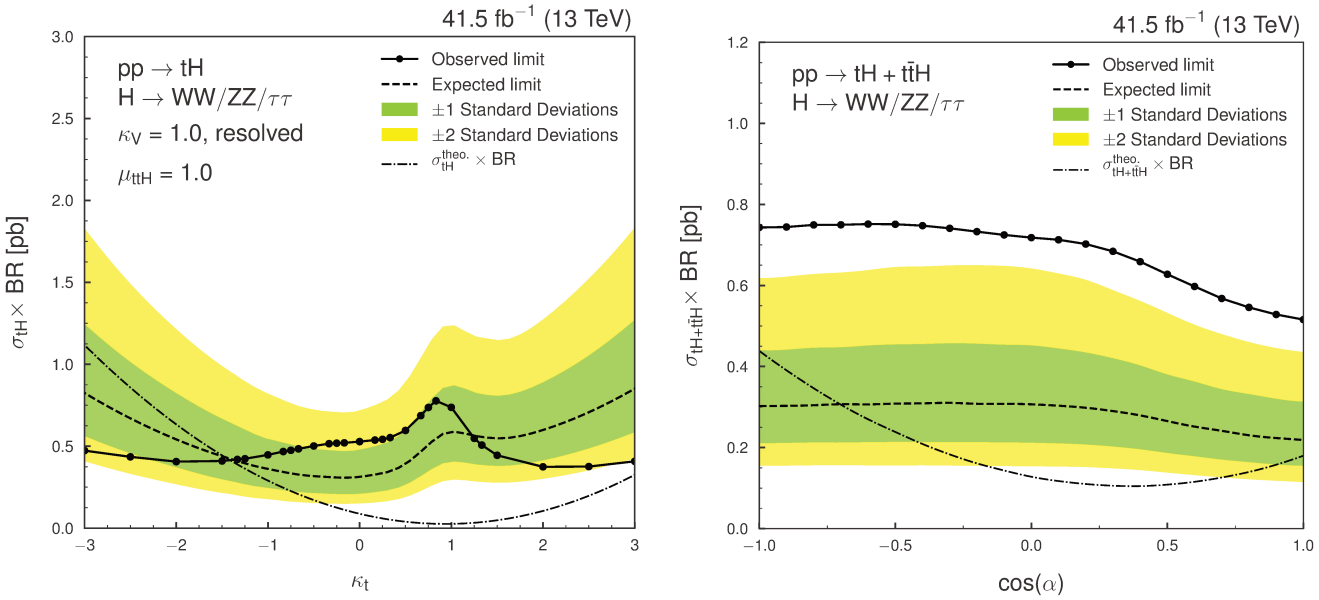

(a) (b)

Figure 5.16: (a) Observed and expected 95% CL upper limits on the tH cross section times H→WW* + ττ+ZZ* branching ratio as a function of κ_t, assuming κ_V = 1.The κ_t-dependent contribution from tt̄H is kept fixed in the fit (μ_{ttH} = 1), while the signal strength μ_{tH} of the tH signal is allowed to float. (b) Observed and expected 95% CL upper limits on the tH + tt̄H cross section times H→WW* + ττ+ZZ* branching ratio as a function of cos(α). Expected limits are derived from background-only Asimov datasets. These figures were produced by the other PhD within the framework of the tt̄H group, using templates I provided.

5.11 Discussion

The expected results are improved with respect to the previous analysis, partly due to the higher integrated luminosity of the 2017 dataset. The observed 95% CL upper limits on the combined tH + tt̄H signal strength are $r < 2.9$ and $r < 1.8$ in the SM and ITC scenarios respectively, which can be compared to the 2016 limits $r < 3.1$ and $r < 1.4$. Thus the present analysis sets a more stringent upper limit on the signal SM cross section. The inclusion of MEM variables was found to improve the expected significance and upper limit by about 3% and 6% respectively in the 3ℓ channel, which is compatible with the results from preliminary studies (see Fig. 5.8 (a)).

The present analysis paves the way towards the upcoming combination of the tH and tt̄H analyses using the complete Run 2 dataset collected between 2016 and 2018. As such, an important effort was dedicated to synchronizing my own framework with that of the tt̄H group, and to performing several studies of common interest (for instance related to the scale and PDF systematic uncertainties, see Sec. 5.8).

In particular, I thoroughly investigated several possibilities in order to make the tH and tt̄H analyses orthogonal. Indeed, although they have slightly different jet multiplicity requirements both in the 2ℓSS and 3ℓ channels, the signal regions defined in each

analysis are mostly overlapping with one another. A $t\bar{t}W$ control region which is fitted in the $t\bar{t}H$ search also overlaps with the $2\ell SS$ signal region of the present analysis. After quantifying these overlaps, I proposed and compared several options to make all the regions orthogonal, based on the maximisation of the expected significance. As a result, I defined a baseline categorisation, which will be used as a benchmark to compare the performance of more involved MVA-based categorisations for the final combination.

This Run 2 *legacy* analysis will have an unprecedented sensitivity to the relative sign of the top quark Yukawa, and is expected to rule out a large range of values of κ_t without relying on any assumption regarding new physics.

5.12 Adapting the analysis to search for new physics via FCNC

This section presents a re-adaptation of the search for tH described above, in order to search for flavour-changing neutral current (FCNC) interactions. This analysis uses the same ingredients (objects, samples, systematic uncertainties, etc.) and follows the same strategy (MVA, background estimation, signal extraction) as the tH analysis described above.

I took in charge the entire analysis up to the final results. After briefly introducing the context of this search in Sec. 5.12.1, the differences with the main tH analysis are highlighted in Sec. 5.12.2. Finally, the results are presented and discussed in Sec. 5.12.3.

5.12.1 Introduction and theoretical model

Context and motivations

As already mentioned in Sec. 1.4.2, FCNC interactions are forbidden at tree level in the SM due to the GIM mechanism, and only arise via higher-order loops with strongly suppressed cross sections. This results for instance in very small predicted [294] branching ratios for FCNC interactions tqH involving the top quark, the Higgs boson and a light quark ($q = u, c$). These branching ratios are of the order of $\mathcal{B}(t \to Hu) \sim 10^{-17}$ and $\mathcal{B}(t \to Hc) \sim 10^{-15}$ (see Table 1.2).

Although this corresponds to cross sections well below any experimental sensitivity which may be reached in the foreseeable future, several BSM scenarios predict significant enhancements of these branching ratios, up to $\mathcal{B}(t \to Hq) \sim 10^{-5} - 10^{-3}$. Examples of such BSM scenarios are the minimal supersymmetric SM (MSSM) [295], two-Higgs-doublet models (2HDM) [296–298], SUSY models with R-parity violation (RPV) [299–301], or models with warped extra dimensions (RS) [302]. While the description of these models goes well beyond the scope of this work, a direct consequence is that any evidence of a FCNC process would constitute an indication of new physics. Therefore, top-Higgs FCNC processes, hereinafter referred to as tH-FCNC, are a sensitive probe for new physics at the LHC.

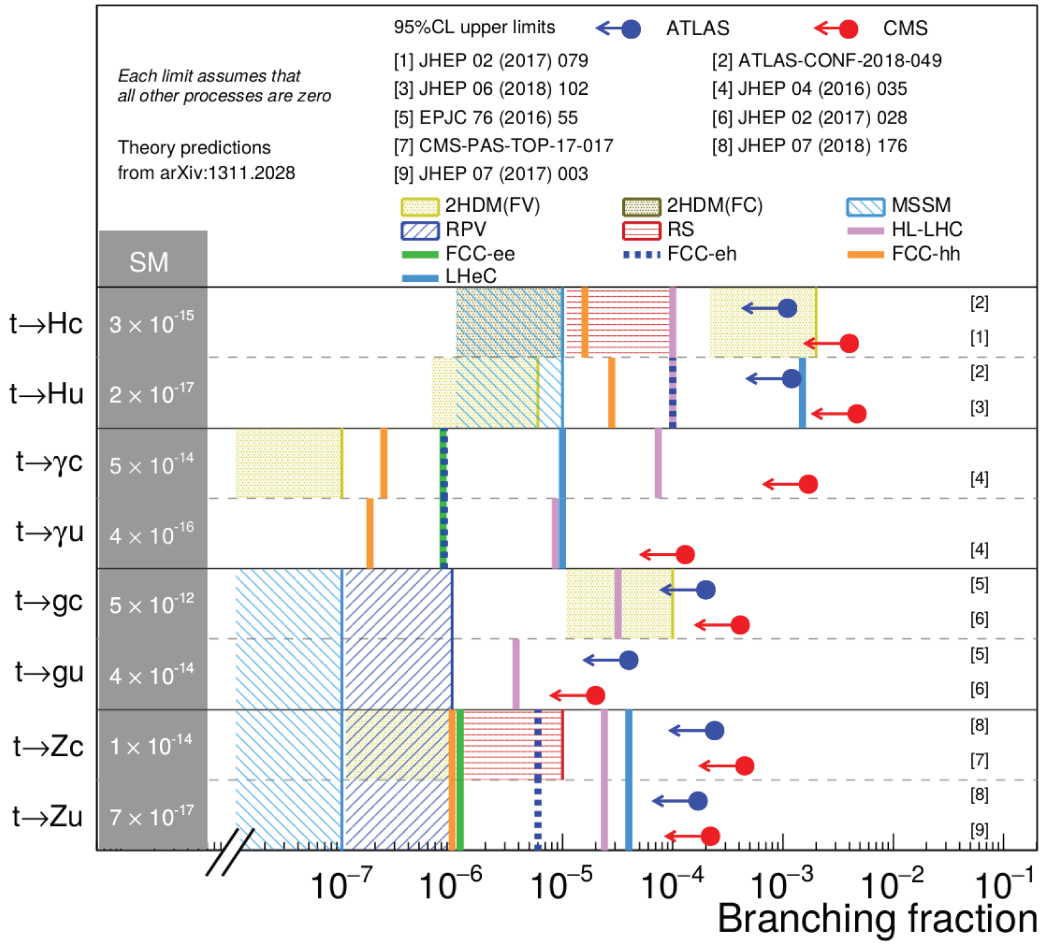

Figure 5.17: Summary of 95% CL upper limits from ATLAS and CMS searches for FCNC interactions involving the top quark. Current limits are compared to predictions from several BSM scenarios, and to prospective limits which may be set at future colliders. Taken from Ref. [303].

The figure 5.17 summarises the current 95% CL upper limits set by the ATLAS and CMS collaborations on the branching ratios of FCNC processes involving the top quark. They are compared to the predictions of several BSM scenarios. Although other FCNC processes involving the top quark are also enhanced in these scenarios, the largest enhancements are generally expected for the tqH couplings, and in particular the tcH coupling.

The tH-FCNC processes may be described with the following effective Lagrangian [304]:

$$\mathcal{L}_{eff}^{tH} = \sum_{q=u,c} \frac{g}{\sqrt{2}} \bar{t}\, \kappa_{tqH} \left(f_{Hq}^{L} P_L + f_{Hq}^{R} P_R\right) q\, H + h.c.\,, \tag{5.8}$$

where H is the SM Higgs boson, g is the weak coupling constant, P_L and P_R are the projection operators of left and right chirality, κ_{tqH} is the anomalous coupling at the tqH vertex, f_{Hq}^{L} and f_{Hq}^{L} are left- and right-handed complex chiral parameters with the unitary

constraint $f_{Hq}^{L} + f_{Hq}^{L} = 1$, and *h.c.* are hermitian conjugates.

The present analysis aims at setting model-independent upper limits on the branching ratios $\mathcal{B}(t \to Hu)$ and $\mathcal{B}(t \to Hc)$. The corresponding signal processes are hereinafter referred to as "FCNC-Hut" and "FCNC-Hct". For the sake of brevity, some figures will be shown for the FCNC-Hut signal only. Once the planned combination of CMS analyses targeting these signals in different decay modes of the Higgs boson will be achieved, these branching ratios could be conveniently re-interpreted in terms of constraints on the effective parameters and relevant EFT operators.

Since the Higgs boson is lighter than the top quark, the tH-FCNC process may be probed both in the associated production of a single top quark with a Higgs boson (ST mode), and in the FCNC decay of a pair-produced top quark (TT mode). Both these processes yield quite similar final states, as can be seen in the Feynman diagrams shown in Fig. 5.18.

While the predicted cross section in the TT mode is independent of the type of coupling, the cross section in the ST mode is 1 order of magnitude larger for the FCNC-Hut signal compared to FCNC-Hct. This significant difference is due to the higher probability density of up quarks in the proton's PDF (see Fig. 1.4), and leads to a better sensitivity to the tuH coupling.

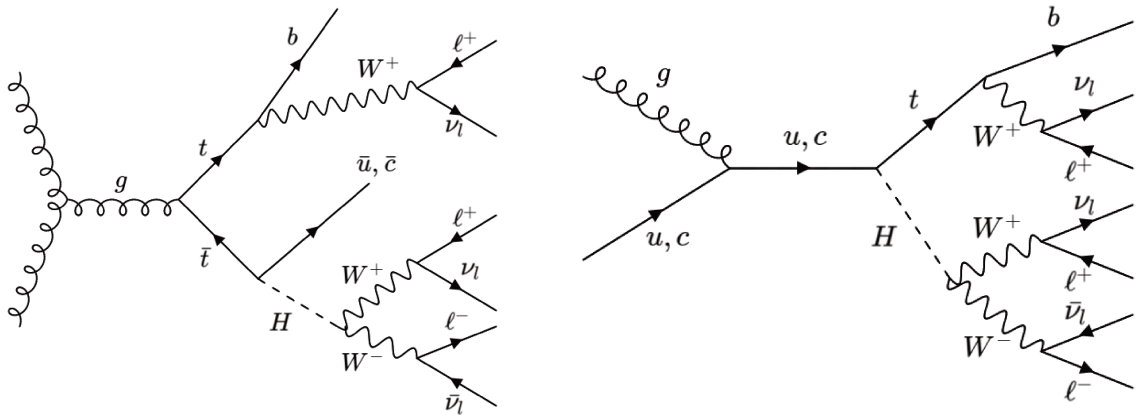

Figure 5.18: Feynman diagrams for tH-FCNC production in the pair (left) and single top (right) production modes, in the 3ℓ final state. The tqH FCNC vertex is present at the decay and at the production, respectively.

Searches for tH-FCNC interactions were already conducted based on Run 1 data by the ATLAS and CMS collaborations [305–307]. During Run 2, CMS only published results in the $H \to b\bar{b}$ channel so far [304].

The most stringent upper limits on the tH-FCNC branching ratios are set by the combination [308] of ATLAS analyses targeting the decay modes $H \to b\bar{b}$, $H \to \tau\tau_{had}$,

$H \to \gamma\gamma$ and $H \to WW^* + \tau_{lep}\bar{\tau}_{lep} + ZZ^*$, based on the 2015 + 2016 dataset corresponding to an integrated luminosity of 36.1 fb^{-1}. The current best observed (expected) 95% CL upper limits are $\mathcal{B}$(t $\to$ Hu) = 0.12% (0.083%), and $\mathcal{B}$(t $\to$ Hc) = 0.11% (0.083%).

The corresponding values from the analysis [309] targeting the $2\ell SS$ and 3ℓ multilepton final states are $\mathcal{B}$(t $\to$ Hu) = 0.19% (0.15%) and $\mathcal{B}$(t $\to$ Hc) = 0.16% (0.15%). It is noteworthy that the ATLAS analyses only consider the TT mode, taking advantage from the fact that its cross section increases much more than that of the ST mode when increasing $\sqrt{s}$ from 8 TeV to 13 TeV. However, the ST mode can still significantly contribute to the total cross section of the FCNC-Hut signal, with a relative contribution of about 20%.

Like the main tH analysis, this search targets both the $2\ell SS$ and 3ℓ final states (electrons or muons, with a contribution from τ leptons), and the Higgs boson decay modes $H \to WW^*$, $\tau\bar{\tau}$, ZZ^*. It uses the dataset collected in 2017 by CMS corresponding to an integrated luminosity of 41.5 fb^{-1}.

Signal simulation

The signal is simulated at leading order with MADGRAPH5_aMC@NLO. It is simulated separately for the FCNC-Hut and FCNC-Hct signals, and in the ST and TT modes. Additional partons are added to the initial LO hard process for the TT mode. In the case of the ST mode, no additional partons are included, as this would lead to interferences with TT diagrams.

Top quarks are forced to decay leptonically, and Higgs bosons are forced to decay as $H \to WW^*$, $\tau\bar{\tau}$, ZZ^*. A small caveat is the absence of top quark decays to τ leptons in the samples. Hence τ leptons are not considered in this analysis, and the corresponding branching ratio is not accounted for in the cross section calculation. The input cross sections of the FCNC signal samples are listed in Table 5.9. Following the convention used in the ATLAS combination, they are calculated for an arbitrary branching ratio $\mathcal{B}(t \to Hq)$ = 1%. The background samples are the same as the ones listed in Table 5.3, and the NPL and charge misidentification backgrounds are estimated as was described in Sec. 5.6.

Table 5.9: Input cross sections for the signal samples, corresponding to an arbitrary branching ratio for the anomalous tqH coupling of 1%. Relative proportion are indicated for the FCNC-Hut and FCNC-Hct signals, and for the ST and TT modes.

	σ_t (pb)	$\sigma_{t\bar{t}}$ (pb)	$\sigma_{t+t\bar{t}}$ (pb)
FCNC-Hut	0.33 *(23 %)*	1.09 *(77 %)*	1.42
FCNC-Hct	0.046 *(4 %)*	1.09 *(96 %)*	1.14

5.12.2 Differences with the main analysis

Object and event selections

The objects used in this search are the same as in the main tH analysis (see Sec. 5.3), except that only central jets with $|\eta| < 2.4$ are considered. Indeed, contrary to the tHq process, the tH-FCNC processes are not expected to feature a recoiling jet at large pseudorapidity.

The event selection is the same as in the main tH analysis (see Sec. 5.4), except for a few changes. The jet multiplicity requirements are chosen based on the exact numbers of jets expected in the ST and TT modes. To increase the acceptance of signal events containing initial- or final-state radiations, the presence of up to 1 additional jet is considered.

The modifications are the following:

- $2\ell SS$ **channel**
  - Events must contain either 2, 3 or 4 jets in total, among which exactly 1 b-tagged jet;
  - The $2\ell SS$ dielectron channel (ee) is included in this analysis. The dielectron invariant mass must satisfy $|m_{ee} - m_Z| > 10$ GeV.
- 3ℓ **channel**
  - Events must contain either 1, 2 or 3 jets in total, among which exactly 1 b-tagged jet;
  - Events are rejected if they contain an OSSF pair of loose leptons having an invariant mass within 10 GeV around the Z boson mass (as in the $t\bar{t}H$ search, while the threshold was optimized to 15 GeV in the tH analysis).

In addition to the data-to-prediction comparisons shown in Fig. 5.6 in the $t\bar{t}Z$ and WZ control regions, comparisons are shown in Fig. 5.19 in a "Z control region" enriched in these 2 backgrounds. This CR is defined by simply reverting the Z boson veto in the 3ℓ SR selection ($|m_{\ell\ell} - m_Z| < 10$ GeV). The data and simulation are in very good agreement.

Multivariate analysis

Although the strategy for signal discrimination is the same as in the main tH analysis, the 4 BDTs (against the $t\bar{t}V$ and $t\bar{t}$ backgrounds, in the $2\ell SS$ and 3ℓ channels) were completely re-optimized.

Different input variables were selected to train each BDT, based on their separation power between the signal and background processes in each channel. All input variables are listed and described in Table 5.10. The same input variables are used to discriminate the FCNC-Hut and FCNC-Hct signals, but the BDT training is done separately for each signal.

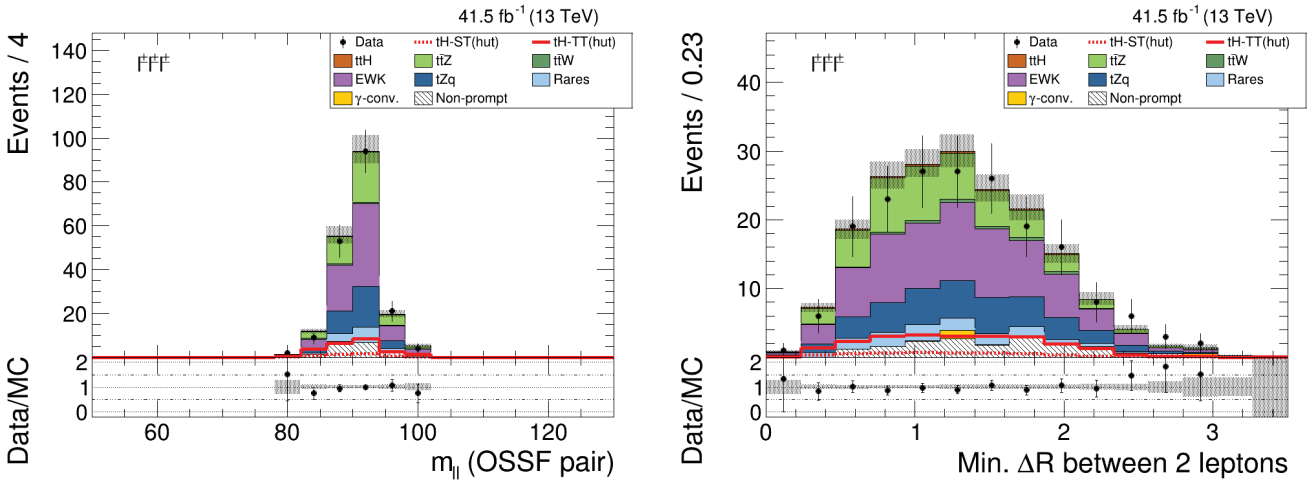

Figure 5.19: Pre-fit data-to-prediction comparison of input variables in the Z control region.

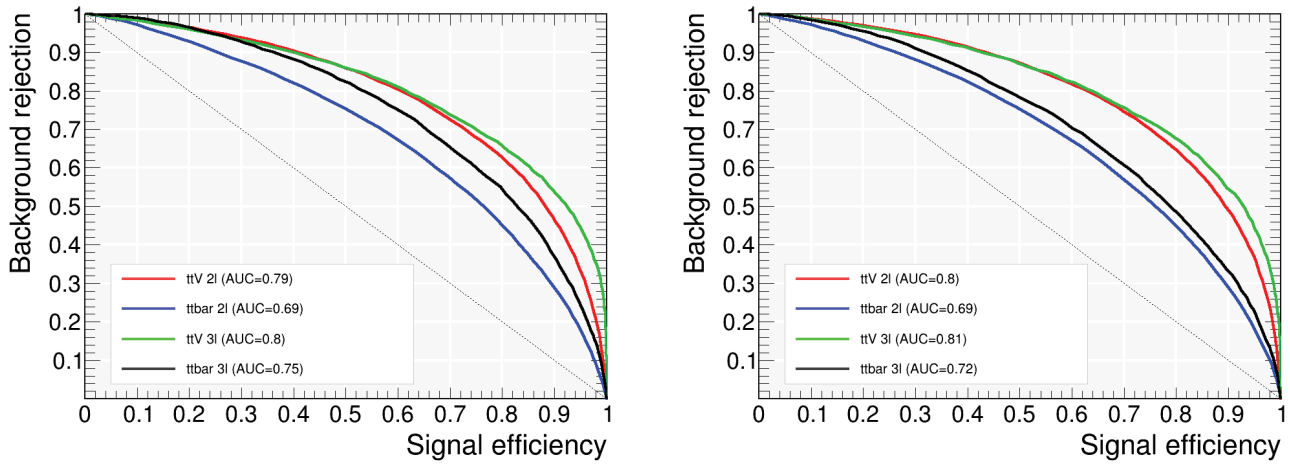

Figure 5.20: Comparison of the ROC curves of the 4 final BDTs trained with the FCNC-Hut (left) and FCNC-Hct (right) signals.

Table 5.10: Input variables of the 4 BDTs used for signal extraction. A cross indicates whether a variable is used in a given training or not.

Description	$\mathbf{t\bar{t} - 2\ell SS}$	$\mathbf{t\bar{t} - 3\ell}$	$\mathbf{t\bar{t}V - 2\ell SS}$	$\mathbf{t\bar{t}V - 3\ell}$
TOTAL	11	12	13	14
Number of selected jets	x	x	x	x
Trilepton (or dilepton) invariant mass	x	x	x	x
Top quark mass			x	x
Ratio between the p_T of the trailing lepton and its closest jet	x			x
η of the most forward lepton	x			
ℓ_W asymmetry ($q(\ell_W) \cdot \lvert\eta(\ell_W)\rvert$)	x			
Minimum ΔR between the leading lepton and any jet	x	x		
Minimum ΔR between the subleading lepton and any jet	x	x		
Transverse mass of the leading lepton	x		x	x
Minimum ΔR between selected leptons	x	x	x	x
p_T of the most forward jet	x		x	
ΔR between the b-tagged jet and recoil jet			x	
p_T of the leading lepton			x	x
p_T of the subleading lepton			x	x
p_T of the trailing lepton		x		x
Invariant mass of the OSSF lepton pair closest to the Z peak		x		x
$\Delta\phi$ between the 2 leptons forming the hardest OS pair		x		
Hadronic Top Tagger		x		x
Maximum ΔR between any 2 jets		x		
Sum of the lepton's charges		x		
W boson transverse mass				x
$\not{E}_T$			x	x
p_T of the leading jet			x	x
p_T of the subleading jet	x	x	x	
p_T of the subsubleading jet			x	

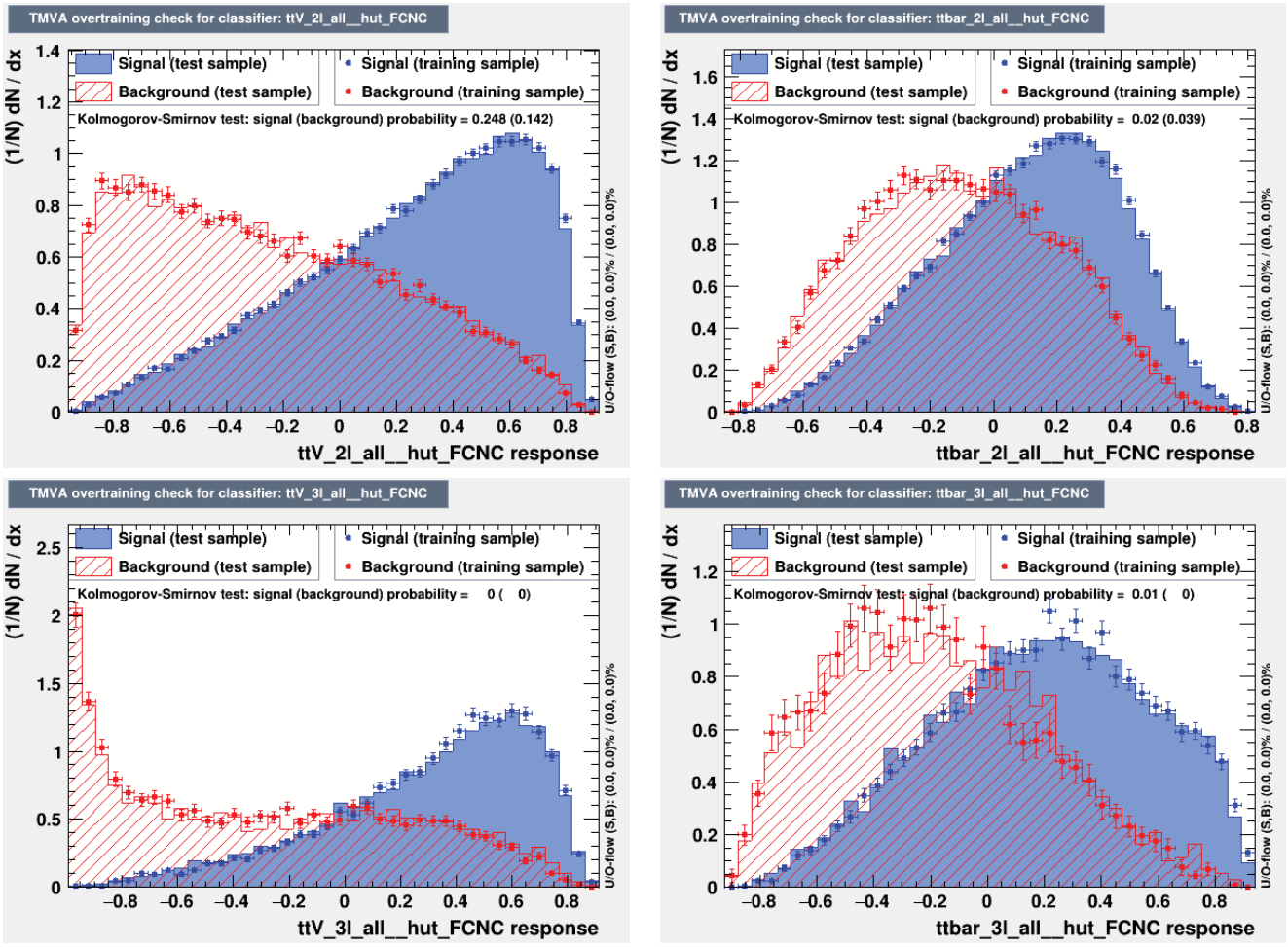

Figure 5.21: Normalized outputs of the BDT-tt̄V-2ℓSS (top left), BDT-tt̄-2ℓSS (top right), BDT-tt̄V-3ℓ (bottom left) and BDT-tt̄-3ℓ (bottom right), for the FCNC-Hut signal (blue) and the backgrounds (red).

ROC curves illustrating the performance of all BDTs are shown in Fig. 5.20. The responses of the BDTs to the FCNC-Hut signal and the backgrounds are presented in Fig. 5.21, and show no sign of overtraining.

As part of the optimization studies, it was tried to split the signal regions based on the jet multiplicities of events, into ST-enriched and TT-enriched sub-regions. Dedicated BDTs were trained with the corresponding signal in each sub-region, and the input variables were optimized separately.

Although this may be an interesting option to investigate further as part of a future analysis, as some gain of performance could be observed in the ROC curves, the limited improvement of $\sim$ 5% on the expected limits did not motivate the implementation of this change as part of this work.

Signal extraction

The 2D→1D bin mapping of the BDT discriminants used for signal extraction in the $2\ell SS$ and 3ℓ channels are optimized with the procedure described in Sec. 5.9.2.

Upper limits are set on the branching ratios $\mathcal{B}(t \to Hq)$ using the CL_s method. The signals are probed independently from one another; therefore, when searching for the FCNC-Hut (FCNC-Hct) signal, the branching ratio of the FCNC-Hct (FCNC-Hut) signal is assumed to be null.

Systematic uncertainties

The systematic uncertainties included as nuisance parameters in the maximum likelihood fit are the same as in the main tH analysis, except that:

- The uncertainty on the normalization of the tZq background is conservatively increased to 15% (instead of the 5% uncertainty related to the theoretical calculation);
- All systematic uncertainties related to closure tests of the fake rate method (see Sec. 5.6), impacting the shape and yield of the NPL background, are conservatively doubled with respect to what is used in the tH analysis. This accounts for the fact that such closure tests were not performed in the specific signal regions of the present analysis.

5.12.3 Results and discussion

Results

After applying the event selection on the dataset, 179 events are observed in the 3ℓ channel, 201 in the $\mu\mu$ channel, 400 in the μe channel, and 156 in the ee channel. Data-to-simulation comparisons for the BDT-based discriminants are shown in Fig. 5.22, before and after the maximum likelihood fit used to extract the results for the FCNC-Hut signal. Since the data disfavour the presence of the signal, it can be seen on the post-fit figures that its cross section is set to 0.

The observed 95% CL upper limits are $\mathcal{B}(t \to Hu) < 0.072\%$ and $\mathcal{B}(t \to Hc) < 0.085\%$. The corresponding expected 95% CL upper limits are $\mathcal{B}(t \to Hu) < 0.086\%$ and $\mathcal{B}(t \to Hc) < 0.11\%$. As expected, the tuH coupling is better constrained, mostly due to the enhanced sensitivity in the ST mode.

The post-fit central values and uncertainties of all the nuisance parameters included in the MLE are shown in Fig. 5.23 for both signals. The data favour a small, negative value of the best fit signal strength for both signals, compatible with 0.

The sensitivity of the analysis is predominantly limited by uncertainties related to the NPL background estimation. The figure 5.24 compares the best fit signal strengths observed in individual channels and their combination. The highest sensitivity is achieved in the μe channel.

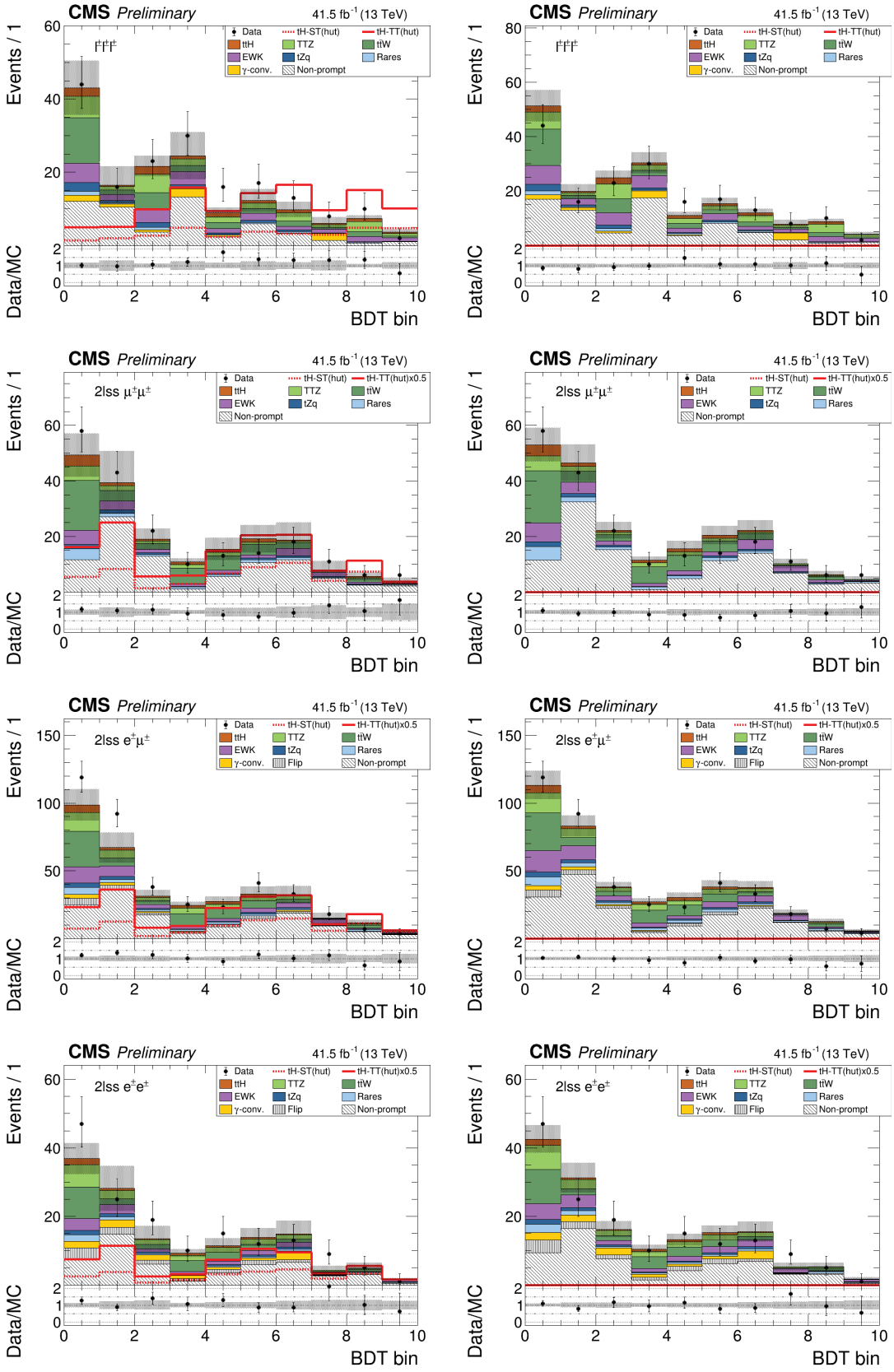

Figure 5.22: Pre-fit (left) and post-fit (right) data-to-prediction comparisons for the BDT-based discriminants in the 3ℓ (1^{st} row), $\mu\mu$ (2^{nd} row), μe (3^{rd} row) and ee (4^{th} row) channels. Only the FCNC-Hut signal is considered.

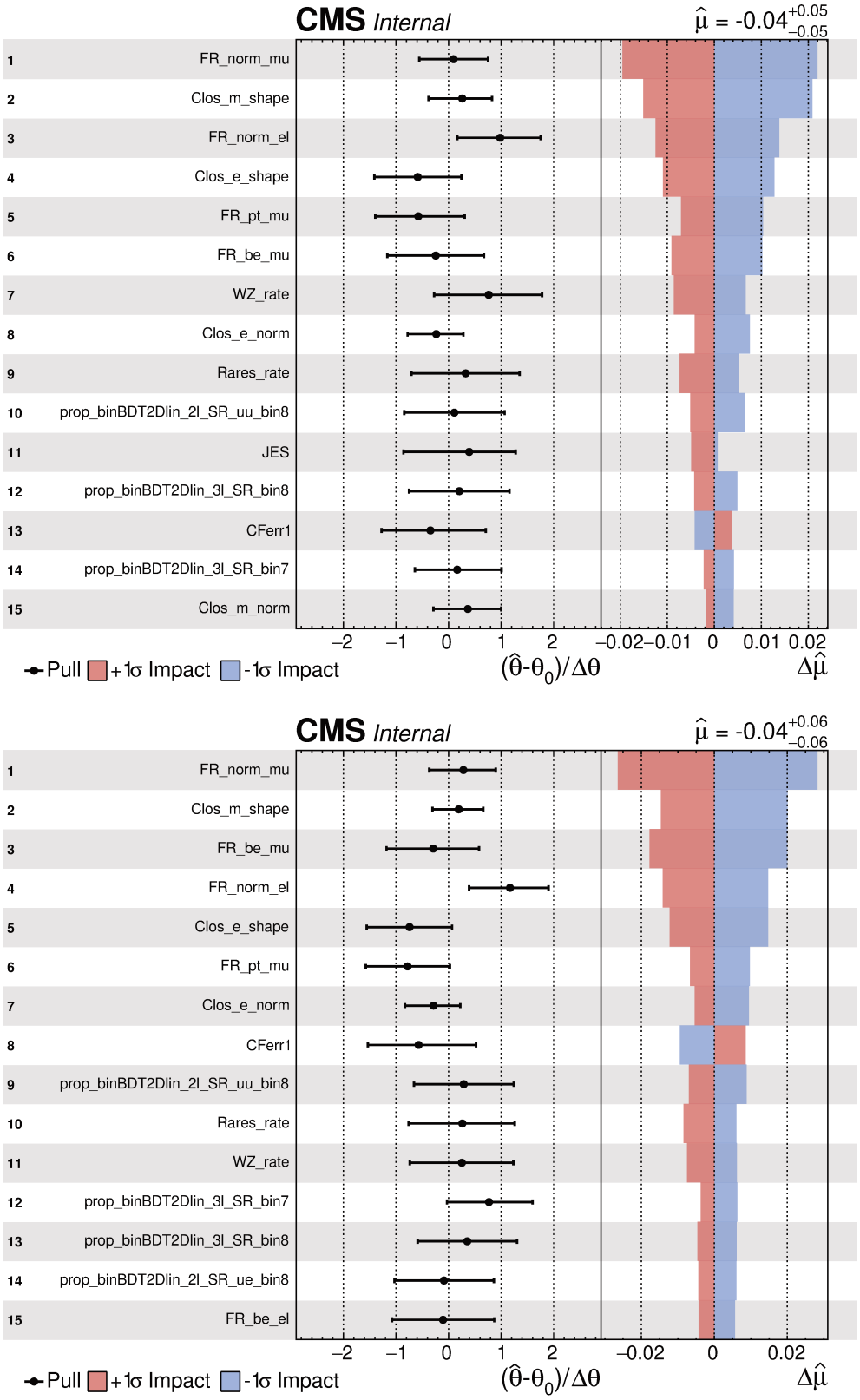

Figure 5.23: Post-fit central values and uncertainties of the nuisance parameters, ranked by decreasing impact on the signal strength. The fit is performed using either the FCNC-Hut (top) or FCNC-Hct (bottom) signal.

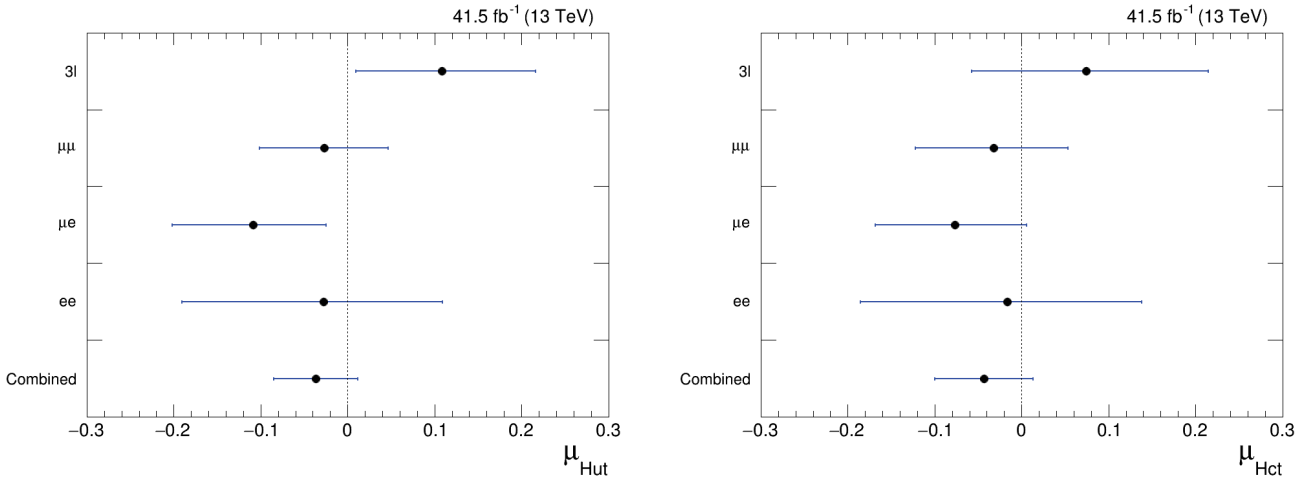

Figure 5.24: Comparison of the signal strengths and their uncertainties obtained in the individual channels and their combination, for the FCNC-Hut (left) and FCNC-Hct (right) signals.

Discussion

This analysis sets the most stringent upper limits to date on the Hqu and Hqc FCNC interactions. The figure 5.25 compares the observed and expected 95% CL upper limits in the individual channels and their combination.

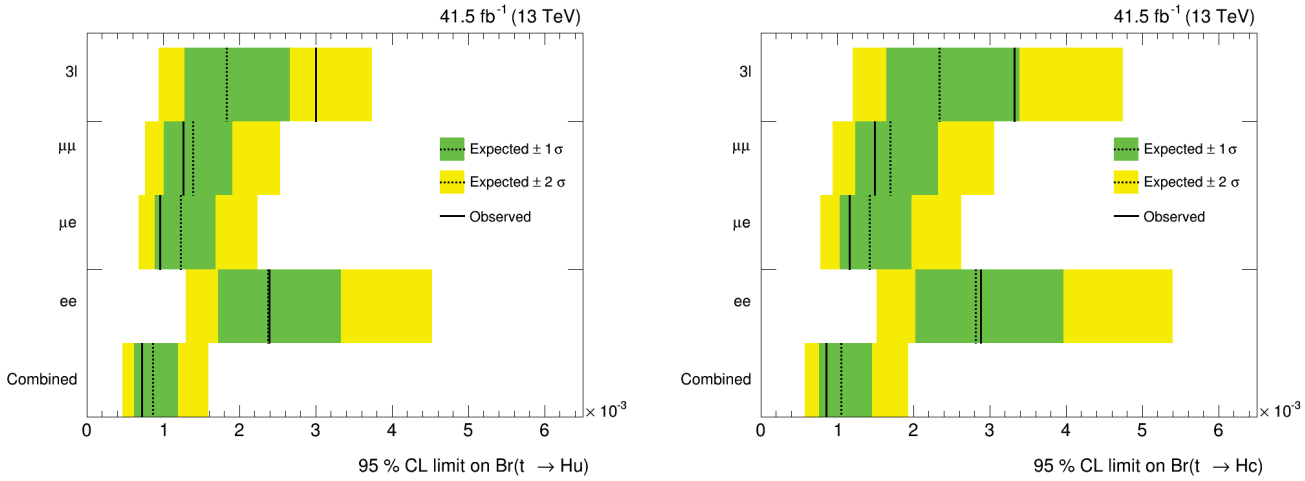

Figure 5.25: 95 % CL upper limits on $\mathcal{B}(t \to Hu)$ (left) and $\mathcal{B}(t \to Hc)$ (right) for the individual channels and their combination. Observed limits (solid lines) are compared to the expected limits under the background-only hypothesis (dotted lines) and the corresponding $\pm 1\sigma$ and $\pm 2\sigma$ intervals.

A cross check study was performed to better understand how this analysis compares with the ATLAS analysis [309] in multilepton final states, which uses a similar overall strategy. The $2\ell SS$ and 3ℓ event selections described in the ATLAS paper were reproduced, and BDTs were re-trained in these regions. The luminosity was reduced

to 36.1 fb^{-1}, and only the TT mode was considered. This results in an expected limit $\mathcal{B}(t \to Hu) < 0.15\%$ for the FCNC-Hut signal, very compatible with the ATLAS limit $\mathcal{B}(t \to Hu) < 0.16\%$. The comparison was only performed for this signal.

However, when comparing yields with the ATLAS analysis, significant differences are found for some processes. Most strikingly, the present analysis seems to be much less contaminated by the NPL background, by about a factor 3. Although better performance can be expected in the present analysis due to the use of the state-of-the-art lepton MVA algorithm to select leptons, further discussions between ATLAS and CMS analysts may be needed in the future to better understand this potentially detector-related difference.

The procedure for the estimation of the NPL background was extensively verified in the $t\bar{t}H$ and tH analyses. Prior to unblinding the present analysis, the data were compared to the predictions in the most background-like bins of the BDTs trained against the $t\bar{t}$ background. These bins are expected to receive a sizeable contribution from the NPL background, and this cross check confirmed that it is indeed well modelled.

This analysis represent a first step towards the upcoming combination of the 2016, 2017 and 2018 datasets to set limits on the tH-FCNC process. Efforts have been dedicated to setting up a general framework in view of this combination, and these promising results are a strong incentive to intensify work in that direction. CMS colleagues will participate in this combination using the same framework as the present analysis. The planned combination with other CMS analyses targeting different decay modes of the Higgs boson is expected to further improve these upper limits, up to the point where it may be possible to start ruling out the predictions of some BSM scenarios (see Fig. 5.17).

Conclusion

Summary

This thesis presents four analyses based on data collected by the CMS experiment during the Run 2 of the Large Hadron Collider (LHC) at a centre-of-mass energy $\sqrt{s} = 13$ TeV. The record energy and high luminosity achieved at the LHC allow for the study of very rare processes, such as the ones at the core of this work, namely the associated production of a single top quark and a Z boson or a Higgs boson (tZq and tH).

The study of these processes is well-motivated, as they provide unique insights on important SM parameters in the top quark and Higgs boson sectors, most notably regarding the couplings of the top quark to the Z and Higgs bosons. They are also sensitive to the possible existence of several processes of new physics, like flavour changing neutral currents (FCNCs), and hence can be used to probe scenarios beyond the standard model (BSM) which aim to address the shortcomings of the SM.

On the other hand, the excellent performance of the LHC machine requires to operate the detectors under harsh conditions. I worked on a study aimed at monitoring the ageing of the sensors of the CMS strip tracker under irradiation, as their properties are expected to be altered in the long-run.

I performed the major part or entirety of these analyses, which gave me the opportunity to work on various aspects of a high-energy physics analysis, from the processing of the data up to the final results. As the tZq and tH analyses target rare signals in the presence of much larger backgrounds, a particular emphasis was put on the design of the event selections and the multivariate analyses (MVA) in order to improve the signal extraction. Moreover, an important effort was dedicated to the study and estimation of the challenging nonprompt lepton (NPL) background, which requires the use of data-driven techniques.

Chapter 3 described a study aimed at monitoring the ageing of the silicon strip tracker, using dedicated data collected during frequent bias voltage scans.

It was shown how the study of observables such as the charge or width of the clusters created by ionising particles in a silicon sensor, as a function of the bias voltage applied to the sensor, can be exploited to infer its full depletion voltage V_{FD}. The full depletion voltage is one of the main parameters of a silicon sensor, and impacts its performance. This parameter is expected to decrease with irradiation, until the point where the sensor "type-inverts" and V_{FD} increases again, potentially degrading the performance of the sensor. Although the ageing of the tracker was anticipated and its sensors were designed to be sufficiently radiation-hard to cope with the LHC environment, it is important to constantly ensure that the situation is under control and to improve our understanding of the complex phenomena at play.

I took in charge this analysis during the 3 years of my PhD, and mostly focused on improving the method used to extract the value of V_{FD} from the data. This resulted in a robust algorithm which allowed extending the analysis from the tracker barrels to the endcaps, and more generally it improved the reliability of the results. The overall agreement with the simulation is satisfying, and several results were officially approved by CMS.

Chapter 4 describes a search for the tZq process, which I took in charge from the event selection up to the final results. It targets events in the trilepton final state, either electrons or muons, and uses the dataset collected in 2016 corresponding to an integrated luminosity of 36.1 fb^{-1}. This process is sensitive to the top-Z and WWZ couplings. Moreover, the precise measurement of its cross section could reveal the presence of new physics, such as vector-like quarks or FCNC interactions. The tZq process is also important to characterize because it represents an irreducible background to other important searches ($t\bar{t}Z$, tH, etc.).

The design of this study was substantially improved with respect to the previous Run 1 analysis, and many options were investigated to improve the sensitivity to this rare signal. Most notably, extensive studies were carried out to refine the modeling of the NPL background, which represents the main factor limiting the sensitivity of this analysis. Dedicated optimization studies led to a MVA achieving good performance, based on boosted decision trees (BDTs) trained to recognize the specific features of signal events. Furthermore, variables obtained with the matrix element method (MEM) were included in the BDTs, and significantly improved their performance.

The signal was extracted by performing a binned maximum likelihood estimation (MLE), simultaneously in the signal region and in control regions enriched in the major $t\bar{t}Z$, WZ+jets and NPL backgrounds, in order to better constrain their normalizations directly from the data. This resulted in an observed cross section for the tZq process of $\sigma(pp \to t\ell^+\ell^- q) = 123^{+33}_{-31}$ (stat) $^{+29}_{-23}$ (syst) fb, where ℓ stands either for electrons, muons, or τ leptons. This is in agreement with the SM prediction. The observed (expected) significance is 3.7σ (3.1σ), corresponding to the first statistical evidence for the existence of the tZq process. These results got published in the journal Physics Letter B [271], and

were presented at conferences. Other analyses at CMS are continuing this work, and the tZq process was recently observed for the first time.

Chapter 5 describes a search for the tH process, which is the only process sensitive at leading-order at the same time to the magnitude of the top-Higgs coupling modifier κ_t, and to its sign relative to the vector boson-Higgs coupling modifier κ_V. Depending on whether the single top quark is produced via the t-channel or the tW-channel, the process is denoted tHq or tHW respectively. This analysis is designed to have maximal sensitivity to the tHq process because of its larger cross section and to exploit its distinctive kinematic features. However, the tHq, tHW and $t\bar{t}H$ processes are all considered as signals for the extraction of results, as all these processes are sensitive to the value of κ_t.

Within the SM ($\kappa_t = \kappa_V = 1$), a negative interference term arising in the leading order diagrams of the tHq and tHW processes gives them small cross sections, below the current sensitivity of CMS. However, in case the relative sign or phase between κ_t and κ_V would differ from the SM predictions, these interferences may become constructive. In particular, in the inverted top coupling (ITC) scenario corresponding to $\kappa_t = -\kappa_V = -1$, the cross sections of these processes are expected to increase tenfold, well within reach of the current sensitivity. Thus this study is primarily aimed at better constraining the possible values of the top-Higgs coupling, and to set an upper limit on tH production.

I implemented the entire analysis. As was made clear in Chapter 5, a few steps were performed together with another PhD colleague also performing the tH analysis, so that we issued a common set of final results. I dedicated an important effort to the synchronization of my framework with that used by the group searching for the $t\bar{t}H$ process, also used by the other PhD. This analysis targets events in the trilepton and same-sign dilepton final states (3ℓ and $2\ell SS$, where ℓ stands either for electron or muon), and the Higgs boson decays to WW^*, $\tau\bar{\tau}$ and ZZ^*. It is based on the dataset collected in 2017 corresponding to an integrated luminosity of 41.5 fb^{-1}.

This analysis follows closely the search for $t\bar{t}H$ in multilepton final states based on the same dataset. Most notably, it follows a similar overall strategy, takes advantage of the state-of-the-art lepton MVA algorithm developed by the $t\bar{t}H$ group to identify prompt leptons, and the estimation of the reducible backgrounds is done in a similar way.

I optimized the MVA by including additional discriminating input variables in the BDT training, some obtained from the MEM, and studied the influence of the binning of the discriminants on the final results. I investigated sources of systematic related to the theory predictions of the cross sections. I also carried out studies in view of the upcoming combination with the search for the $t\bar{t}H$ process.

The signal is extracted from a binned MLE to BDT discriminants in 3 signal regions. For the SM scenario, the observed 95% CL upper limit on the combined tH + $t\bar{t}H$ cross section is 0.52 pb, corresponding to 2.87 times the prediction. For the ITC scenario, the observed 95% CL upper limit on the combined tH + $t\bar{t}H$ cross section is 0.80 pb, corresponding to 1.81 times the prediction. These limits account for the relevant branching ratio $H \to WW^* + \tau\bar{\tau} + ZZ^*$.

Moreover, a likelihood scan is performed as a function of κ_t, assuming $\kappa_V = 1$, resulting in the exclusion at 95% CL of values of κ_t outside the ranges of about [-1.4, -0.7] and [0.7, 1.9], with the data favouring a positive value of κ_t by about 1.5σ. Likewise, a likelihood scan as a function of the CP-violating parameter $\cos(\alpha)$ indicates that the data favour a purely CP-even coupling of the Higgs boson to the top quark over a purely CP-odd coupling by about 2σ. Upper limits on the production cross section of the tH process alone are also derived as a function of the κ_t and $\cos(\alpha)$ parameters.

In addition, I re-adapted the tH analysis in order to search for top-Higgs FCNC interactions. Although such interactions are strongly suppressed within the SM, several BSM scenarios predict significant enhancements of their branching ratios $\mathcal{B}(t \to Hq)$ (q=u,c). This analysis also targets the 3ℓ and $2\ell SS$ final states, with adjusted event selections. The MVA was entirely re-optimized to search for these signals.

The observed 95% CL upper limits are $\mathcal{B}(t \to Hu) < 0.072\%$ and $\mathcal{B}(t \to Hc) < 0.085\%$, which outperform the current best limits on these branching ratios.

These tH and tH-FCNC analyses were reviewed and approved in the context of thesis endorsements carried out by the CMS Higgs and Top groups respectively.

Outlook

It has been a decade since the LHC delivered its first collisions, marking the beginning of a new era in high-energy collider physics. The outstanding performance of this record-breaking machine, which delivered more than its target goal of 150 fb^{-1}, and its versatility in terms of energy and beam configuration, established the great reach of the LHC physics programme. Likewise, the excellent performance and availability of all detectors lived up to the expectations, and already allowed setting several milestones in the field.

The Run 1 data-taking period (2009–2013) led to the landmark discovery of the Higgs boson by ATLAS and CMS, and saw the publication of new results in many diverse areas. Over the course of Run 2 (2015–2018), the experiments collected data at an ever-faster rate, produced at the tremendous centre-of-mass energy $\sqrt{s} = 13$ TeV which notably enhanced the production cross sections of processes involving the Higgs boson or the top quark. The measurements of the properties of these 2 particles were significantly refined, and the use of state-of-the-art analysis techniques allowed establishing for the first time their coupling at tree-level. Overall, the results obtained at the LHC have further validated the predictions of the SM up to unprecedented energy scales.

The ongoing long shutdown (LS2) period will be used to upgrade the entire injection complex delivering bunches to the LHC. This will give physicists the opportunity to perform "legacy" analyses based on the entire Run 2 dataset, with the aim of making the most out of the collected data and leaving no stone unturned. LHC collisions will resume at $\sqrt{s} = 14$ TeV in late 2021, for a Run 3 at an instantaneous luminosity of $\sim 2\text{–}3 \cdot 10^{34}$ $\text{cm}^{-2}\text{s}^{-1}$. This will increase the integrated luminosity of the full LHC dataset to ~ 300 fb^{-1}.

The first bias voltage scans taken durin Run 3 will be particularly interesting to study, as they may soon confirm that parts of the strip tracker have reached type-inversion. This will also depend on the magnitude of annealing during the shutdown period. As the full depletion voltages of the silicon sensors start increasing again, the analysis presented in Chapter 3 will progressively regain sensitivity, and the trend of V_{FD} could be compared to the simulation over a wider range of fluence.

The current shutdown also paves the way towards the planned "Phase-II upgrade" (2024-2026), which will mark the beginning of the High-Luminosity LHC (HL-LHC, 2026–2037) [89]. The HL-LHC will collide protons at $\sqrt{s} = 14$ TeV with an instantaneous luminosity at least five times greater than that of the LHC, and is expected to deliver an integrated luminosity of ~ 3000 fb^{-1}.

To this end, among other improvements, new magnets made of a superconducting niobium-tin (Nb_3Sn) compound will be installed, some already during LS2. This technology can withstand higher electrical currents, thus generating stronger magnetic fields to better focus the beams. Additionally, *crab cavities* will be used to enlarge the overlap area between the colliding bunches, thus increasing the luminosity.

Furthermore, the detectors will be upgraded to cope with the higher irradiation, and most of all to keep on providing precise measurements despite an average pileup rate of 140–200 (compared to 40 currently). Notably, the CMS tracker will be replaced and will cover an extended pseudorapidity range up to $|\eta| \simeq 4$ with increased granularity. The trigger system will be improved, new GEM chambers will be included into the muon system, time-of-flight detectors will be added into the calorimeters to reject pileup events, etc.

Combined with improvements in the theoretical understanding and in extraction techniques, these upgrades are expected to benefit many precision measurements [310, 311], e.g. in the Higgs boson and electroweak sectors. Following CERN's primary mission, the HL-LHC will thus expand our knowledge at the electroweak scale, while pushing back the limits of cutting-edge technologies.

The tenfold increase of the available statistics at the HL-LHC will also significantly benefit single top quark measurements. Based on the tZq cross section measurement presented in Chapter 4, a phenomenological study [312] assessed the current sensitivity of this process to the relevant EFT operators using a simplified procedure. While it concludes that the current sensitivity on the inclusive tZq cross section is not yet sufficient to probe these operators beyond existing limits set by other processes, a prospective study motivates the precise differential measurement of the tZq cross section, as the effects of EFT operators are significantly amplified e.g. in the tail of the top quark p_T distribution.

Using the full HL-LHC dataset, such a measurement may achieve a precision sufficient to constrain these operators beyond existing limits, thus providing valuable insights on BSM scenarios. Another goal of the HL-LHC upgrade is to set more stringent bounds on (or find evidence of) WWZ anomalous gauge coupling and FCNC interactions [310]. This motivates the further study of the tZq process since it is sensitive to

these effects, and because it is an irreducible background for processes where these effects can be looked for.

As mentioned in Chapter 5, the upcoming Run 2 legacy combination of the tH and $t\bar{t}H$ analyses will feature an unprecedented sensitivity to the top quark Yukawa coupling without making any assumption on new physics, and could rule out a large range of values for κ_t. Moreover, prospective studies [313] show that the increase of the available statistics at the end of Run 3 may lead to the exclusion of negative values of κ_t at more than 99% CL, and at more than 5σ with the full HL-LHC dataset, assuming there is no new physics in the data. Otherwise, these datasets may provide evidence for a negative value of κ_t.

Projections for the upper limit on the tHq production rate suggest that this process could be observed at HL-LHC, and motivate a precise simultaneous measurement with the $t\bar{t}H$ cross section in order to get optimal sensitivity. Moreover, the sensitivity to κ_t may further improve by performing a combined analysis including other processes. For instance, upper limits on the top quark Yukawa were recently obtained by a CMS differential measurement of the $t\bar{t}$ cross section [314].

The tHW process has a cross section about 5 times smaller than that of tHq in the SM, and is also expected to become accessible at HL-LHC depending on the improvements achieved regarding systematic uncertainties and signal extraction techniques.

Another interesting rare process is four-top quark production. This mechanism is sensitive to various BSM scenarios predicting significant enhancements of its cross section, and has the highest sensitivity to the four-top-quark EFT operator [310]. This production mode represents another powerful probe of the top Yukawa coupling, without making assumptions on the Higgs boson decays. At $\sqrt{s} = 14$ TeV, this process has a cross section $\sigma(pp \to t\bar{t}t\bar{t}) \sim 15$ fb comparable to that of tHW. A prospective study [315] carried out by ATLAS suggests that the observation of this complex process could already be achieved using only 300 fb^{-1} of HL-LHC data.

Finally, searches for FCNC interactions involving the top quark are also expected to yield exciting results in the foreseeable future. The promising results obtained as part of this work represent a first step towards the upcoming combination of Run 2 legacy analyses targeting several decay modes of the Higgs boson, which will push further the current best limits or could potentially lead to a discovery.

Prospective studies [316] foresee that a sensitivity of the order of $\mathcal{B}(t \to Hq) < \mathcal{O}(10^{-4})$ could be achieved with the full HL-LHC dataset, which would be sufficient to exclude some BSM scenarios like the 2HDM or extra-dimensions models.

Conclusion (FR)

Résumé

Ce manuscript présente quatre analyses basées sur les données collectées par l'expérience CMS durant le Run 2 du Grand Collisionneur de Hadrons (LHC) à une énergie dans le centre de masse $\sqrt{s} = 13$ TeV. L'énergie record et la haute luminosité atteintes au LHC permettent d'étudier des processus extrêmement rares tels que ceux qui sont au centre de ce travail de thèse, à savoir la production associée d'un quark top solitaire et d'un boson Z ou un boson de Higgs (tZq et tH).

Plusieurs raisons justifient l'étude de ces processus. Premièrement, cela permet d'obtenir des informations sur des paramètres importants du model standard (SM) qui sont liés au quark top et au boson de Higgs, et en premier lieu les couplages du quark top au boson Z et au boson de Higgs. Ces processus sont également sensibles à l'éventuelle existence de plusieurs processus de nouvelle physique, tels que les changements de saveur par courant neutre (FCNC) ; ils peuvent donc être utilisés pour sonder différents scénarios "au-delà du modèle standard" (BSM) qui visent à pallier les lacunes du SM et à le dépasser.

D'autre part, les remarquables performances du LHC nécessitent de faire fonctionner les détecteurs dans des conditions extrêmes. J'ai notamment travaillé sur une étude visant à surveiller le vieillissement avec l'irradiation des capteurs du trajectographe à pistes de silicium, car il est attendu que leurs propriétés s'altèrent au cours du temps.

J'ai réalisé la majeure partie ou l'intégralité de ces analyses, ce qui m'a donné l'opportunité de travailler sur différents aspects propres aux analyses de physique des hautes énergies, depuis le traitement des données jusqu'aux résultats finaux. Etant donné que les analyses tZq et tH recherchent des signaux rares en présence de bruits de fond largement plus conséquents, l'accent a été mis sur la définition de la sélection des évènements et l'analyse multivariée (MVA) afin d'améliorer l'extraction du signal. De plus, un effort important a été consacré à l'étude et l'estimation des bruits de fond contenant un lepton *nonprompt* (NPL) directement à partir des données.

Le Chapitre 3 décrit une étude visant à surveiller l'évolution du vieillissement du trajectographe à pistes de CMS, à partir de données collectées régulièrement au cours de balayages en tension.

Il a été montré que des observables telles que la charge ou l'épaisseur des *clusters* générés par le passage de particules ionisantes dans un capteur de silicium, en fonction de la tension appliquée au capteur, peuvent être exploitées pour déterminer la *tension de déplétion complète* V_{FD}. La tension de déplétion complète est l'un des principaux paramètres d'un capteur de silicium, et peut influer sur ses performances. Il est attendu que ce paramètre diminue progressivement avec l'irradiation, jusqu'au phénomène "d'inversion de type" (*type inversion*, $V_{FD} = 0$) à partir duquel V_{FD} commence à augmenter, ce qui pourrait potentiellement dégrader les performances des capteurs. Bien que le vieillissement du trajectographe ait été anticipé avant sa construction et que ses capteurs soit conçus pour être suffisamment résistants à l'irradiation pour fonctionner dans l'environnement du LHC, il est primordial de constamment s'assurer que cette évolution est sous contrôle, et d'améliorer notre compréhension des phénomènes complexes qui entrent en jeu.

J'ai pris en charge cette analyse pendant les 3 années de ma thèse, et me suis particulièrement concentré sur l'amélioration de la méthode utilisée pour extraire la valeur de V_{FD} à partir des données. Ce travail a donné lieu à un algorithme robuste qui a permis d'étendre l'analyse à l'ensemble du sous-détecteurs, notamment aux couches externes pour lesquelles moins de données sont collectées, et qui a permis d'améliorer la précision des résultats. De manière générale l'accord avec la simulation est satisfaisant, et plusieurs résultats ont été officiellement approuvés par la collaboration CMS.

Le Chapitre 4 décrit une recherche de la production associée d'un quark top et d'un boson Z (tZq), que j'ai prise en charge depuis la sélection des évènements jusqu'aux résultats finaux. Les états finaux recherchés contiennent 3 leptons, électrons ou muons. Les données utilisées ont été collectées en 2016 et correspondent à une luminosité intégrée de 36.1 fb^{-1}. Ce processus est sensible à la valeur du couplage top-Z et du couplage trilinéaire WWZ. De plus, la mesure précise de la section efficace de tZq pourrait révéler la présence de nouvelle physique, tels que des *vector-like* quarks ou des interactions FCNC. Un intérêt supplémentaire à l'étude de ce processus est qu'il constitue un bruit de fond irréductible pour d'autres analyses ($t\bar{t}Z$, tH, etc.).

La conception de cette étude a été significativement améliorée par rapport à une analyse précédente utilisant les données du Run 1, et de nombreuses options ont été considérées afin d'améliorer la sensibilité à ce signal rare. En particulier, l'accent a été mis sur la fiabilité et la robustesse de la modélisation du bruit de fond NPL, qui représente le principal facteur limitant pour la sensibilité de cette analyse. Diverses études d'optimisation ont permis de mettre en place une MVA performante, basée sur des arbres de décision boostés (BDTs) entraînés pour distinguer les caractéristiques propres aux évènements de signal. De plus, des variables obtenues avec la méthode des éléments de matrice (MEM) ont été inclues dans les BDTs, et ont significativement amélioré leurs performances.

Le signal est extrait via une estimation du maximum de vraisemblance binnée (MLE), simultanément dans la région de signal et dans 2 régions de contrôle enrichies dans les bruits de fond $t\bar{t}Z$, WZ+jets et NPL, afin de mieux contraindre leurs normalisations respectives directement à partir des données. La

section efficace observée pour le processus tZq est $\sigma(pp \to t\ell^+\ell^- q) = 123^{+33}_{-31}$ (stat) $^{+29}_{-23}$ (syst) fb, où ℓ désigne un électron, muon ou τ. Ce résultat est en accord avec la prédiction du SM aux incertitudes près. La *significance* observée (attendue) est 3.7σ (3.1σ), ce qui correspond à la première évidence (au sens statistique du terme) de l'existence du processus tZq. Ces résultats ont été publiés dans le journal Physics Letter B, et présentés lors de conférences. D'autres analyses de CMS poursuivent ce travail, et le processus tZq a récemment été observé pour la première fois.

Le Chapitre 5 décrit une recherche de la production associée d'un quark top et d'un boson de Higgs (tH), qui est le seul processus sensible à l'ordre dominant à la fois à la magnitude du modificateur de couplage top-Higgs, noté κ_t, ainsi qu'à son signe relatif par rapport au modificateur κ_V du couplage des bosons vecteurs au boson de Higgs. Selon que le top quark solitaire est produit via le canal t ou tW, ce processus est noté tHq ou tHW respectivement. Cette analyse est optimisée pour avoir une sensibilité maximale au processus tHq, car il possède une section efficace plus importante ainsi que des propriétés cinématiques caractéristiques. Cependant, les processus tHq, tHW et $t\bar{t}H$ sont tous considérés comme des signaux lors de l'extraction des résultats, du fait qu'ils soient tous sensible à l'ordre dominant à la valeur de κ_t.

Dans le SM ($\kappa_t = \kappa_V = 1$), les processus tHq et tHW ont de faibles sections efficaces, ce qui est en partie dû à un terme d'interférence négative qui apparaît dans leurs diagrammes à l'ordre dominant. Cependant, dans le cas où le signe relatif ou la phase entre κ_t et κ_V seraient différents des prédictions du SM, cette interférence pourrait devenir constructive. En particulier, dans le scénario de couplage inversé du quark top (ITC) correspondant à $\kappa_t = -\kappa_V = -1$, les sections efficaces de ces processus augmentent d'un ordre de grandeur ; ces processus pourraient alors être mis en évidence avec la sensibilité actuelle. Ainsi cette étude vise en premier lieu à mieux contraindre les valeurs possibles du couplage top-Higgs, et à placer une limite supérieure sur la section efficace de tH.

J'ai implémenté et réalisé l'intégralité de l'analyse. Une partie de mon travail a également consisté à synchroniser mon cadre de travail avec celui utilisé

par le groupe recherchant le processus $t\bar{t}H$ ainsi que par une collègue doctorante qui a également realisé l'analyse tH, afin que nous produisions des résultats en commun. Cette analyse recherche des évènements dans les états finaux trileptonique et dileptonique de même signe (3ℓ et $2\ell SS$, où ℓ désigne un électron ou muon), et où le boson de Higgs se désintègre en WW^*, $\tau\bar{\tau}$ ou ZZ^*. Elle est basée sur les données collectées en 2017, ce qui correspond à une luminosité intégrée de 41.5 fb^{-1}.

La conception de cette analyse suit de près celle de la recherche de $t\bar{t}H$ dans des états finaux multileptoniques qui est basée sur les mêmes données. En particulier, cette analyse utilise la même stragégie générale, bénéficie de l'algorithme "lepton MVA" développé par le groupe $t\bar{t}H$ pour identifier les leptons "prompt", et l'estimation des bruits de fond réductibles utilise la même procédure.

J'ai optimisé la MVA en incluant de nouvelles variables d'entrée discriminantes dans l'entraînement des BDTs, dont certaines obtenues avec la MEM, et ai étudié l'influence du "binning" des discriminants sur le résultat final. J'ai étudié des sources d'incertitude systématique liées aux prédictions théoriques des sections efficaces. J'ai également réalisé des études préliminaires en vue de la combinaison à venir avec la recherche du processus $t\bar{t}H$.

Le signal est extrait via un MLE binné des réponses des BDTs dans 3 régions de signal. Pour le scénario du SM, la limite supérieure observée à 95% CL sur la section efficace combinée tH + $t\bar{t}H$ est 0.52 pb, ce qui correspond à 2.87 fois la valeur prédite. Pour le scénario ITC, la limite supérieure observée à 95% CL sur la section efficace combinée tH + $t\bar{t}H$ est 0.80 pb, ce qui correspond à 1.81 fois la valeur prédite. Ces limites prennent en compte le rapport d'embranchement $H \to WW^* + \tau\bar{\tau} + ZZ^*$.

De plus, un balayage de la fonction du maximum de vraisemblance a été réalisé en fonction de κ_t, en supposant $\kappa_V = 1$, ce qui permet d'exclure à 95% CL les valeurs de κ_t en-dehors des intervalles [-1.4, -0.7] et [0.7, 1.9]. Les données favorisent une valeur positive de κ_t par environ 1.5σ. De même, un balayage de la fonction du maximum de vraisemblance en fonction du paramètre α, lié à une possible violation de la symmétrie CP, indique que les données favorisent le scénario d'un boson de Higgs purement scalaire plutôt que le scénario d'un boson de Higgs complètement pseudo-scalaire par environ 2σ. Des limites supérieures sur la section efficace de production du seul processus

tH sont également obtenues en fonction de κ_t et de $\cos(\alpha)$. Ces résultats ont été accepté par le groupe Higgs de CMS dans le cadre de cette thèse.

Par ailleurs, j'ai ré-adapté l'analyse tH dans le but de rechercher des interactions FCNC mettant en jeu le quark top et le boson de Higgs. Bien que de ce type d'interactions soit très fortement supprimé dans le SM, plusieurs scénarios BSM leur prédisent des rapports d'embranchement $\mathcal{B}(t \to Hq)$ (q=u,c) bien supérieurs. Cette analyse cible également les états finaux 3ℓ et $2\ell SS$, et utilise des sélections d'évènement dédiées. Pour rechercher ces signaux, la MVA a été entièrement ré-optimisée.

Les limites supérieures observées à 95% CL sont $\mathcal{B}(t \to Hu) < 0.072\%$ et $\mathcal{B}(t \to Hc) < 0.085\%$, et surpassent les meilleures limites actuelles sur ces rapports d'embranchement. Ces résultats ont été accepté par le groupe Top de CMS dans le cadre de cette thèse.

Perspectives

Plus d'une décennie s'est écoulée depuis les premières collisions produites au LHC, qui marquèrent le début d'une nouvelle ère pour la physique des hautes énergies sur collisionneur. L'excellente performance de cette machine qui accumule les superlatifs, et qui a d'ores et déjà produit plus que l'objectif initial de 150 fb^{-1}, ainsi que sa versatilité en termes d'énergie et de configurations de faisceaux, ont assuré la grande étendue du programme de physique du LHC. De même, les excellentes performances et disponibilités des détecteurs ont été à la mesure des attentes, et ont déjà permis de réaliser de grandes avancées dans le champ de la physique des particules.

La période de prise de données Run 1 (2009–2013) a permis la découverte historique du boson de Higgs par les collaborations ATLAS et CMS, ainsi que la publication de nombreux résultats dans différents domaines. Durant le Run 2 (2015–2018), les expériences ont collecté à un rythme encore plus rapide des données générées à l'énergie inégalée de $\sqrt{s} = 13$ TeV, qui a notamment conduit à des sections efficaces de production plus élevées du boson de Higgs et du quark top. Les mesures des propriétés de ces deux particules ont été significativement améliorées, et l'utilisation de techniques d'analyse de pointe ont permis d'établir leur couplage à l'ordre dominant avec certitude pour la

première fois. Plus généralement, les résultats obtenus au LHC ont permis de confirmer les prédictions du SM à des échelles de précision et d'énergie sans précédent.

La période d'arrêt prolongé en cours (LS2) sera mise à profit pour améliorer le complexe d'injection qui fournit les paquets de protons au LHC. Ce délai permettra aux physiciens de réaliser des analyses basées sur l'intégralité des données collectées durant le Run 2, avec l'objectif d'extraire un maximum d'informations de ces données et de rechercher dans le plus de directions possible. Les collisions redémarreront au LHC à $\sqrt{s} = 14$ TeV vers fin 2021, pour un Run 3 à une luminosité instantanée de $\sim 2\text{–}3 \cdot 10^{34}$ cm^{-2}s^{-1}. La luminosité intégrée totale du LHC devrait alors atteindre ~ 300 fb^{-1}.

Les premiers balayages en tension du Run 3 seront particulièrement intéressants à étudier, car ils pourraient bientôt confirmer que des parties du trajectographe à pistes de CMS ont atteint l'inversion de type. Cela dépendra également de la magnitude du phénomène de "recuit" (*annealing*) durant la période d'arrêt. A partir de ce stade, à mesure que la tension de déplétion complète des capteurs en silicium augmentera, l'analyse présentée dans le Chapitre 3 regagnera progressivement sa sensibilité, et l'évolution de V_{FD} pourra être comparée à la simulation sur une plus grande échelle de fluence.

La période d'arrêt en cours préfigure également la période d'"amélioration Phase-2" (*Phase-2 Upgrade*, 2024–2026), qui marquera le début du LHC Haute-Luminosité (HL-LHC, 2026–2037) [89]. Le HL-LHC collisionera des protons à $\sqrt{s} = 14$ TeV à une luminosité instantanée au moins 5 fois plus élevée qu'au LHC, et devrait délivrer une luminosité intégrée totale de ~ 3000 fb^{-1}.

A cette fin, entre autres améliorations, de nouveaux aimants constitués d'un alliage superconducteur niobium-étain (Nb_3Sn) seront installés, certains déjà durant le LS2. Cette technologie peut supporter de plus forts courants électriques, générant ainsi des champs magnétiques plus puissants pour mieux focaliser les faisceaux. De plus, des *cavités en crabe* seront utilisées pour accroître la surface de recouvrement des paquets de protons qui entrent en collisions, augmentant ainsi la luminosité.

Par ailleurs, les détecteurs seront améliorés pour fonctionner à de plus hauts niveaux d'irradiation, et surtout pour pouvoir continuer à fournir des mesures précises malgré un taux d'empilement moyen de 140–200 (comparé à envrion 40 actuellement). Notamment, le trajectographe de CMS sera remplacé et couvrira une gamme plus étendue en pseudorapidité jusqu'à $|\eta| \simeq 4$, avec une granularité plus élevée. Le système de déclenchement sera amélioré, de nouvelles chambres GEM seront inclues dans le détecteur à muons, des détecteurs à temps de vol seront ajoutés dans les calorimètres pour rejeter les évènements d'empilement, etc.

En combinaison avec des améliorations sur les plans de la compréhension théorique et des techniques d'extraction du signal, il est prévu que ces améliorations profitent significativement à de nombreuses mesures de précision [310, 311], par exemple dans les secteurs électrofaible et du boson de Higgs. Respectant la mission principale du CERN, le HL-LHC étendra donc notre savoir à l'échelle électrofaible, tout en repoussant les limites de technologies de pointe.

Le décuplement du volume de données disponible au HL-LHC profitera également aux mesures liées au quark top solitaire. A partir de la mesure de section efficace de tZq présentée dans le Chapitre 4, une étude phénoménologique [312] a estimé la sensibilité actuelle de ce processus à certains opérateurs EFT en utilisant une procédure simplifiée. Bien que cette étude conclue que la sensibilité d'une mesure inclusive de la section efficace de tZq ne soit actuellement pas suffisante pour sonder ces opérateurs au-delà des limites existentes obtenues via d'autres processus, une étude prospective incite à réaliser des mesures différentielles précises de la section efficace de tZq ; en effet, par exemple dans la queue de distribution du p_T du quark top, les effets de certains opérateurs EFT se trouvent significativement amplifiés.

En utilisant le jeu de données complet du HL-LHC, une telle mesure pourrait atteindre une précision suffisante pour contraindre ces opérateurs au-delà des limites actuelles, fournissant ainsi des informations précieuses sur des scénarios BSM. Un autre but du HL-LHC est de contraindre plus fortement (ou à l'inverse de mettre en évidence) l'existence d'un couplage de gauge anormal WWZ ainsi que les interactions FCNCs [310]. Ceci incite à étudier plus avant

le processus tZq, étant donné qu'il est sensible à ces effets, et parce qu'il constitue un bruit de fond irréductible pour d'autres processus dans lesquels ces effets peuvent être recherchés.

Comme cela a été mentionné dans le Chapitre 5, la combinaison à venir des données de l'ensemble du Run 2 pour les analyses tH et ttH atteindra une sensibilité sans précédent au couplage de Yukawa du quark top, sans qu'il soit nécessaire de formuler des hypothèses concernant la nouvelle physique, et pourrait permettre d'exclure une vaste gamme de valeurs de κ_t. De plus, des études prospectives [313] montrent que l'accroissement du volume de données disponible à la fin du Run 3 pourrait mener à l'exclusion de valeurs négatives de κ_t à plus de 99% CL, et à plus de 5σ avec l'intégralité des données du HL-LHC (en supposant l'absence de nouvelle physique dans les données). Dans le cas contraire, ces données pourraient fournir la preuve d'une valeur négative de κ_t.

Des projections concernants la limite supérieure placée sur le taux de production de tHq suggèrent que ce processus pourrait être observé au HL-LHC, et incitent à réaliser une mesure simultanée avec la section efficace de $t\bar{t}H$ afin d'atteindre une sensibilité optimale. De plus, la sensibilité à κ_t pourrait être encore améliorée en réalisant une analyse combinée incluant d'autres processus. Par exemple, une limite supérieure sur le couplage de Yukawa du quark top a été récemment obtenue par une mesure différentielle par CMS de la section efficace de $t\bar{t}$ [314].

Le processus tHW a une section efficace environ 5 fois plus faible que celle de tHq dans le SM, et devrait également devenir accessible au HL-LHC, en fonction des améliorations réalisées concernant les incertitudes systématiques et les techniques d'extraction du signal.

Un autre processus rare particulèrement intéressant est la production de quatre quarks top. Ce mécanisme est sensible à différents scénarios BSM qui prédisent des accroissement importants de sa section efficace, et a la meilleure sensibilité à l'opérateur EFT qui correspond à un couplage entre quatre quarks top [310]. Ce mode de production représente une autre sonde puissante du couplage de Yukawa du quark top, sans faire aucun hypothèse sur les désintégrations du boson de Higgs. A $\sqrt{s} = 14$ TeV, ce processus a une section efficace

$\sigma(pp \to t\bar{t}t\bar{t}) \sim 15$ fb comparable à celle de tHW. Une étude prospective [315] réalisée par ATLAS suggère que l'observation de ce processus complexe pourrait déjà avoir lieu en utilisant seulement 300 fb^{-1} de données du HL-LHC.

Finalement, les recherches d'interactions FCNC faisant intervenir le quark top devraient également fournir des résultats excitants dans un futur relativement proche. Les résultats prometteurs obtenus dans le cadre de ce travail représentent une première étape vers la combinaison à venir des analyses basées sur l'intégralité du Run 2 ciblant différents canaux de désintégration du boson de Higgs, ce qui repoussera les meilleures limites actuelles ou pourrait potentiellement mener à une découverte.

Des études prospectives [316] prédisent qu'une sensibilité de l'ordre de $\mathcal{B}(t \to Hq) < \mathcal{O}(10^{-4})$ pourrait être atteinte avec le jeu de données entier du HL-LHC, ce qui serait suffisant pour exclure certains scénarios BSM tels que 2HDM ou des modèles à dimensions supplémentaires (*extra-dimensions models*).

Bibliography

[1] ATLAS Collaboration. "Observation of a new particle in the search for the Standard Model Higgs boson with the ATLAS detector at the LHC". In: *Phys. Lett. B* 716 (2012), pp. 1–29.

[2] CMS Collaboration. "Observation of a new boson at a mass of 125 GeV with the CMS experiment at the LHC". In: *Phys. Lett. B* 716 (2012), pp. 30–61.

[3] L. Evans and P. Bryant. "LHC Machine". In: *JINST* 3 (2008), S08001. DOI: 10.1088/1748-0221/3/08/S08001.

[4] R. Bailey. "An Application for Research: the Large Hadron Collider". In: *CERN Yellow Report CERN-2013-007* (2013), pp. 565–574.

[5] D. Griffiths. *Introduction to Elementary Particles*. 2nd ed. Wiley VCH, 2008. ISBN: 9783527406012.

[6] E. Noether. "Invariant Variation Problems". In: *Transport Theory and Statistical Physics* 1 (1971), pp. 186–207.

[7] M.A. Tavel. "Milestones in mathematical physics Noether's theorem". In: *Transport Theory and Statistical Physics* 1 (1971), pp. 183–185.

[8] R. P. Feynman. "Space-time approach to quantum electrodynamics". In: *Phys. Rev.* 76 (1949), pp. 769–789. DOI: 10.1103/PhysRev.76.769.

[9] R. P. Feynman. *QED : The Strange Theory of Light and Matter*. Princeton University Press, 1988. ISBN: 978-0691024172.

[10] T. Lancaster and S. J. Blundell. *Quantum Field Theory for the Gifted Amateur*. Oxford U. Press, 2014. ISBN: 978-0-19-969932-2.

[11] J. Andrea. "Mesure de la section efficace de production de paires de quarks top dans l'expérience CMS au LHC". Thesis. PhD thesis. Université de Strasbourg, 2009.

[12] M. E. Peskin and D. V. Schroeder. *An Introduction To Quantum Field Theory*. 1st ed. Westview Press, 1995. ISBN: 978-0201503975.

[13] M. Thomson. *Modern Particle Physics*. Cambridge University Press, 2013. ISBN: 978-1107034266.

[14] G.'t Hooft. "Renormalization of massless Yang-Mills fields". In: *Nucl. Phys. B* 33 (1971), pp. 173–199.

[15] G.'t Hooft. "Renormalizable Lagrangians for massive Yang-Mills fields". In: *Nucl. Phys. B* 35 (1971), pp. 167–188.

[16] G.'t Hooft and M. Veltman. "Regularization and renormalization of gauge fields". In: *Nucl. Phys. B* 44 (1972), pp. 189–213.

[17] S. Tomonaga. "On a relativistically invariant formulation of the quantum theory of wave fields". In: *Prog. Theor. Phys.* 1 (1946), pp. 27–42. DOI: 10.1143/PTP.1.27.

[18] Z. Koba, T. Tati, and S. Tomonaga. "On a Relativistically Invariant Formulation of the Quantum Theory of Wave Fields. II: Case of Interacting Electromagnetic and Electron Fields". In: *Prog. Theor. Phys.* 2 (1947), pp. 101–116. DOI: 10.1143/ptp/2.3.101.

[19] J. Schwinger. "On Quantum-Electrodynamics and the Magnetic Moment of the Electron". In: *Phys. Rev.* 73 (1948), pp. 416–417. DOI: 10.1103/PhysRev.73.416. URL: https://link.aps.org/doi/10.1103/PhysRev.73.416.

[20] J. Schwinger. "Quantum Electrodynamics. I. A Covariant Formulation". In: *Phys. Rev.* 74 (1948), pp. 1439–1461. DOI: 10.1103/PhysRev.74.1439. URL: https://link.aps.org/doi/10.1103/PhysRev.74.1439.

[21] J. Schwinger. "Quantum Electrodynamics. II. Vacuum Polarization and Self-Energy". In: *Phys. Rev.* 75 (1949), pp. 651–679. DOI: 10.1103/PhysRev.75.651. URL: https://link.aps.org/doi/10.1103/PhysRev.75.651.

[22] J. Schwinger. "Quantum Electrodynamics. III. The Electromagnetic Properties of the Electron—Radiative Corrections to Scattering". In: *Phys. Rev.* 76 (1949), pp. 790–817. DOI: 10.1103/PhysRev.76.790. URL: https://link.aps.org/doi/10.1103/PhysRev.76.790.

[23] D. Hanneke, S. Fogwell Hoogerheide, and G. Gabrielse. "Cavity control of a single-electron quantum cyclotron: Measuring the electron magnetic moment". In: *Phys. Rev. A 83, 052122* (2011).

[24] M. Tanabashi et al. (Particle Data Group). "The Review of Particle Physics". In: *Phys. Rev. D 98, 030001* (2018).

[25] M.Gell-Mann. "A schematic model of baryons and mesons". In: *Phys. Letters* 8 (1964), pp. 214–215.

[26] J. D. Bjorken. "An SU_3 model for strong interaction symmetry and its breaking". In: *CERN-TH-412* (1964).

[27] E. D. Bloom et al. "High-Energy Inelastic e-p Scattering at 6° and 10°". In: *Phys. Rev. Lett.* 23 (1969), p. 930.

[28] M. Breidenbach et al. "Observed Behavior of Highly Inelastic Electron-Proton Scattering". In: *Phys. Rev. Lett.* 23 (1969), p. 935.

[29] "SLAC Linear Collider Conceptual Design Report". In: *SLAC-R-0229* (1980).

[30] T. Heinze and O. Hallonsten. "The reinvention of the SLAC National Accelerator Laboratory, 1992–2012". In: *History and Technology* 33:3 (2017), pp. 300–332.

[31] E. M. Riordan. "The Discovery of quarks". In: *Science* 256 (1992), pp. 1287–1293. DOI: 10.1126/science.256.5061.1287.

[32] K. G. Wilson. "Confinement of quarks". In: *Phys. Rev. D* 10 (1974), p. 2445.

[33] C. T. H. Davies et al. "High-Precision Lattice QCD Confronts Experiment". In: *Phys. Rev. Lett.* 92 (2004), p. 022001.

[34] J. D. Bjorken. "Asymptotic Sum Rules at Infinite Momentum". In: *Phys. Rev.* 179 (1969), p. 1547.

[35] R.D. Ball et al. "Parton distributions from high-precision collider data". In: *The European Physical Journal C* 77 (2017). DOI: 10.1140/epjc/s10052-017-5199-5. URL: https://doi.org/10.1140/epjc/s10052-017-5199-5.

[36] E. Fermi. "Tentativo di una Teoria Dei Raggi β". In: *Nuovo Cim.* 11 (1934).

[37] C. N. Yang. "Fermi's β-decay Theory". In: *Asia Pacific Physics Newsletter* 1 (2012), pp. 27–30.

[38] C. S. Wu et al. "Experimental Test of Parity Conservation in Beta Decay". In: *Phys. Rev* 105 (1957), p. 1413.

[39] S. L. Glashow. "The renormalizability of vector meson interactions". In: *Nuclear Physics* 10 (1959), pp. 107–117.

[40] A. Salam and J. C. Ward. "Weak and electromagnetic interactions". In: *Nuovo Cim.* 11 (1959), pp. 568–577.

[41] S. Weinberg. "A Model of Leptons". In: *Phys. Rev. Lett.* 19 (1967), p. 1264.

[42] R.R. Volkas. "Sterile Neutrino. A short introduction". In: *Prog. Part. Nucl. Phys.* 48 (2002), pp. 161–174.

[43] J.M. Conrad and M.H. Shaevitz. "Sterile Neutrinos: An Introduction to Experiments". In: *Adv. Ser. Direct. High Energy Phys.* 28 (2018), pp. 391–442.

[44] UA1 Collaboration. "Experimental observation of isolated large transverse energy electrons with associated missing energy at s=540 GeV". In: 122 (1983), pp. 103–116.

[45] UA2 Collaboration. "Observation of single isolated electrons of high transverse momentum in events with missing transverse energy at the CERN pp collider". In: *Phys. Lett. B* 5-6 (1983), pp. 476–485.

[46] P. M. Watkins. "Discovery Of The W And Z Bosons". In: *Contemp. Phys.* 27 (1986), pp. 291–324.

[47] C. Rubbia. "The Discovery Of The W And Z Bosons". In: *Phys. Rept.* 239 (1994), pp. 241–284.

[48] J.A. Aguilar-Saavedra. "Top flavour-changing neutral interactions: theoretical expectations and experimental detection". In: *Acta Phys.Polon. B* 35 (2004), pp. 2695–2710.

[49] L. Maiani. "The GIM Mechanism: origin, predictions and recent uses". In: Opening Talk, Rencontres de Moriond, EW Interactions and Unified Theories, La Thuile, Valle d'Aosta, Italia, 2-9 March. 2013.

[50] N. Cabibbo. "Unitary symmetry and leptonic decays". In: *Phys. Rev. Lett.* 10 (1963), p. 531.

[51] M. Kobayashi and T. Maskawa. "CP-Violation in the Renormalizable Theory of Weak Interaction". In: *Phys. Rev. Lett.* 49 (1973), pp. 652–657.

[52] S. Descotes-Genon and P. Koppenburg. "The CKM Parameters". In: *Annual Review of Nuclear and Particle Science* 67.1 (2017), pp. 97–127. DOI: 10.1146/annurev-nucl-101916-123109.

[53] A. Höcker and Z. Ligeti. "CP Violation and the CKM Matrix". In: *Annual Review of Nuclear and Particle Science* 56.1 (2006), pp. 501–567. DOI: 10.1146/annurev.nucl.56.080805.140456.

[54] Peter W. Higgs. "Broken Symmetries and the Masses of Gauge Bosons". In: *Phys. Rev. Lett.* 13 (1964), p. 508.

[55] F. Englert and R. Brout. "Broken Symmetry and the Mass of Gauge Vector Mesons". In: *Phys. Rev. Lett.* 13 (1964), p. 321.

[56] G. S. Guralnik, C. R. Hagen, and T. W. B. Kibble. "Global Conservation Laws and Massless Particles". In: *Phys. Rev. Lett.* 13 (1964), p. 585.

[57] W. de Boer. "The Discovery of the Higgs Boson with the CMS Detector and its Implications for Supersymmetry and Cosmology". In: *Time and Matter 2013 (TAM2013) Venice, Italy*. 2013.

[58] S. Weinberg. "Physical Processes in a Convergent Theory of the Weak and Electromagnetic Interactions". In: *Phys. Rev. Lett.* 27 (1971), p. 1688.

[59] S. Weinberg. "General Theory of Broken Local Symmetries". In: *Phys. Rev. D* 7 (1973), p. 1068.

[60] H. Yukawa. "On the Interaction of Elementary Particles". In: *Progress of Theoretical Physics Supplement* 1 (1955), pp. 1–10.

[61] A-M. Magnan. *The Higgs boson at the LHC: standard model Higgs properties and beyond standard model searches*. Tech. rep. CERN, 2018. URL: http://cds.cern.ch/record/2633105.

[62] J. Piedra. *New results on Higgs boson properties. New results on Higgs boson properties*. Tech. rep. CERN, 2017. URL: https://cds.cern.ch/record/2289869.

[63] M. L. Perl et al. "Evidence for Anomalous Lepton Production in e^+e^- Annihilation". In: *Phys. Rev. Lett.* 35 (1975).

[64] S. W. Herb et al. "Observation of a Dimuon Resonance at 9.5 GeV in 400-GeV Proton-Nucleus Collisions". In: *Phys. Rev. Lett.* 39 (1977).

[65] R. R. Wilson. "The Tevatron". In: *Physics Today* 30 (1977).

[66] S. Holmes, R. S. Moore, and V. Shiltsev. "Overview of the Tevatron collider complex: goals, operations and performance". In: *JINST* 6 (2011).

[67] V. Lebedev and V. Shiltsev. *Accelerator Physics at the Tevatron Collider*. Springer, 2014. ISBN: 9781493908851.

[68] CDF Collaboration. "Observation of top quark production in $\bar{p}p$ collisions". In: *Phys. Rev. Lett.* 74 (1995), p. 2626.

[69] D0 Collaboration. "Observation of the top quark". In: *Phys. Rev. Lett.* 74 (1995), p. 2632.

[70] G. Dissertori. "The pre-LHC Higgs hunt". In: *Phil. Trans. R. Soc. A* 373 (2015).

[71] CMS Collaboration. "Measurement of the $t\bar{t}$ production cross section using events with one lepton and at least one jet in pp collisions at $\sqrt{s}$ = 13 TeV". In: *JHEP 09 051* (2017).

[72] A. Giammanco and R. Schwienhorst. "Single top-quark production at the Tevatron and the LHC". In: *Rev. Mod. Phys. 90, 35001* (2018).

[73] R. Harlander, M. Kramer, and M. Schumacher. *Bottom-quark associated Higgs-boson production: reconciling the four- and five-flavour scheme approach*. Tech. rep. arXiv:1112.3478. CERN-PH-TH-2011-134. FR-PHENO-2011-009. TTK-11-17. WUB-11-0. 2011. URL: https://cds.cern.ch/record/1407669.

[74] F. Krauss and D. Napoletano. "Towards a fully massive five-flavor scheme". In: *Physical Review D* 98 (2017). DOI: 10.1103/PhysRevD.98.096002.

[75] F. Maltoni, G. Ridolfi, and M. Ubiali. "B-initiated processes at the LHC: A reappraisal". In: *Journal of High Energy Physics* 2013 (2012). DOI: 10.1007/JHEP04(2013)095.

[76] J. M. Campbell et al. "Next-to-Leading-Order Predictions for t-Channel Single-Top Production at Hadron Colliders". In: *Phys. Rev. Lett.* 102 (2009). DOI: 10.1103/PhysRevLett.102.182003.

[77] E. Boos. "The Top Quark". In: *Phys. Usp. 185, 1241* (2015).

[78] A. Lenz. "Constraints on a fourth generation of fermions from Higgs Boson searches". In: *Adv. High Energy Phys.* (2013), p. 910275. DOI: 10.1155/2013/910275.

[79] M. Frandsen, I. Masina, and F. Sannino. "Fourth Lepton Family is Natural in Technicolor". In: *Physical Review D* 81 (2009). DOI: 10.1103/PhysRevD.81.035010.

[80] D. Das, A. Kundu, and I. Saha. "Higgs data does not rule out a sequential fourth generation with an extended scalar sector". In: *Physical Review D* 97 (2018). DOI: 10.1103/PhysRevD.97.011701.

[81] R. Sharafiddinov. "A New Family with a Fourth Lepton Flavour". In: *Phys. Essays* 30 (2012), pp. 150–155. DOI: 10.4006/0836-1398-30.2.150.

[82] T. M. P. Tait and C.-P. Yuan. "Single Top Production as a Window to Physics Beyond the Standard Model". In: *Phys. Rev. D* 63 (2000), pp. 014–018.

[83] *Useful Diagrams of Top Signals and Backgrounds*. https://www-d0.fnal.gov/Run2Physics/top/top_public_web_pages/top_feynman_diagrams.html.

[84] CMS Collaboration. "Combined measurements of Higgs boson couplings in proton-proton collisions at $\sqrt{s}$= 13 TeV". In: *Submitted to Eur. Phys. J. C* (2018).

[85] F. Maltoni. "Higgs physics". Lecture given at the 2018 European School of High-Energy Physics (ESHEP). 2018.

[86] ATLAS Collaboration. "Observation of Higgs boson production in association with a top quark pair at the LHC with the ATLAS detector". In: *Phys. Lett. B 784 173* (2018).

[87] CMS Collaboration. "Observation of $t\bar{t}H$ production". In: *Phys. Rev. Lett.* 120 (2018), 231801. 17 p. DOI: 10.1103/PhysRevLett.120.231801. URL: https://cds.cern.ch/record/2312113.

[88] N. Deutschmann et al. "Top-Yukawa contributions to bbH production at the LHC". In: *CERN-TH-2018-175, CP3-18-52, NIKHEF/2018-037* (2018).

[89] G. Apollinari et al. "High Luminosity Large Hadron Collider HL-LHC". In: *CERN Yellow Report* (2015), pp. 1–19.

[90] *Prospects for the measurement of the rare Higgs boson decay $H \to \mu\mu$ with 3000 fb^{-1} of pp collisions collected at $\sqrt{s} = 14$ TeV by the ATLAS experiment*. Tech. rep. CERN, 2018. URL: https://cds.cern.ch/record/2319741.

[91] X. Chen. *Prospects of LHC Higgs Physics at the end of Run III - Talk presented at the International Workshop on Future Linear Colliders (LCWS2016), Morioka, Japan, 5-9 December 2016*. Tech. rep. 2017. URL: https://cds.cern.ch/record/2260490.

[92] J. Brau, Y. Okada, and N. Walker et al. "Top-Yukawa contributions to bbH production at the LHC". In: *FERMILAB-DESIGN-2007-03, FERMILAB-PUB-07-794-E* (2007).

[93] F. Zwicky. "The Redshift of Extragalactic Nebulae". In: *Helvetica Physica Acta* 6 (1933), pp. 110–127.

[94] F.S. Queiroz. "WIMP Theory Review". In: *PoS EPS-HEP2017* 080 (2017).

[95] L. Roszkowski, E.M. Sessolo, and S. Troja. "WIMP dark matter candidates and searches—current status and future prospects". In: *Rept. Prog. Phys.* 81 (2018), pp. 95–123.

[96] Planck Collaboration. "Planck 2018 results. VI. Cosmological parameters". 2018. URL: https://arxiv.org/abs/1807.062094.

[97] J.D. Wells. "Higgs naturalness and the scalar boson proliferation instability problem". In: *Synthese* 94 (2017), pp. 477–490.

[98] S.P. Martin. "A Supersymmetry primer". In: *Adv. Ser. Direct. High Energy Phys.* 21 (2010), pp. 1–153.

[99] Y. Shadmi. "Introduction to Supersymmetry". In: *CERN Yellow Report CERN* 003 (2016), pp. 95–123.

[100] C.P. Burgess. "Ann. Rev. Nucl. Part. Sci." In: *Phys. Rev. Lett.* 57 (2007), pp. 329–362.

[101] S. Weinberg. "Baryon- and Lepton-Nonconserving Processes". In: *Phys. Rev. Lett.* 43 (1979).

[102] B. Grzadkowski et al. "Dimension-Six Terms in the Standard Model Lagrangian". In: *JHEP* 85 (2010).

[103] D. M. Sendall. "The World-Wide Web past present and future, and its application to medicine". In: CERN-OPEN-97-005 (1997). URL: http://cds.cern.ch/record/321530.

[104] *LEP design report*. Tech. rep. CERN-LEP-84-01. 1984. URL: https://cds.cern.ch/record/102083.

[105] G. Giacomelli and R. Giacomelli. "The LEP Legacy". In: hep-ex/0503050 (2005), 218–232. 15 p. DOI: 10.1142/9789812701893_0016. URL: http://cds.cern.ch/record/830222.

[106] A.S. Thompson. "Mass measurement of the W-boson using the ALEPH detector at LEP". In: *Nucl. Phys. A* (2000), pp. 132–136.

[107] OPAL Collaboration. "Measurement of the Z^0 Mass and Width with the OPAL Detector at LEP". In: *Phys. Lett. B* 231 (1989), pp. 530–538.

[108] R. Barate et al. "Search for the standard model Higgs boson at LEP". In: *Phys. Lett.* B565 (2003), pp. 61–75. DOI: 10.1016/S0370-2693(03)00614-2.

[109] G. Brumfiel. "Eight-month delay for LHC". In: *Nature* 455 (2008), pp. 1015–1015. DOI: doi:10.1038/4551015a.

[110] *CERN releases analysis of LHC incident*. https://home.cern/news/press-release/cern/cern-releases-analysis-lhc-incident.

[111] E. Mobs. "The CERN accelerator complex - August 2018. Complexe des accélérateurs du CERN - Août 2018". 2018. URL: https://cds.cern.ch/record/2636343.

[112] *Definition of a duoplasmatron*. https://writing-guidelines.web.cern.ch/entries/duoplasmatron.

[113] M. Davier. *LHC : le boson de Higgs*. Chap. 7. Le collège, 2013. ISBN: 978-2746506770.

[114] S. Angius et al. "The Upgrade of MA.RI.S.A. Facility from 6.5 to 10 Tesla Design, Construction and Preliminary Test". In: *11th International Conference on Magnet Technology (MT-11). Springer, Dordrecht* (1990).

[115] L.R.F. Castillo. "The Large Hadron Collider". In: *The Search and Discovery of the Higgs Boson*. Morgan and Claypool Publishers, 2015. ISBN: 978-1-6817-4078-2. DOI: 10.1088/978-1-6817-4078-2ch3. URL: http://dx.doi.org/10.1088/978-1-6817-4078-2ch3.

[116] ATLAS Collaboration. "The ATLAS Experiment at the CERN Large Hadron Collider". In: *JINST 3 S08003* (2008).

[117] CMS Collaboration. "The CMS experiment at the CERN LHC". In: *JINST 3 S08004* (2008).

[118] ALICE Collaboration. "The ALICE experiment at the CERN LHC". In: *International Journal of Modern Physics A* 3.08 (2008), S08002–S08002.

[119] ALICE Collaboration. "Performance of the ALICE experiment at the CERN LHC". In: *International Journal of Modern Physics A* 29 (2014).

[120] H. Satz. "The Quark-Gluon Plasma – A Short Introduction". In: *Nuclear Physics A* 862-863 (2011), pp. 4–14. URL: https://doi.org/10.1016/j.nuclphysa.2011.05.014.

[121] LHCb Collaboration. "The LHCb Detector at the LHC". In: *JINST 3* (2008).

[122] LHCb Collaboration. *Observation of CP violation in charm decays*. Tech. rep. arXiv:1903.08726. LHCB-PAPER-2019-006. 2019. URL: http://cds.cern.ch/record/2668357.

[123] L. Pescatore. "Lepton flavour and lepton number violation searches at the LHCb experiment". In: *39th International Conference on High Energy Physics (ICHEP 2018) Seoul, Gangnam-Gu, Korea, Republic of, July 4-11, 2018*. eprint: 1809.06756.

[124] TOTEM Collaboration. "The TOTEM Experiment at the CERN Large Hadron Collider". In: *Journal of Instrumentation* 3.08 (2008), S08007–S08007. DOI: 10.1088/1748-0221/3/08/s08007. URL: https://doi.org/10.1088\%2F1748-0221\%2F3\%2F08\%2Fs08007.

[125] G. Latino. "The TOTEM Experiment at the LHC". In: *Proceedings of XLIIIth Rencontres de Moriond - QCD session, La Thuile (Italy), March 14th - 21st, 2009* ().

[126] A. Giovanni et al. "TOTEM experiment at the LHC: status and program". In: 2006. DOI: 10.22323/1.035.0019.

[127] S.A. Khalek et al. "The ALFA Roman Pot Detectors of ATLAS". In: *JINST 11 (2016) P11013* ().

[128] B. Acharya et al. "The physics programme of the MoEDAL experiment at the LHC". In: *International Journal of Modern Physics A* 29 (2014).

[129] V.A. Mitsou for the MoEDAL Collaboration. "The MoEDAL experiment at the LHC: status and results". In: *J. Phys. Conf. Ser.* 873 (2017).

[130] S. Takashi et al. "Results of the LHCf experiment and the forward measurements at the LHC". In: *EPJ Web of Conferences* 145 (2017), p. 09002. DOI: 10.1051/epjconf/201614509002.

[131] W. Herr and B. Muratori. "Concept of luminosity". 2006. URL: https://cds.cern.ch/record/941318.

[132] *LHC report : full house for the LHC*. https://home.cern/news/news/accelerators/lhc-report-full-house-lhc.

[133] *LHC report : imaginative injectors*. https://cds.cern.ch/journal/CERNBulletin/2016/32/News%20Articles/2201549?ln=en.

[134] *New bunch production scheme breaks luminosity record*. https://cerncourier.com/new-bunch-production-scheme-breaks-luminosity-record/.

[135] *RF manipulations for higher brightness LHC-type beams*. 4th International Particle Accelerator Conference, Shanghai, China, 12 - 17 May 2013, pp.2600.

[136] *The Tevatron legacy : a luminosity story*. https://cerncourier.com/the-tevatron-legacy-a-luminosity-story/.

[137] *CMS public results on luminosity*. https://twiki.cern.ch/twiki/bin/view/CMSPublic/LumiPublicResults.

[138] *78 reconstructed vertices in event from high-pileup run 198609*. https://cds.cern.ch/record/1479324.

[139] Z. Marshall. "Simulation of Pile-up in the ATLAS Experiment". In: *J. Phys.: Conf. Ser* 513 (2014).

[140] *Pileup mitigation at CMS in 13 TeV data*. Tech. rep. 2019. URL: http://cds.cern.ch/record/2683784.

[141] G. Soyez. "Pileup mitigation at the LHC: A theorist's view". In: *Phys. Rept.* 803 (2019), pp. 1–158. DOI: 10.1016/j.physrep.2019.01.007.

[142] *CMS detector design*. https://cms.cern/news/cms-detector-design.

[143] *CMS people statistics*. https://cms.cern/collaboration/people-statistics.

[144] *Performance of reconstruction and identification of tau leptons in their decays to hadrons and tau neutrino in LHC Run-2*. Tech. rep. CERN, 2016. URL: https://cds.cern.ch/record/2196972.

[145] M. Cacciari and G.P. Salam. "Pileup subtraction using jet areas". In: *Phys. Lett. B* 659 (2008), pp. 119–126. DOI: https://doi.org/10.1016/j.physletb.2007.09.077.

[146] *The CMS magnet project: Technical Design Report*. Technical Design Report CMS. CERN, 1997. URL: https://cds.cern.ch/record/331056.

[147] V. Klyukhin et al. "The CMS Magnetic Field Map Performance". In: *IEEE Trans. Appl. Supercond.* 20 (2010). DOI: 10.1109/TASC.2010.2041200.

[148] CMS Collaboration. *The CMS tracker system project: Technical Design Report*. Technical Design Report CMS. 1997. URL: https://cds.cern.ch/record/368412.

[149] *The CMS tracker: addendum to the Technical Design Report*. Technical Design Report CMS. CERN, 2000. URL: https://cds.cern.ch/record/490194.

[150] CMS Collaboration. "Description and performance of track and primary-vertex reconstruction with the CMS tracker". In: *JINST 9* (2014).

[151] *Studies of Tracker Material*. Tech. rep. CMS-PAS-TRK-10-003. 2010. URL: http://cds.cern.ch/record/1279138.

[152] *CMS Tracker Material Budget plots*. https://twiki.cern.ch/twiki/bin/view/CMSPublic/TrackerMaterialBudgetplots.

[153] V.R. Tavolaro. "The Phase 1 CMS Pixel detector upgrade". In: *Journal of Instrumentation* 11 (2016), pp. C12010–C12010. DOI: 10.1088/1748-0221/11/12/c12010. URL: https://doi.org/10.1088%2F1748-0221%2F11%2F12%2Fc12010.

[154] A. Dominguez et al. *CMS Technical Design Report for the Pixel Detector Upgrade*. Tech. rep. CERN-LHCC-2012-016. CMS-TDR-11. 2012. URL: https://cds.cern.ch/record/1481838.

[155] M. Dragicevic et al. "Test Beam Performance Measurements for the Phase I Upgrade of the CMS Pixel Detector". In: *JINST* 12 (2017), P05022. DOI: 10.1088/1748-0221/12/05/P05022.

[156] G.H. Dirkes. "Construction of the CMS silicon strip tracker". In: *Nucl. Instrum. Methods Phys. Res., A* 581 (2007), pp. 299–302. URL: http://cds.cern.ch/record/1065409.

[157] L.L. Jones et al. "The APV25 deep submicron readout chip for CMS detectors". In: *Conf. Proc.* C9909201 (1999), pp. 162–166.

[158] C. Genta and G. Sansone. "Module integration on the inner shells (TIB) of the CMS tracker". In: *IEEE Nuclear Science Symposium Conference Record* (2006). DOI: 10.1109/NSSMIC.2006.355992.

[159] *The CMS electromagnetic calorimeter project: Technical Design Report*. Technical Design Report CMS. CERN, 1997. URL: https://cds.cern.ch/record/349375.

[160] M. Anfreville et al. "Laser monitoring system for the CMS lead tungstate crystal calorimeter". In: *Nucl. Instrum. Meth. A594* (2008), pp. 292–320.

[161] R. Teixeira. "Overview of Energy Reconstruction, and Electron and Photon Performances with the CMS ECAL in Run II". In: *Journal of Physics: Conference Series* 928 (2017).

[162] *CMS Technical Design Report for the Phase 1 Upgrade of the Hadron Calorimeter*. Technical Design Report CMS. CERN, 2012. URL: https://cds.cern.ch/record/1481837?ln=fr.

[163] A. Colaleo et al. *CMS Technical Design Report for the Muon Endcap GEM Upgrade*. Tech. rep. CERN-LHCC-2015-012. CMS-TDR-013. 2015. URL: https://cds.cern.ch/record/2021453.

[164] CMS Collaboration. "Performance of the CMS muon detector and muon reconstruction with proton-proton collisions at $\sqrt{s} = 13$ TeV". In: *JINST* 13 (2018), P06015.

[165] V. Yu. Karjavin. "The upgrade of endcap CMS muon system". In: *Physics of Particles and Nuclei* 49 (2018), pp. 54–59.

[166] W. Ahmed et al. "The Triple GEM Detector Control System for CMS forward muon spectrometer upgrade". In: *Journal of Instrumentation* 12 (2017), P02003–P02003. DOI: 10.1088/1748-0221/12/02/p02003. URL: https://doi.org/10.1088%2F1748-0221%2F12%2F02%2Fp02003.

[167] CMS Collaboration. "The CMS trigger system". In: *JINST* 12 (2017), pp. 10–20.

[168] A. Tapper and A. Darin. *CMS Technical Design Report for the Level-1 Trigger Upgrade*. Tech. rep. CERN-LHCC-2013-011. CMS-TDR-12. 2013. URL: https://cds.cern.ch/record/1556311.

[169] M. Jeitler. *The upgrade of the CMS trigger system*. Tech. rep. CMS-CR-2014-079. 2014. URL: https://cds.cern.ch/record/1703266.

[170] *Worldwide LHC Computing Grid*. http://wlcg.web.cern.ch/.

[171] D. Bonacorsi. "The CMS Computing Model". In: *Nuclear Physics B - Proceedings Supplements* 172 (2007), pp. 53–56.

[172] J. Adelman et al. "CMS computing operations during run 1". In: *Journal of Physics: Conference Series* 513 (2014), p. 032040. DOI: 10.1088/1742-6596/513/3/032040. URL: https://doi.org/10.1088%2F1742-6596%2F513%2F3%2F032040.

[173] CMS Collaboration. "Particle-flow reconstruction and global event description with the CMS detector". In: *JINST* 12 (2017), P10003. DOI: 10.1088/1748-0221/12/10/P10003.

[174] R. Fruhwirth. "Application of Kalman filtering to track and vertex fitting". In: *Nucl. Instrum. Meth.* A262 (1987), pp. 444–450. DOI: 10.1016/0168-9002(87)90887-4.

[175] P. Billoir. "Progressive track recognition with a Kalman like fitting procedure". In: *Comput. Phys. Commun.* 57 (1989).

[176] P. Billoir and S. Qian. "Simultaneous pattern recognition and track fitting by the Kalman filtering method". In: *Nucl. Instrum. Meth. A* 294 (1990), pp. 219–228.

[177] W. Adam et al. "Reconstruction of electrons with the Gaussian-sum filter in the CMS tracker at LHC". In: *eConf C0303241 (2003) TULT009; J.Phys. G31 (2005) N9* 10 (2003), P06005–P06005. DOI: 10.1088/0954-3899/31/9/N01.

[178] CMS Collaboration. "Performance of electron reconstruction and selection with the CMS detector in proton-proton collisions at $\sqrt{s}$= 8 TeV". In: *Journal of Instrumentation* 10 (2015), P06005–P06005. DOI: 10.1088/1748-0221/10/06/p06005.

[179] CMS Collaboration. "Reconstruction and identification of lepton decays to hadrons and at CMS". In: *JINST* 11 (2016), P01019. DOI: 10.1088/1748-0221/11/01/P01019.

[180] CMS Collaboration. "Performance of photon reconstruction and identification with the CMS detector in proton-proton collisions at $\sqrt{s}$ = 8 TeV". In: *JINST* 10 (2015), P08010. DOI: 10.1088/1748-0221/10/08/P08010.

[181] M. Cacciari, G.P. Salam, and G. Soyez. "The anti-k_t jet clustering algorithm". In: *JHEP* 04 (2008), p. 063. DOI: 10.1088/1126-6708/2008/04/063.

[182] *FastJet user manual*. Tech. rep. CERN, 2011. URL: 10.1140/epjc/s10052-012-1896-2.

[183] *Jet algorithms performance in 13 TeV data*. Tech. rep. CERN, 2017. URL: https://cds.cern.ch/record/2256875.

[184] CMS Collaboration. "Jet energy scale and resolution in the CMS experiment in pp collisions at 8 TeV". In: *Journal of Instrumentation* 12 (2017), P02014–P02014. DOI: 10.1088/1748-0221/12/02/p02014.

[185] CMS collaboration. "Identification of heavy-flavour jets with the CMS detector in pp collisions at 13 TeV". In: *JINST* 13 (2018), P05011. DOI: 10.1088/1748-0221/13/05/P05011.

[186] *Performance of missing energy reconstruction in 13 TeV pp collision data using the CMS detector*. Tech. rep. CMS-PAS-JME-16-004. 2016. URL: https://cds.cern.ch/record/2205284.

[187] S. Banerjee. "Readiness of CMS simulation towards LHC startup". In: 119 (2008), p. 032006. DOI: 10.1088/1742-6596/119/3/032006. URL: https://doi.org/10.1088%2F1742-6596%2F119%2F3%2F032006.

[188] D.J. Lange et al. "Upgrades for the CMS simulation". In: *Journal of Physics: Conference Series* 608 (2015), p. 012056. DOI: 10.1088/1742-6596/608/1/012056.

[189] G. Boudoul et al. "Monte Carlo Production Management at CMS". In: *Journal of Physics: Conference Series* 664 (2015), p. 072018. DOI: 10.1088/1742-6596/664/7/072018. URL: https://doi.org/10.1088%2F1742-6596%2F664%2F7%2F072018.

[190] C. Wissing. "Managing the CMS Data and Monte Carlo Processing during LHC Run 2". In: *Journal of Physics: Conference Series* 898 (2017), p. 052012. DOI: 10.1088/1742-6596/898/5/052012.

[191] S. Weinzierl. "Introduction to Monte Carlo methods". In: *Topical lectures given at the Research School Subatomic Physics, Amsterdam* (2000).

[192] A. Buckley et al. *Monte Carlo event generators for high energy particle physics event simulation*. Tech. rep. arXiv:1902.01674. 2019. URL: http://cds.cern.ch/record/2657127.

[193] A. Buckley et al. "General-purpose event generators for LHC physics". In: *Physics Reports* 504 (2011), pp. 145 –233. DOI: https://doi.org/10.1016/j.physrep.2011.03.005.

[194] T. Sjöstrand et al. "An Introduction to PYTHIA 8.2". In: *Comput. Phys. Commun.* 191 (2015), pp. 159–177. DOI: 10.1016/j.cpc.2015.01.024.

[195] M. Bahr et al. "Herwig++ Physics and Manual". In: *Eur. Phys. J.* C58 (2008), pp. 639–707. DOI: 10.1140/epjc/s10052-008-0798-9.

[196] J. Alwall et al. "The automated computation of tree-level and next-to-leading order differential cross sections, and their matching to parton shower simulations". In: *JHEP* 07 (2014), p. 079. DOI: 10.1007/JHEP07(2014)079.

[197] C. Oleari. "The POWHEG BOX". In: *Nuclear Physics B - Proceedings Supplements* 205-206 (2010), pp. 36–41. DOI: 10.1016/j.nuclphysbps.2010.08.016.

[198] CMS Collaboration. "Event generator tunes obtained from underlying event and multiparton scattering measurements". In: *The European Physical Journal C* 76 (2016). DOI: 10.1140/epjc/s10052-016-3988-x.

[199] S. Agostinelli et al. "GEANT4: A Simulation toolkit". In: *Nucl. Instrum. Meth.* A506 (2003), pp. 250–303. DOI: 10.1016/S0168-9002(03)01368-8.

[200] M. Hildreth et al. "CMS Full Simulation for Run-2". In: *Journal of Physics: Conference Series* 664 (2015), p. 072022. DOI: 10.1088/1742-6596/664/7/072022. URL: https://doi.org/10.1088%2F1742-6596%2F664%2F7%2F072022.

[201] R. Rahmat, R. Kroeger, and A. Giammanco. "The fast simulation of the CMS experiment". In: *J. Phys. Conf. Ser.* 396 (2012).

[202] *Strip Tracker radiation damages results*. https://twiki.cern.ch/twiki/bin/view/CMSPublic/StripsRadiationPlots2017.

[203] *Strip Tracker radiation damages results*. https://twiki.cern.ch/twiki/bin/view/CMSPublic/StripRadiationFeb2019StripDepletionVoltages.

[204] "Silicon Strip Tracker Performance results 2018". 2018. URL: https://cds.cern.ch/record/2638062.

[205] S. Ramo. "Currents Induced by Electron Motion". In: *Proceedings of the IRE* 27 (1939), pp. 584–585. DOI: 10.1109/JRPROC.1939.228757.

[206] Z. He. "Review of the Shockley–Ramo theorem and its application in semiconductor gamma-ray detectors". In: *Nucl. Inst. Meth. in Phys. Res. A* 463 (2001), pp. 250–267.

[207] F. Hartmann. *Evolution of Silicon Sensor Technology in Particle Physics*. Springer, 2009. ISBN: 978-3-642-06416-6.

[208] J. Kemmer. "Fabrication of low noise silicon radiation detectors by the planar process". In: *Nucl. Instrum. Meth.* 169 (1980), pp. 499–502. DOI: 10.1016/0029-554X(80)90948-9.

[209] J. Kemmer. "Improvement of Detector Fabrication by the planar Process". In: *Nucl. Instrum. Meth.* A226 (1984).

[210] D. Bortoletto. "How and why silicon sensors are becoming more and more intelligent?" In: *Journal of Instrumentation* 10 (2015). DOI: 10.1088/1748-0221/10/08/C08016.

[211] T. Bergauer. "Process Quality Control of Silicon Strip Detectors for the CMS Tracker". MA thesis. Institut fur Hochenergiephysik, 2004.

[212] ROSE Collaboration. *2nd RD48 Status Report: R&D on silicon for future experiments*. Tech. rep. CERN-LHCC-98-039. CERN, 1998. URL: http://cds.cern.ch/record/376432.

[213] M. Moll. "Radiation damage in silicon particle detectors: Microscopic defects and macroscopic properties". PhD thesis. Hamburg U., 1999. URL: http://www-library.desy.de/cgi-bin/showprep.pl?desy-thesis99-040.

[214] C. Barth. "Physikalische Analyse des Ansprechverhaltens des CMS Siliziumdetektors beim Betrieb am LHC". Dr. Karlsruher Institut für Technologie (KIT), 2013. URL: https://ekp-invenio.physik.uni-karlsruhe.de/record/48288.

[215] A. Ruzin et al. "Studies of radiation hardness of oxygen enriched silicon detectors". In: *Nuclear Instruments and Methods in Physics Research Section A: Accelerators, Spectrometers, Detectors and Associated Equipment* 426 (1999), pp. 94 –98. ISSN: 0168-9002. DOI: https://doi.org/10.1016/S0168-9002(98)01476-4. URL: http://www.sciencedirect.com/science/article/pii/S0168900298014764.

[216] B.C. MacEvoy, G. Hall, and K. Gill. "Defect evolution in irradiated silicon detector material". In: *Nuclear Instruments and Methods in Physics Research Section A: Accelerators, Spectrometers, Detectors and Associated Equipment* 374 (1996), pp. 12 –26. ISSN: 0168-9002. DOI: https://doi.org/10.1016/0168-9002(96)37410-X. URL: http://www.sciencedirect.com/science/article/pii/016890029637410X.

[217] S.J. Moloi and M. McPherson. "Reverse annealing studies of irradiated silicon by use of current–voltage measurements". In: *Nuclear Instruments and Methods in Physics Research Section B: Beam Interactions with Materials and Atoms* 440 (2019), pp. 64 –67. ISSN: 0168-583X. DOI: https://doi.org/10.1016/j.nimb.2018.11.025. URL: http://www.sciencedirect.com/science/article/pii/S0168583X18306712.

[218] S. Paoletti et al. "The powering scheme of the CMS tracker". In: 2004.

[219] G. Magazzu, A. Marchioro, and P. Moreira. "The detector control unit: an ASIC for the monitoring of the CMS silicon tracker". In: *IEEE Trans. on Nucl. Science* 51 (2004).

[220] T. Böhlen et al. "The FLUKA Code: Developments and Challenges for High Energy and Medical Applications". In: *Nucl. Data Sheets* 120 (2014). DOI: 10.1016/j.nds.2014.07.049.

[221] J. A. Aguilar-Saavedra et al. "Handbook of vectorlike quarks: Mixing and single production". In: *Phys. Rev.* D88.9 (2013), p. 094010. DOI: 10.1103/PhysRevD.88.094010.

[222] CMS Collaboration. "Search for single production of vector-like quarks decaying to a Z boson and a top or a bottom quark in proton-proton collisions at $\sqrt{s} =$ 13 TeV". In: *JHEP* 1705.CMS-B2G-16-001. CMS-B2G-16-001 (2017). DOI: 10.1007/JHEP05(2017)029. URL: https://cds.cern.ch/record/2243017.

[223] CMS Collaboration. "Search for vector-like T and B quark pairs in final states with leptons at $\sqrt{s} = 13$ TeV". In: *JHEP* 08 (2018), p. 177. DOI: 10.1007/JHEP08(2018)177.

[224] F. Maltoni et al. "Choosing the Factorization Scale in Perturbative QCD". 2007.

[225] R.D. Ball et al. "Parton distributions for the LHC Run II". In: *JHEP* 04 (2015), p. 040. DOI: 10.1007/JHEP04(2015)040.

[226] J. R. Klein and A. Roodman. "Blind analysis in nuclear and particle physics". In: *Ann. Rev. Nucl. Part. Sci.* 55 (2005), pp. 141–163. DOI: 10.1146/annurev.nucl.55.090704.151521.

[227] CMS collaboration. "Search for associated production of a Z boson with a single top quark and for tZ flavour-changing interactions in pp collisions at $\sqrt{s}$=8 TeV". In: *Journal of High Energy Physics* 2017 (2017). DOI: 10.1007/JHEP07(2017)003.

[228] ATLAS Collaboration. "Measurement of the production cross-section of a single top quark in association with a Z boson in proton–proton collisions at 13 TeV with the ATLAS detector". In: *Physics Letters B* 780 (2018), pp. 557 –577. ISSN: 0370-2693. DOI: https://doi.org/10.1016/j.physletb.2018.03.023.

[229] CMS Collaboration. "Observation of Single Top Quark Production in Association with a Z Boson in Proton-Proton Collisions at $\sqrt{s}$=13 TeV". In: *Phys. Rev. Lett.* 122 (2019). DOI: 10.1103/PhysRevLett.122.132003.

[230] *Summaries of CMS cross section measurements*. https://twiki.cern.ch/twiki/bin/view/CMSPublic/PhysicsResultsCombined.

[231] R. Frederix, E. Re, and P. Torrielli. "Single-top t-channel hadroproduction in the four-flavour scheme with POWHEG and aMC@NLO". In: *Journal of High Energy Physics* 2012 (2012). DOI: 10.1007/JHEP09(2012)130.

[232] CMS collaboration. "Identification of b-quark jets with the CMS experiment". In: *Journal of Instrumentation* 8 (2013), P04013–P04013. DOI: 10.1088/1748-0221/8/04/p04013. URL: https://doi.org/10.1088%2F1748-0221%2F8%2F04%2Fp04013.

[233] CMS Collaboration. *Identification of b quark jets at the CMS Experiment in the LHC Run 2*. CMS Physics Analysis Summary CMS-PAS-BTV-15-001. 2016. URL: https://cds.cern.ch/record/2138504.

[234] CMS Collaboration. "Search for associated production of a Z boson with a single top quark and for tZ flavour-changing interactions in pp collisions at $\sqrt{s} = 8$ TeV". In: *JHEP 07 (2017) 003* (), p. 2445.

[235] J. Duarte et al. "Fast inference of deep neural networks in FPGAs for particle physics". In: *JINST* 13 (2018). DOI: 10.1088/1748-0221/13/07/P07027.

[236] K. Albertsson et al. "Machine Learning in High Energy Physics Community White Paper". In: *J. Phys. Conf. Ser.* 1085 (2018). DOI: 10.1088/1742-6596/1085/2/022008.

[237] A. Hoecker et al. "TMVA: Toolkit for Multivariate Data Analysis". In: *PoS* ACAT (2007).

[238] L. Breiman et al. *Classification and Regression Trees*. Chapman and Hall, 1984. ISBN: 9780412048418.

[239] S. B. Kotsiantis. "Decision trees: a recent overview". In: *Artificial Intelligence Review* 39 (2013). DOI: 10.1007/s10462-011-9272-4.

[240] Y. Coadou. "Boosted Decision Trees and Applications". In: *EPJ Web of Conferences* 55 (2013). DOI: 10.1051/epjconf/20135502004.

[241] I. Goodfellow, Y. Bengio, and A. Courville. *Deep Learning*. http://www.deeplearningbook.org. MIT Press, 2016.

[242] D. Guest, K. Cranmer, and D. Whiteson. "Deep Learning and its Application to LHC Physics". In: *Ann. Rev. Nucl. Part. Sci.* 68 (2018), pp. 161–181. DOI: 10.1146/annurev-nucl-101917-021019.

[243] J. Alwall et al. "The automated computation of tree-level and next-to-leading order differential cross sections, and their matching to parton shower simulations". In: *HEP 07 (2014) 079* ().

[244] I. Volobouev. "Matrix Element Method in HEP: Transfer Functions, Efficiencies, and Likelihood Normalization". 2011. URL: https://arxiv.org/abs/1101.2259.

[245] F. Fiedler et al. "The matrix element method and its application to measurements of the top quark mass". In: *Nuclear Instruments and Methods in Physics Research Section A: Accelerators, Spectrometers, Detectors and Associated Equipment* 624 (2010), pp. 203 –218. DOI: https://doi.org/10.1016/j.nima.2010.09.024.

[246] D0 Collaboration. "A precision measurement of the mass of the top quark". In: *Nature* 429 (2004), pp. 638–642. DOI: 10.1038/nature02589.

[247] D0 Collaboration. "Observation of Single Top-Quark Production". In: *Phys. Rev. Lett.* 103 (2009). DOI: 10.1103/PhysRevLett.103.092001.

[248] CDF Collaboration. "Observation of Electroweak Single Top-Quark Production". In: *Phys. Rev. Lett.* 103 (2009). DOI: 10.1103/PhysRevLett.103.092002.

[249] CDF Collaboration. "Precision measurement of the top-quark mass from dilepton events at CDF II". In: *Phys. Rev. D* 75 (2007). DOI: 10.1103/PhysRevD.75.031105.

[250] CMS Collaboration. "Search for a standard model Higgs boson produced in association with a top-quark pair and decaying to bottom quarks using a matrix element method". In: *The European Physical Journal C* 75 (2015). DOI: 10.1140/epjc/s10052-015-3454-1.

[251] ATLAS Collaboration. "Search for the Standard Model Higgs boson produced in association with top quarks and decaying into $b\bar{b}$ in pp collisions at $\sqrt{s}$=8TeV with the ATLAS detector". In: *The European Physical Journal C* 75 (2015). DOI: 10.1140/epjc/s10052-015-3543-1.

[252] J. Alwall, A. Freitas, and O. Mattelaer. "Matrix element method and QCD radiation". In: *Phys. Rev. D* 83 (2011). DOI: 10.1103/PhysRevD.83.074010.

[253] *Github repository of the MEM code*. https://github.com/nchanon/MEMmultilepton.

[254] P.Artoisenet et al. "Automation of the matrix element reweighting method". In: *JHEP* 12 (2010), p. 068. DOI: 10.1007/JHEP12(2010)068.

[255] G. Lepage. "A new algorithm for adaptive multidimensional integration". In: *Journal of Computational Physics* 27 (1978). DOI: https://doi.org/10.1016/0021-9991(78)90004-9.

[256] A. Buckley et al. "LHAPDF6: parton density access in the LHC precision era". In: *Eur. Phys. J.* C75 (2015), p. 132. DOI: 10.1140/epjc/s10052-015-3318-8.

[257] *CMS Luminosity Measurements for the 2016 Data Taking Period*. Tech. rep. CERN, 2017. URL: https://cds.cern.ch/record/2257069.

[258] J. Butterworth et al. "PDF4LHC recommendations for LHC Run II". In: *J. Phys.* G43 (2016), p. 023001. DOI: 10.1088/0954-3899/43/2/023001.

[259] *Combine Tool*. http://cms-analysis.github.io/HiggsAnalysis-CombinedLimit/.

[260] ATLAS Collaboration, CMS Collaboration, LHC Higgs Combination Group. *Procedure for the LHC Higgs boson search combination in Summer 2011*. Tech. rep. CMS-NOTE-2011-005. ATL-PHYS-PUB-2011-11. 2011. URL: https://cds.cern.ch/record/1379837.

[261] G. Cowan et al. "Asymptotic formulae for likelihood-based tests of new physics". In: *The European Physical Journal C* 71 (2011). DOI: 10.1140/epjc/s10052-011-1554-0.

[262] L. Moneta et al. "The RooStats Project". In: *PoS* ACAT2010 (2010), p. 057. DOI: 10.22323/1.093.0057.

[263] J.S. Conway. "Incorporating Nuisance Parameters in Likelihoods for Multisource Spectra". 2011. URL: https://cds.cern.ch/record/1333496.

[264] R. Barlow and C. Beeston. "Fitting using finite Monte Carlo samples". In: *Computer Physics Communications* 77 (1993), pp. 219 –228. ISSN: 0010-4655. DOI: https://doi.org/10.1016/0010-4655(93)90005-W.

[265] F. James and M. Roos. "Minuit: A System for Function Minimization and Analysis of the Parameter Errors and Correlations". In: *Comput. Phys. Commun.* 10 (1975), pp. 343–367. DOI: 10.1016/0010-4655(75)90039-9.

[266] S.S. Wilks. "The Large-Sample Distribution of the Likelihood Ratio for Testing Composite Hypotheses". In: *Annals Math. Statist.* 9.1 (1938), pp. 60–62. DOI: 10.1214/aoms/1177732360.

[267] G. Ranucci. "The Profile likelihood ratio and the look elsewhere effect in high energy physics". In: *Nucl. Instrum. Meth.* A661 (2012), pp. 77–85. DOI: 10.1016/j.nima.2011.09.047.

[268] A. Wald. "Tests of Statistical Hypotheses Concerning Several Parameters When the Number of Observations is Large". In: *Transactions of the American Mathematical Society* 54 (1943), pp. 426–482. ISSN: 00029947. URL: http://www.jstor.org/stable/1990256.

[269] L. Demortier and L. Lyons. "Everything you always wanted to know about pulls". 2002. URL: http://physics.rockefeller.edu/luc/technical_reports/cdf5776_pulls.pdf.

[270] CMS Collaboration. "Measurement of the WZ production cross section in pp collisions at s=13 TeV". In: *Physics Letters B* 766 (2017), pp. 268 –290. ISSN: 0370-2693. DOI: https://doi.org/10.1016/j.physletb.2017.01.011.

[271] CMS Collaboration. "Measurement of the associated production of a single top quark and a Z boson in pp collisions at $\sqrt{s}$=13TeV". In: *Physics Letters B* 779 (2018), pp. 358 –384. DOI: https://doi.org/10.1016/j.physletb.2018.02.025.

[272] *Search for production of a Higgs boson and a single top quark in multilepton final states in proton collisions at* $\sqrt{s} = 13$ *TeV*. Tech. rep. CMS-PAS-HIG-17-005. 2017. URL: https://cds.cern.ch/record/2264553.

[273] *Measurement of the associated production of a Higgs boson with a top quark pair in final states with electrons, muons and hadronically decaying* τ *leptons in data recorded in 2017 at* $\sqrt{s} = 13$ *TeV*. Tech. rep. 2018. URL: http://cds.cern.ch/record/2649199.

[274] *Measurements of the Higgs boson production and decay rates and constraints on its couplings from a combined ATLAS and CMS analysis of the LHC pp collision data at* $\sqrt{s}$ *= 7 and 8 TeV*. Tech. rep. CMS-PAS-HIG-15-002. ATLAS-CONF-2015-044. CERN, 2015. URL: https://cds.cern.ch/record/2053103.

[275] F. Bezrukov and M. Shaposhnikov. "Why should we care about the top quark Yukawa coupling?" In: *Z. Eksp. Teor. Fiz.* 147 (2014), 389. 8 p. DOI: 10.7868/S0044451015030015. URL: https://cds.cern.ch/record/1968356.

[276] M. Chala and J. Santiago. "Physics of the Interplay Between the Top Quark and the Higgs Boson". In: *Journal of Physics: Conference Series* 452 (2013), p. 012008. DOI: 10.1088/1742-6596/452/1/012008. URL: https://doi.org/10.1088%2F1742-6596%2F452%2F1%2F012008.

[277] *Search for the tH(H*$\rightarrow b\bar{b}$*) process in pp collisions at* $\sqrt{s} = 13$ *TeV and study of Higgs boson couplings*. Tech. rep. CERN, 2018. URL: https://cds.cern.ch/record/2621422.

[278] M. Farina et al. "Lifting degeneracies in Higgs couplings using single top production in association with a Higgs boson". In: *Journal of High Energy Physics* 2013 (2012). DOI: 10.1007/JHEP05(2013)022.

[279] F. Demartin et al. "Higgs production in association with a single top quark at the LHC". In: *Eur. Phys. J.* C75 (2015), p. 267. DOI: 10.1140/epjc/s10052-015-3475-9.

[280] F. Demartin et al. "tWH associated production at the LHC". In: *Eur. Phys. J.* C77 (2017), p. 34. DOI: 10.1140/epjc/s10052-017-4601-7.

[281] S. D. Rindani, P. Sharma, and A. Shivaji. "Unraveling the CP phase of top-Higgs coupling in associated production at the LHC". In: *Physics Letters B* 761 (2016), pp. 25 –30. DOI: https://doi.org/10.1016/j.physletb.2016.08.002. URL: http://www.sciencedirect.com/science/article/pii/S0370269316304221.

[282] *Studies of Tracker Material*. Tech. rep. CMS-PAS-TRK-10-003. 2010. URL: http://cds.cern.ch/record/1279138.

[283] *Optimisation of the ATLAS b-tagging performance for the 2016 LHC Run*. Tech. rep. ATL-PHYS-PUB-2016-012. CERN, 2016. URL: https://cds.cern.ch/record/2160731.

[284] *Performance of the DeepJet b tagging algorithm using 41.9 fbp−1 of data from proton-proton collisions at 13 TeV with Phase 1 CMS detector*. Tech. rep. 2018. URL: https://cds.cern.ch/record/2646773.

[285] *Keras documentation*. https://keras.io/.

[286] CMS Collaboration. *CMS luminosity measurement for the 2017 data-taking period at $\sqrt{s}$ = 13 TeV*. CMS Physics Analysis Summary CMS-PAS-LUM-17-004. CERN, 2017.

[287] S. Heinemeyer et al. *Handbook of LHC Higgs Cross Sections: 3. Higgs Properties: Report of the LHC Higgs Cross Section Working Group*. CERN Yellow Reports: Monographs. 2013. URL: http://cds.cern.ch/record/1559921.

[288] *List and description of the official LHAPDF 6.2 PDF sets*. https://lhapdf.hepforge.org/pdfsets.html.

[289] G. Cowan. "Statistics for Searches at the LHC". In: *Proceedings, 69th Scottish Universities Summer School in Physics : LHC Phenomenology (SUSSP69): St.Andrews, Scotland, August 19-September 1, 2012*, pp. 321–355. DOI: 10.1007/978-3-319-05362-2_9.

[290] A.L. Read. "Presentation of search results: The CL_s technique". In: *J. Phys. G* 28 (2002), p. 2693. DOI: 10.1088/0954-3899/28/10/313.

[291] T. Junk. "Confidence level computation for combining searches with small statistics". In: *Nucl. Instrum. Meth. A* 434 (1999), p. 435. DOI: 10.1016/S0168-9002(99)00498-2.

[292] R. Barate et al. "Search for the standard model Higgs boson at LEP". In: *Phys. Lett.* B565 (2003), pp. 61–75. DOI: 10.1016/S0370-2693(03)00614-2.

[293] T. Aaltonen et al. "Combination of Tevatron Searches for the Standard Model Higgs Boson in the W^+W^- Decay Mode". In: *Phys. Rev. Lett.* 104 (2010), p. 061802. DOI: 10.1103/PhysRevLett.104.061802.

[294] K. Agashe et al., ed. *Snowmass 2013 Top quark working group report*. 2013 Community Summer Study on the Future of U.S. Particle Physics: Snowmass on the Mississippi (CSS2013): Minneapolis, MN, USA, July 29-August 6, 2013. The organization. 2013. URL: https://arxiv.org/abs/1311.2028.

[295] J. J. Cao et al. "SUSY-induced FCNC top-quark processes at the large hadron collider". In: *Phys. Rev.* D75 (2007), p. 075021. DOI: 10.1103/PhysRevD.75.075021.

[296] D. Atwood, L. Reina, and A. Soni. "Phenomenology of two Higgs doublet models with flavor changing neutral currents". In: *Phys. Rev.* D55 (1997), pp. 3156–3176. DOI: 10.1103/PhysRevD.55.3156.

[297] G.C. Branco et al. "Theory and phenomenology of two-Higgs-doublet models". In: *Physics Reports* 516 (2012), pp. 1 –102. DOI: https://doi.org/10.1016/j.physrep.2012.02.002. URL: http://www.sciencedirect.com/science/article/pii/S0370157312000695.

[298] S. Bejar. "Flavor changing neutral decay effects in models with two Higgs boson doublets: Applications to LHC Physics". PhD thesis. Barcelona, Autonoma U., 2006.

[299] J.M. Yang, B.L Lin Young, and X. Zhang. "Top-quark rare decay $t \to ch$ in R-parity-violating SUSY". In: *Phys. Lett. B* 510 (2001), pp. 227–235. URL: http://cds.cern.ch/record/486156.

[300] R. Barbier et al. "R-parity violating supersymmetry". In: *Phys. Rept.* 420 (2005), pp. 1–202. DOI: 10.1016/j.physrep.2005.08.006.

[301] G. Eilam et al. "Top-quark rare decay $t \to ch$ in R-parity-violating SUSY". In: *Phys. Lett. B* 510 (2001), pp. 227–235. URL: http://cds.cern.ch/record/486156.

[302] K. Agashe, G. Perez, and A. Soni. "Collider Signals of Top Quark Flavor Violation from a Warped Extra Dimension". In: *Phys. Rev.* D75 (2007), p. 015002. DOI: 10.1103/PhysRevD.75.015002.

[303] FCC Collboration. *Future Circular Collider*. Tech. rep. CERN-ACC-2018-0056. Submitted for publication to Eur. Phys. J. C. CERN, 2018. URL: https://cds.cern.ch/record/2651294.

[304] CMS collaboration. "Search for the flavor-changing neutral current interactions of the top quark and the Higgs boson which decays into a pair of b quarks at $\sqrt{s} = 13$ TeV". In: *Journal of High Energy Physics* 2018 (2018), p. 102. DOI: 10.1007/JHEP06(2018)102. URL: https://doi.org/10.1007/JHEP06(2018)102.

[305] ATLAS collaboration. "Search for flavour-changing neutral current top quark decays t $\to$ Hq in pp collisions at $\sqrt{s} = 8$ TeV with the ATLAS detector". In: *Journal of High Energy Physics* 2015 (2015). DOI: 10.1007/JHEP12(2015)061. URL: https://doi.org/10.1007/JHEP12(2015)061.

[306] ATLAS collaboration. "Search for top quark decays t $\to$ qH with H $\to \gamma\gamma$ using the ATLAS detector". In: *Journal of High Energy Physics* 2014 (2014). DOI: 10.1007/JHEP06(2014)008. URL: https://doi.org/10.1007/JHEP06(2014)008.

[307] CMS collaboration. "Search for top quark decays via Higgs-boson-mediated flavor-changing neutral currents in pp collisions $\sqrt{s} = 8$ TeV". In: *Journal of High Energy Physics* 2017.2 (2017), p. 79. DOI: 10.1007/JHEP02(2017)079. URL: https://doi.org/10.1007/JHEP02(2017)079.

[308] *Search for top quark decays t→Hq with 36fb^{1} of pp collision data at $\sqrt{s}$ = 13 TeV with ATLAS detector*. Tech. rep. 2018. URL: http://cds.cern.ch/record/2639676.

[309] "Search for flavor-changing neutral currents in top quark decays $t \to Hc$ and $t \to Hu$ in multilepton final states in proton-proton collisions at $\sqrt{s} = 13$ TeV with the ATLAS detector". In: *Phys. Rev. D* 98 (2018), p. 032002. DOI: 10.1103/PhysRevD.98.032002.

[310] P. Azzi et al. *Standard Model Physics at the HL-LHC and HE-LHC*. Tech. rep. 2018. URL: https://cds.cern.ch/record/2650160.

[311] X. Cid Vidal et al. *Beyond the Standard Model Physics at the HL-LHC and HE-LHC*. Tech. rep. CERN, 2018. URL: https://cds.cern.ch/record/2650173.

[312] C. Degrande et al. "Single-top associated production with a Z or H boson at the LHC: the SMEFT interpretation". In: *Journal of High Energy Physics* 2018 (2018). DOI: 10.1007/JHEP10(2018)005.

[313] *Sensitivity projections for Higgs boson properties measurements at the HL-LHC*. Tech. rep. CMS-PAS-FTR-18-011. 2018. URL: https://cds.cern.ch/record/2647699.

[314] CMS Collaboration. *Measurement of the top quark Yukawa coupling from $\mathrm{t\bar{t}}$ kinematic distributions in the lepton+jets final state in proton-proton collisions at $\sqrt{s} = 13$ TeV*. Tech. rep. arXiv:1907.01590. CMS-TOP-17-004-003. Submitted to Phys. Rev. D. 2019. URL: http://cds.cern.ch/record/2681021.

[315] *HL-LHC prospects for the measurement of the Standard Model four-top-quark production cross-section*. Tech. rep. 2018. URL: https://cds.cern.ch/record/2651870.

[316] *Expected sensitivity of ATLAS to FCNC top quark decays $t \to Zu$ and $t \to Hq$ at the High Luminosity LHC*. Tech. rep. 2016. URL: https://cds.cern.ch/record/2209126.

Université de Strasbourg

Nicolas Tonon

cnrs dépasser les frontières

Recherche de la production d'un quark top solitaire associé à un boson Z ou un boson de Higgs avec l'expérience CMS au LHC

RÉSUMÉ :

Cette thèse présente 4 études basées sur les données collectées par l'expérience CMS durant le Run 2 du LHC. Premièrement, une recherche de la production associée d'un quark top solitaire et d'un boson Z (tZq) est réalisée. La mesure de la section efficace de ce processus rare permet de sonder des couplages prédits par le Modèle Standard (MS), et est sensible à des processus de nouvelle physique. Cette étude utilise les données collectées en 2016 et cible des états finaux multileptoniques. Dans le cadre de cette thèse, l'analyse est réalisée depuis la sélection d'évènements jusqu'aux résultats finaux. L'accent est notamment mis sur l'extraction du signal avec des techniques avancées, et sur l'estimation à partir des données des bruits de fond réductibles. La première mise en évidence du processus tZq est présentée.

La deuxième analyse recherche la production associée d'un quark top solitaire et d'un boson de Higgs (tH) dans des états finaux multileptoniques. Il s'agit du seul processus sensible à l'ordre dominant à la magnitude et au signe du couplage de Yukawa du quark top, qui pourrait fournir des indications sur le MS et la nouvelle physique. L'intégralité de l'analyse est réalisée, avec les données collectées en 2017. Des contraintes sont notamment placées sur la valeur du couplage de Yukawa du top, et sur la section efficace de tH. De plus, l'analyse est ré-adaptée afin de rechercher des processus top-Higgs FCNC ayant des états finaux similaires. Les meilleures limites actuelles sont obtenues pour ces processus.

La dernière analyse vise à étudier le vieillissement dû à l'irradiation du trajectographe à pistes de silicium de CMS. Ce détecteur est soumis à une importante dose de radiation qui modifie les propriétés de ses senseurs avec le temps. Des balayages en tension ont été régulièrement analysés pour surveiller l'évolution du paramètre de tension de déplétion complète. L'algorithme utilisé pour extraire les informations pertinentes des données a été amélioré, et l'analyse a été étendue à l'ensemble du sous-détecteur.

ABSTRACT:

This thesis presents 4 different studies based on the data collected by the CMS experiment during the Run 2 of the LHC. Firstly, a search for the associated production of a single top quark and a Z boson (tZq) is conducted. The measurement of the cross section of this rare process probes Standard Model (SM) couplings, and is sensitive to Beyond the Standard Model (BSM) processes. This search uses data collected in 2016 and targets the trilepton final state. As part of this thesis, the analysis is carried out from the event selection up to the final results. A particular emphasis is put on the signal extraction, using advanced techniques, and on the data-driven estimation of reducible backgrounds. The first evidence for the tZq process is presented.

The second analysis targets the associated production of a single top quark and a Higgs boson (tH) in multilepton final states. It is the only process sensitive at leading order both to the magnitude and sign of the top quark Yukawa coupling, which may provide insights on both SM and BSM physics. The entire analysis is performed, using 2017 data. Notably, constraints are placed on the value of the top Yukawa, and on the tH cross section. In addition, the analysis is re-adapted to search for top-Higgs FCNC processes with similar final states. The most stringent upper limits to date are set for these processes.

The last study aims at monitoring the ageing of the silicon strip tracker of CMS with irradiation. This detector is subjected to high levels of radiation, which is expected to change the properties of its sensors over time. Dedicated bias scans were regularly analysed to monitor the evolution of the important full depletion voltage parameter. The algorithm extracting the relevant information from the data was improved, and the analysis was extended to the entire subdetector.

KEYWORDS: LHC, CMS, single top quark, tZq, tHq, top Yukawa, FCNC, tracker, ageing